Anna M. Track

Modifying Surfaces Relevant for Organic Devices: An Experimental and Theoretical Investigation

DISSERTATION

zur Erlangung des akademischen Grades
Doktorin der technischen Wissenschaften

Doktoratsstudium der technischen Wissenschaften
Technische Physik

Technische Universität Graz

Betreuer:

Ao.Univ.-Prof. Dipl.-Ing. Dr.techn. Egbert Zojer

Institut für Festkörperphysik, Technische Universität Graz

Mitbetreuer:

Ao.Univ.-Prof. Mag. Dr.rer.nat. Dr.techn. Michael G. Ramsey

Institut für Physik, Karl-Franzens-Universität Graz

Graz, Mai 2010

Für meine Eltern

Wer schaffen will, muß fröhlich sein

Theodor Fontane

Du wirst es nie zu Tüchtgem bringen
Bei deines Grames Träumereien,
die Tränen lassen nichts gelingen:
Wer schaffen will muß fröhlich sein.

Wohl Keime wecken mag der Regen,
der in die Scholle niederbricht,
doch golden Korn und Erntesegen
reift nur heran bei Sonnenlicht.

Acknowledgments

I want to thank my supervisors Prof. Egbert Zojer and Prof. Mike Ramsey. You gave me the opportunity to open my chemical mind to the exiting field of physics. It was a pleasure for me to discover surface science from two different sides and to discover the different ways you guided me the last years. I would not miss a second. Thank you!

I want to thank Georg Koller. You had calm and time for me and my research problems. Thank you!

I want to thank in particular all current and former members of the 'Egbert' group - in alphabetical order: Andrej, David, Ferdinand, Gery, Harald, Lorenz, Lukas L., Lukas W., Marco, Oliver, Peter, Simon, Stefan, Thomas, Veronika - and Piet from the TU Graz. Thanks for your friendship!

I want to thank all current and former working colleagues and professors from the surface science group, especially, Alexander, Andreas, Margareta, Martin, Sina, Steve, Thomas U., Thomas H., Prof. Sarko Surnev and Prof. Falko Netzer for integrating me in the group.

I want to thank Georg Heimel for his support and his suggestions during the whole time of my thesis. Without him I would not have been able to accomplish any reasonable theoretical results.

I want to thank Alexandra Lex-Balducci, Thomas Höfler, Thomas Griesser, Matthias Edler, Gregor Trimmel and Prof. Wolfgang Kern. Thank you for taking over the chemical part of my thesis, including nearly all sample preparations and all molecule synthesis.

I want to thank Philipp Stadler. The cooperation with you was very interesting and successful.

I want to thank Prof. Gregor Witte and his current and former working group for their cooperation and the possibility to visit Marburg (Germany).

I want to thank my parents, my sister, my brother and Stefan for their love and support.

Deutsche Fassung:
Beschluss der Curricula-Kommission für Bachelor-, Master- und Diplomstudien vom 10.11.2008
Genehmigung des Senates am 1.12.2008

EIDESSTATTLICHE ERKLÄRUNG

Ich erkläre an Eides statt, dass ich die vorliegende Arbeit selbstständig verfasst, andere als die angegebenen Quellen/Hilfsmittel nicht benutzt, und die den benutzten Quellen wörtlich und inhaltlich entnommene Stellen als solche kenntlich gemacht habe.

Graz, am …… ……..
(Unterschrift)

Englische Fassung:

STATUTORY DECLARATION

I declare that I have authored this thesis independently, that I have not used other than the declared sources / resources, and that I have explicitly marked all material which has been quoted either literally or by content from the used sources.

…… ……..
date (signature)

Abstract of the
PhD Thesis

Modifying Surfaces Relevant for Organic Devices: An Experimental and Theoretical Investigation

Anna M. Track
Institut für Festkörperphysik, Technische Universität Graz
and
Institut für Physik, Karl-Franzens-Universität Graz

The modification of surfaces is an important and ubiquitous issue in the field of organic electronics. The possibility to change the properties of surfaces using organic thin layers is discussed in this thesis. To obtain a better control of such modified surfaces and to understand their properties, various techniques have been applied. Experimentally, thin films are investigated using X-ray photoelectron spectroscopy. Specifically, self-assembled monolayers (SAMs) and thin films on gold and silicon-oxide substrates with various functional photoreactive head groups were studied with respect to their surface chemistry and selectivity. Furthermore, applying surface science techniques to an organic thin film transistor, a direct relation between the threshold voltage shift and the change of the work function of the organic semiconductor can be established. Ultraviolet photoemission spectroscopy shows, that a built-in potential of the interface of the polymeric interlayer (BCB) with the organic semiconductor (C_{60}) is the reason for the improved device performance. Finally, theoretical band structure calculations were performed, to get a deeper insight into binding preferences, the molecular arrangement and the electronic structure of different SAMs on Au(111). The impact of sulfur and selenium as docking atoms, and the change due to the methyl-, phenyl- and anthracene-backbones is investigated.

Kurzfassung der
Doktorarbeit

Modifikation von Oberflächen für organische Bauelemente: Eine experimentelle und theoretische Studie

Anna M. Track
Institut für Festkörperphysik, Technische Universität Graz
und
Institut für Physik, Karl-Franzens-Universität Graz

Im Forschungsgebiet der organischen Bauelemente ist es von besonderer Bedeutung, die Eigenschaften von Grenzflächen kontrolliert zu verändern. Durch organische Zwischenschichten können Oberflächen modifiziert werden und somit Bauteile verbessert werden. Um eine bessere Kontrolle und ein besseres Verständnis für diese modifizierten Oberflächen zu erhalten, sind unterschiedliche Techniken und Methoden notwendig. In dieser Arbeit wurden verschiedene organische Schichten experimentell mit Hilfe der Röntgenphotoelektronenspektroskopie untersucht. Im Speziellen wurden selbstassemblierte Monolagen (SAMs) und dünne Schichten auf Gold und Siliziumoxid mit verschiedenen funktionalen und photoreaktiven Gruppen in Bezug auf ihre chemischen Eigenschaften und ihre Selektivität studiert. Weiters konnte durch Verwendung oberflächensensitiver Methoden ein direkter Zusammenhang zwischen der Verschiebung der Schwellenspannung und der Änderung der Austrittsarbeit des organischen Halbleiters eines Dünnschichttransistors gefunden werden. Messungen mit UV-Photoelektronenspektroskopie zeigten, dass durch die Modifikation des Potenzials an der Grenzfläche zwischen der Polymer-Schicht (BCB) und dem organische Halbleiter (C_{60}) der Transistor verbessert wurde. Abschließend wurden theoretische Bandstrukturrechungen durchgeführt, die einen tieferen Einblick in das Bindungsverhalten, die molekulare Anordnung und die damit zusammenhängende elektronische Struktur von selbstassemblierte Monolagen von Anthracenthiolat auf Au(111) ermöglichen. Der Rolle von Schwefel und Selen als Ankeratom und der Einfluss von Methyl, Phenyl und Anthracen als organischer Rest wurden untersucht.

Contents

1 Introduction

In the last decades organic electronics has become a research area of increasing importance. The field covers a multitude of different devices. The most common ones are organic thin film transistors, organic light emitting devices, organic solar cell, and organic sensors (see e. g. reference 1,2,3,4. The biggest advantage of organic electronics over inorganic devices is their flexibility, on the one hand, referring to their mechanical properties and, on the other hand, meaning that the whole universe of organic chemistry can be exploited to find organic compounds useful both in terms of processability and property tuning.

One important research field in the area of organic electronics is the modification of surfaces.[5,6,7] The reason for modifying the surface properties in organic devices can range from work-function modification over adhesion changes to polarity changes, to list a few considered in this thesis. Furthermore, often the surfaces are patterned to obtain different surface properties in the same device.

To obtain a comprehensive knowledge of surface modification in organic devices experimental and theoretical investigations have to be performed. This requires an interdisciplinary research network including chemistry, physics and surface science. In this thesis, investigations of surface modifications and surface patterning have been performed experimentally and theoretically with the goal of obtaining better control and knowledge of surfaces. In the following, a short overview of the thesis is given.

In the first part of the thesis (section 2), the used experimental and theoretical methods are introduced. On one hand, the focus lies on photoelectron spectroscopy, which has been performed under the supervision of Prof. Michael G. Ramsey and Priv.-Doz. Georg Koller (Institute of Physics, Karl-Franzens-Universität Graz). On the other hand, band-structure calculations based on density functional theory , which have been carried out in the group of Prof. Egbert Zojer (Institute if Solid State Physics, TU Graz) are presented. Furthermore, the basic functionality of organic thin-film transistors is described.

The following chapters contain the results gained throughout the thesis.

Starting with the experimental results obtained by surface modifications, section 3 shows the possibility of patterning thin layers and self-assembled monolayers. X-ray photoelectron spectroscopy was used to investigate the modified surfaces and to evaluate the reproducibility of the film preparation, regarding the chemical composition and the film thickness. This work has been performed in intensive collaboration with the group of Univ.-Doz. Gregor Trimmel (Institute of Chemistry and Technology of Materials, Technische Universität Graz) and Prof. Wolfgang Kern (Institute of Chemistry of Polymeric Materials, Montanuniversität Leoben). Dr. Alexandra Lex-Balducci, Dr. Thomas Höfler and Dr. Thomas Griesser produced novel silane and thiol molecules bearing a photo-reactive functional head group. They prepared thin films and self-assembled monolayers on silicon oxide or

gold as substrate. The results obtained by the X-ray photoelectron spectroscopy measurements were supported and confirmed by contact angle measurements (Dr. Alexandra Lex, Dr. Thomas Höfler form Technische Universität Graz and Dr. Thomas Griesser from Montanuniversität Leoben), atomic force microscopy measurements (Prof. Christian Teichert, Dr. Gregor Hlawacek, Quan Shen from the Montanuniversität Leoben), X-ray reflectivity measurements (Prof. Roland Resel, Dr. Oliver Werzer, Heinz-Georg Flesch from Technische Universität Graz) and Fourier-transformation infrared spectroscopy (Prof. Robert Schenach, Dr. Peter Pacher from Technische Universität Graz). The results within this collaborations are partly published in reference 8, 9 and 10. Furthermore, the preparation of substrates for truly self-assembled monolayers and the analysis of the ordering of a thiol-based molecules on these surfaces was done by the help of the group of Prof. Gregor Witte (Molecular Solid State Physics, Philipps-Universität Marburg). The latter measurements were conducted during a research stay in Germany using atomic force microscopy and scanning-tunneling microscopy.

The next chapter (section 4) gives an insight into the application of surface modification in an organic field effect transistor. Controlled experiments were devised, such that the electronic band alignment, as measured by valence bond photoemission, at each step of the prototype device production could be followed. In collaboration with Philipp Stadler from the group of Prof. N. Serdar Sariciftci (Johannes Kepler University Linz) a direct relation between the threshold voltage shift and the change of the work function of the organic semiconductor due to an built-in potential step at the polymeric interlayer (BCB) is proven. Moreover, this method allowed to determine, which interface is the critical determinant for device improvement. In contrast to speculations in the device literature, it was found to be the polymer/organic semiconductor interface, rather than the polymer/inorganic interface. The results are published in reference 11.

Finally, the modification of surfaces was investigated theoretically in section 5 using band-structure calculations to obtain a deeper insight in the structure of self-assembled monolayers. At the beginning of this chapter, the fundamental questions of the binding preferences of small thiolate and selenolate molecules on Au(111) are discussed and compared. Then, theoretical calculations of anthracene-2-selenolate on Au(111) have been performed. This system has been well characterized experimentally, in terms of its geometric and electronic structure, in the in the group of Prof. Gregor Witte by Dr. Daniel Käfer and Dr. Asif Bashir.[12] With the theoretical calculations, it was possible to evaluate the exact molecular packing arrangement of this self-assembled monolayers. It was shown, that the molecular packing arrangement as well as the tilt angle have as strong impact on simulated scanning tunneling microscopy images. Furthermore, a significant effect on the intermolecular interaction is seen in the change of the dispersion in the two-dimensional band structure caused by the different tilt and packing arrangement. To obtain reason-

able tilt angles, the internal coordination optimization software GADGET developed by Dr. Tomáš Bučko from the Center for Computational Materials Science (Vienna) was used. Finally, the calculated work-function modification was shown to be in perfect agreement with the experimentally derived value. The calculated local density of states agrees reasonably with the well measured ultraviolet photoemission spectrum. The results of this cooperation are published in reference 13.

All used abbreviations and references are listed at the end of the thesis.

2 Experimental and Theoretical Background

2.1 Introduction

To obtain an overview of the different topics of this thesis, in this section all main concepts relevant when investigating organic molecules on surfaces are introduced shortly.

In the first part the experimental methods to study the surfaces are explained. These are mainly ultrahigh vacuum (UHV) based methods. Therefore, a short introduction of the used UHV machine and the basics of the primarily used X-ray photoelectron spectroscopy (XPS) and ultraviolet photoelectron spectroscopy (UPS) are given in this section.

After introduction of the used experimental methods, it is important to understand the functionality of the organic devices to allow a proper interpretation of the experimental results. We are particular interested in organic thin-film transistor (OTFT), which are described in the second part.

In the last part the principles of theoretical calculations are explained with emphasis on the calculation of scanning tunneling microscopy (STM) images, the importance of the proper use of different geometry optimization method and the calculation of band structures. These theoretical calculations have been used to gain a deeper insight in interfaces of organic molecules.

2.2 Photoelectron Spectroscopy

For compiling this section the following textbooks and scrips were used: reference 14, 15 and 16.

Photoelectron spectroscopy (PES) is also known as photoemission spectroscopy and it is a common method to investigate all kind of surfaces. With this method occupied states at the surface and near the surface are probed to get information of the composition and electronic structure of the sample.

PES is based on the photoelectric effect, which can be described as a one photon in - one electron out process. This means that an electron with a certain binding energy (E_b) absorbs a photon of an energy $h\nu$ and leaves the surface with a kinetic energy (E_{kin}) after overcoming the work function (Φ) of the surface. In the simplest case, if the Koopman's theorem is fulfilled and the electron orbital energies before and after the emission process are the same, the E_{kin} is defined as following

$$E_{kin} = h\nu - E_b - \Phi \tag{1}$$

where h is the Planck constant and ν is the frequency the photon.

Depending on the excitation source and concomitant the photon energy, one can differ between X-ray photoelectron spectroscopy (XPS) and ultraviolet photoelectron spectroscopy

(UPS). With X-ray photoelectron spectroscopy (XPS) X-ray radiation is used with a photon energy between 100 eV and 10000 eV. This photon energy corresponds to a wavelength between 100 and 10 Å and as a consequence the core-levels are probed. Ultraviolet photons with an energy of 10 to 100 eV (wavelength between 1000 and 100 Å) are used for UPS. Here valence levels are probed. The photoemission process and the measured spectra are schematically shown in figure 2.

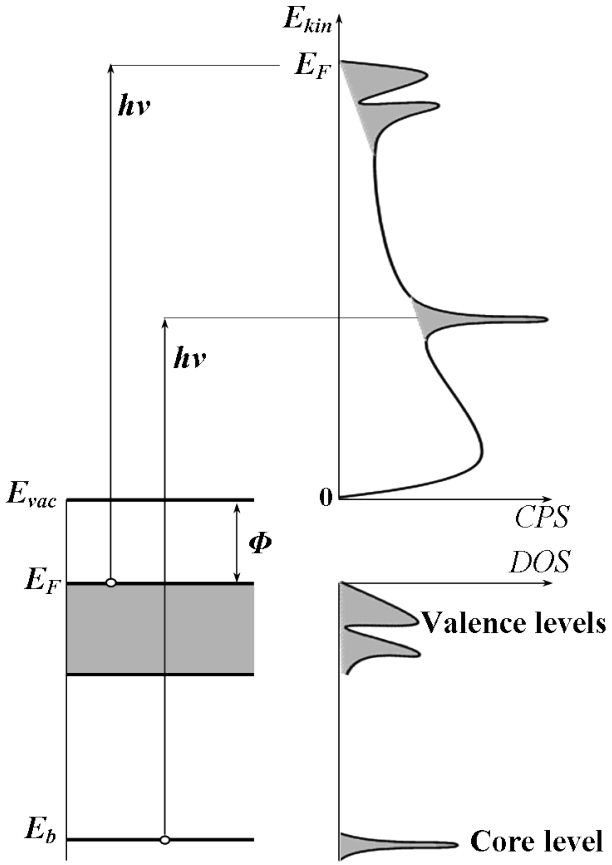

Figure 2: Schematic picture of photoemission from a core level and valence level and its connection to a photoemission spectra (CPS) and the density of states (DOS). The relation between the binding energy (E_B), the kinetic energy (E_{Kin}) and the work function(Φ) is shown.

An important issue for surface sensitive methods is the inelastic mean free path length (λ) of the electrons which are emitted from the sample. The dependence of λ on the emitted electron energy for different elements was measured first by Seah and Dench [17]. With this 'universal' graph it is possible to estimate the depth of the probed surface as a function of the electron energy. Note, that the energy of the incoming and emitted electrons should be the same when considering the *inelastic* mean free path length. Just electrons between

10 and 100 eV can be used to ensure surface sensitive photoemission spectroscopy, because this energy window corresponds to a λ of 10 Å which is the depth of about three monolayers. Thus UPS is very surface sensitive while photoemission features in an XPS spectrum are probing depths dependent on their particular E_{kin}. This best illustrated when comparing the C1s signal (XPS) and the HOMO-peak (UPS) of an organic sample: The C1s signal can be attributed to the whole organic layer whereas the HOMO signal arises just from the uppermost layer and is therefore surface sensitive.

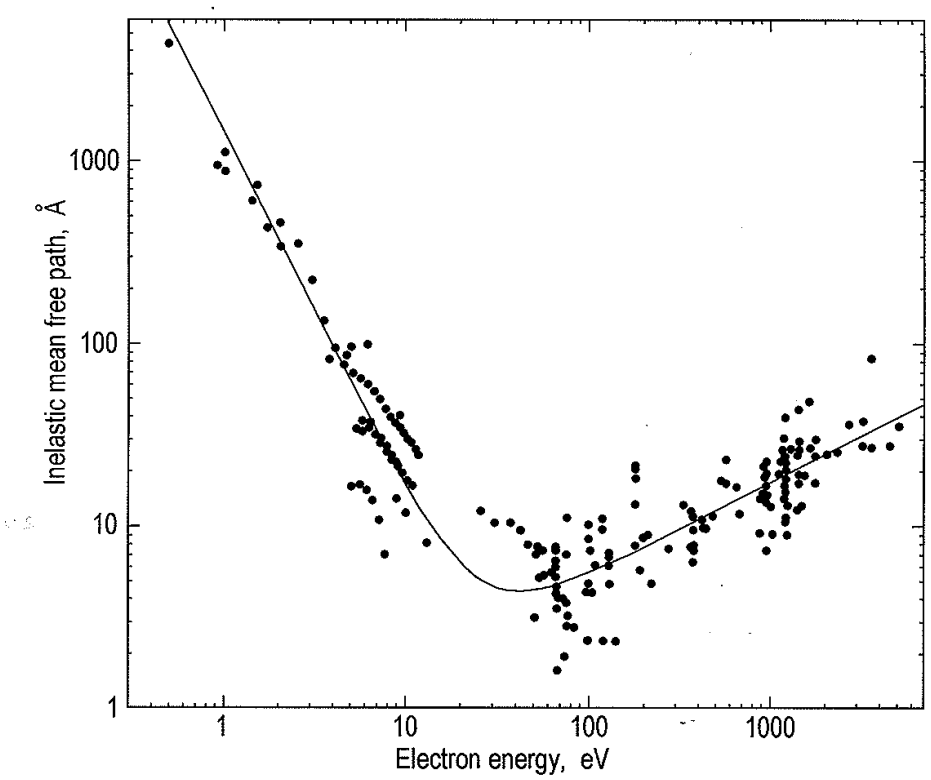

Figure 3: The inelastic mean free path as a function of the emitted electron energy.[14]

2.2.1 Specs-System

The used UHV system for XPS and UPS measurements was purchased from Specs in 2006.(see figure 4) It essentially consists of three chambers - the preparation chamber and the analysis chamber - and a fast entry chamber.

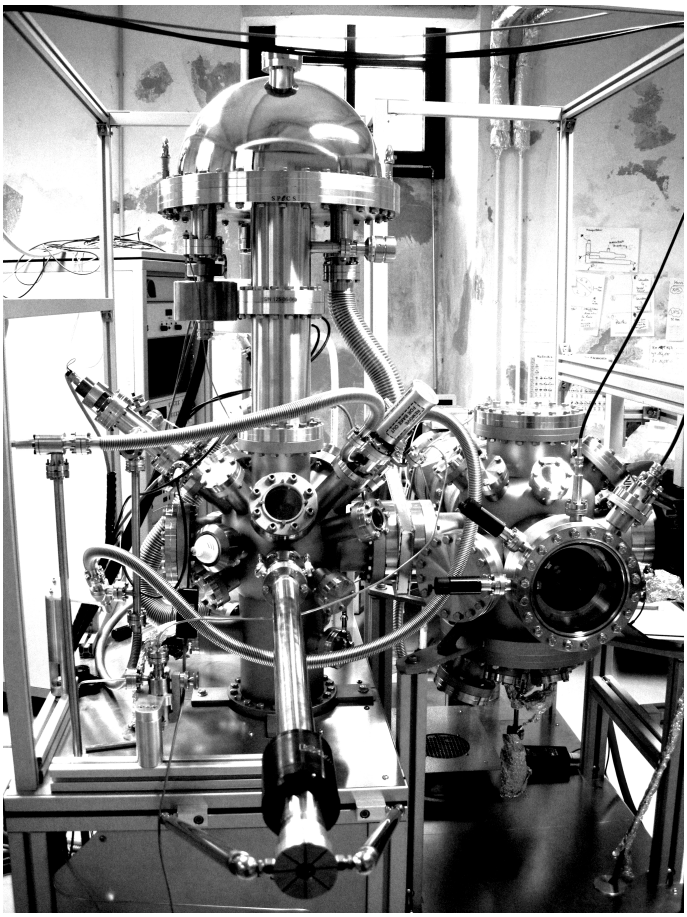

Figure 4: Photo of the used UHV system

In the analysis chamber the main component is the hemispherical analyzer PHOIBOS 100 MCD to detect the photoelectrons.It is controlled by a computer and supported by the software package SpecsLab. The photoelectrons are induced either by a X-ray gun or an ultraviolet (UV) Helium lamp. (See figure 5) The water cooled X-ray source SPECS-XR50 has two anodes: a Mg-anode, which emits $Mg - K_\alpha$ electrons with $h\nu$ of 1253.6 eV and an Al-anode ($Al - K_\alpha$) where $h\nu$ is 1486.6 eV. In this thesis only the Mg-anode was used, because it has a better resolution and is slightly more sensitive to Carbon. The X-ray source is mounted at an angle of 45° with respect to the surface normal of the sample, when measuring in normal emission. The maximum power of the X-ray source is 300 W. It was set to 150 W when investigate organic samples to avoid sample damage. The UV discharge lamp SPECS-UVS10/35 is able to emit He I ($h\nu$=21.2 eV) or He II ($h\nu$=40.8 eV), which is controlled by differential pumping stages. Pumping stage 1 is pumped with a roughing oil pump, whereas pumping stage 2 is connected with the fast entry chamber. The pressures before and during UPS measurements are summarized in table 1.

Table 1: Differential pumping pressures before UPS measurements and for HeI or HeII emission.

	p_{stage1} /mbar	p_{stage2} /mbar	$p_{analysis\,chamber}$ /mbar
base pressure	6×10^{-3}	3.5×10^{-8}	2×10^{-10}
He I	2×10^{-1}	7×10^{-5}	4×10^{-8}
He II	6.2×10^{-2}	8×10^{-6}	-

Additionally, an ion gun (SPECSIQE-11/35) is attached to the analysis chamber to clean surfaces by sputtering argon ions on the surface or doing depth profiles. This technique was not used during this work, because only ex-situ prepared samples were investigated.

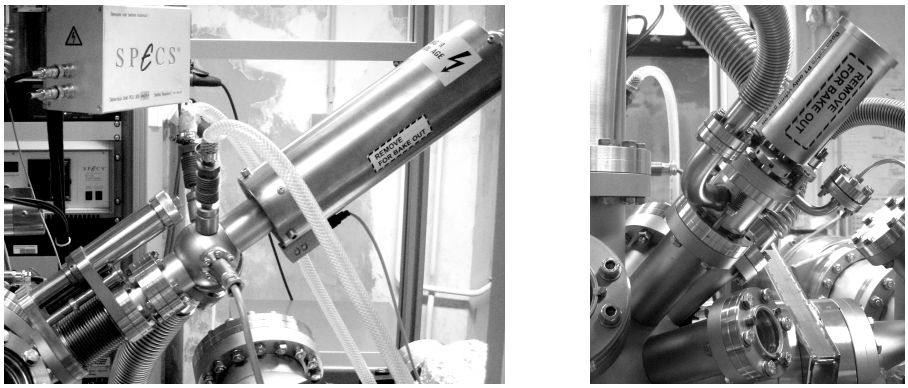

(a) (b)

Figure 5: (a) X-Ray gun and (b) UV-lamp of the Specs system.

The preparation chamber is equipped (since few month) with a low-energy electron diffraction (LEED), compact mass spectrometer system, a micro balance, and a thermal evaporator.

The fast entry chamber is a real load lock which allows to insert samples in the main chamber without loss of the UHV via a special sample wheel which is separated from the fast entry and the main chamber by two gate valves (compare figure 9 and figure 6)

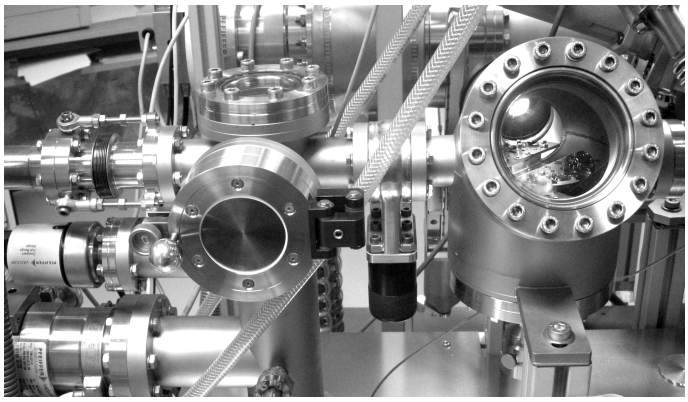

Figure 6: Fast entry chamber (load lock) of the Specs system. Through the window the sample wheel for six samples is visible, which is can be separated from the fast entry chamber and the main chamber by two gate valves (only one gate valve is visible).

For all measurements and preparations the sample is mounted on the manipulator. This allows a rotation and positioning of the sample to achieve the optimal position for the used method. (Figure 7) The used position parameters are summarized in table 7. The rotation can be performed automatically with a motor e. g. during depth profile measurements. Furthermore, there is a the possibility to heat (or cool) the samples but this has never been done during this thesis to avoid damaging the organic samples.

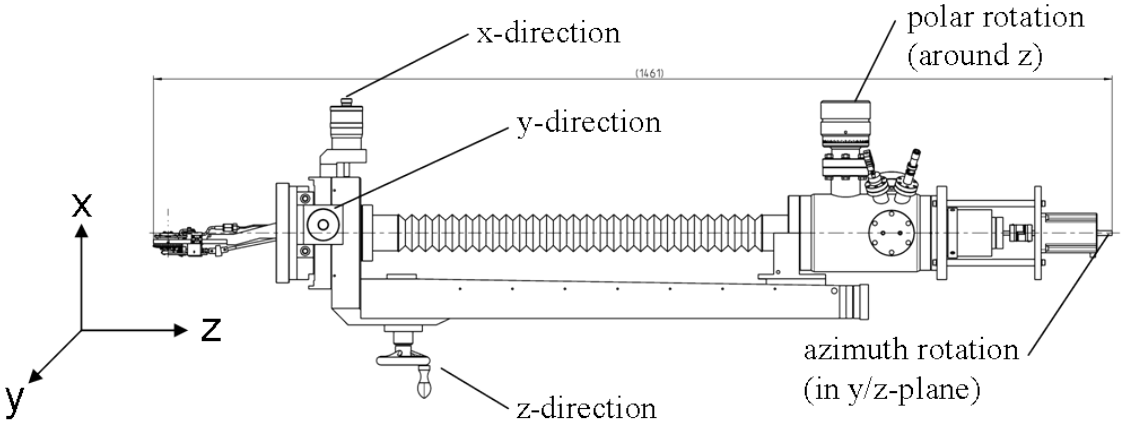

Figure 7: Manipulator of the Specs system. The three directions and the possible rotation of the sample are shown.

Table 2: Position parameters of the manipulator for XPS and UPS measurements. When using this parameters the center of the sample plate is measured.

	x /mm	y /mm	z /mm
XPS	10.3	10.15	10.25
UPS	10.0	9.5	8.0

To obtain a working pressure of about 3×10^{-10} mbar different pumps are used in the SPECS system: two titan sublimation pumps (TSP) in both chambers, an ion pump (VARIAB) and two turbomulecular pumps (Pfeiffer-Vacuum TMU071 and TMU521) with two oil-free scroll pumps (VARIAN SH-110) for priming. The exact positions of the pumps are shown in figure 8. Two ionization gauges are mounted in each chamber to monitor the pressure.

To avoid venting of the whole system during a power failure and / or to separate the different chambers from each other, four UHV gate valves (VAT) are placed in the system. The exact positions of these valves are shown in figure 8.

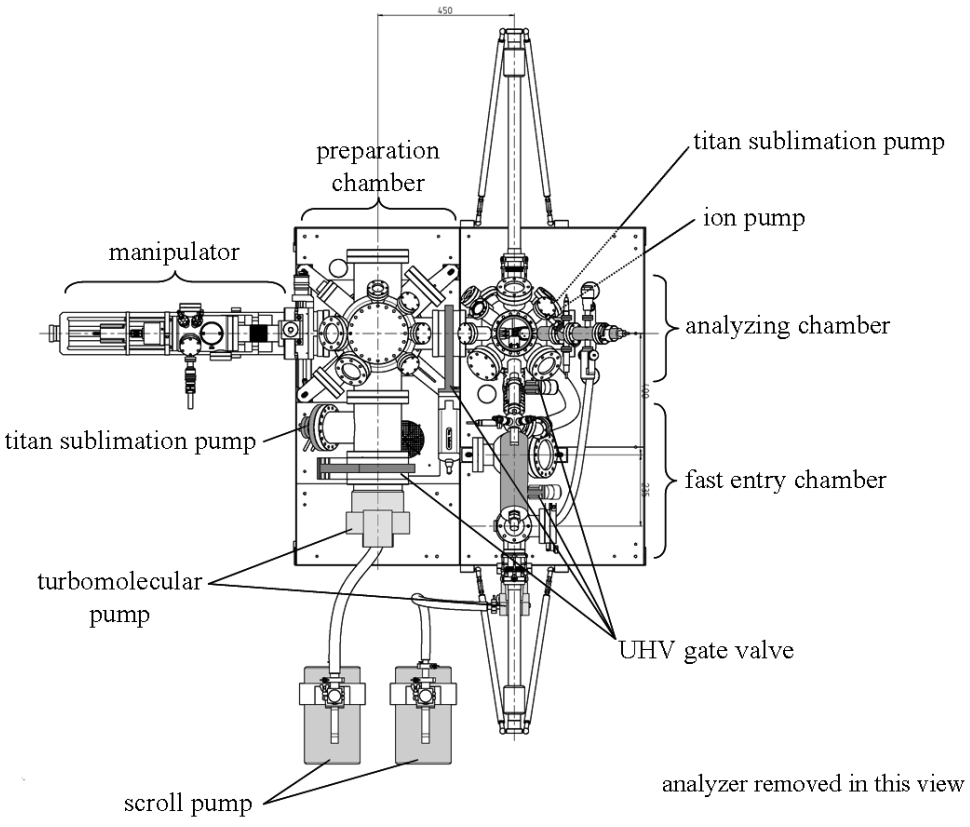

Figure 8: Schematic drawing of the Specs system with all pumps, chambers and valves indicated. Drawing done by Specs.

The positions of the sample and the photon source relative to the hemispherical analyzer are schematically shown in figure 9. The angle between the sample and the analyzer denoted as θ can be changed by rotating the manipulator. The bigger θ the more surface sensitive the measurements become. Usually normal emission (θ=0) is used. The electrons leaving the sample are collected via a lens system and additionally bundled with an iris before entering the analyzer. In the analyzer, a voltage between the inner and outer hemisphere (called pass energy) is used to screen electrons with a specific energy dispersion. Finally, differently shaped slits are used before the electrons approaching the five channeltrons in the analyzer.

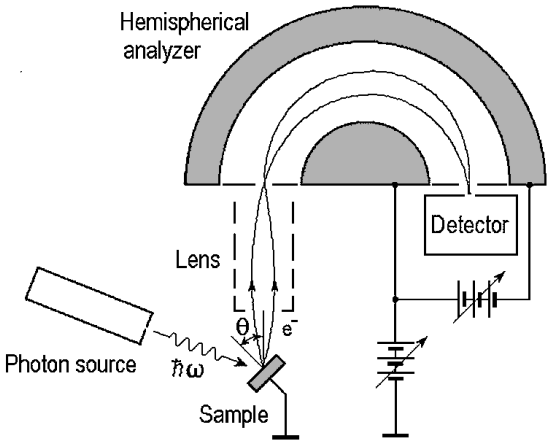

Figure 9: Schematic drawing of a hemispherical analyzer and the experimental setup. Tis picture is taken from refernce 14.

Generally used settings of the analyzer for large-area and small-area mode for XPS measurements are shown in table 3 and two survey spectra measured with the two different area modes are shown in figure 10. Although the small-area mode lowers the counts significantly and hence a larger number of scans have to be measured to obtain a reasonable signal-to-noise ratio, this method was used to get more reproducible results, when investigating the two halves of a patterned sample, as described in section 3. With the small-area mode the spot size of the detected area is lowered so that both halves could be measured separately and a change due to the patterning could be investigated quantitative without interference from different chargings, different film thicknesses or different batches of the samples.

Table 3: Settings for XPS measurements

mode	detected area Ø	spectra	number of scans	pass energy	slit	iris Ø	energy step
large area	5 mm	survey	1	20 eV	7x20 mm	45 mm	0.5 eV
large area	5 mm	element scan		15 eV	7x20 mm	45 mm	0.1 eV
small area	1 mm	survey	6	20 eV	Ø 7 mm	20 mm	0.5 eV
small area	1 mm	element scan		20 eV	Ø 7 mm	20 mm	0.1 eV

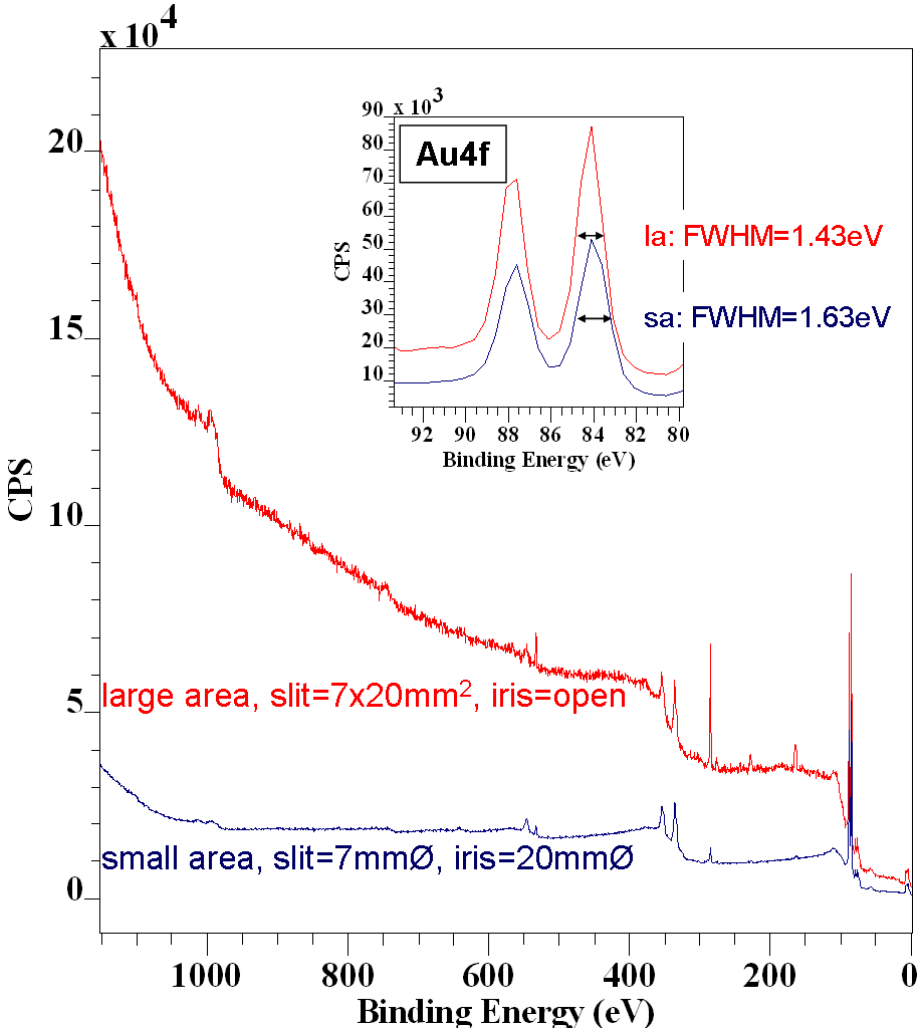

Figure 10: XPS survey spectra of a SAM on gold measured with different area mode (not the same sample). As inset the Au4f region and the resulting FWHM is shown for both modes. **Red**: **large** area mode, slit=7x20 mm^2, open iris, 75W; **Dark blue**: **small** area mode, slit=7 mm diameter, iris=20 mm diameter, 75W;

2.2.2 X-Ray Photoelectron Spectroscopy

The XPS is also known as electron spectroscopy for chemical analysis (ESCA) and in this thesis it would be the proper notation. With this method, core electrons are excited by X-rays photons and photo electrons are emitted with element specific energies. Depending on the chemical environment, thebinding energy (E_b) shifts. This shift is referred to the chemical shift and two relevant and representative examples of the photoemission from a silicon-oxide substrate covered with a self-assembled monolayer (SAM) and a SAM covered with $C_{60}$are shown in figure 11 and figure 12 to exemplify the effect. With this property, XPS is a very advantageous method to investigate organic molecules on inorganic surfaces, because one can distinguish between chemically differently bonded atoms.

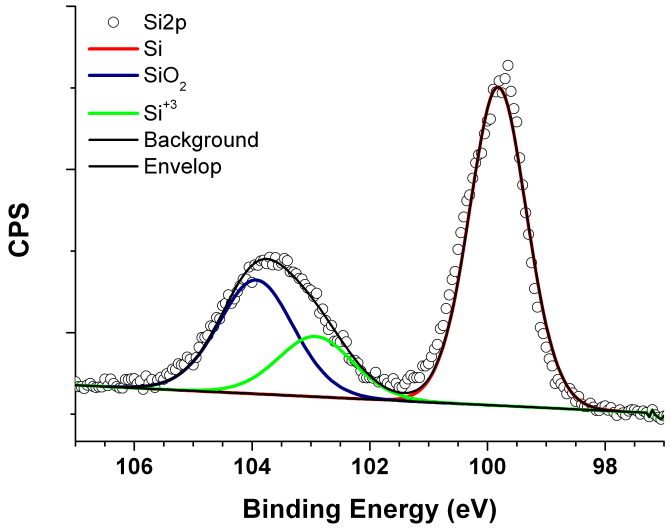

(a)

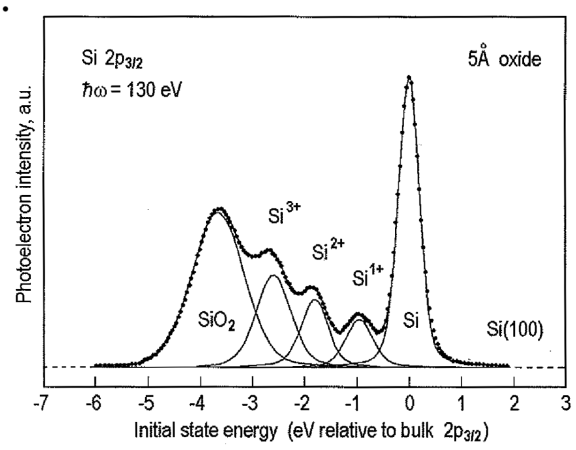

(b)

Figure 11: (a) Si2p region of an Silicon waver with a native silicon oxide layer and a self assembled monolayer (Si-SCN) on top. Measured at the SPECS system. (b) $Si2p_(3/2)$ core level spectrum of an ultra thin SiO_2 over layer on a Si(100) surface (note, that the $Si2p_(1/2)$ contribution has been subtracted). This image was taken from reference 14. In both images the difference in binding energy between elemental Si and Si bonded to oxygen is visible.

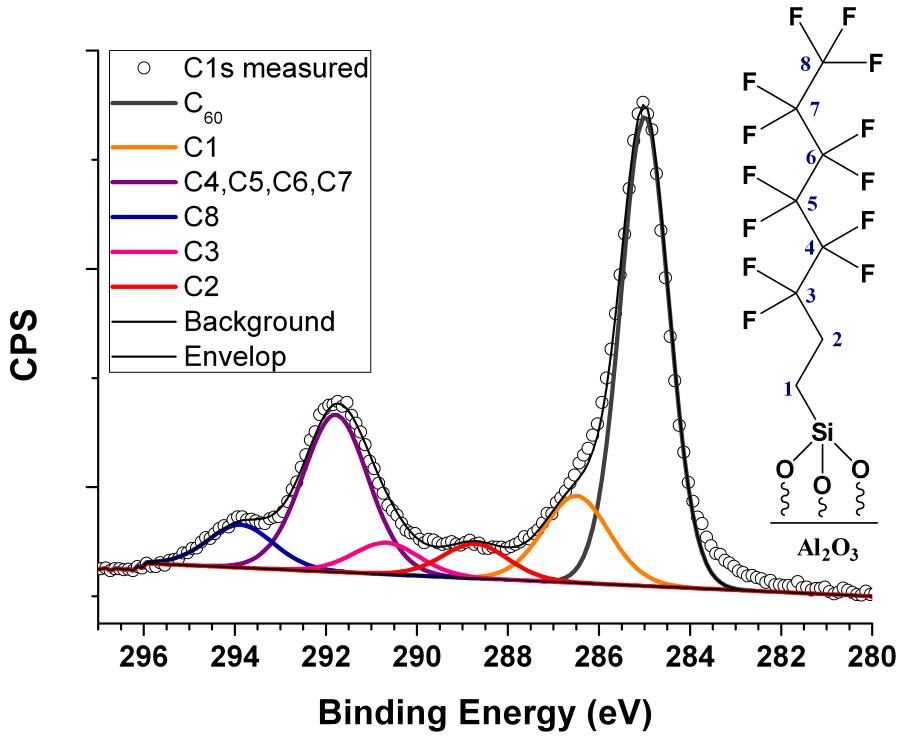

Figure 12: XPS image of the C1s region of C_{60} on top of the fluorinated (Trideca-1,1,2,2-tetrahydro)octyltrichlorosilane SAM on Al_2O_3. The binding energy of C1s shifts to higher binding energy when a F-atom is bonded next to the carbon atom. The values are in perfect agreement with chemical shifts of C1s of F-containing polymers.[18] The spectrum has been measured with the SPECS system.

In addition to the emission of a photoelectrons, other processes occur after absorption of a X-ray photons. The most prominent one is the emission of an Auger electron which is depicted in figure 13b .

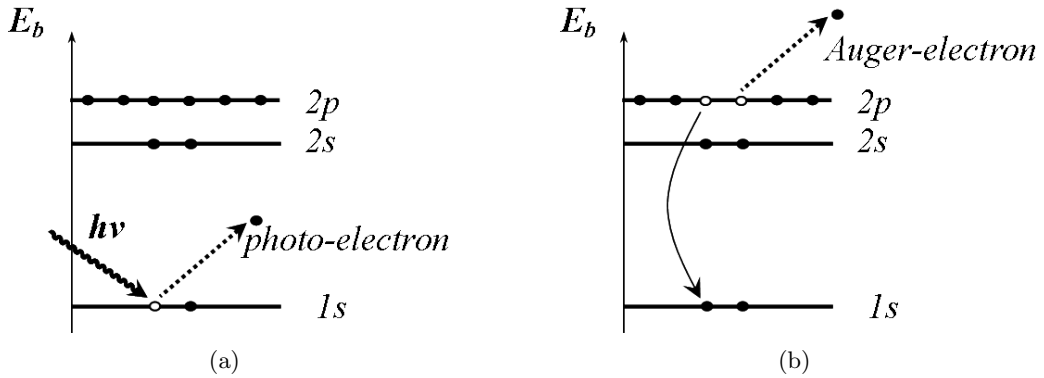

Figure 13: (a) Process of the emission of a photo electron from the core levels. The remaining hole is indicated as an open circle. (b) The hole can be filled by an electron from higher levels and simultaneously another electron is emitted which is called Auger electron.

Aside from these two main processes during XPS measurements, many other lines can appear in a spectrum. X-ray satellites arise from minor X-ray components at higher photon energies emitted from the X-ray source for each photon electron signal in the spectrum. The energies of these satellites and their relative heights are given in table 4. Furthermore, X-ray 'ghost'-lines can appear due to impurities in the anode material of the X-ray source (e. g. aluminum impurities in the Mg anode). Other spectral features are shake-up and shake-down lines, which occur when a photo electron is emitted not from the ground state of the molecule/atom. Shake-up lines are very often seen in unsaturated organic compounds, involving the $\pi \rightarrow \pi^*$ transition. Further energy losses plasmons may be visible (often seen for Si2p and Si2s). Finally, in the XPS spectrum emission from the valence states are visible, however, for a detailed analysis of this features UPS is used.

Table 4: Energy displacements and relative intensities for $Mg - K_\alpha$ X-ray satellites.[19]

	$\alpha_{1,2}$	α_3	α_4	α_5	α_6	β
Displacement /eV	0	8.4	10.2	17.5	20.0	48.5
Relative Intensity	100	8.0	4.1	0.55	0.45m	0.5

For experimental determination of the binding energy ($E_{b,S}$) of the individual elements of the sample one has to adapt equation 1 to

$$E_{kin,A} = h\nu - E_{b,S} - \Phi_A \tag{2}$$

and transform it to

$$E_{b,S} = h\nu - E_{kin,A} - \Phi_A = h\nu - E_{kin,S} - \Phi_S \tag{3}$$

where the index S stands for sample and the index A for analyzer. In practice, the sample grounded, the X-ray wavelength is known, the work function of the analyzer is constant and the kinetic energy of the analyzer ($E_{kin,A}$) is measured.[A] To obtain the real kinetic energy of the sample ($E_{kin,S}$) the work function of the sample (Φ_S) has to measured first. Φ_S can be easily measured with UPS as indicated in figure 2 and figure 16; however, care must be taken, when Φ_S is lower than Φ_A and the vacuum level of the sample is lower than the the vacuum level of the analyzer. To avoid this, a negative bias is applied to the sample to shift the emission cut-off above the vacuum level of the analyzer. The relation between the sample and the analyzer is shown in figure 14.

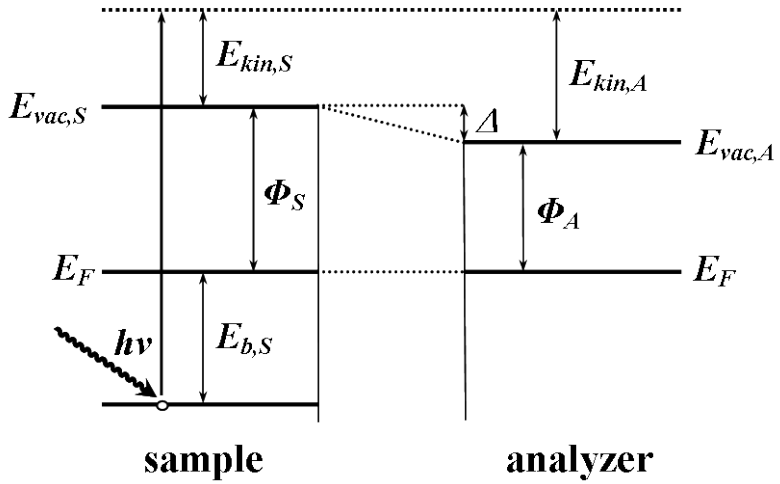

Figure 14: Schematic drawing of the energetic levels of the sample relative to the analyzer. When the sample is grounded the Fermi energy (E_F) of the sample and the analyzer are the same. This allows to obtain the binding energy of a sample core level ($E_{b,S}$) via the measured kinetic energy of the analyzer ($E_{kin,A}$). If Φ_S is smaller then Φ_A a negative bias has to be applied to the sample to shift the vacuum level of the sample ($E_{vac,S}$) above the vacuum level of the analyzer ($E_{vac,A}$).

For the quantitative analysis of a XPS spectrum it is important to determine the relative concentration of the different elements of the sample. Each element has a specific atomic sensitivity factor (ASF) (also depending on the position of the analyzer to the sample). In this work, the ASFs of reference 19, appendix E, are used. For calculating the relative concentrations, the software CasaXPS[20] was used. The energetic resolution of a XPS-signal

[A] The analyzer is calibrated by measuring the Fermi edge of a metallic substrate with UPS.

is given by the full width at half maximum (FWHM) and arises form the energy resolution of the analyzer, the line width of the x-ray and the intrinsic width of the photo emission signal. The smaller the FWHM the better is the resolution of different chemical shifts.

To obtain information on the depth of the probed element, depth profiles can be performed. This is a combination of sequent argon sputtering and XPS measurement cycles. With this one can follow the increase or decrease of the investigated element through a defined layer thickness. Before starting a depth profile, the sputter rate has to be calibrated. Usually this is done with Tantalum oxide with a defined oxide thickness of 1000 Å on the metallic Tantalum. Following sputter-parameters were used:

- sputtered area: $5 \times 5\,mm^2$
- energy: 3000 V
- emission current: 10 mA
- time: 300 s per cycle
- Argon pressure: 5×10^{-7} mbar
- sample current: $7.3\,\mu$A

During the sputter cycles, the decrease of the Ta4f signal and of the O1s arising from Tantalum oxide can be observed. Simultaneously the increase of Ta4f arising from metallic Tantalum (at lower binding energies) is seen. (see figure 15a and 15b) To analyze the relationship between the sputter time and the sputter depth a sigmoidal fit has been applied to the change in the O1s area shown in figure 15c.

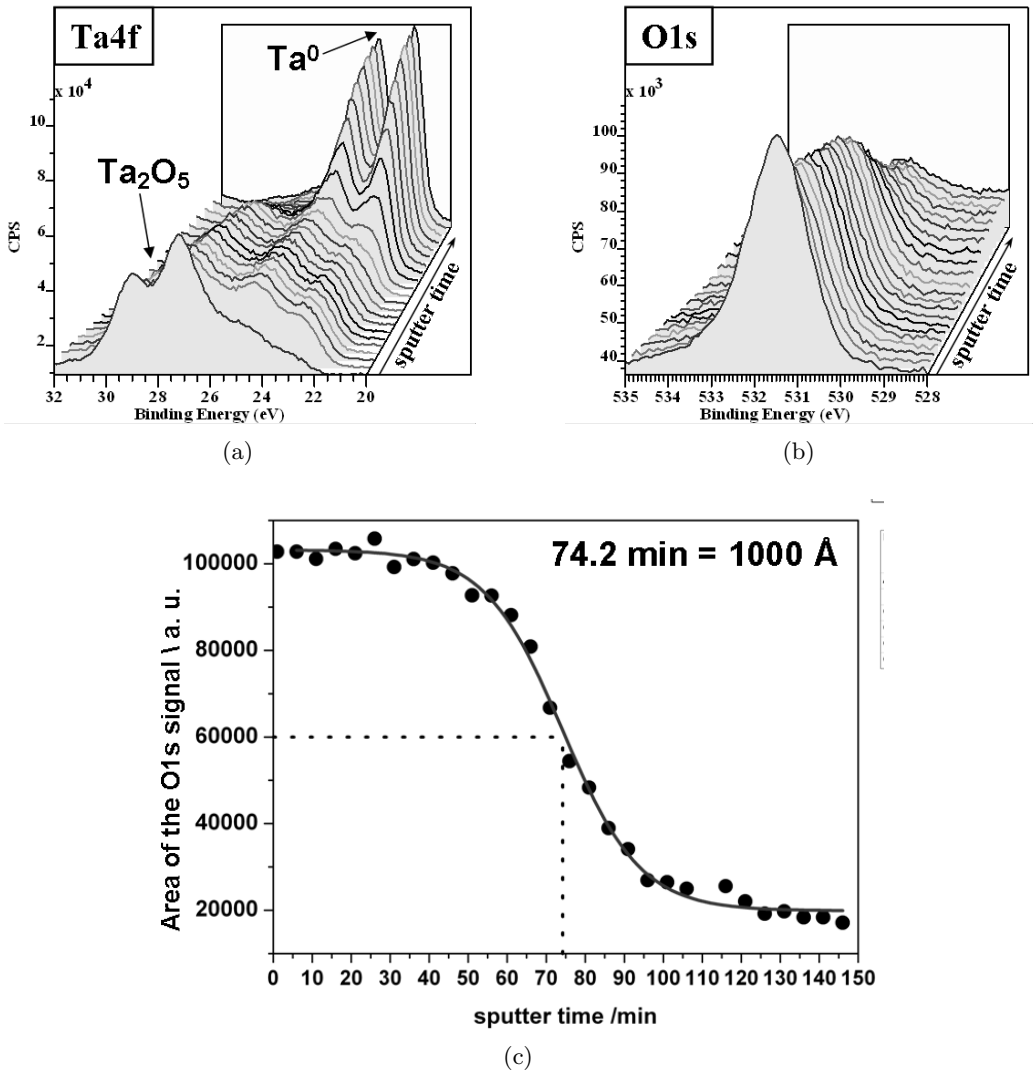

(a) (b)

(c)

Figure 15: (a) Decrease of oxidic Tantalum (4f 7/2) at 27.2 eV and increase of metallic Tantalum (4f 7/2) at 21 eV with sputter time. (b) Decrease of O1s from Ta_2O_5 with sputter time. (c) O1s area for different sputter times (filled cycles) to evaluate the sputter rate. A Boltzmann fit (red line) shows that after 74.2 min 1000 Å have been sputtered.

2.2.3 Ultraviolet Photoemission Spectroscopy

As mentioned in section 2.2, ultraviolet photoelectron spectroscopy (UPS) is related to XPS. But in contrast to XPS, for UPS UV-light is used and with that it is possible to probe only the valence electron of the sample. Furthermore, the line width of the UV-light is much smaller (e. g. $Mg - K_\alpha$: FWHM = 700 meV and HeI: FWHM = 3 meV). Therefore, with UPS it is possible to resolve the fine structure of the valence region, i. e.,

with UPS it is possible to measure slight differences between molecular orbitals or the physical environment (e. g. adsorbates on the surface).

A typical UPS spectrum of a semiconductor with adsorbed molecules is shown in figure 16.

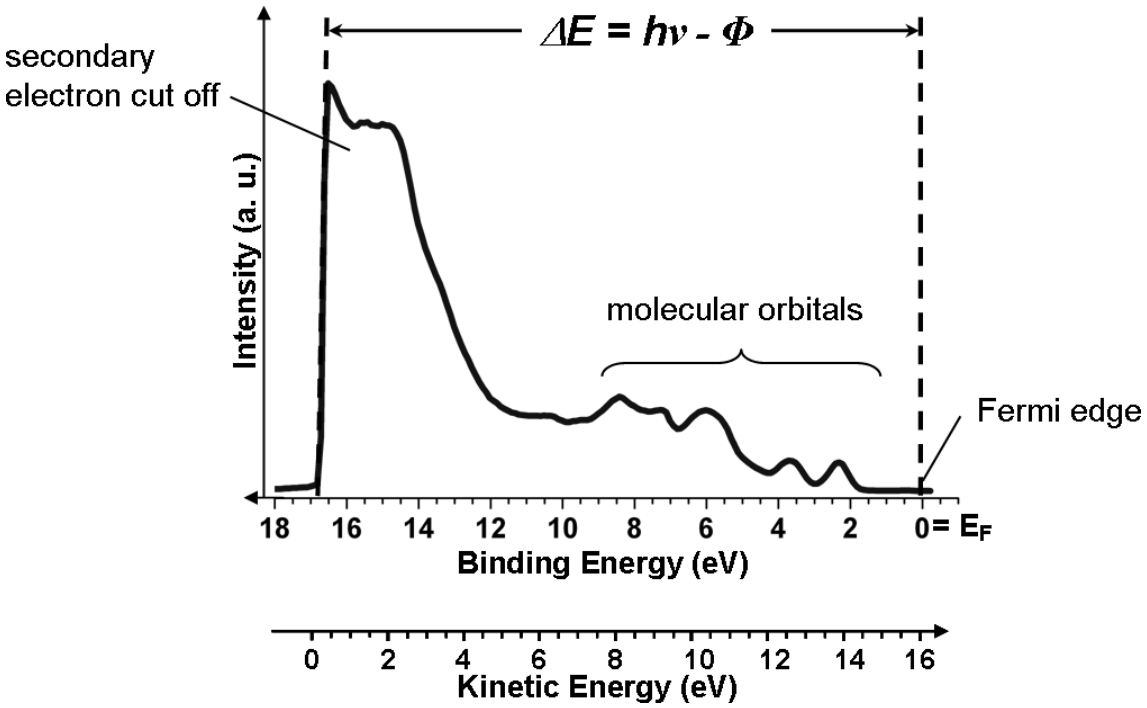

Figure 16: UPS spectrum of C_{60} adsorbed on a silicon wafer with a natively grown SiO_2 layer. At high binding energies the secondary electrons of the sample are seen. The Fermi edge is not visible, because the substrate is a semiconductor and has a band gap. The molecular orbitals of C_{60} are clearly visible. The fist peaks at 2.32 eV and 3.72 eV can be associated explicitly to the HOMO and HOMO-1 of C_{60} respectively (compare reference[21]). The difference between the minimal binding energy ($E_F = 0$) and the maximal binding (secondary cut off) is denoted as ΔE.

To calculate the work function, ΔE is needed. It can be calculated from the difference between the maximal and minimal kinetic energy (see figure 14) as shown by

$$E_{kin,A,max} = h\nu - \Phi_A \tag{4}$$

$$E_{kin,A,min} = \Phi_S - \Phi_A \tag{5}$$

$$\Delta E = E_{kin,A,max} - E_{kin,A,min} = h\nu - \Phi_S \tag{6}$$

$$\Phi_S = h\nu - \Delta E \tag{7}$$

There are three basic methods to measure UPS. With the first method, one obtains energy distribution curves (EDC) using constant photon energy. Here initial states and final states are changed and and the joint density of states (JDOS) is measured. The relative intensities of the JDOS depends on the combination of both states. The second method is used to obtain the actual density of states (DOS) of the initial states. Here, the detected kinetic energy is held constant, and the photon energy is tuned. This leads to change only in the initial state and the relative intensities are only effected by the DOS of the initial state. With the third method the DOS of the final states can be measured by varying the photon energy and the kinetic energy by the same amount. This leads to spectra where the relative intensities are related only to the DOS of the final states. Only the first (and most simple) one can be realized with an UV lamp like the one in the specs system (section 2.2.1). The other two methods require synchrotron radiation with tunable photon energies.

Furthermore, two different methods to measure UPS are possible: angle-integrated and angle-resolved UPS.

In the angle-integrated UPS, all electrons above the of the sample are collected with, e. g., a retarding field analyzer.

In the angle-resolved ultraviolet photoelectron spectroscopy (ARUPS) electrons of a defined direction are collected, e. g., with a hemispherical analyzer. This method allows to measure the different electron energies as well as the corresponding wave vector and provides the possibility to obtain information about the band dispersion.[B]

Experimentally, the kinetic energy kinetic energy (E_{kin}) of the photo electron is measured and the momentum is selected by the position of the analyzer with respect to the sample. The wave vector (which is proportional to the momentum) can be partitioned into the wave vector parallel to the surface ($k_{\parallel}$) and the wave vector perpendicular to the surface ($k_{\perp}$).

$$E_{kin} = \frac{\hbar^2(k_{\perp}^{ex^2} + k_{\parallel}^{ex^2})}{2m} \tag{8}$$

The subscript 'ex' means external and the wave vector $\mathbf{k}^{ex}$ refers to a free electron, which has already escaped from the solid to the vacuum. This is in contrast to the wave vector of an electron in the solid (internal) k^{in}. With changing the angel θ between the surface normal and $\mathbf{k}^{ex}$ (see figure 17), one can write

$$k_{\parallel}^{ex} = k^{ex} sin\theta = \sqrt{\frac{2mE_{kin}}{\hbar^2}} sin\theta. \tag{9}$$

When considering the momentum of the photo electron inside the solid $\mathbf{k}^{in}$, one should remember that only the parallel part of the momentum is conserved when passing from the

[B] This section follows reference 14.

solid to the vacuum.

$$\mathbf{k}_{\parallel}^{ex} = \mathbf{k}_{\parallel}^{in} \tag{10}$$

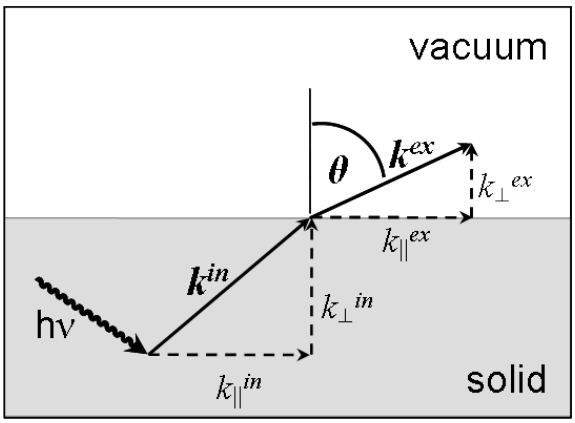

Figure 17: Wave vector of an photo electron formed in a solid. When passing from solid to the vacuum only, the wave vector parallel to the surface is conserved.

In experiments only the $k_{\parallel}^{ex}$ is considered and therefore strictly speaking the $E_{kin,\parallel}^{ex}$ is measured.

2.3 Organic Thin Film Transistors

For this section the following textbook and scrip were used: reference 22 and reference 23

Generally, transistors are electronic devices to switch or amplify an electric signal. In the case of organic thin-film transistors (OTFTs) the particular feature is an organic semiconducting layer.[C] The principal structure of an OTFT is shown in figure 18 and it consists of three electrodes (referred to as source, drain and gate), a semiconductor layer, an insulator and a substrate. There are many possibilities to arrange these components. In this thesis bottom gate structures with top contacts are used (as shown in figure 18).[D] The most important geometric parameters of an OTFT are the channel width Z and the channel length L.

Furthermore, one can distinguish not only between geometric differences but also the type of used semiconductor. It is possible to build n- and p- devices, depending on the type of mobile carriers: electrons or holes, respectively. In a p-channel OTFT, a negative bias between the source and the gate is applied and holes are accumulated in the channel, whereas in a n-channel device electrons are accumulated with a positive bias.

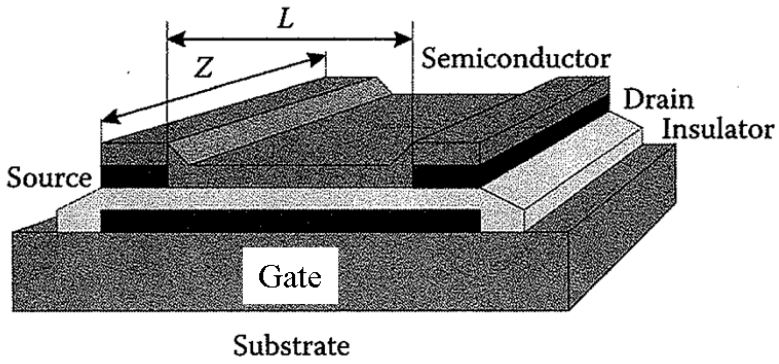

Figure 18: Bottom gate, bottom contact structure (3D) of an organic thin-film transistor. The Channel width (Z) and the channel length (L) are indicated. This image is taken from reference 22.

When operating an OTFT one applies a bias (as mentioned above) between the source and drain (U_{drain}) and between gate and source (U_{gate}). The magnitude of the current through the channel (measured at the drain) is determined by the channel resistance (during optimal operation), which can be controlled by the voltage between the gate and the source (U_{drain}).

[C] In comparison to inorganic field-effect transistors no doping, no p-n junction is present. Furthermore the structure is compleatly different.

[D] By now also top gate structures become common, because with the use of organic dielectrics such structures are more accessible.

For the I-V-characterization of an OTFT two plots are recorded: the output-characteristic and the transfer-characteristics. (See figure 19)

In the output-characteristics, the drain current versus the drain voltage is measured. Here, two regimes are prominent: the linear and the saturation regime. In the linear regime (compare figure 20: top) the charge density is approximately constant between the source and the drain, because the gate voltage is much larger than the drain voltage ($|U_{gate}| > |U_{drain}|$). Here the drain current increases linearly with higher drain voltage. The saturation regime is encountered when $|U_{drain}| > |U_{gate}|$. This leads to a charge density drop to zero in the vicinity of the drain[22] and the drain current saturates at higher drain voltages. The transfer characteristic shows the dependence of the drain current on the gate voltage as depicted in the bottom panel of figure 20. From the transfer characteristic the most important parameters can be extracted, e. g., the charge carrier mobility (μ), the on-off ratio and the threshold voltage (U_{th}).

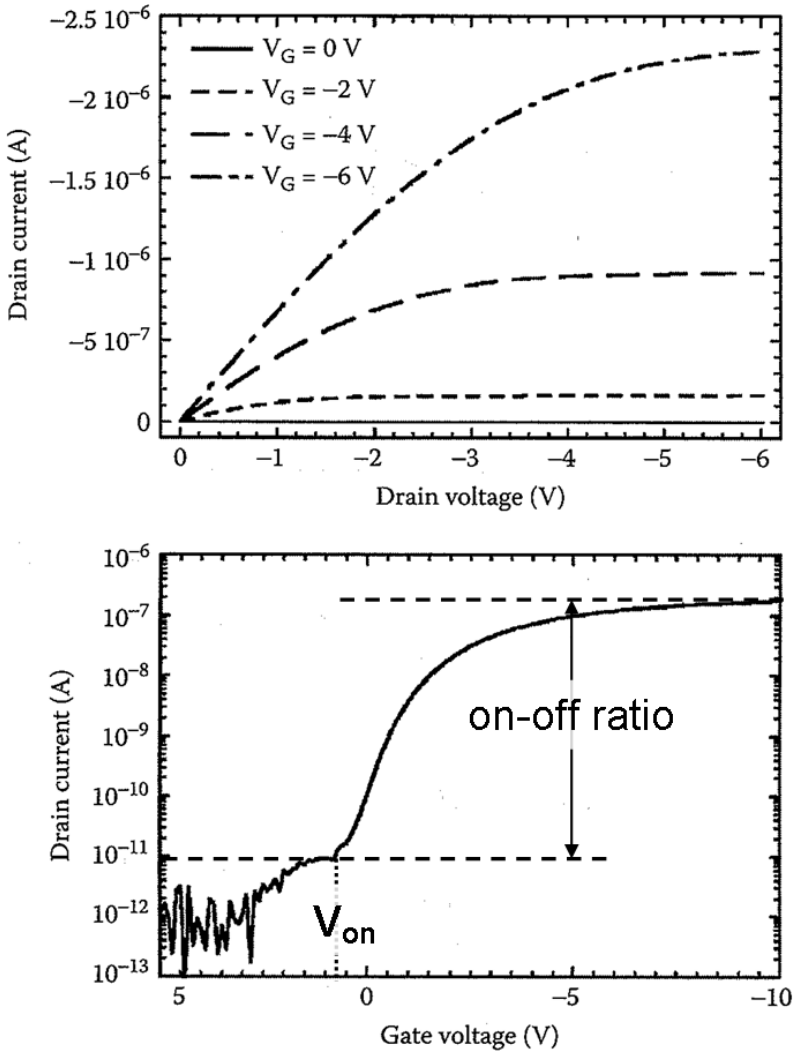

Figure 19: Top: Output characteristic of an organic transistor showing the drain current as a function of the drain voltage. In the linear regime (at low drain voltage) the drain current increases linearly with the drain voltage. When the drain voltage is higher than the gate voltage the drain current saturates (higher drain voltages). Bottom: Transfer characteristic of an organic transistor. It shows the drain current (logarithmic scale) as a function of the gate voltage. The on-off ration and the on-voltage (V_{on}) is indicated. The picture is taken from reference 22. No elaboration of used layers and structure have been given.

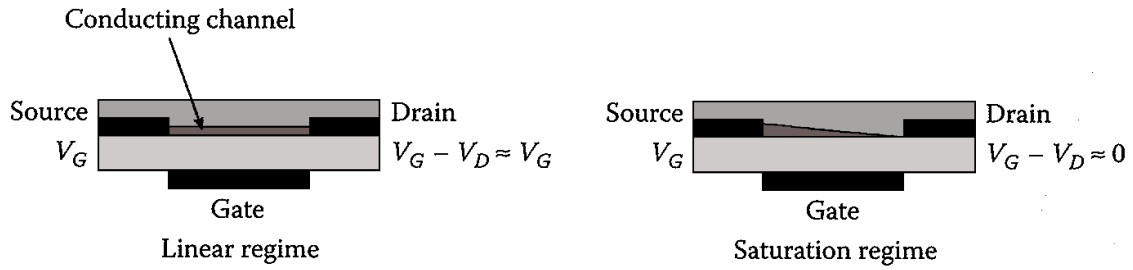

Figure 20: Charge distribution in an OTFT along the channel. In the linear regime (left) a conduction channel is formed and the charge density is constant along the channel. In the saturation regime (right) the charge density drops to zero from the source to the drain electrode. This scheme is taken from reference 22.

To calculate the threshold voltage and the charge carrier mobility, the following two equations are used:

$$I_{drain,lin} = \frac{Z}{L} C_i \mu \left[\left(U_{gate} - U_{th} \right) U_{drain} D - \frac{U_{drain}^2}{2} \right] \tag{11}$$

and

$$I_{drain,sat} = \frac{Z}{2L} C_i \mu \left(U_{gate} - U_{th} \right)^2 \tag{12}$$

where $I_{drain,lin}$ is the drain current in the linear regime or $I_{drain,sat}$ is the drain current in the saturation regime, Z is the channel width, L is the channel length, C_i is the capacitance of the channel, μ is the charge carrier mobility, U_{gate} is the gate voltage, U_{th} is the threshold voltage and U_{drain} is the drain voltage.

The exact extraction of the threshold voltage as well of the charge carrier mobility is somehow problematic. In the case of the carrier mobility (μ) one has to consider the dependence of μ on the charge carrier density, which is not constant in the saturation regime. A more reliable value of μ is usually extracted from the linear regime (and equation 11). To extract the threshold voltage various methods are known in literature (see, e. g., reference 24) in both regimes. The physical meaning of the threshold in OTFTs is jet not understand and defined completely[25,26,27] and a more meaningful value is the on-voltage. It is defied as the voltage at which the first mobile charge is formed.[28] For the evaluation of the U_{th} we used the second derivative (SD) method[29] (see section 4). Here the threshold voltage is located at the maximum of the second derivative of the transfer characteristic in the linear regime. The method is highly sensitive to measurement errors and noise.[24] Further methods to extract the threshold voltage from the linear regime are, e. g., the ratio method (RM) and the linear cofactor difference operator (LCDO) method. In principle evaluating the U_{th} from the linear regime should be favored in comparison to the extraction in the saturation regime, because more parameters are constant (e. g., the mobility).

2.4 Density Functional Theory

This section is generally based on reference 30,31,32.

Conceptually, in density functional theory (DFT), the total energy and, in fact, all ground state properties of molecules, solids, and surfaces are calculated relying only on the electron density of the system, instead of solving the Schrödinger equation of the many particle problem.

The nonrelativistic Schrödinger equation of the many particle (electrons and nuclei) problem has a well-defined Hamiltonian given by

$$\widehat{h} = \widehat{T}_{nucl} + \widehat{T}_{el} + \widehat{V}_{nucl-nucl} + \widehat{V}_{nucl-el} + \widehat{V}_{el-el} \tag{13}$$

where $\widehat{T}_{nucl}$ and $\widehat{T}_{el}$ are the kinetic energies of the nuclei and the electrons, respectively.[30] The other therms describe the electrostatic interaction between the positively charged nuclei and the negatively charged electrons, and among themselves. They are given by (here spins are neglected for the sake of clarity)[30]

$$\widehat{T}_{nucl} = \sum_{I}^{L} \frac{\nabla_I^2}{2M_I} \ , \tag{14}$$

$$\widehat{T}_{el} = \sum_{i}^{N} \frac{\nabla_i^2}{2m} \ , \tag{15}$$

$$\widehat{V}_{nucl-nucl} = \frac{1}{2} \sum_{I \neq J} \frac{Z_I Z_J e^2}{|R_I - R_J|} \ , \tag{16}$$

$$\widehat{V}_{nucl-el} = -\sum_{i,I} \frac{Z_I e^2}{|r_i - R_I|} \ , \tag{17}$$

and

$$\widehat{V}_{el-el} = \frac{1}{2} \sum_{i \neq j} \frac{e^2}{|r_i - r_j|} \ . \tag{18}$$

Unfortunately, the solution of the Schrödinger equation

$$\widehat{h}\Phi(\mathbf{R}, \mathbf{r}) = E\Phi(\mathbf{R}, \mathbf{r}) \tag{19}$$

in a closed form in not possible.[30] A first approximation which can be introduced is the Born-Oppenheimer approximation.[33] Here the underlying idea is the separation in time scale of processes involving electrons and nuclei. Because the mass of the electrons is much smaller than the mass of the nuclei, the electrons are much 'faster'.[30] So the Hamiltonian

can be split up into two parts ($\widehat{h}_{el}$ and $\widehat{h}_{nucl}$), whereas $\widehat{h}_{el}$ is given for fixed nuclear positions

$$\widehat{h}_{el} = \widehat{T}_{el} + \widehat{V}_{nucl-nucl} + \widehat{V}_{nucl-el} + \widehat{V}_{el-el}. \tag{20}$$

This leads to a the Schrödinger equation for electrons with a fixed configuration of nuclei

$$\widehat{h}_{el}\Psi(\mathbf{r}) = E\Psi(\mathbf{r}) \tag{21}$$

After a short introduction of the basic form of the Hamiltonian and the electronic Hamiltonian now the basics of DFT is introduced here, as an alternative way to solve the Schrödinger equation. The basics of DFT as we know it today were introduced in 1964 by Hohenberg und Kohn[34] and the first Hohenberg-Kohn theorem (Proof of Existence) states that the ground state electron energy of a system is uniquely defined via the electron density $n(r)$.[31] This leads to the fact that the total energy and hence all properties of a system are determined uniquely when the electron density is known.[32] A big advantage of this approach is the density only depends on just three spatial coordinates (x, y, and z) and are independent of the number of electrons in the system (whereas when solving the Schrödinger equation of the many particle problem, the total energy depends on the three spatial coordinates of *each* electron).[31] According to the second Hohenberg-Kohn theorem (Variational Principle) only the true ground state density delivers the minimal ground state energy of a system.[32] The remaining problem is to find the correct functional connecting the ground state energy and the electron density.

Therefore, the suggestions of Kohn and Sham[35] on how to approximate this functional in 1965 were crucial to the success of modern DFT.[31] They introduced orbitals of non-interacting particles - so called Kohn-Sham (KS) orbitals - to calculate the kinetic energy.[31,E] Then the KS equation is given as following:[30]

$$\left[-\frac{1}{2}\nabla^2 + v_{ext}(\mathbf{r}) + v_H(\mathbf{r}) + v_{xc}(\mathbf{r})\right]\psi_i(\mathbf{r}) = \epsilon_i\psi_i(\mathbf{r}) \tag{22}$$

The single-particle wave functions ψ_i and the eigenenergies ϵ_i are determined by equation (22). The effective one-electron potential (v_{eff}) acting on the electron in the Kohn-Sham formalism is given by

$$v_{eff}(\mathbf{r}) = v_{ext}(\mathbf{r}) + v_H(\mathbf{r}) + v_{xc}(\mathbf{r}) \tag{23}$$

with v_{ext} and v_H being the external potential and the classic electrostatic interaction potential (corresponding to the Hartree potential), respectively. The energy obtained by any interaction of the KS-orbitals is given in the so called exchange-correlation term. The

[E] Orbital free methods usually give bad results for the kinetic energy e. g. the Thomas-Fermi-Dirac model.[36,37,38,39]

exchange correlation potential v_{xc} is a functional derived from the exchange-correlation functional E_{xc}

$$v_{xc}(\mathbf{r}) = \frac{\delta E_{xc}(n)}{\delta n} \tag{24}$$

The connection between the artificial non-interacting orbitals and the system we are really interested in is given through the summation of the squared orbitals ψ_i, which describes the ground state density of the real system (with interacting electrons).[32]

$$n_{KS}(\mathbf{r}) = \sum_{i}^{N} |\psi_i(\mathbf{r})|^2 \tag{25}$$

Here, the number of particles is given by N. This relation requires, that the correct functional has been found.

By reintroducing orbitals the complexity is again increased compared to the original idea of a purely density dependent functional. However this approach is still more convenient than solving the original many particle Schrödinger equation.

The complication of the Kohn-Sham approximation is that the exact form of E_{xc} is not known. The choice of the functional form to obtain approximations to the exchange-correlation energy lead to various different DFT variants.[31] Today, the quality of a particular DFT approach depends only on the accuracy of the chosen approximation of E_{xc}.[32]

A widely used approach is the local density approximation (LDA). Here one assumes that the exchange correlation for a given density can be treated by the expression for a hypothetical uniform electron gas. This model works well for metals but for molecules it is far from any realistic situations because the no variation of the density within the molecule are considered.[32] The exchange-correlation energy in the LDA E_{xc}^{LDA} can be written as

$$E_{xc}^{LDA}[n] = \int d^3\mathbf{r} n(\mathbf{r}) \varepsilon_{xc}^{LDA}(n(\mathbf{r})). \tag{26}$$

The expression $\varepsilon_{xc}^{LDA}(n(r))$ gives the exchange-correlation energy per particle of a uniform electron gas density $n(r)$.[32]

To obtain more reliable results when investigating, e. g., molecules (not metals) the generalized gradient approximation (GGA) is often used. Here, besides the density itself also the gradient of the density is included as a variable to calculate the exchange-correlation energy E_{XC}^{GGA} (see equation 27).

$$E_{xc}^{GGA}[n] = \int d^3 r n(\mathbf{r}) \varepsilon_{xc}^{GGA}(n(\mathbf{r}), |\nabla n(\mathbf{r})|) \tag{27}$$

The GGA is sometimes also referred to a 'non-local' method (in comparison to the local density approximation) but this is somehow misleading since the functional is only depending

on the density at a given point (plus the derivative at this point).[31] Real-non-local functionals can describe non-local properties like the van der Waals interactions. The simplest form for such a functional is given by

$$E_c^{nl}[n] = \frac{1}{2}\int d^3r d^3r' n(\mathbf{r})\phi(\mathbf{r},\mathbf{r}')n(\mathbf{r}') \tag{28}$$

where $\phi(\mathbf{r},\mathbf{r}')$ a gerneal, given function depending on $\mathbf{r}-\mathbf{r}'$ and the densities in the vicinity of $\mathbf{r}$ and $\mathbf{r}'$.[40,41,42] Note, that just the correlation is calculated with this expression, because the van der Waals interactions has only correlation contributions and no exchange contributions.

In our group mostly the PW91 (Perdew-Wang 1991)[43] and the PBE (Perdew-Bruke-Ernzerhof)[44] functionals are used.

2.4.1 DFT for Periodic Systems

This section follows reference 45.

To calculate periodic systems with DFT a good starting point is the Bloch theorem[46] which stats that the solution of the wave function for periodic systems can be expressed as:[47]

$$\psi_k(\mathbf{r}) = u_k(\mathbf{r})\, exp(i\mathbf{k}\cdot\mathbf{r}). \tag{29}$$

The first factor, $u_k(\mathbf{r})$, represents the periodic part of the wave function and therefore has the same periodicity as the unit cell. This can be written as

$$u_k(\mathbf{r}) = u_k(\mathbf{r} + n_1\mathbf{a}_1 + n_2\mathbf{a}_2 + n_3\mathbf{a}_3) \tag{30}$$

with $\mathbf{a}_1$, $\mathbf{a}_2$ and $\mathbf{a}_3$ being the lattice vectors of the unit cell and n_1, n_2 and n_3 are integers. The second factor of equation 29, $exp(i\mathbf{k}\cdot\mathbf{r})$, is the plane wave.[45]

To describe periodicity, it is useful to introduce the reciprocal space[47], also named k-space, here. The reciprocal lattice vectors are defined to be

$$\mathbf{b}_1 = 2\pi\frac{\mathbf{a}_2\times\mathbf{a}_3}{\mathbf{a}_1\cdot(\mathbf{a}_2\times\mathbf{a}_3)}, \mathbf{b}_2 = 2\pi\frac{\mathbf{a}_3\times\mathbf{a}_1}{\mathbf{a}_2\cdot(\mathbf{a}_3\times\mathbf{a}_1)}, \mathbf{b}_3 = 2\pi\frac{\mathbf{a}_1\times\mathbf{a}_2}{\mathbf{a}_3\cdot(\mathbf{a}_1\times\mathbf{a}_2)} \tag{31}$$

and $a_i\cdot b_j$ is 2π if $i=j$ and 0 if $i\neq j$.[45] In reciprocal space the smallest repetition unit is called the Brillouin zone (BZ). It is the reciprocal match to the Wigner-Seitz cell. The most important point in the BZ is the Γ point at $\mathbf{k}=0$. The relation between the volume of the BZ (V_{BZ}) and the Wigner-Seitz cell (V_{cell})[45] is

$$V_{BZ} = \frac{(2\pi)^3}{V_{cell}}. \tag{32}$$

The functions $u_k(\mathbf{r})$ (equation 29) can be expanded in terms of a Fourier series leading to

$$u_{\mathbf{k}}(\mathbf{r}) = \sum_{\mathbf{G}} c_{\mathbf{G}}\, exp(i\mathbf{G}\cdot\mathbf{r}) \tag{33}$$

where $\mathbf{G}$ are the reciprocal lattice vectors defined as $\mathbf{G} = m_1\mathbf{b}_1 + m_2\mathbf{b}_2 + m_3\mathbf{b}_3$ with integer values for m_i.[45] By combining equation 29 and equation 33 the electron wave function can be written as a linear combination of plane waves:

$$\psi_k(r) = \sum_{\mathbf{G}} c_{\mathbf{k}+\mathbf{G}}\, exp[i(\mathbf{k}+\mathbf{G})\mathbf{r}]. \tag{34}$$

This series is infinite, because the solution at a single k-point implies summation over an infinite number of $\mathbf{G}$ values.

Until now a exact solution for $\psi_k(r)$ can be calculated, but often this is very complex and therefore, basis sets are introduced. The easiest method is using plane waves as basis set. Another widely used basis set are based on linear combinations of atomic orbitals (LCAO). When using a plane-wave basis set, a limitation has do be done in terms to solve the Kohn-Sham equation.

The plane waves in equation 34 can be associated with a kinetic energy of $\frac{\hbar^2}{2m}|\mathbf{k}+\mathbf{G}|^2$. Because plane waves with low kinetic energy are physically more important than those of high energy, when reaching for an approximate expression for $\psi_k(r)$, one can introduce a kinetic energy cut-off E_{cut}

$$E_{cut} = \frac{\hbar^2}{2m} G_{cut}^2. \tag{35}$$

This results in

$$\psi_k(\mathbf{r}) \approx \sum_{|\mathbf{G}+\mathbf{k}|<G_{cut}} c_{\mathbf{k}+\mathbf{G}}\, exp[i(\mathbf{k}+\mathbf{G})\mathbf{r}]\ . \tag{36}$$

The cut-off energy is an important parameter in plane-wave DFT calculations. Large energy cut-offs are used to describe plane waves with a short oscillation length (small wave legnth) in real space and especially core electrons are associated with such plane waves. Therefore, each element requires a different energy cut-off, so that it is worthwhile to use the highest value as the overall E_{cut} when different species are present in a calculation. Furthermore the same value should be used in all calculations one wants to compare.[45]

To avoid using very high E_{cut} (the higher the value the higher the effort of the calculation), it is possible to describe the core electrons separately from the valence electrons. This leads to the introduction of pseudopotentials, with the properties of the core electrons being fixed (frozen core). This separation is reasonable when considering, that the core electrons are not especially important for the process of bonding[45] and the electronic properties of materials.

In pseudopotentials usually a minimum cut-off energy is suggested. One distinguishes between hard pseudopotentials having a high E_{cut} and soft pseudopotentials requiring only a low energy cut-off. In our calculations the projector augmented-wave (PAW) approach was used, originally introduced by Blöchl[48] and later adapted for plane-wave calculations by Kresse and Joubert.[49] Here, the PAW wave function has two contributions: a valence term, which is expanded in a plane wave basis and a second term, which are dedicated to the contribution from the region within the core radius of each nucleus, evaluated on a grid.[31,F]

2.4.2 Slab-Type Calculations of Surfaces

This section follows reference 45.

Now it is time to explain how surfaces can be calculated. It would be useful to use periodic boundary conditions, but only in 2 dimensions (x- and y-axis). Common codes allow periodic boundary conditions only in all three dimensions. Therefore the surface is introduced by inserting a vacuum gap as illustrated in figure 21. The vacuum gap has to be chosen to be large enough to exclude interaction between two in z-direction successive slabs.[45] In this thesis, slabs consisting of five (or four) metal layers are used onto which molecules are adsorbed.

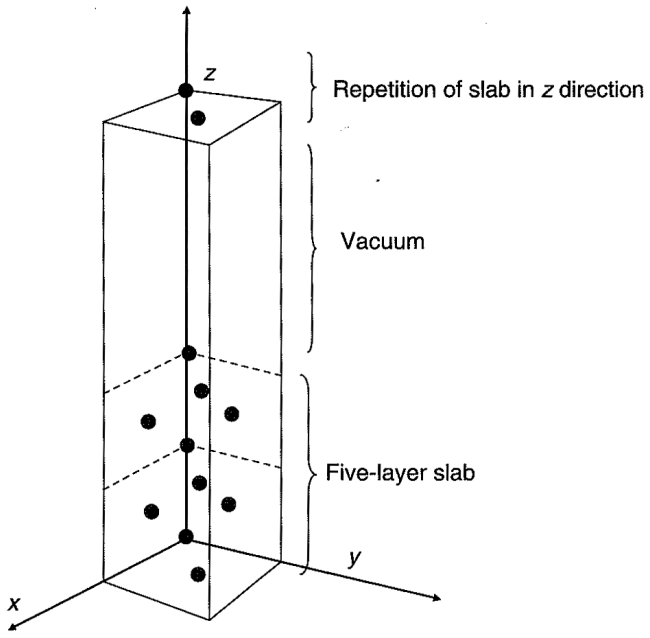

Figure 21: Scheme of an unit cell used with periodic boundary conditions. In z-direction an vacuum gap is introduced to simulate a surface.[45]

[F] In other words, PAW is a linear transformation from pseudo wave functions to all-electron wave functions.

The asymmetry in z-direction in the unit cell, which arises due to the vacuum gab, requires an asymmetric k-point sampling.[G] The common Monkhorst-Pack method[50] is used to select the k-points in x- and y-direction in our calculations, whereas, in the z-direction every time only one k-point is considered. The convergence of the number of k-points in x- and y- direction has to be tested for each unit cell and care has to be taken when changing the size of the unit cell (an increased unit cell requires fewer k-points). To allow comparison between different calculations (of one unit cell) the density of k-points should never be changed.[45]

Due to the asymmetry of the slab, arising from the adsorbed molecules, a dipole is formed which cases a homogeneous electrostatic field along the z-direction of the unit cell. To compensate this field, a dipole layer is introduced in the middle of the vacuum gap.[51] Another possibility to overcome this problem is the use of symmetric slabs. In this case the molecules are adsorbed on both sides of the slabs. By doing so no dipole and with it no electrostatic field arises. This method was not used in this thesis because a larger amount of atoms (twice as much molecules) is needed, which expands the calculation-time significantly.

2.4.3 Internal Coordinate Optimization

This section follows mostly reference 52.

When optimizing the geometry of a system by minimizing its total energy as a function of the nuclear coordinates different methods can be used. For the reduction of the optimization time it would be beneficial to use an optimal geometry optimization scheme, which needs just few steps to obtain the final structure.

Often Cartesian coordinates system is used in band-structure codes (e. g. in Vienna ab-initio simulation package (VASP)[53]) in which the geometry optimization is performed. The coordinate system is defined by a point of origin and - in the three dimensional case - three coordinate axis which traverse in the origin. Here the position of each atom is defined by their x-, y- and z- coordinates denoted here as $\mathbf{s}$.[52] In periodic systems additionally three lattice vectors ($\mathbf{h}$) are used to describe the system completely.[52] Often the algorithm to optimize the geometry is based on a local harmonic expansion of the total energy in terms of the present geometry (equation 37).[52]

$$E(\mathbf{x}+\delta\mathbf{x}) - E(\mathbf{x}) = -f^{\boldsymbol{t}}\delta\mathbf{x} + \frac{1}{2}\delta\mathbf{x}^{\boldsymbol{t}}\mathbf{F}\delta\mathbf{x} + ... \tag{37}$$

with $\delta\mathbf{x} = \{\delta\mathbf{s}, \delta\mathbf{h}\}$.[H] The exact first and the approximated second derivatives are used

[G] A discrete number of k-points is chosen to overcome the computational effort to solve the integral over the Brillouin zone. This is done by evaluating the function to be integrated at a set of discrete points and summing the function values with appropriate weight for each point.[45]

[H] Note, that in our calculations only the coordinate position ($\mathbf{s}$) and not the size of the unit cell $\mathbf{h}$ is

to predict a new structure.[52] The first part contains the force vector $\mathbf{f} = -dE/dx$. The second part corresponds to an extended Hessian matrix built of the second derivatives of the energy with respect to the atomic position.[52]

Another possibility to define the structure of the investigated system is the use of internal coordinates $\delta\boldsymbol{\xi} = \{\delta\mathbf{q}, \delta\widehat{\mathbf{q}}\}$. Here only internal degrees of freedom (e. g. bond length, bond angle and dihedral angle) are involved. These internal atomic coordinates are, in general, nonlinear functions of the Cartesian coordinates. Therefore, internal coordinate deformations are related to external coordinates deformation by a nonlinear transformation usually obtained by a truncated Taylor expansion given in equation 38[52]

$$\delta\boldsymbol{\xi}_i = (\mathbf{B}\delta\mathbf{x})_i + \frac{1}{2}\delta\mathbf{x}^{\boldsymbol{t}}\mathbf{C}^i\delta\mathbf{x} + ... \quad . \tag{38}$$

This leads to following formalism[52]

$$E(\boldsymbol{\xi} + \delta\boldsymbol{\xi}) - E(\boldsymbol{\xi}) = -\varphi^{\boldsymbol{t}}\delta\boldsymbol{\xi} + \frac{1}{2}\delta\boldsymbol{\xi}^{\boldsymbol{t}}\mathbf{H}\delta\boldsymbol{\xi}. \tag{39}$$

The relationship between external and internal force components (equation 37,38 and 39) is given by[52]

$$\mathbf{B}^{\boldsymbol{t}}\varphi = \mathbf{f} \tag{40}$$

and the relationship between internal and external deformation is[52]

$$\mathbf{B}\delta\mathbf{x} = \delta\boldsymbol{\xi} \ . \tag{41}$$

The matrix $\mathbf{B}$ is the connection (transformation) between the Cartesian and internal coordinate system. $\mathbf{B}$ is called the Wilson's B-matrix[54] for periodic systems.[52]

For some of our calculations, the GADGET[52] optimization tool was used. Here delocalized internal coordinates are considered where linear combinations are used to produce non-redundant internal coordinates (for more details see reference 52) and the optimization strategy is based on the geometrical direct inversion in the iterative subspace (DIIS).[55,56] In practice the GADGET is used to optimize the geometry of the system. The structure found be GADGET is the the input for VASP, which optimized the charge density of the system. In contrast our standard optimizations in Cartesian coordinates with VASP[53] use a simple damped molecular dynamics (dMD) scheme.

2.4.4 Calculation of STM Images

To allow comparison between experimental and theoretical results, the knowledge of the unit cell, the number of molecules per unit cell and the molecular arrangement within

optimized.

the unit cell is a crucial point. To obtain these properties, scanning tunneling microscopy (STM) is a powerful experimental tool. If it is possible to reproduce the STM-image by simulation, one can assume that the calculated molecular arrangement correlates with the real structure.

The concept of STM is based on quantum tunneling. A sharp conducting tip is placed very near to the surface of the sample and then scans the surface.While scanning, a bias voltage V is applied between the STM-tip and the sample.

The resulting tunneling current density j is a function of the tip position, the applied voltage V and the local electron density of state $LDOS$. In simplified form the tunneling current density j can be written as[14]

$$j = \frac{LDOS \cdot V}{d} exp(-A\phi_B^{1/2} d) \ . \tag{42}$$

Here d is the distance (gap) between the sample and the tip, $LDOS$ reflects the electron state densities, A is a constant and ϕ_B is the effective barrier height of the junction[14], compare figure 22.

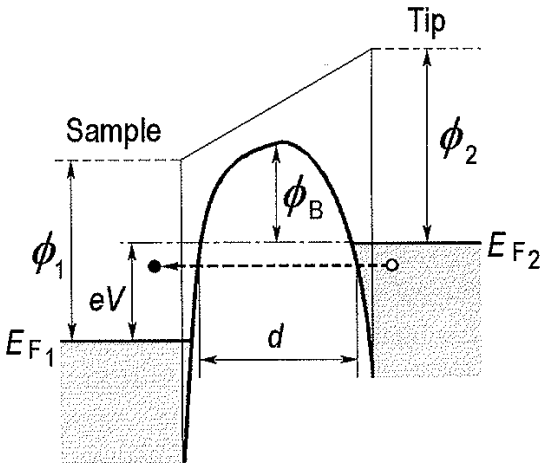

Figure 22: Schematic energy diagram of the tunneling contact between the sample and the STM-tip. E_{F_1} and E_{F_2} are the Fermi energies for the sample and the tip and ϕ_1 and ϕ_2 are their work functions, respectively. d is the effective tunneling gap, ϕ_B is the effective barrier height, and V is the bias voltage.This image was taken from reference 14.

The local density of states (LDOS) is defined as the summation of the density of states at a position $\mathbf{r}$ between the Fermi Energy (E_F) and the tip bias V (valid for $i = E_F - V < \epsilon_i < E_F$ for occupied states / positive tip bias and $i = V - E_F > \epsilon_i > E_F$ for unoccupied

states / negative tip bias).

$$LDOS(V) = \sum_i |\varphi_i(\mathbf{r})|^2 \delta(E - \epsilon_i) \tag{43}$$

Here, the Kohn-Sham orbitals are denoted as $\varphi_i(\mathbf{r})$ at the position $\mathbf{r}$ and the energy eigenvalues are denoted as ϵ_i [57].

There are three main experimental parameters in STM: the tunneling current I, the bias voltage v and the tip (including the lateral coordinates x, y and z).[14] Alternating these parameters lead to three STM-operating modes. From the *constant-current mode* and the *constant height mode* STM images are obtained (see figure 23), whereas in *Scanning tunneling spectroscopy*, the outputs are diagrams of the LDOS as a function of the energy with varying V.[14]

For the constant current mode, images the tunneling current I and the tip bias V are held constant and the height of the tip (z) is measured (compare figure 23a).[14] This method is the most widely used, because surface which are not atomically flat can be probed and the quantitative determination of the height is quite accurate due to the use of piezoelectric drivers. The calculated STM-images for this mode are a representation of the integrated (between the interested orbital feature in the DOS and the Fermi energy) and averaged (implemented tip) isosurface of the LDOS at a specific iso-value (in electrons/$\mathring{\text{A}}^3$). In this thesis, all STM-images (experimental and calculated) are made using the constant current mode.

In the constant height mode the height z of the tip and the tip bias V are constant and the tunneling current I is measured as sketched in figure 23b.[14] This method allows a very fast imaging of the sample, which is in particular interesting for studying real-time dynamics processes. To calculate images in this mode, the averaged and energy-integrated LDOS is imaged at a specific height.

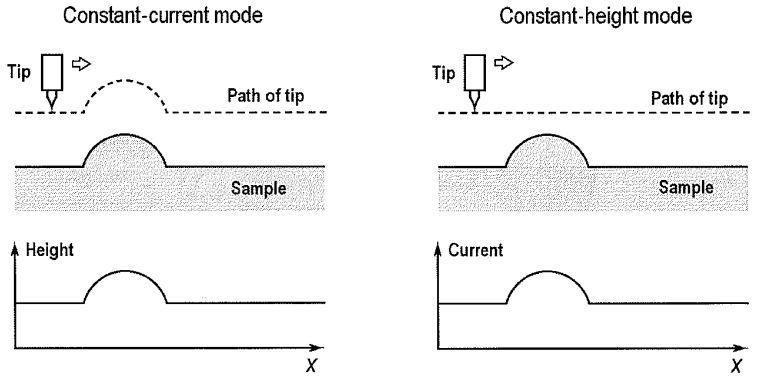

(a) (b)

Figure 23: Schematic illustration STM imaging techniques with different modes: (a) constant-current mode and (b) constant-height mode. This images were taken from reference 14.

To calculate STM images the main three experimental parameters, mentioned above, have to be known, calculated and approximated. The tunneling current is given by the Bardeen's formalism[58]

$$I = \frac{2\pi e}{\hbar} \sum_{\mu,\nu} f(E_\nu) \left[1 - f(E_\nu + eV)\right] |M_{\mu\nu}|^2 \delta(E_\mu - E_\nu) \tag{44}$$

where $f(E_\nu)$ is the Fermi function at the energy E_ν, e is the elementary charge, V is the applied voltage, $M_{\mu\nu}$ is the tunneling matrix element between states ψ_μ of the tip and ψ_ν of the surface, and E_μ is the energy of state ψ_μ in the absence of tunneling.[59,60] The main problem is the calculation of the tunneling matrix element $M_{\mu\nu}$, which is given by

$$M_{\mu\nu} = \frac{\hbar^2}{2m} \int dS(\psi_\mu^* \nabla\psi_\nu - \psi_\nu^* \nabla\psi_\mu) \tag{45}$$

where the integral is taken over any surface, which is completely lying in the region of the potential barrier between the two electrodes (sample and tip)[59,60] and m denotes the masses of the electrodes. The expression in the brackets is the current density j (compare equation 42).[60] The wave function of the tip ψ_μ is not known adn approximations have to be done. Therefor, the Tersoff-Hamann approach[59,61] is used, which states, a tip with a spherical s-orbital symmetry, low temperatures and small applied tunneling voltage V. The tunneling current can then by simplified as[59,61,60]

$$I \approx V n_t(E_F) e^{-2\kappa d} \sum_{\nu} |\psi_{r_t}|^2 \delta(E_\mu - E_\nu) \tag{46}$$

with $\kappa = (2m\phi_B/\hbar^2)^{1/2}$, ϕ_B is the effect barrier height, $n_t(E_F)$ is the density of states at E_F, d is the distance between the tip and the sample and r_t the center of the tip.

In this thesis, the simulated STM images where obtained by the implementation of the Tersoff-Hamann approach into the VASP-code,[53] where the LDOS is evaluated on a dense real-space grid. This leads to an image resolution of about 0.1Å. The resulting calculated STM images would be much to 'accurate' and therefore sometimes 'unrealistic' in comparison to experimental STM images, because the small 'tip' can penetrate between the individual molecules down to the metal slab. To avoid this when calculating the STM images, the LDOS is averaged over a finite spherical tip with a approximately diameter of 2 Å, shown in figure 24.[57]

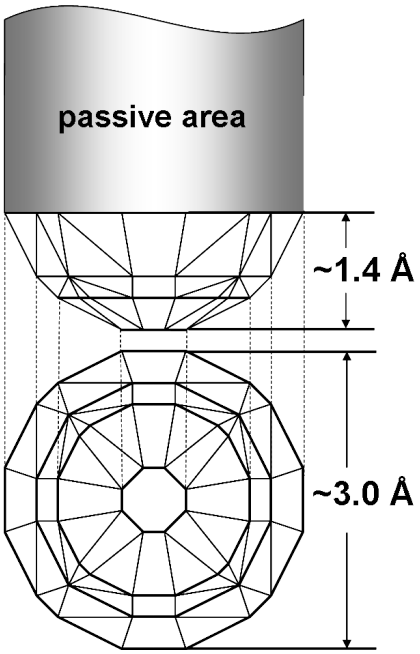

Figure 24: Top and side view of an scheme of the finite tip used to calculate STM-images averaging the LDOS at 56 points. This images was is taken from reference 57.

2.4.5 Calculation of Band Structures

The electronic behavior of an organic layer on a metal surface is of particular interest when thinking of organic electronics. (compare section 2.3) Since these organic layers are extended theoretically infinitely in two directions, it is obvious to investigate the band structure of such layers. An example is given in figure 25.

The band dispersion (or band width) is determined by the overlap (or interaction) of the orbitals. The greater the overlap the greater the band dispersion. Depending on the symmetry of the orbitals they have minimal or maximal energy at a specific k-value. The

number of occupied bands is equivalent to halve of the number of electrons in the unit cell (for a semiconductor).[62] Usually there is a large number of states on a surface. The number of states increases with the number of electrons in the unit cell and this leads to a large number of bands which are often very complex and confusing. Therefore the density of states (DOS) is often easier to understand. The DOS is defined as the number of energy levels between a defined energy range $E - \epsilon_i$ (compare section 2.4.4).

$$DOS(E) = \sum_i \delta(E - \epsilon_i) \tag{47}$$

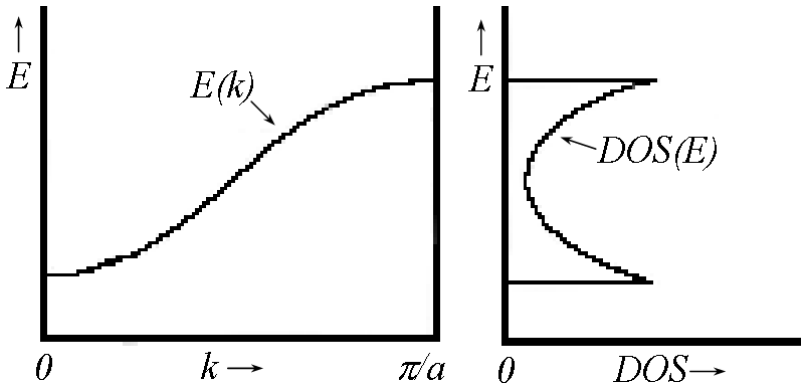

Figure 25: Schematic drawing of one band and the corresponding DOS. Figure is taken from reference 62.

In general, the DOS is proportional to the inverse of the slope of the $E(k)$ or in other words the more flat the band the greater the density of states.[62]

In this thesis, we calculated the band structures via following procedure: first the charge density is calculated for a fully selfconsistent calculation with a full k-point grid.[I] In a next step the obtained charge density is used for a non-selfconsistent run (CHGCAR=11) with 'strings' of k-points connecting specific points in the Brillouin zone. Usually these 'strings' of k-points are chosen to be along high-symmetry directions in the Brillouin zone.

[I] Here, the Monkhorst-Pack grid is used (compare section 2.4.2).

3 Experimental Investigations of Photochemically Patterned Organic Surfaces

3.1 Introduction

Changing the properties of inorganic surfaces is widely applied and plays an increasing role in nanotechnology, biotechnology and molecular electronics.[63,64,65,66,67,68] For tailoring the surface properties for individual applications, self-assembled monolayers (SAMs) are often used. They can act as coatings, as corrosion protections[69], as wetting[70] and adhesion[71] layer or more actively as interlayer to change the work function[6] in devices.

Generally SAMs can be described as molecular aggregates of bifunctional molecules which spontaneously form monolayers on a surface. The bifunctionality is used to introduce a docking group, which selectively forms a covalent bond with the surface and a head group (often also called functional group), which can be varied to obtain the new properties of the surface. For hydroxyl terminated oxidic surfaces like SiO_2 and Al_2O_3 silanes are widely used as docking group, whereas for metals like gold, silver and copper thiol docking groups are used. As head group, an infinite number of possibilities are accessible due to the diversity of organic synthesis. This opens the possibility for the head group to fulfill a defined task, like being chemical reactive, having a specific polarity, or being inert.

A particular interest is the finding of switchable SAMs to change the surface properties after the layer is formed.[72,73] This idea can be extended to perform 2D or 3D micro- or nano-patterns on the surface. An elegant method to pattern the surface is the use of photolithographic techniques. Due to the thinness of SAMs, a better spatial resolution in the photo-patterning is possible. An example for this process is the photo-oxidation of alkyl chains[74] or, when the irradiation energy is higher, the removal of the organic layer in the illuminated areas[75,76] Another very convenient approach is the use of molecules which are already bearing a photoreactive head group. One example is the introduction of an azobenzene group in which one can switch between the *trans*- and *cis*-isomer having different steric expansions.[77]

In this section, different novel photoreactive molecules are introduced to form SAMs. On one hand, a molecule bearing benzyl thiocyanate (-SCN) as functional head group is investigated. This group can photo-isomerise due to ultraviolet (UV) illumination to benzyl isothiocyanate (-NCS), which is chemically more reactive. On the other hand different, aryl esters were implemented as head groups allowing to change the surface polarity via the photo-Fries rearrangement using UV-light leading to the corresponding hydroxy ketone. With those photo-reactive head groups, a patterning of the surface reaching nanometer structures is possible.[78] Additionally, the difference in reactivity due to the illumination was exploited by selective postmodification of specific molecules in the illuminated areas

of the pattern. This leads to a more pronounced pattern not only with varied polarity but also with different height, friction and surface energy. Furthermore, the patterning has been extended to various substrates by employing different docking groups (silanes and thiols) on the molecules.

An important aspect was to prove the UV-induced changes and patterning on the surface with X-ray photoelectron spectroscopy (XPS)[A] supported by atomic force microscopy (AFM), Fourier-transformation infrared (FT-IR) and X-ray refectometry (XRR). XPS is a powerful tool to investigate SAMs since it is surface sensitive and chemical changes can be detected due to chemical shifts in the spectra. Especially the selective post modification can be followed easily, if heteroatoms are immobilized. In addition, the estimation of the layer thickness is possible, which is particularly relevant for silane-SAMs, where the formation of the self-assembled **monolayers** is somewhat problematic.

XPS was also important for controlling both the process of SAM production and the level of contamination arising during the process. Many problems could be detected and removed due to the XPS-feedback and with it XPS act as a very important general tool to obtain more reproducible SAMs.

[A] All XPS and UPS measurements have been performed by me at the Institut für Physik, Karl-Franzens Universität Graz under the suppervison of Prof. Michael G. Ramsey and Priv.-Doz. Georg Koller.

3.2 Silanes

3.2.1 Detailed Analysis of the Pretreatment of the Silicon Wafer Substrates Important for the Preparation of Thin Silane Films

At the beginning of this section the used substrate is investigated. The detailed knowledge of the change of the silicon oxide substrate during each the pretreatment step and during the thin film formation is crucial for obtaining relaible films and results.

Foreword and Introduction This investigation have been performed in cooperation with Dr. Thomas Höfler. Together we prepared the samples and measured the contact angle. Additionally XPS measurements have been performed. All results are also presented in his thesis.[79]

For the preparation of SAMs on silicon/silicon oxide wafers the surface plays an important role. Thorough cleaning of that surface is a prerequisite to obtain (well ordered) SAMs. The pretreatment ensures clean oxidic layers with high density of reactive silanol groups (Si-OH) on the surface.[68] The hydroxylated (hydrophilic) surfaces are required to allow the covalent bond formation of the SAM-molecule and the substrate usually via silanol groups of the silane molecule. Additionally the Si-OH groups on the substrate permit the formation of a thin water layer which is needed during the covalent bonding process (hydrolysis).[68]

For industrial processes usually the RCA cleaning procedure is used to remove organic and ionic contaminations. It is a three step process in which first the organic contaminants, the the silicon oxide and finally the ionic contamination is removed.[68] The Si-OH groups are then formed by a water dipping.

Similar (but less time consuming) results can be obtained by plasma etching (e g. with oxygen plasma) or with piranha solution. The plasma etching removes impurities by sputtering the surface and a subsequent water dipping leads to the formation of the active Si-OH group containing surface. The use of piranha solution (3:1 mixture of concentrated sulfuric acid and H_2O_2,30%) is rather dangorous, because it is a strong oxidant; The oxidation process is exothermic (up to 120°C) and can cause explosions. Nevertheless, in this short study of the pretreatment of the used substrates, piranha solution and a subsequent water dipping was used to activate the surface.

Experimental Section For the investigations silicon wafers with a native grown oxide layer (about 1-1.5 nm thick) were used. The pretreatment of the substrate involves six steps:

1. substrate cutting and removal of dust with a stream of compressed CO_2

2. etching the substrate with piranha solution (30 min) and subsequent water dipping and ultra-sonication (2 min) in deionized water; drying the sample with a stream of compressed CO_2

3. dipping the sample in toluene (anhydrous, in inert atmosphere) to control the SAM solvent; drying the sample with a stream of compressed CO_2

4. inserting the sample for 16 h in a 7 mmol solution of 11-(trichlorosilyl)undecanoic--acid-phenyl-ester (Si-PF-long) (see figure 26)in anhydrous toluene; short rinsing with clean anhydrous toluene and drying with a stream of compressed CO_2 (all done in inert atmosphere)

5. rinsing the substrate with HPLC grade toluene and drying with a stream of compressed CO_2 (under ambient conditions)

6. annealing the sample for 30 min at 100°C in vacuum

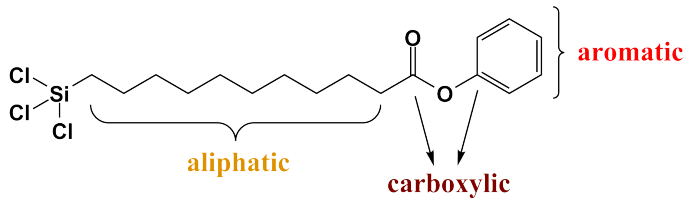

Figure 26: 11-(Trichlorosilyl)undecanoic-acid-phenyl-ester (Si-PF-long).

For the contact measurement samples where used after step 1, 2 and 6. XPS measurements have been taken after each step. Altogether ten samples have been prepared and after each step the amount of samples which were need for the investigations was removed.

The XPS parameters are described above. For the contact measurement the sessile drop method with a Drop Shape Analysis System DSA 100 (Krüss GmbH) with a liquid volume of about 3 μl was used. For every sample the contact angle was measured at least five times.

Results and Discussion The change of the surface properties was investigated with contact angle measurements. The surface of the wafer with the native grown silicon oxide was rather hydrophilic before any pretreatment (after step one). The contact angle of water was about 32° (with dichloromethane about 47°). After cleaning and activation of the surface with piranha solution (step 2) the water contact angle decreased below 10°(with dichloromethane about 39°) due the formed Si-OH groups, which are leading to a very hydrophilic surface. After forming a layer of Si-PF-long on the surface (removed after step 6) the contact angle of water increases significantly to 68° (with dichloromethane about

48°) reflecting a hydrophobic surface. In figure 27 the photos of the contact measurements with water are shown and demonstrate the changes wetting behaviors of the surface during the SAM preparation.

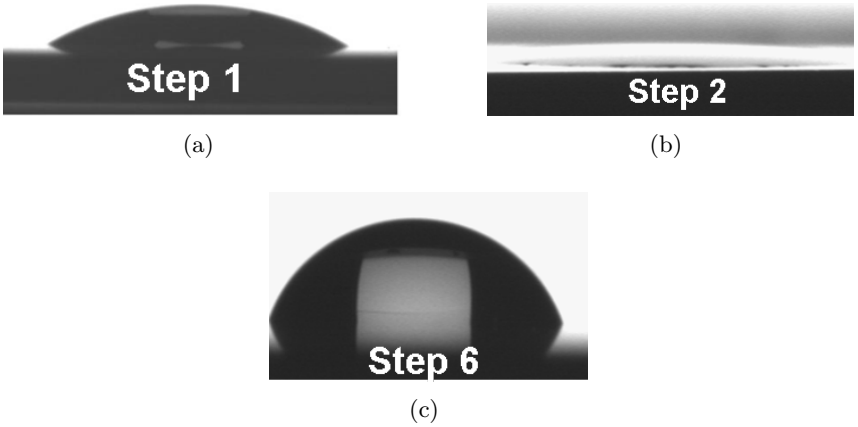

(a) (b)

(c)

Figure 27: Photos of the water droplet for contact angle measurement on a silicon/silicon oxide wafer (a) after cutting the wafer, (b) after cleaning and activating the surface with piranha solution and water dipping and (c) after SAM growth and annealing.

The XPS measurement have been performed after each step to get a deeper insight in the chemical changes during the SAM preparation. Summary of all obtained survey-spectra are shown in figure 28.

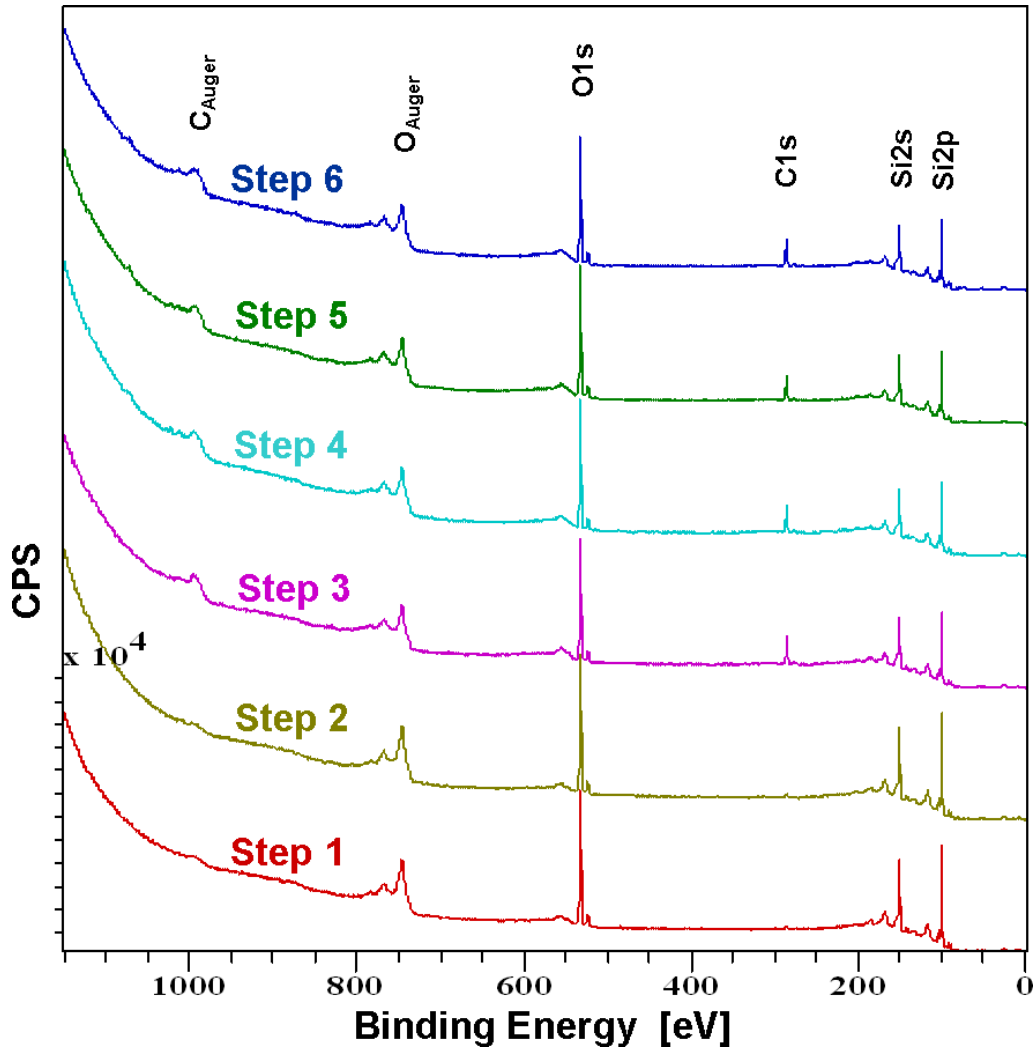

Figure 28: XPS survey spectra measured after each step during sample preparation.

After cutting the wafer (Step 1) only a trace amount of carbon at a binding energy of 285.3 eV was found on the surface. This can be attributed to organic contamination from ambient air. No other contaminations were found (e. g. nitrogen) on the surface. The ratio between the native grown oxide silicon and elemental silicon Si2p(SiO_x):Si2p(Si) was calculated to be 0.17 .

After the treatment with piranha solution and a subsequent water dipping (Step 2) the carbon amount decreases slightly but did not vanish completely due to ambient conditions. Note the C_{Auger} signal seen at a binding energy of 1000 eV is more sensitive to this surface contamination then the C1s signal due to the higher surface sensitivity at lower kinetic energy. For truly carbon free surfaces, preparation in ultrahigh vacuum (UHV) has do be done by argon sputtering. The silicon ratio stayed the same (the value and the image of the Si2p region is shown later in section 3.2.4.) and no further contaminations were introduced.

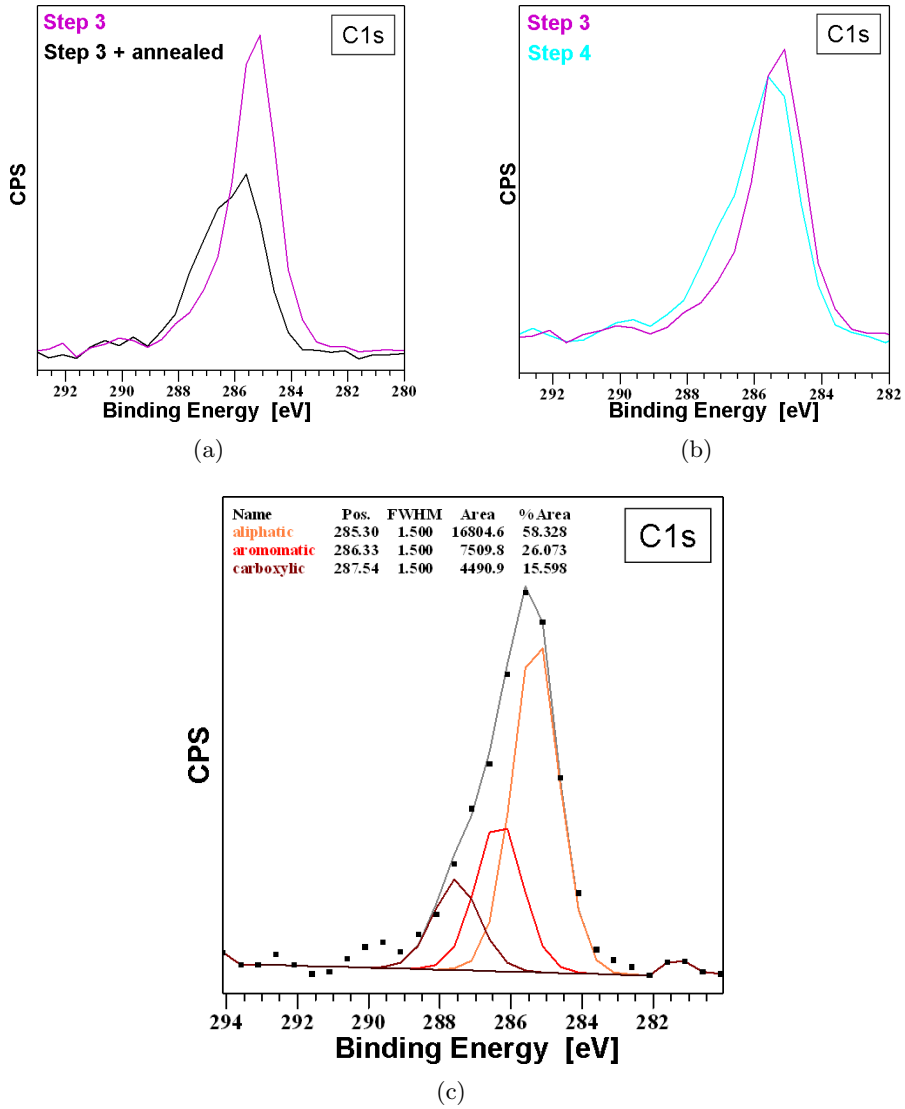

Figure 29: C1s region of (a) the treated substrate after the step 3 (magenta) in comparison with the spectra obtained after subsequent annealing (black), (b) the substrate after step 3 (magenta) and after step 4 (cyan), and (c) the substrate after step 4 (black squares). Here th relative composition of the different bonded carbons (orange, red, brown) and the resulting envelop (gray) is shown.

After depositing the substrate in toluene (Step 3) the carbon amount increases strongly due to adsorption of solvent on the surface. A additional annealing step of the same sample in the UHV-chamber did lower the carbon content. (See figure 29a). If the solvent adsorbed on the surface the SAM formations hindered and a additional annealing step during the preparation would be helpful.

Due to the SAM adsorption (Step 4) the carbon amount did not changed a lot, but

the shape of the C1s peak changed. (compare figure 29b.) A shoulder at higher binding energies arises from the different carbon-bonds (aliphatic, aromatic and carboxylic) in the Si-PF-long molecule. The exact ratio between the different carbon atoms C(aliphatic): C(aromatic):C(carboxylic) =10:5:2=1.0:0.5:0.2 as indicated in figure 26. The calculated ratio is shown in figure 29c (58:26:16=1.0:0.43:0.27) and is good agreement with the exact values. This allows the assumption that the SAM completely replaces the solvent from the surface. The chemical shift for the different bonded carbon is in good agreement with literature.[18]

During step 5 (rinsing) and step 6 (annealing) the surface composition did not change anymore.

3.2.2 Patterning of Si/SiO_2 Surfaces using Thiocyanate-Functionalized Trialkoxysilanes

After getting a detailed insight in the sample pretreatment and preparation, the novel silane molecule containing thiocyanate as a photo-reactive functional head group is investigated.

Foreword This work was performed in collaboration with Dr. Alexandra Lex-Balducci from the Institute of Chemistry and Technology of Organic Materials (renamed to 'Institute for Chemistry and Technology of Materials'). The following section largely reproduces the contents of 80. However, the experimental data performed by others coworkers is given in an abridged description, whereas the XPS results going far beyond what is included in reference 80 are presented in the 'Results and Discussion' section.

Chem. Mater. **2008,** *20,* 2009–2015

Synthesis of a Photosensitive Thiocyanate-Functionalized Trialkoxysilane and Its Application in Patterned Surface Modifications

Alexandra Lex,[†] Peter Pacher,[‡] Oliver Werzer,[‡] Anna Track,[‡,§] Quan Shen,[∥] Robert Schennach,[‡] Georg Koller,[§] Gregor Hlawacek,[∥] Egbert Zojer,[‡] Roland Resel,[‡] Michael Ramsey,[§] Christian Teichert,[∥] Wolfgang Kern,[†,⊥] and Gregor Trimmel*[,†]

Institute for Chemistry and Technology of Organic Materials, Graz University of Technology, Stremayrgasse 16, 8010 Graz, Austria, Institute of Solid State Physics, Graz University of Technology, Petersgasse 16, 8010 Graz, Austria, Institute of Physics, University of Graz, Universitätsplatz 5, 8010 Graz, Austria, Institute of Physics, Montanuniversität Leoben, Franz Josef Strasse 18, 8700 Leoben, Austria, and Institute of Chemistry of Polymeric Materials, Montanuniversität Leoben, Franz Josef Strasse 18, 8700 Leoben, Austria

Figure 30: Copy of part of the first page of reference 80 including all coauthors and their affiliations

In this collaboration the bifunctional molecule trimethoxy[4-(thiocyanatomethyl)phenyl]silane was synthesized by Dr. Lex-Balducci. The bifunctionality is given by a photoreactive head group, the benzyl thiocyanate unit, and a docking group, the trimethoxysilyl unit. The docking group allows the formation of SAMs or thin films on oxidic surfaces containing hydroxy groups. The photoreactive head group undergoes a photoisomerisation upon irradiation with UV-light in which the benzyl thiocyanate (-SCN) group forms the corresponding isothiocyanate (-NCS).[81,82] Due to this isomerisation, the refractive index and the chemical reactivity and polarity of the material changes.[83] In particular, we focus on the reaction in thin films of the molecule formed on Si/SiO_2 surfaces occurring through irradiation and the possibility to change the polarity and functionality of these thin films by an ex-situ reaction of the formed NCS-group with amines. The reaction and the properties of the film are monitored with X-ray photoelectron spectroscopy (XPS), reflection absorption and transmission Fourier transform infrared spectroscopy (RAIRS/FTIR) (by

P. Pacher), X-ray refectometry (XRR) (by O. Werzer) and atomic force microscopy (AFM) (by Q. Shen and G. Hlawacek).

Introduction The photoreaction and the post modification reaction of trimethoxy[4-(thiocyanatomethyl)phenyl]silane (Si-SCN) can be followed by FT-IR spectroscopy.[B] Spectra of the thin films have been recored prior UV illumination, after illumination and after subsequent reaction with propylamine. (Figure 31) Here the stretching vibration of the CN triple bond at 2154 cm^{-1} is almost completely replaced by the vibration signals of the -NCS group at 2177 cm^{-1} and 2097 cm^{-1}. Furthermore the disappearance of the -NCS stretching vibration due to the formation of the thiourea group after the postmodification is visible. IR-spectra of the photoreaction and postmodification of a lager wavenumber range are shown for liquid films in reference 80. Although in the FT-IR spectra of the thin films the signal-to-noise ratio is rather low, the occurring changes due to illumination and postmodification can be identified unambiguously.

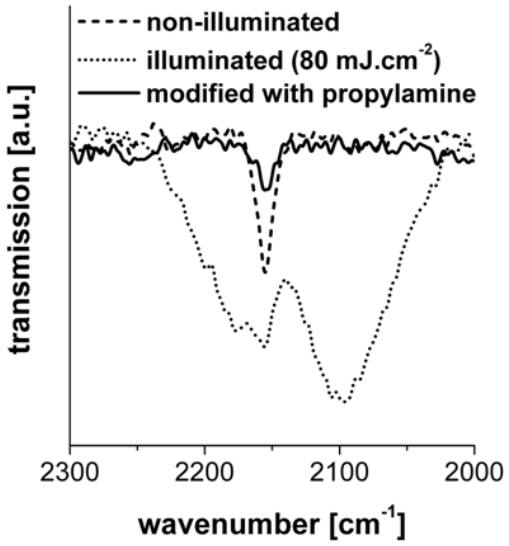

Figure 31: FTIR spectra of the thin film of Si-SCN before (dashed line) and after (dotted line) illumination and for the postmodified (solid line) illuminated layers of the -CN stretching region. Picture obtained from reference 80

The thickness of the Si-SCN layers on activated Si/SiO_2-wafers have been obtained by XRR measurements[C] shown in figure 32. It was possible to determine the thickness of the

[B] The FT-IR measurements have been performed on a Bruker IFS 66v/S IR spectrometer (MCT detector cooled with liquid N_2). The sample was positioned at an angle of 74° with respect to the IR-beam at a pressure below 4 mbar. The resolution was 4 cm^{-1} and 2048 scans have been averaged.

[C] The XRR measurements have been performed on a Bruker D8-Discover diffractometer using Cu Kα radiation. The sample was set in a parallel beam configuration using 0.1 mm slits and a secondary side

native grown silicon oxide layer to be 2.0 nm whereas the thickness of the Si-SCN layer was 6.3 nm (rms roughness of 0.8 nm). The later value is much too high for a single monolayer, which has been suggested if an optimal SAM would have been formed. The height of 6.3 nm rather corresponds to 5 to 6 layers if upright standing molecules are assumed. This increased thickness due the multilayer formation is attributed to a cross-linking of the trimethoxysilane group in the presence of water.[86]

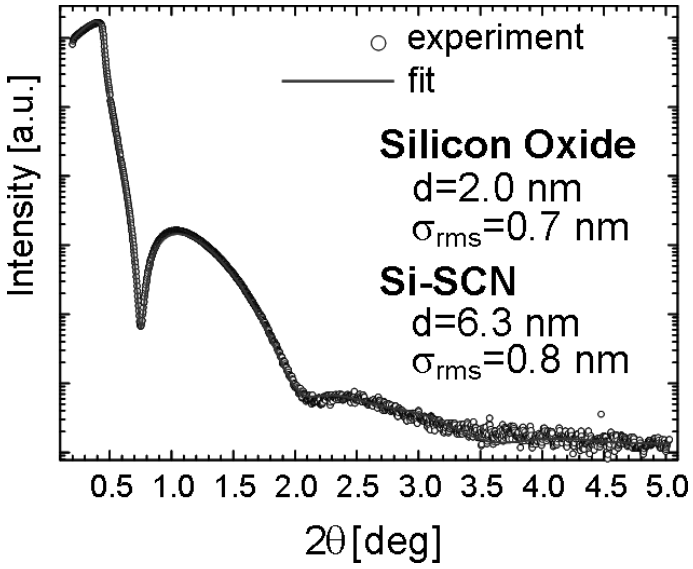

Figure 32: Experimental (open circles) and fitted (solid line) XRR results of a thin layer of Si-SCN on an activated Si/SiO_2-wafer. (Largely identical to reference 80.)

The preparation of micropatterned layers using lithography techniques is demonstrated by AFM measurements.[D] For this purpose a contact mask (chromium on SiO_2, 10 μm lines and 10 μm spaces, shown in figure 33a) was placed on a thin layer of Si-SCN. Then the sample was illuminated through this mask with UV-light (254 nm). After removal of the mask the sample was exposed to vapors of propylamine. The so formed pattern was investigated by FFM under ambient condition. In this mode a soft cantilever scans perpendicular to its long axis and through the lateral forces resulting from the interaction of the tip with the sample the cantilever twists, which is detected by a four-quadrant photosensitive diode. The twist is sensitive to the different polarity of the end groups on the surface. Therefore, a visualization of the pattern should be possible since the interaction

monochromator. The measurements have been performed using a integration time of 3 s and a step width of 0.005° from 0.1° up to 6°. The roughness was included by a Nevot-Croce model.[84,85]

[D] The AFM measurements have been performed on a Digital Instrument Multimode IIIa under ambient condition. The intermittent-contact mode and the lateral force mode (FFM) was used to operate in contact mode. Conventional Si cantilevers were used for the intermittent-contact AFM with a typical resonance frequency of 300 kHz and a force constant of 40 nN nm^{-1}. For the FFM measurements the force constant was typically 0.2 nN nm^{-1}.

of the cantilever with the modified (illuminated, propylamine end group) and unmodified (unilluminated -SCN end group) areas is different.[87] The comparison of the topographical FFM image (figure 33b) with the friction force image (figure 33c) proves this assumption. No height differences resulting from the patterning process are visible, whereas an evident striped pattern is visible for areas with low and high friction. This proves that chemical patterning through illumination and selective post modification is possible.

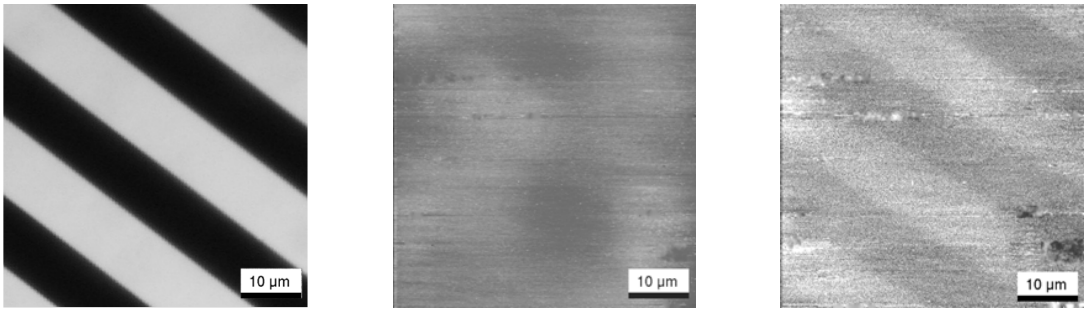

(a) (b) (c)

Figure 33: (a) Microscope image of the used mask for the patterning process. (b) Morphological and (c) friction contrast FFM image of a thin Si-SCN layer obtained after patterning with UV-light and subsequent selective reaction with propylamine. (Largely identical to reference 80.)

Sample Preparation, Irradiation and Post-Modification As substrates p-type-doped (with Boron) single-side polished silicon wafers with a native silicon oxide[E] (from Infineon technologies Austria AG) were used. The wafers were pretreated by etching and simultaneously cleaning the surface with oxygen-plasma (30 s) or with Piranha solution (3:1 concentrated H_2SO_4/33% H_2O_2). Afterwards they were dipped into deionized water (18 MΩ cm, Milli-Q) to allow formation of hydroxyl-groups on the surface (activation of the surface) and then dried with a stream of CO_2.

All glassware was cleaned with Piranha solution, washed several times with deionized water, sonicated in a 2% Hellmanex solution for 20 min, rinsed with deionized wter and dried at 80°C overnight.

The cleaned and activated wafers were placed in a 0.1 vol% solution of the Si-SCN in toluene (HPLC-grade) at room temperature for 3-4 days under ambient conditions. Afterwards they were sonicated in toluene for 2 min, rinsed with toluene, dried with CO_2 and finally annealed for 30 min at 100°C in vaccum.

The irradiation of the thin Si-SCN layers on the Si/SiO_2-wafer were carried out in argon atmosphere using a ozone-free mercury low-pressure UV-lamp (Heraeus Noblelight; 254nm)

[E] with XRR the thickness was measured to be 2 nm.

or a UV-lamp (UVP, UVLMS-38 3) with a wavelength of 254 nm. To obtain patterned structures a contact mask was directly placed on the Si-SCN film before illumination. (For more details see reference 80) For the XPS measurement just one half of the sample was covered with a mask (non-transparent for the UV-light at any position) to obtain half illuminated samples. This pattering process was applied to allow XPS measuring of the pristine and modified layer on the same sample. Changes of the samples due to different film thicknesses, charging and contamination can be excluded which is necessary for quantitative XPS-analysation.

After illumination it was possible to post-modify the organic film with propylamine or 2,2,2-triflouroethylamine by exposing the sample to the vapor of these amines.

During this preparative work care of hazardous chemicals has to be taken and the possibility of exothermic reactions (Piranha solution) showed be considered.

XPS Measurements All XPS measurement have been performed in an UHV chamber which was described in section 2.2.1 at a pressure of 1×10^{-10} mbar. For all experiments $Mg - K_\alpha$ (1253.6 eV) radiation was used with a total energy resolution determined to be 1.2 eV. The spectra were all recored at normal emission. To minimize possible photoisomerization and irradiation damage caused by X-rays, a low excitation power of 100 W was used and the sequence of the measurements has been considered.

All samples had a size of 1x1 cm^2 and only one half was illuminated. With an analyzer focus spot size of 1 mm diameter (compare section 2.2.1), we could thus measure each half separately. The Si2p peak was always measured and used as an internal standard and energy reference. All spectra reported here have been adjusted to yield constant 99.4 eV binding energy for the unoxidized substrate Si2p-line. For all analyses Shirley background subtractions were performed and for fitting a standard Gaussian-Lorentzian line shape was used.

Results and Discussion The photoreaction of the benzyl thiocyanate group was first investigated by Mazzucato et al.[81] and Parks et al.[82]. Upon irradiation, the thiocyanate (-SCN) group undergoes a photoisomerization via a radical mechanism to the corresponding isothiocyanate (-NCS) group. (Figure 34) This leads to a drastic change of the physical and chemical reactivity. This has been extensively shown in polymers (see e.g. in references 88,8)

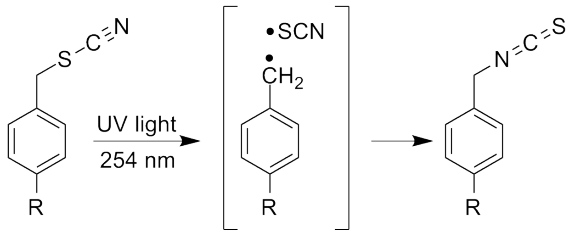

Figure 34: Scheme of the photoisomerization of benzyl thiocyanate to benzyl isothiocyanate via a biradical[80]

This photoreactivity is now transfered from polymers to single molecules. By introducing a second functionality - the trimethoxysilyl docking group - the molecule can form thin layer on surfaces bearing hydroxyl groups (in the optimal case SAMs are formed). This novel molecule has been synthesized as described in 80 and the photoreaction and the subsequent postmodification (forming a thiourea derivate) is shown in figure 35

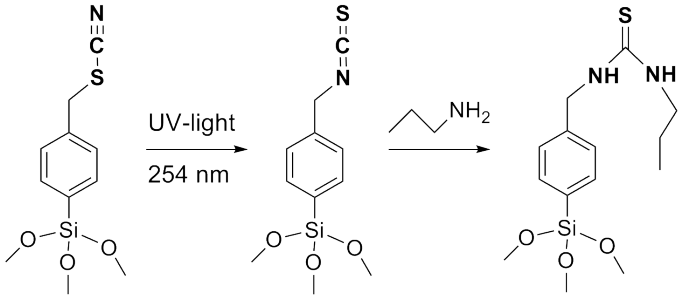

Figure 35: Photoreaction of Si-SCN and postmodification reaction with propylamine[80]

The photoisomerization and postmodification reaction in the thin Si-SCN layers were investigated by spatially resolved XPS. For that reason, samples where only one half of the layer has been UV illuminated (or illuminated and subsequently modified with a gaseous amine, respectively), and the second half remains nonilluminated have been used. From this technique, a comparison of pristine and modified layers of Si-SCN on the same substrate and with the same SAM preparation can be carried out to avoid differences in terms of charging and reproducibility.

The photoisomerization from the thiocyanate (-SCN) to the corresponding isothiocyanate (-NCS) is best seen in the XPS of the sulfur core levels. In the literature, the S2p peak is commonly used in XPS analysis. However, in the thin film samples investigated here, the S2p peak overlaps with a plasmon loss peak of the Si2s substrates core level.[89] Therefore, the S2s peak is used which is less intense and broader then the S2p peak resulting in a smaller signal to noise ratio. Nevertheless the S2s signal is usable and chemical shifts can be measured.

In figure 36, the S2s emission in the nonilluminated (red squares) and in the illuminated

region (green diamonds) of the Si-SCN layer are compared. The fitted peak maximum of the S2s signal of pristine Si-SCN is at a binding energy of 228.7 eV (full width at half maximum (FWHM)=3.1 eV) and after illumination the maximum shifts to 228.2 eV (FWHM=3.1 eV). This 0.5 eV shift to lower binding energy indicates the photoisomerization of the SCN group (single bonded Sulfur) to the NCS (double bonded Sulfur) group and is in agreement with values reported in the literature.[90,91]

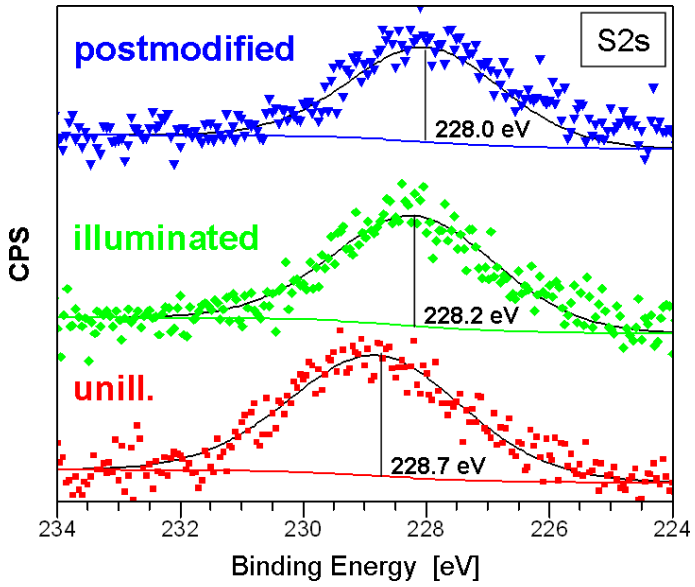

Figure 36: XPS spectra of the S2s region of a pristine thin layer (red squares), after illumination with UV-light (green diamonds) and after subsequent reaction with 2,2,2-triflouroethylamine (blue triangle). (Largely identical to reference 80.)

Because of the low yield of the photoreaction (approx. 30%, for more details please compare reference 80), and the possible formation of by-products, samples subsequently exposed to vapors of propylamine showed only a slight change in the S2s XPS-spectra. For better illustration of the post-modification reaction we thus chose a fluorinated amine, 2,2,2-trifluoroethylamine, as a selective postmodification reagent since fluorine can be easily detected by XPS. In order to avoid fluorine contamination during the plasma etching step, the sample surface was activated by immersing the substrates in piranha solution as described in section 3.2.2. Again, only one half of the sample was illuminated with 254 nm UV-light, and the sample was subsequently exposed to the vapors of 2,2,2-trifluoroethylamine. As expected, the S2s core level spectrum of the nonilluminated region of this sample has a value of 228.7 eV and is identical with the spectrum in Figure 36(red squares). The S2s signal recorded in the other region (illuminated and postmodified) has its maximum at 228.0 eV. Compared to the sample that was only illuminated (and not further modified), there is an additional (small) shift of 0.2 eV to lower binding energies, cf. Figure 36 (green

diamonds) and Figure 36 (blue triangle).

In Figure 37, we compare the F1s signal recorded in the modified region of the Si-SCN layer (blue triangle) to the F1s signal in the nonilluminated region (red squares). The F1s core level in the illuminated and modified region is at a binding energy of 688.7 eV, which can be attributed to an organic fluorine compound.[18] Surprisingly, a small quantity of fluorine was also detected in the nonilluminated zone (30% of the amount detected in the modified region). A possible explanation can be a contamination during processing or a partial reaction of 2,2,2-trifluoroethylamine with nonirradiated Si-SCN via a nucleophilic substitution reaction. However, these points are quite speculative and have to be further investigated

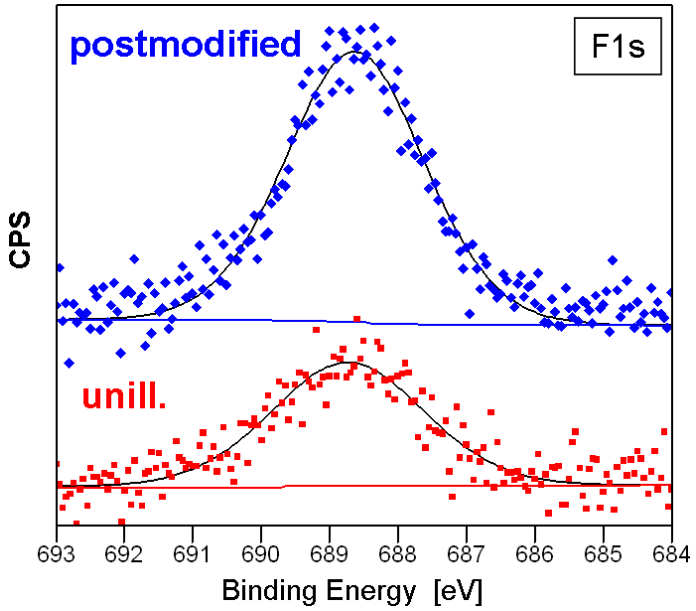

Figure 37: XPS spectra of the F1s region of a pristine thin layer (red squares) and after subsequent reaction with 2,2,2-triflouroethylamine (blue diamonds). (Largely identical to reference 80.)

In the following also the survey spectra, the N1s region and the Si2p region of the the half modified Si-SCN films are discussed to give a complete characterization with XPS.

The quantitative analysis of the unilluminated Si-SCN layer is shown in figure 38.

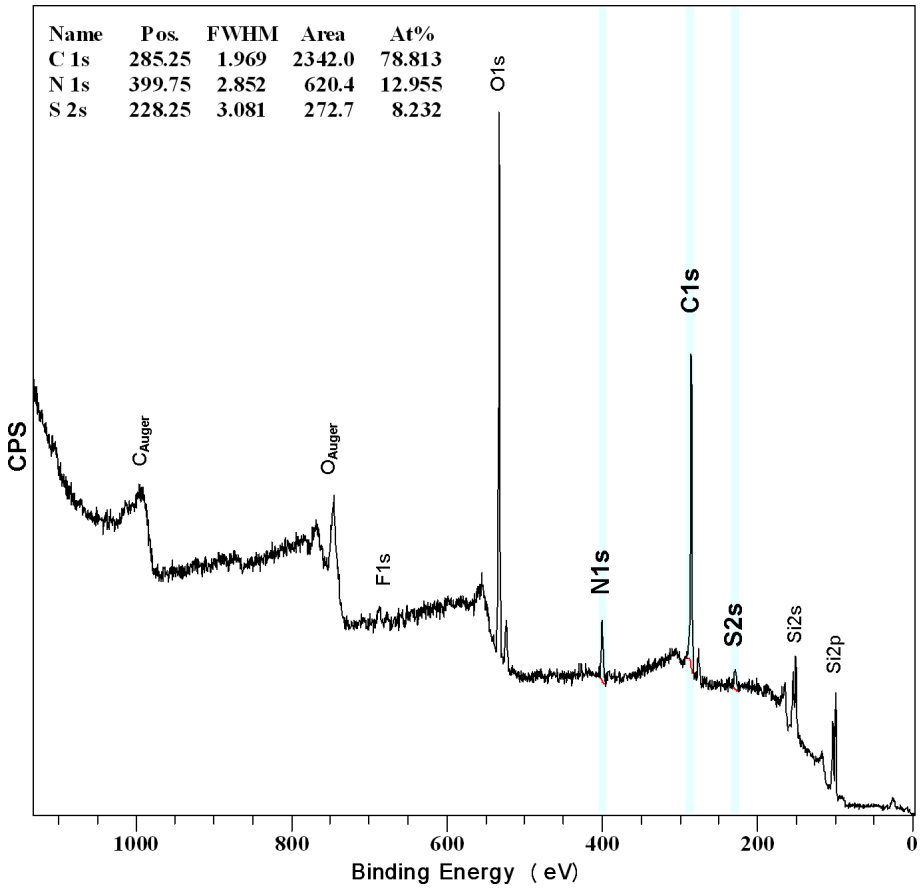

Figure 38: XPS survey spectra of the pristine Si-SCN layer. The quantitative areas are indicated in light blue and their relative composition is indicated.

Due to the low power (100 W), which was used to avoid damaging, the signal-to-noise ratio after 6 scanning cycles is low. Nevertheless, the relative composition carbon, nitrogen and sulfur of pristine Si-SCN can be calculated from this survey spectra. The atomic sensitivity factor (ASF)-value has been obtained from reference 92. The ratio C:N:S is 79:13:8, which is in good agreement with the theoretical composition of Si-SCN of 8:1:1. The relative composition of an illuminated and with 2,2,2-triflouroethylamine postmodified Si-SCN layer is not shown but was calculated to be in both cases C:N:S = 85:10:5 . The higher carbon amount can be explained by the possible side reactions[93] shown in figure 39

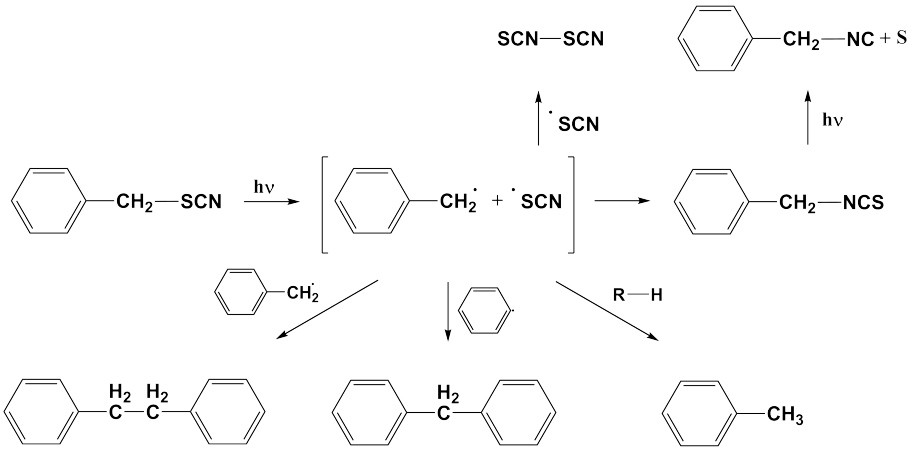

Figure 39: Possible side-reaction[93] of the free radicals, which are formed during the photoisomeristion of benzylthionate.

The N1s core level shifts between the unilluminated and illuminated (figure 40a) and the unilluminated and illuminated and subsequent postmodified (figure 40b) can be used to calculate the yield of the photoreaction.

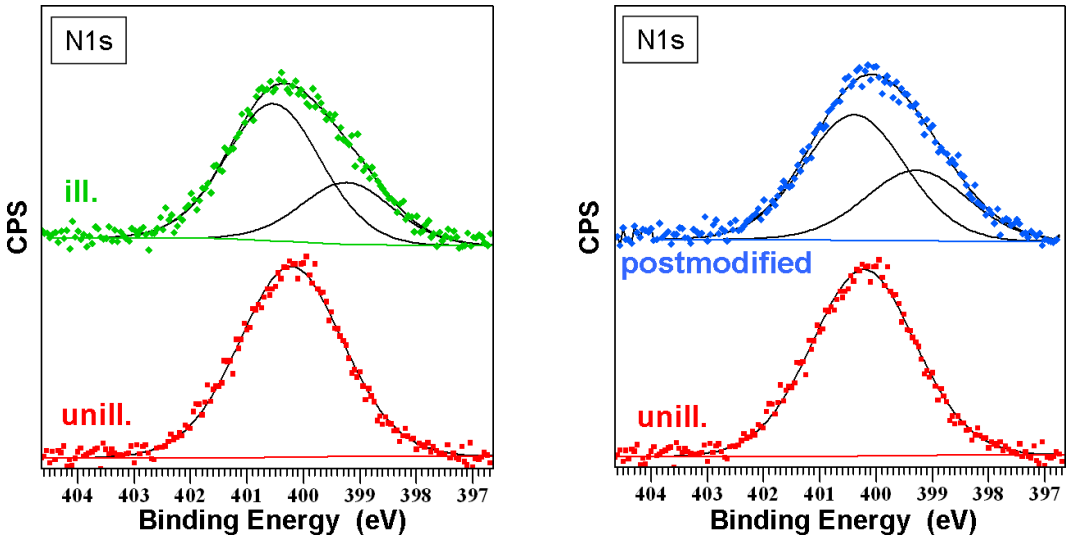

(a) (b)

Figure 40: XPS N1s region of (a) unilliuminated (red squares) and illuminated (green diamonds) Si-SCN layer and (b) unilliuminated (red squares) and illuminated and subsequent postmodified (blue diamonds) Si-SCN layer.

The N1s peak of the unilluminated Si-SCN film (-SCN group) has a maximum at 400.2 eV (FWHM=2.2 eV) . In the illuminated Si-SCN layer the N1s signal shows a shoulder at lower binding energies. Two peaks can be fitted with maxima at 400.5 eV (FWHM=2.0 eV) and

at 399.2 eV (FWHM=1.9 eV). The compound with the higher binding energy represents not photoisomerized -SCN groups whereas the compound at lower binding energy arises from the nitrogen in the -NCS group. Through the area-ratio of the N1s(NCS):N1s(SCN) one obtains a photoismerisation-yield of 43%. The N1s peak of the illuminated and with 2,2,2-triflouroethylamine subsequent postmodified Si-SCN layer is similar to the illuminated Si-SCN layer. This is comprehensible since the chemical shift of the nitrogen bonded in the thio urea is similar to the one in the isothiocyanate and the photoisomeristion yield should not change. The fitted maxima are 400.4 eV (FWHM=2.1 eV) for the -SCN componant and 399.3 eV (FWHM=2.1 eV) of the thio urea component. The calculated yield of the photoreaction is slightly higher (57%).

The calculation of the photoisomerization yield from the N1s XPS signals is in both cases a little higher than obtained experimentally with FT-IR.[8] The deviation can be explained through the thickness differences of the samples used in the different methods. To obtain the yield FT-IR has been performed on liquid films (2 μm) whereas for XPS investigations always thin layers (6 nm) have been used.

For the sake of completeness, the Si2p region and the C1s region are shown in figure 41.

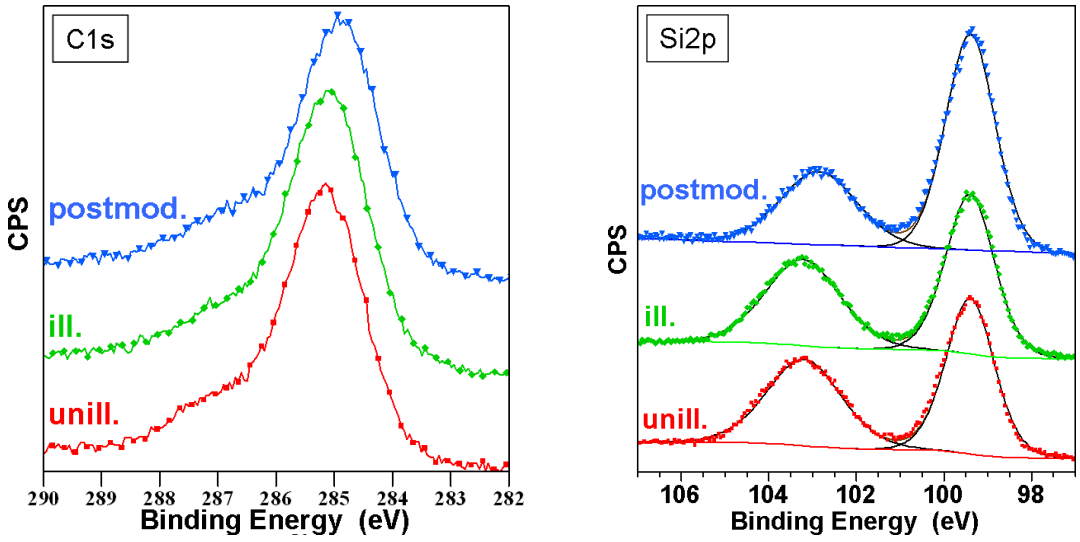

(a) (b)

Figure 41: XPS signal of the (a) C1s and the (b) Si2p region of the pristine (red squares), the illuminated (green diamonds) and the illuminated and subsequent with 2,2,2-triflouroethylamine postmodified Si-SCN layer (blue triangles).

The C1s peaks have a shoulder at higher binding energies due to the chemical shift occurring when carbon is bonded to more electronegative elements like nitrogen and fluorine. The peak maximum is always around 285 eV, which results from the aromatic carbon groups.[18] The Si2p signal has two distinct maxima which arise from the elemental substrate

silicon (referenced to 99.4 eV) and from the silicon dioxide film (103.2 eV to 102.9 eV) on it. The ratio between $Si : SiO_x$ is in good agreement with the film thicknesses measured with XRR shown in section 3.2.2. Since the mean free path length of the photoelectrons is about 10 nm (compare figure 3), it is reasonable to obtain a signal of the elemental silicon underneath the activated silicon oxide (2.0 nm) and the Si-SCN layer (6.3 nm).

Additionally, the selectivity of the photoisomerization was tested using $AgNO_3$ as post-modification regent. In the diploma thesis of Alexandra Lex[94] and Christoph Auner[95] the selective deposition of $AgNO_3$ on UV-patterned polymer layers containing the SCN-group has been shown. On the illuminated areas of the polymer layers the color changed from colorless (unilluminated) to brownish (illuminated). Unfortunately, the investigations of these layers with X-ray diffraction (XRD) and XPS where not clear enough to determine the actual reaction of $AgNO_3$ with the SCN- and the NCS-group.

Therefore, we studied the behavior of $AgNO_3$ on Si-SCN layers patterned with UV-light. The XPS spectra of the Ag3d, N1s and S2s regions are shown in figure 42.

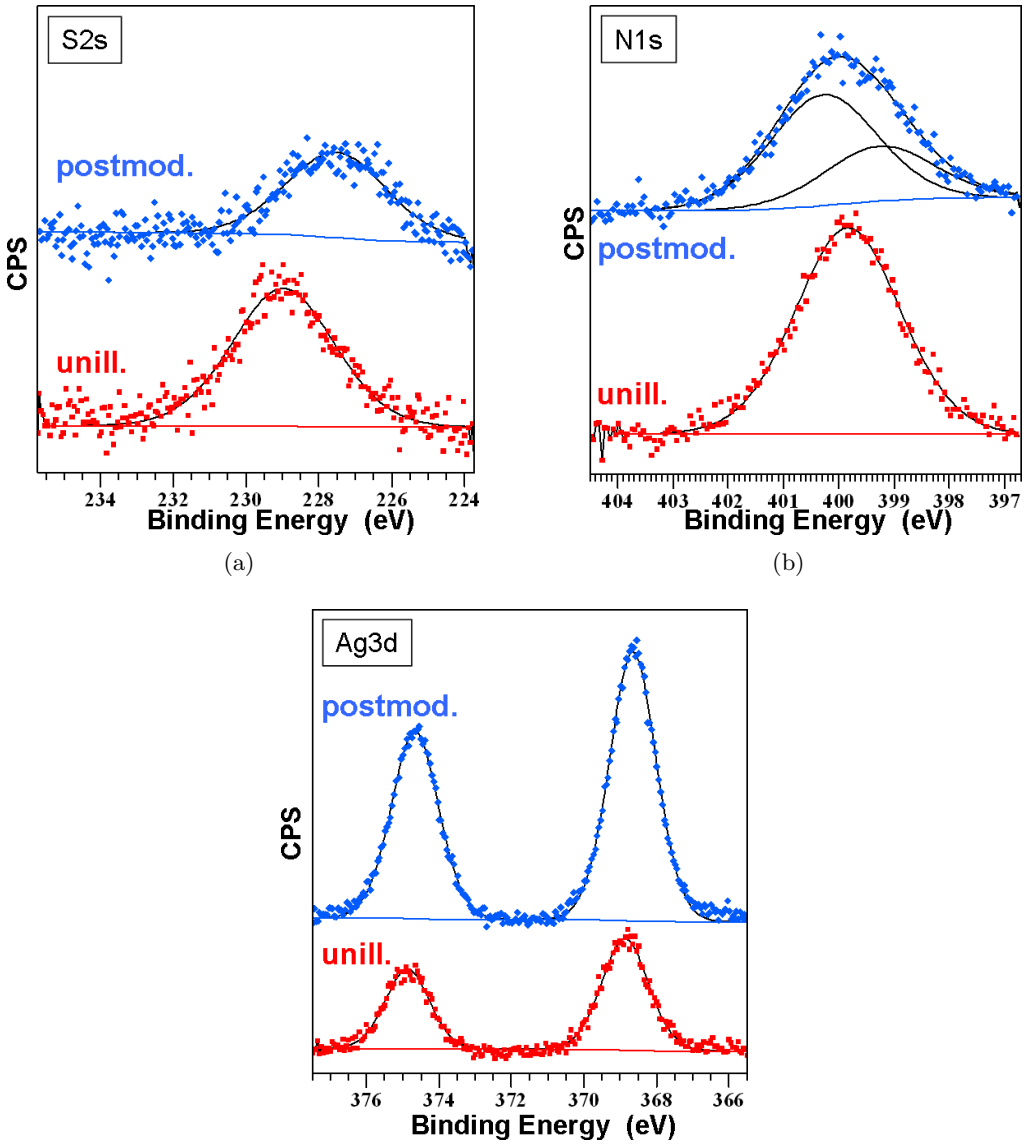

(a) (b) (c)

Figure 42: XPS spectra of (a) the S2s region, (b) the N1s region and (c) the Ag3d region of half patterned samples inserted in a solution of $AgNO_3$. The spectra acquired in the unilluminated area are depicted as red squares and the results of the illumianted area are depicted as blue diamonds.

The S2s peak shifts after illumiantion and postmodification from 229.0 eV to 227.5 eV leading to a chemical shift of 1.5 eV. This shift is twice as large compared to the results obtained by subsequent postmodification with 2,2,2-triflouroethylamine (figure 36) with 228.7 eV for the unilluminated layer and 228.0 eV for the illuminated and subsequent postmodified layer. The reason of this large shift is probably due to the bonding of the sulfur

to the silver. Furthermore, a decrease of the sulfur signal of about 40% has been detected due to the illumination. The N1s signal of the unilluminated Si-SCN layer has a maximum at 399.8 eV which is slightly lower in binding energy compared to the results obtained using 2,2,2-triflouroethylamine for selective postmodification. The N1s signal of the iluminted and with $AgNO_3$ subsequened post-modified Si-SCN layer is slightly broader and two differnt nitrogen compounds can be fitted due to the incomplete conversion of the SCN-group to the NCS-group. The maxima are at 400.3 eV and 399.3 eV, which is again in good agreemnet with the results shown in figure 40.

The most interesting change between the unilluminated and illuminated areas after the selective postmodification with $AgNO_3$ can be seen in the silver XPS signal. The selectivity of the postmodification is comparable to the selectivity of the reaction with 2,2,2-triflouroethylamine (30%). Here, the ratio of the Ag3d5/2 between the unillumiated:illuminted area is 377:900, which is about 40%. Furthermore, there is a shift in binding energy between the silver deposited on the unilluminated and illuminated Si-SCN film of 0.22 eV. This shift has been reproduced several times, although it is quite small. The binding energy of the Ag3d5/2 peak arising form the unilluminated Si-SCN film is 368.87 eV and the Ag3d5/2 peak on the illuminated Si-SCN films has a binding energy at 368.65 eV. Both values are very high compared to literature values for the Ag3d5/2 peak. The only comparable results can be found in refernce 96. There, different results for organic-bonded silver are reported. It is likely that the silver is bonded somehow to the sulfer in a differnt way depending on the present sulfur group (-SCN or -NCS). The existence of metallic silver, which was suggested due to the brownish colouring, can be excluded, because the binding energy would be about 368.0 eV[19] for the Ag3d5/2 peak, which is much smaller the the measured values. Also silver (I) and (II) oxides (from 367.2 - 367.8 eV) are not present on the Si-SCN layers modified with $AgNO_3$.

3.2.3 Photo-patterning of Phenyl Ester Silane Layers due to the Photo-Fries Rearrangement

In this section, a different photoreactive functional head group has been used to pattern and modify the surface.

Foreword The following study has been carried out in collaboration with Dr. Thomas Höfler when he was employed at the Institute of Chemistry and Technology of Organic Materials (renamed to 'Institute for Chemistry and Technology of Materials'). This section largely reproduces the paper 'Photoreactive Molecular Layers Containing Aryl Ester Units: Preparation, UV Patterning and Post-Exposure Modification' (see reference 9), whereas the experimental details performed by others are summarized in an introductory section and the results gained with XPS are presented in more detail in the 'results and Discussion' section.

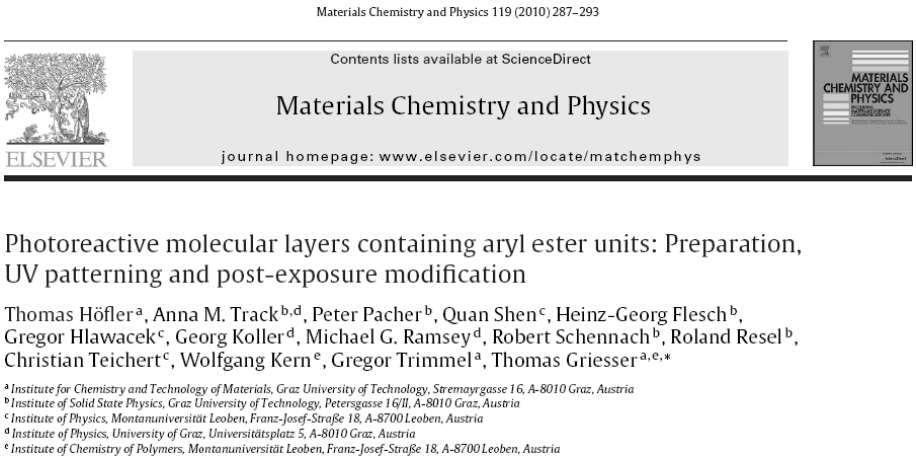

Materials Chemistry and Physics 119 (2010) 287–293

Contents lists available at ScienceDirect

Materials Chemistry and Physics

journal homepage: www.elsevier.com/locate/matchemphys

Photoreactive molecular layers containing aryl ester units: Preparation, UV patterning and post-exposure modification

Thomas Höfler[a], Anna M. Track[b,d], Peter Pacher[b], Quan Shen[c], Heinz-Georg Flesch[b], Gregor Hlawacek[c], Georg Koller[d], Michael G. Ramsey[d], Robert Schennach[b], Roland Resel[b], Christian Teichert[c], Wolfgang Kern[e], Gregor Trimmel[a], Thomas Griesser[a,e,*]

[a] Institute for Chemistry and Technology of Materials, Graz University of Technology, Stremayrgasse 16, A-8010 Graz, Austria
[b] Institute of Solid State Physics, Graz University of Technology, Petersgasse 16/II, A-8010 Graz, Austria
[c] Institute of Physics, Montanuniversität Leoben, Franz-Josef-Straße 18, A-8700 Leoben, Austria
[d] Institute of Physics, University of Graz, Universitätsplatz 5, A-8010 Graz, Austria
[e] Institute of Chemistry of Polymers, Montanuniversität Leoben, Franz-Josef-Straße 18, A-8700 Leoben, Austria

Figure 43: Copy of part of the first page of reference 9 including all coauthors and their affiliations.

Here, new functional trichloro organosilanes (Thomas Höfler) bearing photoreactive aryl ester groups are presented and their application as thin silane layers on silicon oxide surfaces. The trichlorosilyl group acts as anchoring unit to the inorganic surface and the aryl ester group undergoes the photo-Fries rearrangement upon illumination with UV-light of 254 nm to yield hydroxyketones which leads to a change in chemical reactivity of the surface. The photo-generated hydroxy groups can react subsequently with perfluorobutyryl chloride to the corresponding perfluorinated ester compound, which allows further tuning of surface properties. The layer formation, the photoreaction and the postmodification was monitored by FT-IR spectroscopy (Dr. Peter Pacher) and XPS. The thickness of the obtained thin layers was determined by XRR (Heinz-Georg Flesch). Photo-patterned surfaces were obtained using a contact mask during illumination followed by the postmodification

reaction. Friction force microscopy (FFM) (Quan Shen) revealed the contrast between modified and unmodified regions of the patterned samples.

Additionally, in section 3.2.1 the pretreatment of the surfaces is characterized with XPS and contact angle measurements.

Introduction The thickness of the formed thin layers of 4-(2-(trichlorosilyl)ethyl)phenylester (Si-PF) were determined with XRR[F] (shown in figure 44).

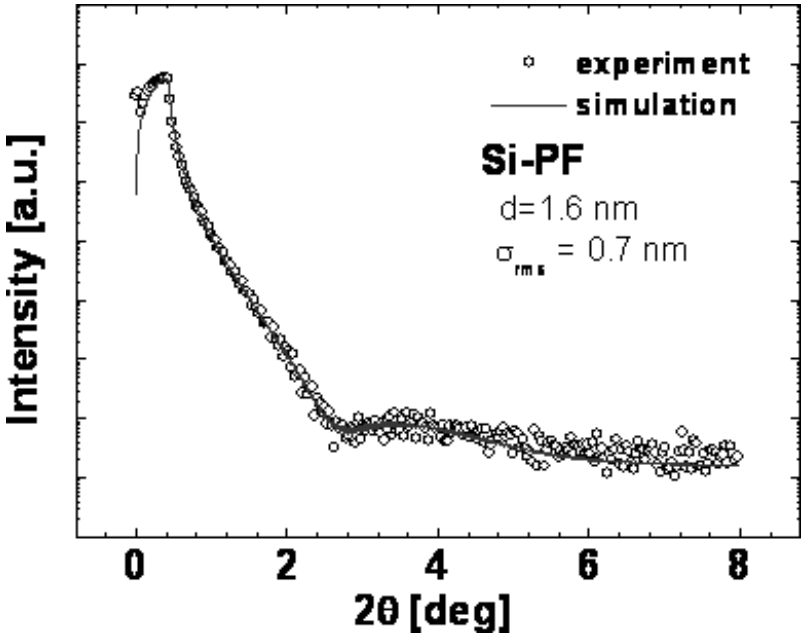

Figure 44: XRR spectra (open circles: experimental spectrum and red line: simulated spectrum) of the thin Si-PF layer prepared under ultra dry conditions. (Largely identical to reference 9.)

It was possible to observe from the oscillations the thickness of the thermally grown silicon oxide layer[G] and the Si-PF layer to be 163 nm and 1.6 nm, respectively, when the thin film was grown under ultra dry conditions (compare section 3.2.3). When assuming upright standing Si-PF molecules the theoretical thickness should be approximately 1.1 nm.

[F] All XRR measurements were performed using CuKα radiation on a Bruker D8 Discover diffractometer. As setup Bragg Brentano configuration was used having 0.05 mm slits on the primary side and 0.1 slits on the detector side together with a secondary side graphite monochromator. Measurements were performed from 0.1° (0.007^{-1}) up to 7° (0.498^{-1}) with a step width of 0.005° in 2 theta using an integration time of 2 s. The Parrat algorithm was used to calculate the layer thickness and roughness was included by the Nevot-Croce model.[84,85] The experimental data could be simulated using a three layer model (Si/SiO_2/adsorbate).

[G] Only for XRR measurements a thermally grown silicon oxide was used as substrates. For all other measurements (XPS, FT-IR, AFM) a native grown silicon oxide layer was used. Usage of the native oxide reduces charging during XPS measurements and allows measuring in transmission mode with FT-IR.

The observed increased thickness is attributed to cross linking of the trichloro-silane groups in the presence of water which results in multilayer growth.[86]

Preparation under ambient conditions favors multilayer growth due to the higher water content during layer formation. Film thicknesses from 3.6 nm up to 8 nm were measured. However, these thin films were also homogeneous. The 8 nm thick layers have thus been used for FT-IR measurements as the signal to noise ratio was too low for thinner samples and to allow a complete characterization the same film was used for XPS measurements.

The photoreaction and the postmodification reaction were investigated with FT-IR[H] (figure 45) by irradiating the 8 nm thin Si-PF layer with UV-light of 254 nm and than subsequently followed by exposure of the illuminated layer to vapors of perfluorobutyryl chloride. The resulting FT-IR spectra are in good agreement with FT-IR measurements of liquid layers of Si-PF[9] and polymers containing the same photoreactive benzyl ester group (compare e. g. reference 97).

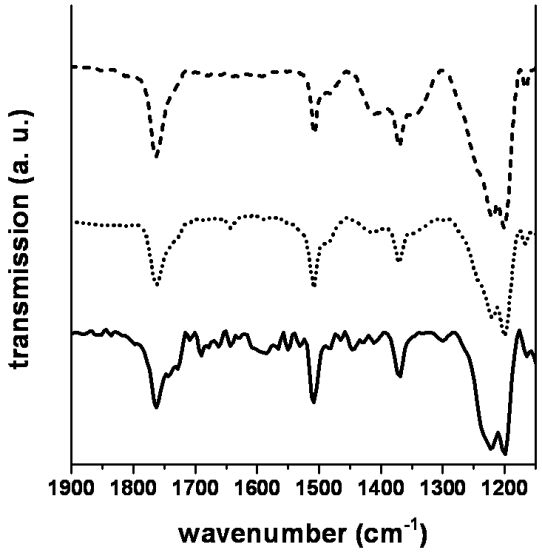

Figure 45: FTIR spectra of a thin Si-PF layer grown under ambient conditions before illumination (dashed line), after illumination (dotted line) and after postmodification with perfluorobutyryl chloride (solid line). (Largely identical to reference 9.)

In the pristine film the signal at 1763 cm^{-1} can be attributed to the ester group (C=O)

[H] All FT-IR spectra of the samples were recorded in transmission mode using a Bruker IFS 66v/S FTIR spectrometer equipped with a mercury-cadmium-telluride (MCT) detector at an angle of 74° between the IR-beam and the sample normal. The sample chamber was evacuated for at least 40 min (pressure of less than 4 mbar, resolution 4 cm^{-1}/8 cm^{-1}, 30000 scans). The baseline was subtracted and the spectra are shown without any smoothing. All spectra are referenced against a sample that was treated the same way as the studied samples except that it was immersed into a toluene solution containing no silane molecules.

vibration. After UV irradiation this ester signal has considerably decreased whereas a new band at 1643 cm^{-1} can be observed.[I] This signal is assigned to the formation of a (2-hydroxyphenyl)ketone. After exposure of the Si-PF thin film to the vapours of perfluorobutyryl chloride the formation of a carboxylic acid ester leads to a second ester signal at 1730 cm^{-1} (C=O stretch) in the FT-IR spectrum. Also a broader shoulder at 1240 cm^{-1} shows the existence of a C-F stretching vibration due to fluorine groups of the acid chloride.

To demonstrate the possibility to prepare patterned Si-PF layers, the photoreaction was carried out in combination with lithographic techniques. Here the thin Si-PF layer was illuminated through a contact mask (chromium on SiO_2, 3 μm lines and spaces) with UV-light of 254 nm. After removal of the contact mask, the whole sample was exposed to perfluorobutyryl chloride to achieve a selective postmodification. To visualize the obtained contrast of the surface properties between the unmodified and modified regions of the patterned samples, friction force microscopy (FFM) and AFM[J] was performed under ambient conditions.[87] A significant change of friction is visible between the unilluminated and illuminated areas of the sample shown in figure 46b. The exposed regions, in which the photoreaction and the subsequently derivatized with perfluorobutyryl chloride has occurred, yield to a brighter contrast, whereas the masked areas exhibit darker contrast.

In this friction force microscopy (FFM) image parallel stripes with a period of 3 μm can be seen, which corresponds to the mask used for the patterning process. The inset in figure 46b shows a one dimensional Fast Fourier Transformation (FFT) of the FFM image in a direction perpendicular to the stripes. Clear peaks in reciprocal space corresponding to 6 μm and 3 μm in real space demonstrate the high accuracy of the patterning technique.

[I] The yield of the photo-Fries rearrangement was observed to be 15%.[9] Therefore it is understandable that the signals arrising due the illumiation are quite weak.

[J] AFM was employed in the intermittent contact mode and lateral force mode (also termed friction-force microscopy; FFM) to characterize the surface properties of the thin layers. Intermittent contact mode AFM allows characterizing the surface morphology in the absence of lateral forces that might alter the tip or surface morphology. In the FFM mode the cantilever is scanned across the surface perpendicular to its long axis in contact mode and lateral forces depending on the friction properties of the tip surface pairing will twist the cantilever. The resulting lateral deflection of the laser is used as the measurement signal. All measurements were done under ambient conditions on a Digital Instruments Multimode IIIa instrument. For intermittent contact AFM, conventional Si-cantilevers with a typical resonance frequency of 300 kHz and a force constant of 40 nN/nm were used. FFM was performed with probes designed for friction force measurements with a force constant of typically 0.2 nN/nm.

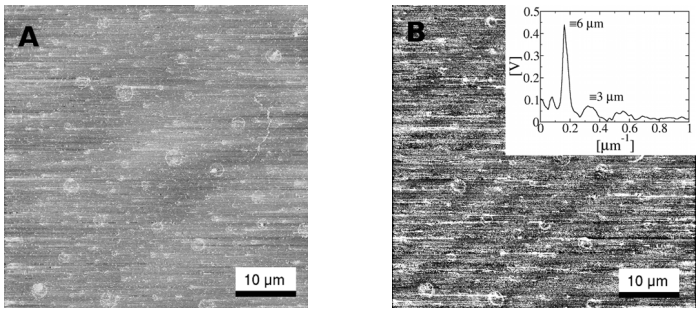

(a) (b)

Figure 46: (a) Morphological and (b) friction contrast FFM image of a 8 nm Si-PF layer obtained after patterning. The inset in (b) shows a 1-dim Fast Fourier Transformation (FFT) perpendicular to the stripes.[9]

In contrast the topographical image (figure 46a), no structural features resulting from the patterning process are visible. This fact can be explained that the obtained height difference (estimated to be approximately 1 to 2 nm) upon the post modification reaction by a lateral distance of 3 μm can hardly be analyzed by this technique.

Substrates, Sample Preparation, Irradiation and Post-Modification All glassware was cleaned with Helmanex solution (2%, 20 min in ultrasonic bath) and then rinsed with deionized water (18 MΩ cm, Milli-Q water) and dried in an oven at 80°C overnight.

For FT-IR spectroscopy measurements, AFM measurements and XPS measurements single-side-polished p-type-doped (B) silicon wafers with native silicon oxide (resistivity 9-18 Ω cm) from Infineon Technologies Austria AG were used.[K]

For XRR and AFM measurements the substrates were activated with a 30 s oxygen plasma etching step. For the XPS measurements the activation of the surface has been obtained by etching with Piranha solution[L] (3:1 concentrated H_2SO_4/33% H_2O_2) for 30 min. Afterwards all samples were dipped into deionized water (18 MΩ cm, Milli-Q) and were dried with a stream of CO_2. This treatment allowed the realization of a highly hydrophilic surface[M] with a water contact angle of less than 10° compared to 70-90° on the pristine substrates (see section3.2.1 for more information).

The clean Si/SiO_2 substrates were placed, immediately after the water dip step, in a 7 mmol solution of Si-PF in pure toluene for 16 hrs, then rinsed with toluene and dried with a stream of CO_2. The preparation of thin layers were either performed under inert gas conditions (N_2 glove box, anhydrous toluene) or under ambient atmosphere using HPLC-

[K] The thickness of the native oxide was determined to be 2 nm as shown in section 3.2.2.

[L] Piranha solution is highly oxidizing, and its preparation is highly exothermic (up to 120°C). Therefore reactions must be carried out in a fume hood and protective gloves and goggles must be taken.

[M] Hydroxyl groups are formed on the surface.

grade toluene. The resulting thickness of the layers was determined by XRR.

Irradiation experiments were carried out under inert atmosphere (N_2) using an ozone free mercury low pressure UV-lamp (Hereaus Noblelight) with a wavelength of 254 nm. The light intensity at the sample surface was measured with a spectroradiometer (Solatell, Sola Scope 2000TM, spectral range from 230 to 470 nm) to be 1.35 mW cm^{-2}. Thin layers with patterned structures were obtained by using a contact mask with lines and spaces (Cr pattern on quartz, custom made by Austria Microsystems, Unterpremstätten, Austria) directly onto the organic layer prior to illumination. After illumination of the samples, subsequent postmodifications were carried out by placing the illuminated substrate in a solution containing 5 ml of dry CH_2Cl_2, 0.3 ml of perfluorobutyryl chloride and 0.3 ml of pyridine. After 2 hours the substrate was rinsed with CH_2Cl_2 and dried in a stream of CO_2. All reactions were conducted in a glove box (Argon filled).

XPS Measurements All measurements were performed in a UHV chamber (for more information see section 2.2.1) with a base pressure of 1×10^{-10} mbar. XPS experiments were carried out using $Mg - K_\alpha$ radiation (1253.6 eV). The overall energy resolution was 1.2 eV. All spectra were recorded in normal emission geometry with a photon incidence angle of 55°. To minimize possible photo-rearrangement and irradiation damage caused by X-rays, a low excitation power of 100 W was used and the sequence of the measurements was considered. All samples had a size of 1×1 cm^2 and only one half was UV illuminated while the other half was covered. The spatial resolution of the analyzer (<1 mm diameter) ensured that each half could be measured separately. The Si2p signal was always measured and used as an internal energy reference. All spectra reported here have been adjusted to yield constant 99.4 eV binding energy for the metallic silicon Si2p line. For all quantitative analyses, Shirley background subtraction was performed and a standard Gaussian-Lorentzian line shape was used.

Results and Discussion The surface properties can be tailored over a wide range due to the plenitude of available and described silanes which can be varied by the choice of the tail group that spans from apolar to polar, by anionic to cationic head groups or by acid to basic groups.[98]

SAMs are also well-defined platforms for nano-fabrication of patterns.[67] A very convenient way for two-dimensional (2D) patterning of surface properties is the use of photo lithographic techniques. Here we investigate the applicability of a new functional trichlorosilane bearing a photoreactive phenyl ester. The ester group undergoes the photo-Fries rearrangement under illumination with UV-light. Thereby the aryl ester transforms into hydroxy ketones upon irradiation of UV-light as first described by Anderson and Reese.[99,100] In this rearrangement a scission of the C-O bonds leads to the formation of an acyl and

phenoxy radical pair. The photo generated radicals can recombine to the *ortho*- and *para*-hydroxyketones as the 'cage products',[101] also the formation of the escape product (decarboxylation and the formation of phenol) as a side reaction can occur. The whole mechanism is shown in figure 47.

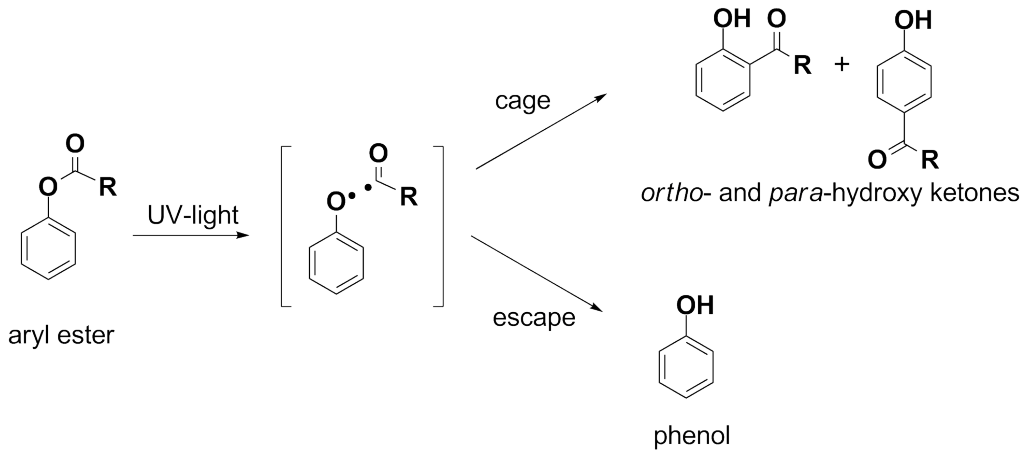

Figure 47: Scheme of the photo-Fries rearrangement. The main product are hydroxy ketones whereas as side product phenols are formed. (Largely identical to reference 9.)

The formed hydroxy ketones have been shown to be a platform for a wide range of chemical postmodification reactions as shown in polymeric materials[97] and in thiol based SAMs on gold surfaces.[78,10]

In this work, perfluorobutyryl chloride was applied as reagent to perform the esterfication of the hydroxy ketone formed after illumination (compare figure 48). This compound was chosen because of its high vapor pressure and the fluorine atoms, which facilitate a further proof of the reaction by XPS.

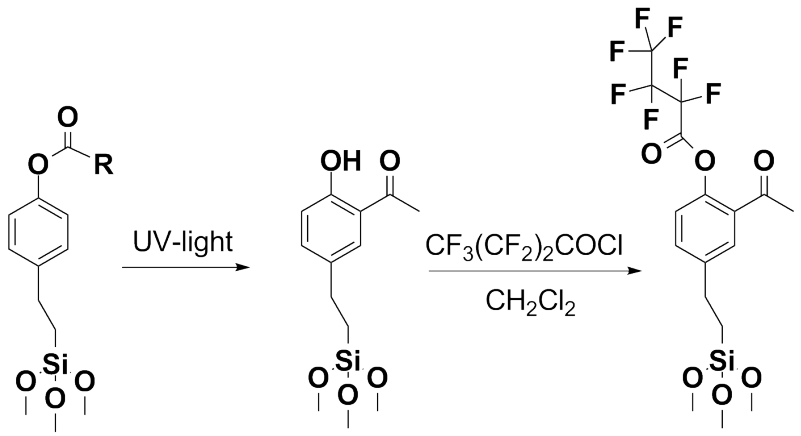

Figure 48: Photoreaction and postmodification of Si-PF using perfluorobutyryl chloride. (Largely identical to reference 9.)

The samples with a film thickness of 8 nm (compare section 3.2.3) were investigated by XPS. Practically no difference could be detected in the spectra before and after UV-irradiation of the thin layers as the chemical composition of the layers was the same, and the change in binding energies of the original ester versus the photo-generated hydroxy ketone was too small to be detectable within the resolution limits of the instrument used.

However the selective postmodification reaction with perfluorobutyryl chloride (compare figure 48) should be easily identified by XPS. To avoid fluorine contamination during the plasma-etching step[N], the sample surface was activated by immersing the substrates in piranha solution.

For these investigations, just one-half of the Si-PF layer (8 nm) was illuminated using a shadow mask. Subsequently, the whole sample was treated with a solution of perfluorobutyryl chloride and pyridine in dichloromethane. In this step only the illuminated side should react with the acid chloride. Using this technique, a comparison of pristine and modified layers of Si-PF on the same substrate is possible.

After the post-modification reaction with perfluorobutyric chloride, the illuminated side shows a strong F1s signal as depicted in figure 49. The binding energies of the F1s signal is 689.3 eV, which can be attributed to an organic fluorine compound.[18]. However, a very small signal is also observed in the pristine layer. The fluorine contamination can be attributed to reaction of perfluorobutyryl chloride with residual OH-groups on the activated surface. But the comparison of the signal integrals (fluorine ratio illiuminated:unilluminated side = 1:0.09) shows the high selectivity of this post modification reaction in the illuminated areas.

[N] On all samples that were plasma etched a small content of fluorine was detected with XPS caused by Teflon sealing of the used apparatus.

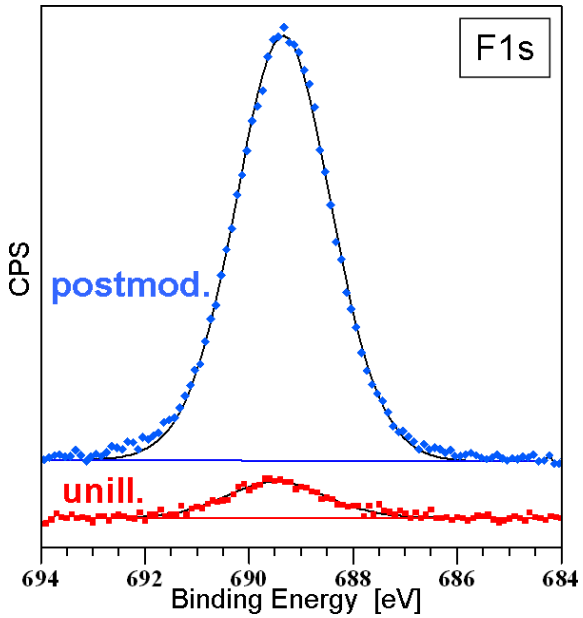

Figure 49: F1s region of the XPS spectra of the pristine Si-PF layer (red squares) and of the selective postmodified layer (blue diamonds) after illumination with UV-light. (Largely identical to reference 9.)

Moreover, the post modification reaction also leads to a significant change in the region of the Si2p core level signals as depicted in figure 50. The pristine layer shows two distinct signals in this region: at 99.4 eV attributed to the silicon of the wafer substrates and at 103.3 eV attributed to the SiO_2 of the native oxide and the docking group of the Si-PF layer. The post-treatment with perfluorobutyric chloride after illumination leads to the disappearance of the Si2p signal of the bulk Si (at 99.4 eV) and to a significant decrease of the Si2p signal of the SiO_2-layer (at 103.3 eV) of about 15%. This fact can be attributed to a significant increase of the overall film thickness after the reaction with perfluorobutyryl chloride.

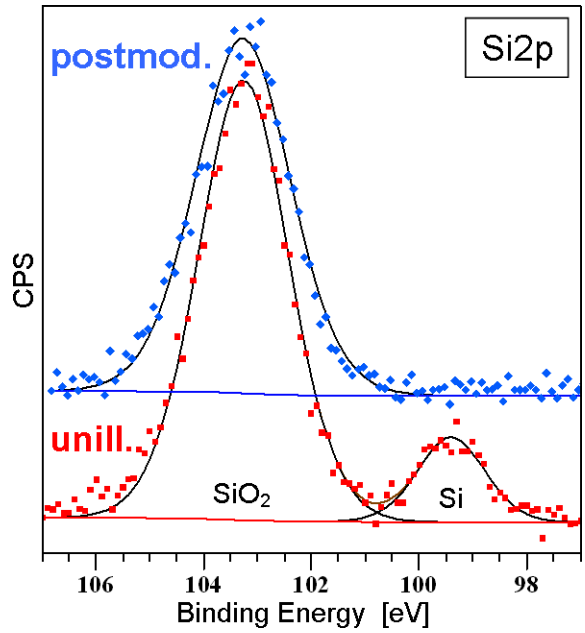

Figure 50: Si2p region of the XPS spectra obtained of the unilluminated Si-PF layer (red squares) and the after illumination selective postmodified Si-PF layer (blue diamonds). (Largely identical to reference 9.)

Due to the change in film-thickness (as shown in the Si2p region) the O1s signal decreases in comparison between the pristine and the illuminated and selective postmodified Si-PF layer as shown in figure 51. Furthermore two different components can be fitted in both O1s peak. For the unilluminated Si-PF layer component one has a maximum at 532.9 eV (FWHM=1.8 eV) which can be attributed to the oxygen bonded to silicon oxide (O(Si))[89] and the second component has a maximum at 534.4 eV (FWHM=2.1 eV) which arises from organic bonded oxygen (O(C))[18] (e. g. esters). On the illuminated and subsequent postmodified Si-PF layer quasi the same components could be fitted at 532.9 eV (FWHM=1.9 eV) and 534.4 eV (FWHM=2.5 eV), respectively. No chemical shift of the O1s region of the organic boned oxygen could be detected, only the FWHM increases slightly which indicates the presence of more different organic C-O species. The relative ration between the silicon bonded oxygen and organic bonded oxygen O(Si):O(C) is for both investigated Si-PF layers 0.3.

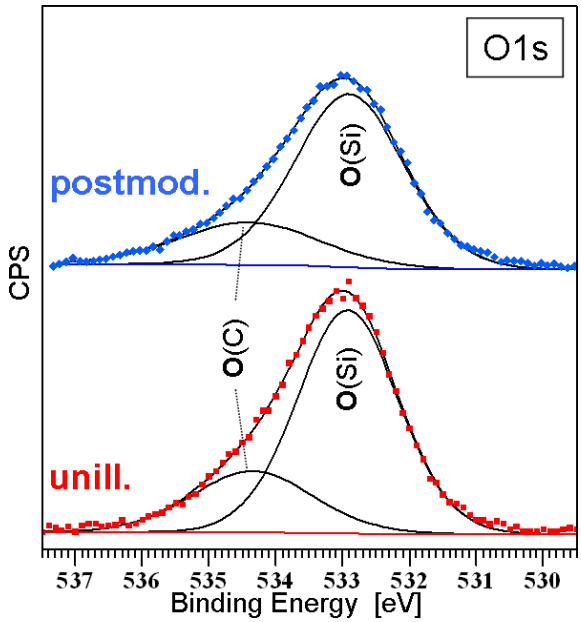

Figure 51: O1s region of the XPS spectra of the unilluminated Si-PF layer (red squares) and the after illumination selective postmodified Si-PF layer (blue diamonds).

The quantitative ratio between carbon and fluorine was calculated from the survey spectra of the pristine and illuminated/postmodified Si-PF layer which are shown in figure 52. The unilluminated layer has only a little amount of fluorine on the surface which leads to a F:C ration of 0.03. The F:C ratio increases for the illuminated and selective postmodified Si-PF layer to 0.27. The maximal ration would be 0.5 since the molecule nominally has a ration of F:C=7:14. This leads to a yield of the photo-Fries rearrangement of about 50%.

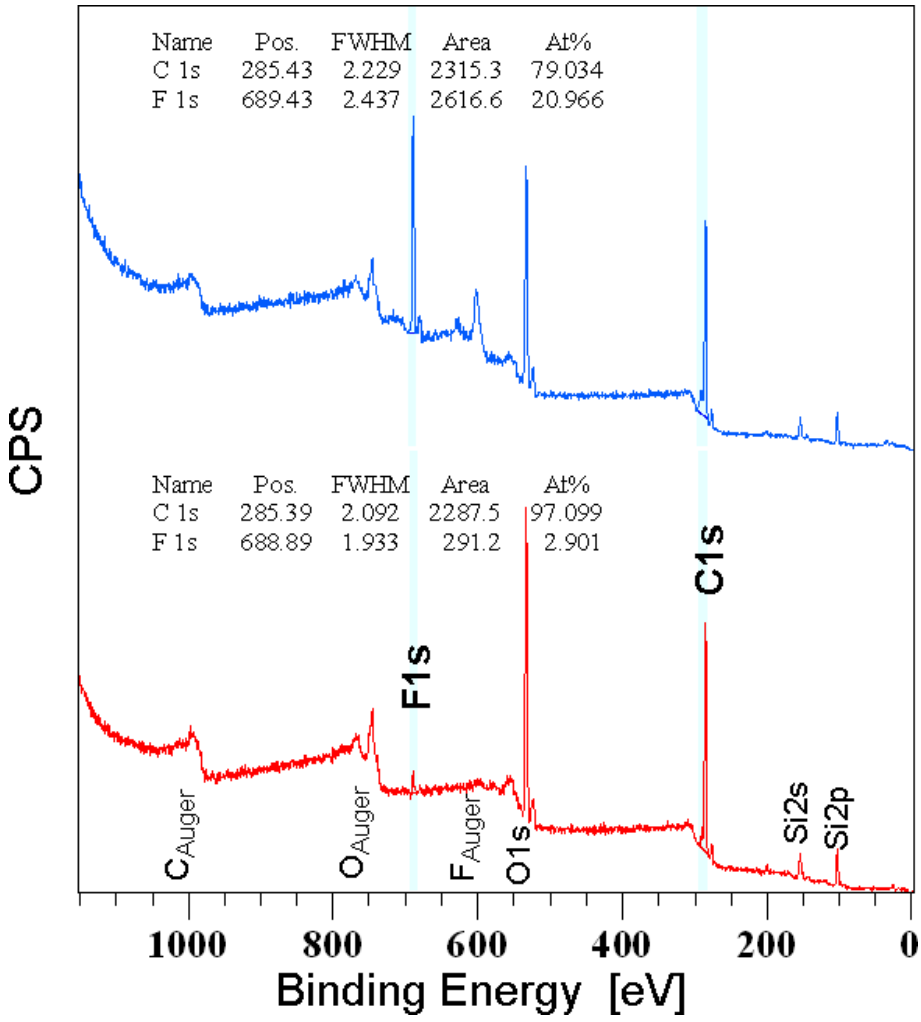

Figure 52: Survey XPS spectra of the unilluminated Si-PF layer (red) and the after illumination selective postmodified Si-PF layer (blue). The relative ratio between carbon and fluorine is shown.

3.2.4 Thickness Investigations of Thin Silane Layers with XPS

Forword and Introduction This work has been performed in Collaboration with Dr. Thomas Höfler. He synthesized different silane molecules with different spacer length containing a benzyl ester head group to perform the Photo-Fries rearrangement.Furthermore he prepared the investigated samples. Depending on the preparation method and the spacer length different layer thicknesses are obtained. The dependence was investigated with XRR, done by Heinz-Georg Flesch, and XPS.

To obtain real single layer SAMs of silane molecules on oxidic surfaces is difficult, because adding the needed amount of water is quite hard. Too much water leads to cross-linking of the silane molecules as depicted in figure 53.[102] Therefore the investigation of the film thickness is important to allow reproduciable results.

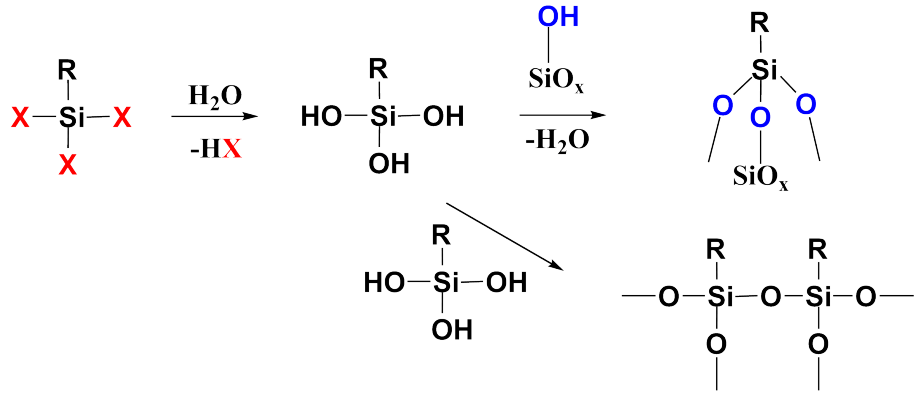

Figure 53: Possible reaction of the silane docking group to the surface or with other silane molecules (cross linking)

Experimental Section Here two different silane molecules are investigated in terms of film thickness. The molecules already have been discussed above and are shown here again in figure 54. The height of Si-PF is about 1.1 nm, whereas Si-PF-long is with a height of about 2.0 nm twice as long.[O]

[O] The height (or length) of the molecules was optimized with Gaussian (B3LYP) and measured manually in the visualization Program Molden.

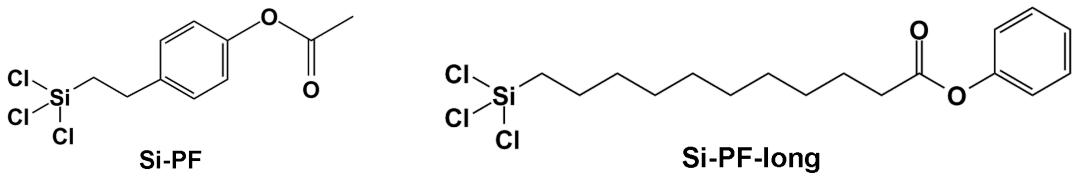

(a) (b)

Figure 54: Molecular structure of (a) 4-(2-(trichlorosilyl)ethyl)-phenyl-ester (Si-PF) and (b) 11-(Trichlorosilyl)undecanoic-acid-phenyl-ester (Si-PF-long).

The preparation, illumination and subsequent postmodification, as well as the investigation methods have been described above.

Results and Discussion Preparing the thin layers under ultra dry or ambient condition results in different film thickness. With the short spacer molecule (Si-PF) layers of a thickness of 8 nm are obtained when growing the layer under ambient conditions, whereas growing them under ultra dry conditions leads to thicknesses of 1.6 nm.[P] The XRR result for the thinner Si-PF layer is shown in section 3.2.3 (figure 44) The thicker layer corresponds to network of approximately 8-9 layers, whereas the thiner layer can be attributed to a mono- or bilayer when assuming upright standing molecules.

The films formed with Si-PF-long gain thicknesses from 2.7 nm and 1.7 nm prepared under ambient conditions and ultra dry conditions, respectively. The XRR results are shown in figure 55. Here the thicknesses corresponds to bilayer and monolayer assuming not perfectly upright standing molecules, respectively.

[P] The XRR data are only available for the growth under ultra dry conditions.

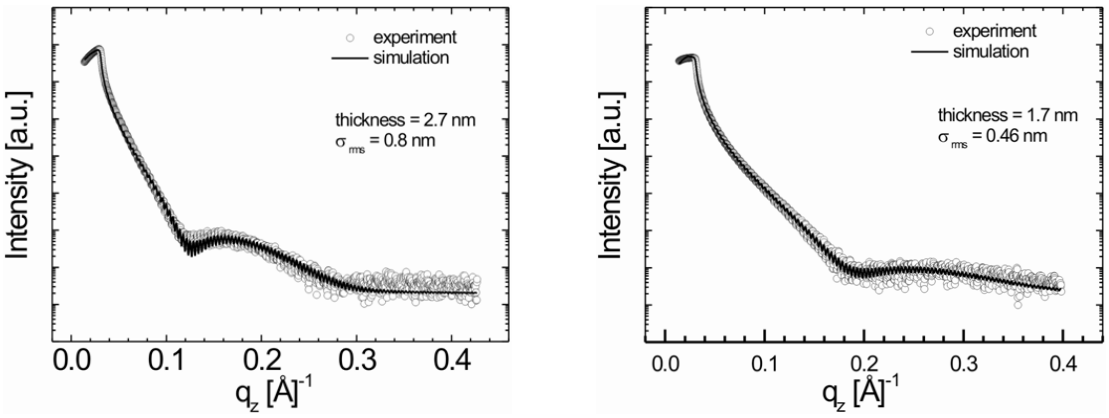

(a) (b)

Figure 55: Experimental (open circle) and simulated (solid line) XRR results of (a) a multilayer layer of Si-PF-long grown under ambient condition and (b) a monolayer of Si-PF-long grown under ultra dry condition.

The change in thickness can also be observed when looking at the Si2p region in the XPS measurements. As reference the Si2p spectrum (figure 56) of the sample investigated in section 3.2.1 after step 2 is used. This native oxidized silicon wafer has been cleaned, activated in Piranha solution and water dipped.

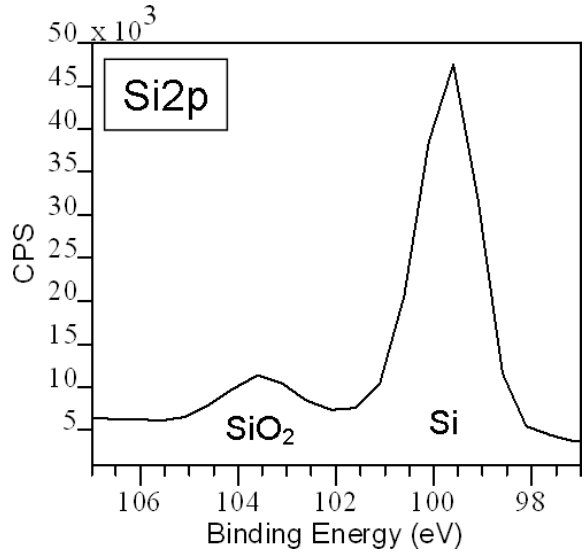

Figure 56: The Si2p region of a cleaned and activated native grown silicon oxide.

The accepted value of the thickness of the native oxide is assumed to be approximately 1 nm.[103,104] The ratio between the silicon oxide and elemental silicon of the substrate is $\frac{\mathrm{Si2p(SiO_x)}}{\mathrm{Si2p(Si)}} = \frac{13.8\%}{86.2\%}$. This means if 13.8% of the whole Si2p signal is atributed to silicon oxide the layer has a thickness of 1 nm. This ratio is important to calcualte the layerthickness of

so called SAMs as discribed later.

The Si2p spectra of the layers prepared under ambient and ultra dry conditions of two different molecules (Si-PF and Si-PF-long) are shown in figure 57.

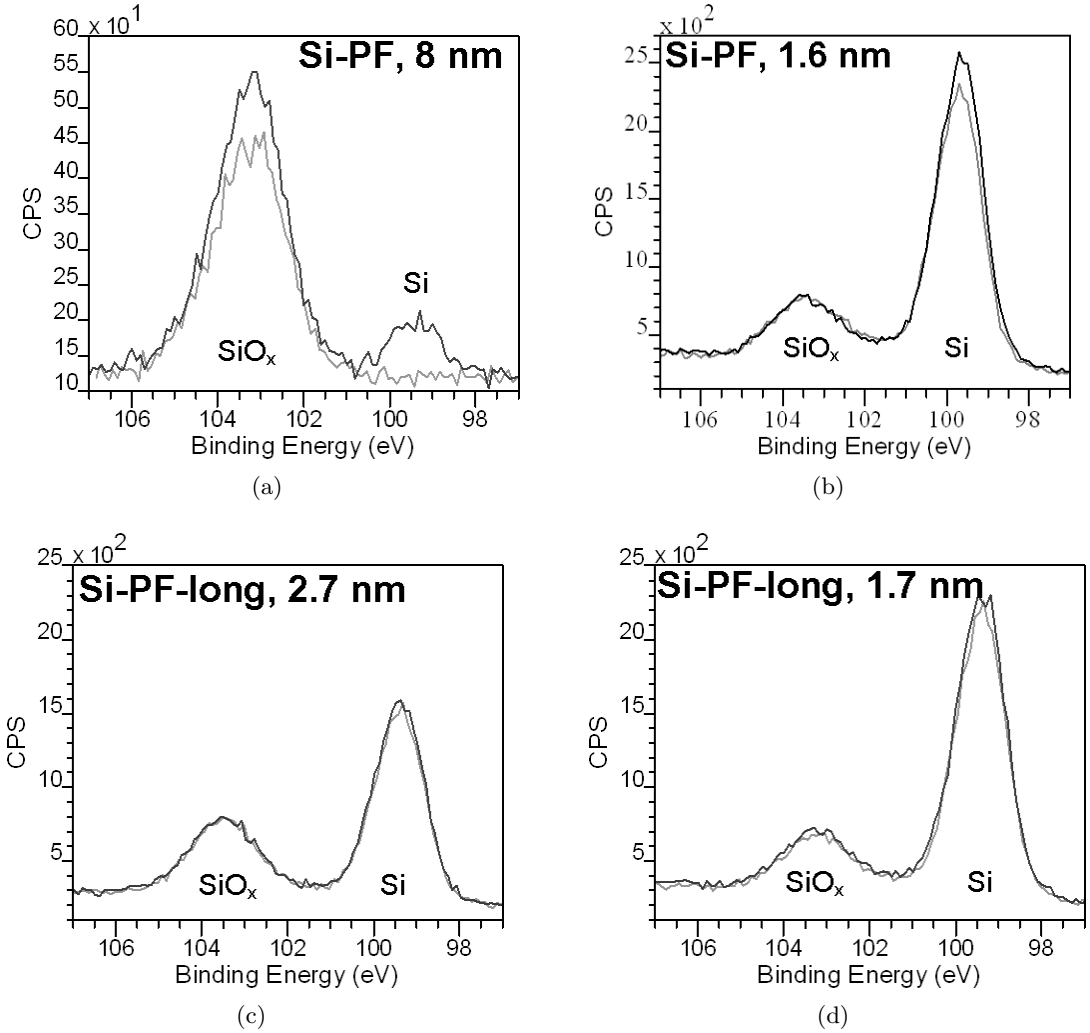

Figure 57: Si2p region of (a) Si-PF prepared under ambient conditions, (b) Si-PF prepared under ultra dry conditions, (c) Si-PF-long prepared under ambient conditions and (d) Si-PF-long prepared under ultra dry conditions. Pristine layers (dark gray) and illumination and subsequent post modified layer (light gray) on native grown silicon oxide. The thickness measured with XRR is indicated.

By comparing the spectra, it is clearly visible that the film thickness in all four layers is different due to a changing Si:SiO_x ratio. To calculate the layer thickness, the relative percentage of the silicon oxide in the whole Si2p signal was quantified (labeled as SiO_x in table 5). From this the combined layer thickness, consisting of the native oxide layer and the adsorbed SAM on top of it (labeled as 'd(native oxide+Silane SAM)' in table 5), can be

calculated by referencing the 'SiO_x' of the investigate film to the 'SiO_x' of a cleaned wafer, characterized above (see figure 56). The calculated values of the 'd(native oxide+Silane SAM)' can then be compared with the measured film thickness using XRR and are in good agreement (see table 5).

To evaluate how many molecular layers are adsorbed, an assumption has to be made. In the Si2p signal only the silicon component of the silane SAM is visible. To quantify the number of adsorbed layers, the 'thickness' or 'height' of the silane group has to be known. This value is estimated by adding the van der Waals radii of oxygen (0.152 nm) and silicon (0.21 nm) to predict the length of the Si-O bond in the silane docking group. After subtracting the native oxide thickness (1 nm) from the combined thickness 'd(native oxide+Silane SAM)' and dividing the value through the Si-O bond length of 0.362 nm, one obtains the number of adsorbed SAM molecules. With this method one can see, that the Si-PF-long arrange in less layers than the Si-PF under the same preparation conditions. This behavior is explained through the more flexible (longer) spacer. The flexibility allows a better ordering of the aromatic functional head group or the flexible spacers tent to conglomerate which leads to less densely packed layers and thinner film thicknesses. The second explanation is more likely, because the calculated length of the Si-PF-long (see above) of 2.0 nm is higher than the measured film thickness (1.5 nm with XPS and 1.7 nm with XRR) formed under inert conditions. However, it is not known exactly and can not be determined with the available experimental methods.

Table 5: Results to calculate the layer thickness using the Si2p region of differently prepared ('prep. conditions') silane SAMs and the reference surface without adsorbed organic molecules. The percentage of the Si2p component at 103.2 eV is labeled as SiO_x and the ration of the Si2p component at 103.2 eV and at 99.4 eV is labeled as $\frac{SiO_x}{Si}$. The calculated thicknesses of the native grown silicon oxide and the silane SAM is labeled as d(SiO_x+SAM) and the thickness measured with XRR is given as d(XRR). All thicknesses are given in nm. Finally the calculated number of adsorbed SAM layers is labeled as 'SAM layers'.

	prep. conditions	SiO_x	$\frac{SiO_x}{Si}$	d(SiO_x+SAM)	d(XRR)	SAM layers
Reference	-	13.8%	0.16	1	-	0
Si-PF	ambient	87.4%	6.94	6.33	8	14.7
Si-PF	inert	22.7%	0.29	1.64	1.6	1.8
Si-PF-long	ambient	31.0%	0.45	2.25	2.7	3.5
Si-PF-long	inert	20.7%	0.26	1.50	1.7	1.4

With XPS it is possible to calculate the thickness of SAMs, if a reference sample with defined silicon oxide thickness is available and the elemental silicon of the substrate is

visible. When comparing results of this XPS based method with measured filmed thickness from XRR just a small deviation is found. But with XRR it is more difficult to measure thin film thicknesses. For example with XRR it is not possible to determine the thickness of a native oxide layer with enough accuracy.

3.2.5 Conclusion

First, the change of the surface wettability during sample preparation of thin silane films is investigated by contact angle measurement and XPS to establish the basis for the following sections.

Then, it was shown, that the modification and patterning of silicon oxide substrates with silane molecules bearing different functional photoreactive head groups is possible. The patterning of silicon oxide has been obtained with two molecules, containing different photoreactive functional head groups.

At the beginning, the new functional photoreactive trialkoxysilane Si-SCN molecules have been introduced bearing the benzyl thiocyanate group. Upon irradiation with UV-light of 254 nm, the thiocyanate group (-SCN) isomerizes to give the corresponding isothiocyanate (-NCS). Thin layers of Si-SCN were prepared on activated silicon/silicon oxide substrates with a layer thickness of approximately 6 nm (measured with XRR). The photochemistry and the selective postmodification with amines in these very thin layers was proven spatially resolved XPS.

A second novel molecules containing a phenyl ester as functional photoreactive head group was investigated. Upon irradiation with UV-light of 254 nm, the phenyl ester groups undergo the photo-Fries rearrangement with a 50%yield forming the corresponding hydroxy ketones which are chemically more reactive than the ester units in the non-irradiated areas. Using a postmodification reaction, perfluorinated alkyl groups were selectively immobilized. The photoreaction as well as the postmodification reaction was again proven by spatially resolved XPS measurements.

It is possible to estimate the film thickness of different silane layers via the ratio between Si:SiO_x of the Si2p signal if a decent reference sample is measured. Therefore, the space length of the silane molecule containing the phenyl ester group was varied and the obtained changes in film thickness could be evaluated with XPS. Additionally, the number of adsorbed molecular layer can be estimated. This shows that molecules with the longer spacer (Si-PF-long) are likely to adsorb with less molecular layers than the molecule with a shorter spacer (Si-PF) at the same processing conditions.

3.3 Thiols

After investigating layers formed of silane molecules bearing different photoreactive functional head groups, the formation of similar layers on gold as substrate is shown in this section. The possibility to form pattern-able organic layers is thus extended for larger amount of applications.

3.3.1 Photoreactive Phenyl Esters Forming Self-Assembled Monolayers on Gold

Foreword The results shown in this section have been achieved in collaboration with Dr. Thomas Griesser during his PhD at the Institute of Chemistry and Technology of Organic Materials (Graz University of Technology) and during his work at the Institute of Chemistry of Polymeric Materials (University of Leoben) in the framework of the National Research Network (NFN). In the following section the results of the joint paper (see reference[10]) are largely reproduced and further investigations are additionally included.

Photoreactive Self Assembled Monolayers for Tuning the Surface Polarity

Thomas Griesser[1,2*], Anna Track[3], Georg Koller[3], Michael Ramsey[3] Wolfgang Kern[1,2] and Gregor Trimmel[1*]

[1] Institute for Chemistry and Technology of Materials, Graz University of Technology, Stremayrgasse 16, Graz, Austria
E-mail: gregor.trimmel@tugraz.at
[2] Institute of Chemistry of Polymeric Materials, Montanuniversität Leoben, Franz-Josef Strasse 18, 8700 Leoben, Austria.
E-mail: thomas.griesser@unileoben.ac.at
[3] Institute of Physics, University of Graz, Universitätsplatz 5, 8010 Graz, Austria

Figure 58: Copy of part of the first page of reference 10 including all coauthors and their affiliations

The modification of gold substrates with SAMs of photo reactive molecules containing a phenyl ester head group to perform the Photo-Fries rearrangement is presented here. Two novel molecules with different spacer length have been used. The phenyl ester head groups of both molecules photoisomerize upon UV irradiation to the corresponding hydroxy ketone, which leads to a dramatic change in surface polarity and reactivity. The photo-generated hydroxyl groups were selectively postmodified with perfluorobutyryl chlorid or used to link fullerene derivatives selectively onto the surface. This patterning process was followed with XPS and contact angle measurements.

Experimental Section

Preparation, Patterning and Postmodification As substrates we used gold films which were evaporated on glass, purchased by Arrandee^{TM}(Germany). In more details the substrates contains of borosiliclate glass with a thickness of 1.1±0.1 mm, a chromium adhesion layer of 2.5±1.5 nm and a final 250±50 nm gold layer.[Q]

To clean these substrates Piranha solution has been used. For that reason concentrated H_2SO_4 is given to 33% H_2O_2 in a relation of 2:1 and then the substrates are inserted into this mixture for maximal 15 minutes. Be aware of the risk using Piranha solution by avoiding strong exothermic reaction using dirty glass ware and dispose the used solution with a profuse amount of water. The cleaned substrates are rinsed several times with destiled water and subsequently with 18 MΩ cm water before drying the substrates for one hour in a dry box at 80°C.

The 2 mM SAM solution is prepared under inert conditions using freshly distilled ethanol as solvent. For complete dissolvation the solution is put into an ultrasonic bath for 15 to 30 minutes at 50°C.[R] Finally the clean substrates are immersed for 24 hours in the SAM solution under dark and inert conditions. Afterwards the formed SAM is rinsed with absolute ethanol and dried with a nitrogen stream.

For the patterning of the SAM one half of the sample is covered with aluminum foil and this construction is mounted in a nitrogen floated chamber[S] having a quartz glass, through which the UV-light shines on the sample. An ozone free, low pressure UV lamp (Heraeus Noblelight) with a wavelength of 254 nm and a power density of 1.35 mW/cm^2 is used. To avoid changes in the intensity of the UV irradiation, the quartz glass is cleaned (inside and outside) before each illumination procedure. Furthermore the UV-lamp is switched on 20 minutes before usage to avoid an intensity gradient during the illumination of the SAM. The illumination time to pattern the SAM is 15 minutes.

After the conversion of the phenyl ester to the hydroxy ketone due to the illumination, the sample is inserted into a argon glove box. Under inert conditions the SAM is selectively postmodified with two different compounds.

On one hand the sample was immersed in a solution of 200 µl perflourobutyryl chloride and 50 µl triethylamine or pyridine in 2 ml dichloromethane for 20 minutes and then washed with dichloromethane and dried with a stream of nitrogen.

On the other hand a fullerene derivative is attached selectively on the illuminated areas of the SAM. In this case the SAM has do be dipped in three different solutions. First it is immersed in a solution of 200 µl adipoyl dichloride and 50 µl triethylamine or pyridine into 2 ml dichloromethane for one hour and subsequently washed with dichloromethane. Then the substrates are dipped in a solution of 100 µl ethylenediamine for 20 minutes

[Q] The suggested flame annealing step using a propane/butane flame has not been performed.
[R] All steps have to provide the exclusion of light to avoid uncontrolled photo-isomerisation
[S] The chamber is flushed with nitrogen gas for about 20 minutes to minimize the presence of reactive gases like oxygen during the illumination.

and again washed with dichloromethane. Finally the SAM is inserted into a solution of 2 mg fullerene, 2 ml bromobenzene, 2 ml dimethyl sulfoxide (DMSO) and 1 mg N,N´-dicyclohexylcarbodiimide (DCC) for three days. For the XPS measurements the SAM is subsequently washed with bromobenzene and dichloromethane several times and dried with a stream of nitrogen.

Contact Angle Measurements The contact angel θ measurements were obtained with a Drop Shape Analysis System DSA100 (Krüss GmbH, Hamburg, Germany) using water and diiodomethane as test liquids. The contact angles were measured by the sessile drop method within two seconds and the surface tension γ as well as the dispersive and polar components (γ^D and γ^P) were calculated based on the Owens-Wendt method.[105]

XPS Measurements XPS measurements were carried out with a XPS equipment (SPECS) in ultra high vacuum (1×10^{-10} mbar) using $Mg - K_\alpha$ radiation (1253.6 eV) and a hemispherical analyzer (Phoibos100) with an energy resolution of 1.2 eV which was focused to about 1 mm diameter (compare section 2.2.1). All spectra were normalized to Au4f7/2-peak having the binding energy of 84.0 eV.

Results and Discussion Two different molecules, 11-mercaptoundecanoic-acid-phenyl--ester (Au-PF)[10] and 16-mercaptohexadecanoic-acid-phenyl-ester (Au-PF-long)[78], containing both the phenyl ester head group were used to form SAMs on gold. The SAMs were prepared by immersing gold substrates into a solution of these molecules. In the next step, only one half of these films were illuminated using UV-light of 254 nm. Thereby, the phenyl ester groups undergo the photo-Fries rearrangement to the corresponding hydroxy ketones (compare references in section 3.2.3) in the illuminated areas. The photo-generated hydroxy-groups are more reactive than the ester groups, as demonstrated by a successive post-modification step with different chemicals. The molecular structure of Au-PF and Au-PF-long, the photo reaction, and the selective postmodification are schematically depicted in figures 59 and 60.

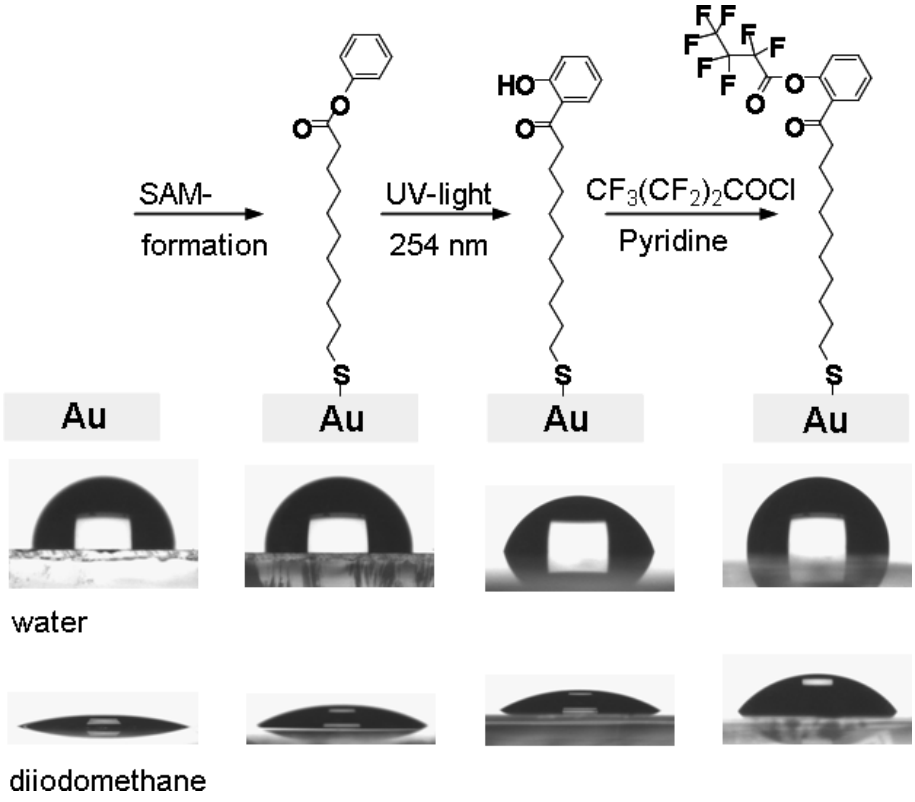

Figure 59: Scheme of the SAM formation of Au-PF on gold, the photo-Fries rearrangement due to illumination and the postmodification reaction with perfluoroburyryl chloride. Underneath the images to calculate the contact angel of water and diiodomethane on each surface. (Largely identical to reference 10.)

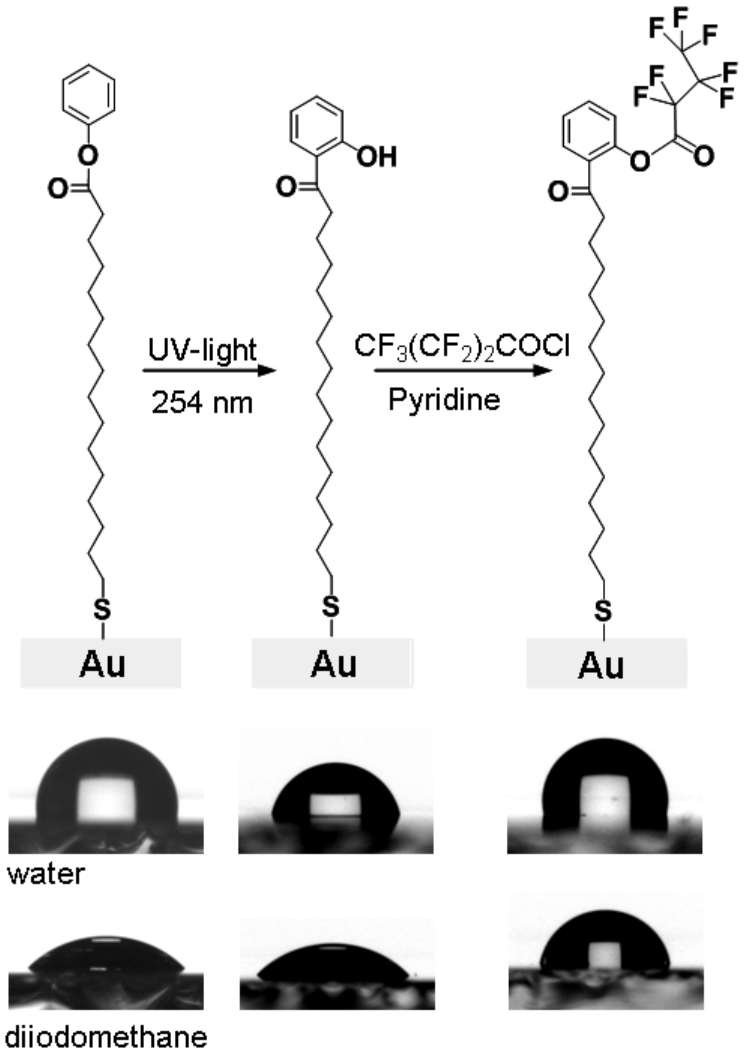

Figure 60: Scheme of the Au-PF-long SAM on gold, the photo-Fries rearrangement due to illumination and the postmodification reaction with perfluoroburyryl chloride. Underneath the images to calculate the contact angel of water and diiodomethane on each surface.

The change of the surface polarity was investigated by contact angle measurements. Images of water and diiodomethane droplets of the original gold substrate, of the SAM before and after UV-illumination, as well as after the post-modification with perfluorobutyryl chloride are presented in figure 59 for SAMs formed with both molecules. The contact angles and the calculated surface tension are summarized in Table 6 for Au-PF monolayers and in table 7 for Au-PF-long SAMs.

Table 6: Contact angle θ (water and diiodomethan) and surface tension γ (γ^D: dispersive component, γ^P: polar component; surface polarity $= 100\,(\gamma^P/\gamma)$) data of the gold substrate, the Au-PF SAM layer before and after illumination, and after post-modification with perfluorobutyryl chloride. (Largely identical to reference 10.)

	θ_{H_2O} / °	$\theta_{CH_2I_2}$ / °	γ / mJ/m^2	γ^D / mJ/m^2	γ^D / mJ/m^2	polarity / %
gold	88 ± 3	23 ± 1	47.5 ± 0.2	46.8 ± 0.1	0.7 ± 0.1	1.5 ± 0.1
Au-PF	91 ± 1	32 ± 3	43.8 ± 0.0	43.4 ± 0.0	0.4 ± 0.0	0.9 ± 0.0
illuminated	78 ± 1	35 ± 0	45.8 ± 0.1	42.2 ± 0.0	3.7 ± 0.0	8.1 ± 0.1
illuminated+modified	93 ± 1	52 ± 1	34.2 ± 0.1	33.1 ± 0.1	1.1 ± 0.0	3.2 ± 0.1

Table 7: Contact angle θ (water and diiodomethan) and surface tension γ (γ^D: dispersive component, γ^P: polar component; surface polarity $= 100\,(\gamma^P/\gamma)$) data of the Au-PF-long SAM layer on gold before illumination, after illumination and after illumination and subsequent post-modification with perfluorobutyryl chloride.

	θ_{H_2O} / °	$\theta_{CH_2I_2}$ / °	γ / mJ/m^2	γ^D / mJ/m^2	γ^D / mJ/m^2	polarity / %
Au-PF-long	97.5	45.1	37.19	36.98	0.21	0.56
illuminated	78.7	45.8	41.16	36.59	4.56	11.08
illuminated+modified	102.9	88.7	15.79	13.30	2.49	15.77

Due to the formation of the Au-PF SAM, the contact angles increase both for water (from 88° to 91°) and for diiodomethane (from 23° to 32°). This is a consequence of the reduced overall surface tension caused by the adsorption of the molecule. With the adsorption of Au-PF-long on gold the contact angle is slightly higher for both test liquids (97.9° and 45.1°) than for the bare gold substrate. Although not enough measurements for error analysis of Au-PF-long have been done, the trends are the same as for Au-PF. The UV-illumination decreases the contact angle of water to 78° for both molecules, whereas the contact angle of CH_2I_2 only slightly increases. After treatment with perfluorobutyryl chloride, both contact angles rise to the highest observed values for both molecules, whereas the surface tension is the lowest value of this series due to the selective reaction with fluorine containing compound.

To confirm the selectivity of the postmodification step, XPS measurements have been performed for both SAM molecules on half illuminated samples. Similar measurements have been reported in reference[78].

The selective reaction with perfluorobutyryl chloride is investigated by measuring the F1s

signal of half illuminated samples. The F1s spectra for both molecules are shown in figure 61 and it is clearly visible, that the fluorinated compound attaches only on the illuminated molecules, since only on this side an intense F1s signal was found. This clearly indicates that the desired selective surface chemistry is occurring and patterning is possible.

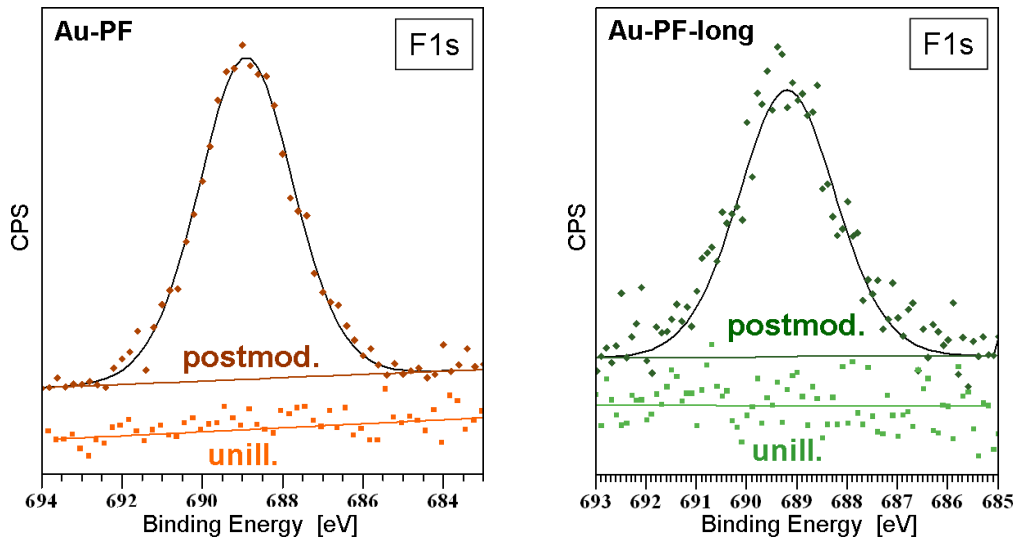

(a) (b)

Figure 61: F1s signal of the pristine (orange and light green squares) and the illuminated and selective postmodified (brown and dark green diamonds) half of (a) Au-PF and (b) Au-PF-long SAM layers. ((a) Largely identical to reference 10.)

XPS survey spectra confirm the SAM formation as the corresponding carbon, sulfur and oxygen signals were found on both half of the samples for both molecules. As example the survey spectra of the illuminated and unilluminated side of the selective post modified Au-PF layer is shown in figure 62. Furthermore the relative ratio between C:F has been calculated.[T] The expected C:F=21:7 could not be found, which indicates a not 100% photorearrangement. Longer illumination times would increase the photorearrngement yield but would simultaneouly increase the layer degratation due to bond breaking with UV-light.

[T] RSF(C1s)=0.296, RSF(F1s)=1

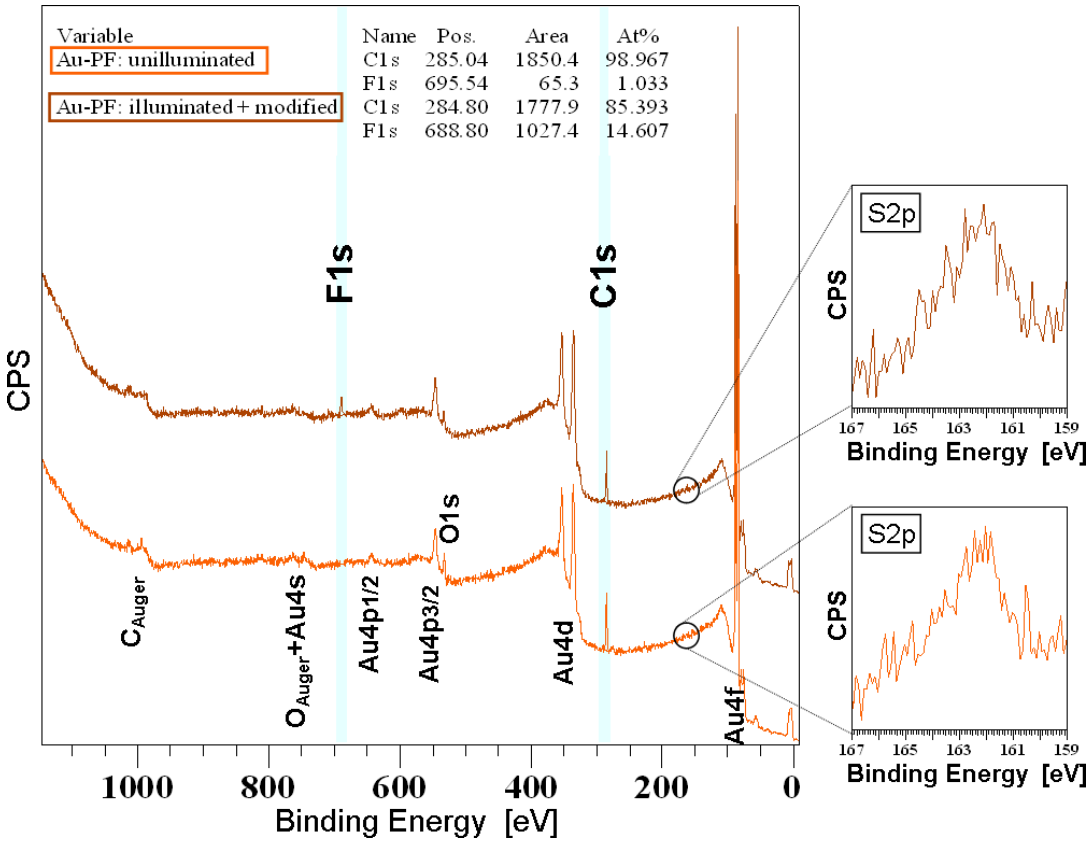

Figure 62: Survey spectra of the pristine (orange) and illuminated (brown) half after subsequent postmodification with perfluorobutyryl chloride of Au-PF SAMs on gold. The S2p region of both halves is shown in more detail because only a small amount could be detected. The relative ratio of C:F has been calculated. (Due to the vanishing amount of F1s on the pristine layer, the binding energy could not be extracted properly by the analyzing program CasaXPS.)

A postmodification to immobilize fullerenes on the surface selectively also has been investigated with XPS for SAMs of Au-PF-long.[U] The molecular structures before and after illumination and subsequent postmodification are shown in figure 63. Note, that the postmodification reaction has performed in three separate steps and only if each postmodification reagent reacts selectively with the illuminated molecule the immobilization of fullerenes is possible.

[U] The preliminary stage of this selective post modification has been investigated in reference [78]

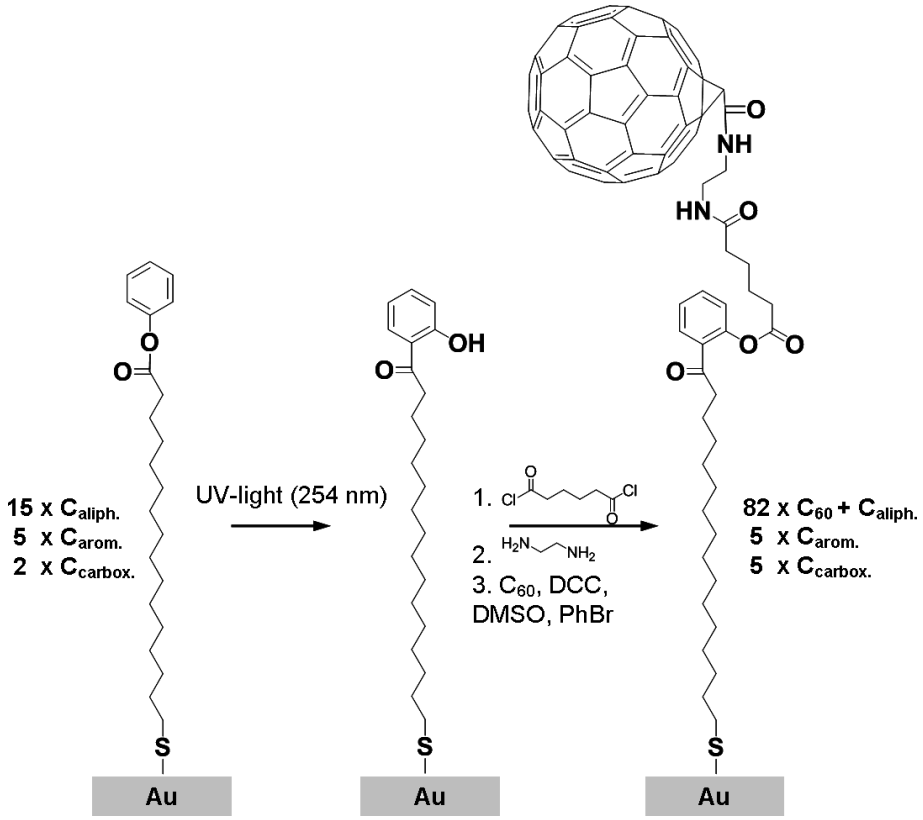

Figure 63: Scheme of the photo-Fries rearrangement and the postmodification to immobilize fullerene on the patterned surface.

The patterning is best seen with the appearance of a N1s signal and the doubling of the O1s signal due to the selective reaction on the illuminated side (c. f. figure 63). This postmodification leads furthermore to an increase in film thickness which is seen in the decrease of the Au4f signal. All corresponding spectra are shown in figure 64.

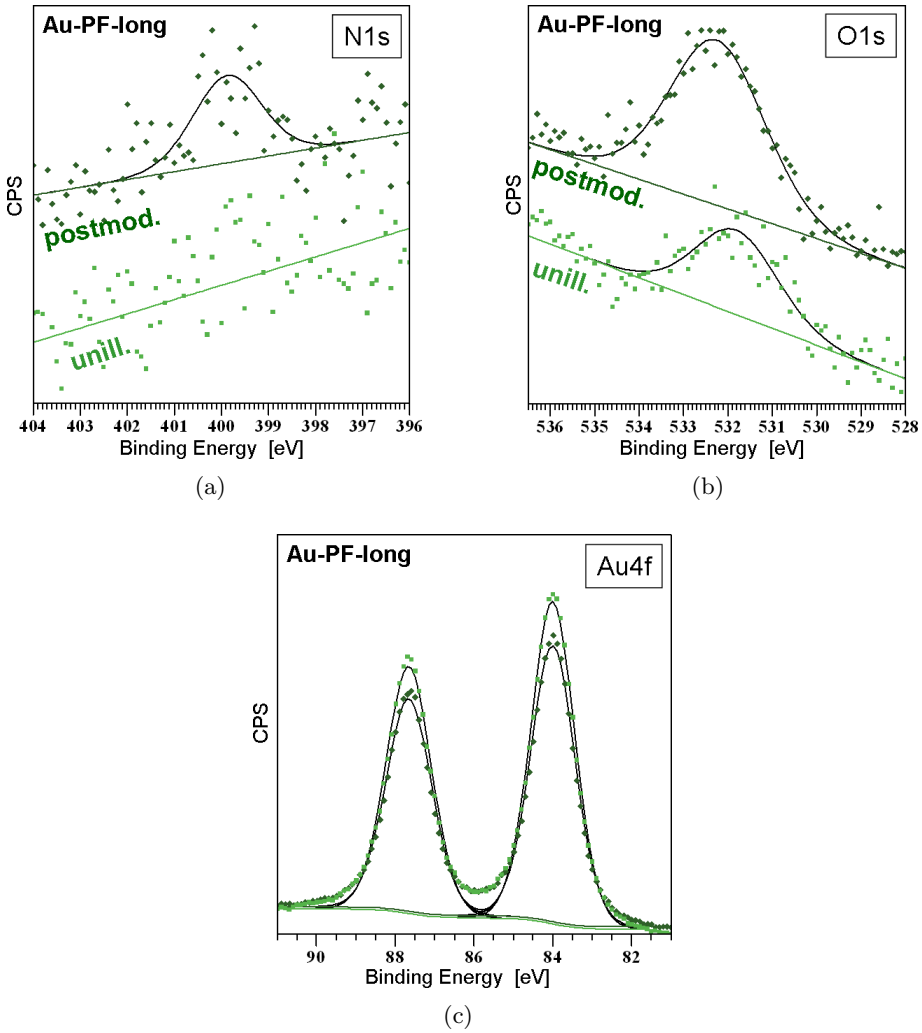

Figure 64: XPS spectra of the pristine (light-green squares) and subsequent postmodified (dark-green diamonds) of (a) the N1s region), (b) the O1s region and of the (c) Au4f region.

Furthermore, the change of the C1s signal is investigated, because also here the selective postmodification should be visible. An obvious increase of the C1s signal in figure 65 of the immobilization of C_{60} on the surface is seen. Additionally, a quantitative analyzation of the different carbon species has been done, which emphasize the presence of fullerenes on the illuminated areas of the sample. The amount of carbon at a binding energy of 284.5 eV which is attributed to the carbon atoms in fullerene and aliphatic carbon as well as the carboxylic carbon amount at a binding energy of 288.0 eV increases (compare area-values in figure 65). The values for the differently bonded carbon species are in good agreement with literature.

From the difference in the ratios of the differently bonded carbon species, again the

selectivity of the postmodification reaction can be seen by comparing the values obtained with the quantitative analysis and the theoretical rations of the molecular structures as shown in figure 63.

For the pristine molecule ,a ratio of $C_{apliph.} : C_{arom.} : C_{carbox.} = 15 : 5 : 2 = 68.2\% : 22.7\% : 9.1\%$ is expected from the molecular structure, which is in perfect agreement with the values calculated in the quantitative analysis $C_{apliph.} : C_{arom.} : C_{carbox.} = 64.8\% : 26.6\% : 8.6\%$.

The theoretical carbon ratio of the molecule containing the fullerene changes to $C_{apliph.+C_{60}} : C_{arom.} : C_{carbox.} = 82 : 5 : 5 = 75.4\% : 4.6\% : 4.6\%$. Tis change is also reflected in the qunatitative analsis of the C1s region ($C_{apliph.+C_{60}} : C_{arom.} : C_{carbox.} = 79.7\% : 13.8\%6.5\%$).

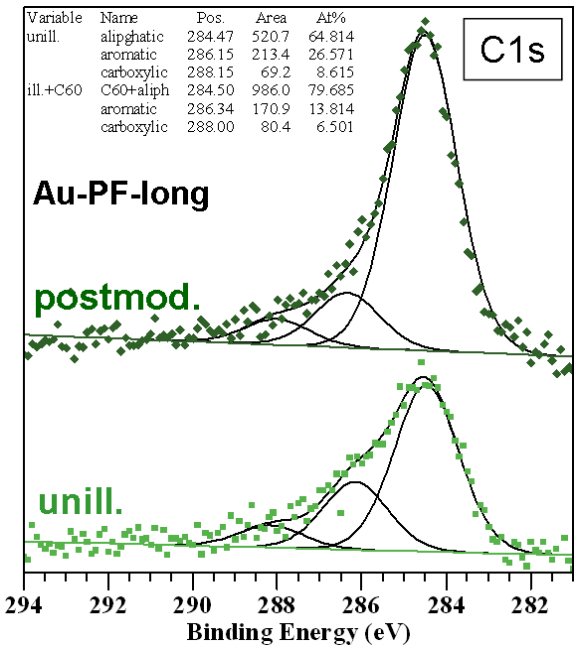

Figure 65: C1s spectra of the pristine and selective postmodified Au-PF-long SAM. The relative ratios of the different bonded carbon atoms are depicted for each spectrum.

We did try selective immobilization with other molecules such as Dansylchloride, Biotinhydrazid and Norborneneacidchloride but the results where never as clear or selective as with the immobilization of C_{60}. The reason why the three step process worked that well is not yet clear.

3.3.2 Surface Characterization of Gold Covered with Molecules Containing a Naphthyl Ester Head Group.

Foreword For this study a new molecule was synthesized by Dr. Thomas Griesser. The molecule is similar to the Au-PF-long, which was discussed in the section 3.3.1. Instead of a phenyl ester head group a naphthyl ester was introduced leading to 16-mercapto-hexadecanoic-acid-naphth-1-yl-ester (Au-Naphthyl). The ability to perform the photo-Fries rearrangement of Au-Naphthyl was observed with FT-IR spectroscopy in Leoben with Dr. Thomas Griesser. Due to the stronger van der Waals interaction between the naphthyl rings compared to the phenyl rings a better long range ordering of the SAM was expected (compare e. g. with reference 106 and 12).

I spent two weeks in the group of Prof. Gregor Witte (AG Molekulare Festkörperphysik, Philipps-Universität Marburg, Germany) to investigate the ordering of the Au-Naphthyl SAMs and get an insight of preparing gold substrates properly. The PhD students Mira El Helou, Christian Schmidt and Jan Götzen supported the low-energy electron diffraction (LEED), AFM and scanning tunneling microscopy (STM) measurements.

Experimental Section

Gold on Mica: Substrate Preparation Mica substrates with an evaporated gold layer purchased by Georg Albert Physical Vapor Deposition (PVD)[V] have been cut in the proper size with a glass cutter to $7 \times 7\,\mathrm{mm}^2$. To obtain the largest size of Au(111) terraces, the substrate has to be flame annealed using a butane-oxygen flame. Moving the substrate in circular movements (gold layer pointing away from the burner) avoids a too fast increase of the temperature which can break the mice layers[W] due to evaporation of crystallization water. This procedure has been repeated 20 times.

Afterwards the sample is mounted on a special sample plate for inserting in the UHV chamber. The gold substrate is sputtered with argon at a pressure of $5 \times 10^{-6}\,\mathrm{mbar}$ at room temperature ($1.5\,\mu\mathrm{A}$ and $745\,\mathrm{eV}$). Then the sample was flashed to 477°C (16.1 V and 2.3 A) for 5 to 10 minutes. Here again care should be taken during the increase of the temperature up to 120°C because of the evaporation of the crystallization water. The sputtering and annealing steps are repeated until in LEED the Au(111) unit cell is clearly visible.

SAM Formation The pretreated substrate (gold/mica) is immersed in a 4 mM solution of Au-Naphthyl in absolute ethanol, which was been heated and sonicated for 30 minutes at 50°C to assure that the whole compound is dissolved. After 18 hours the SAM is rinsed with absolute ethanol and dried with a stream of nitrogen.

[V] http : //www.georg − albert − pvd.de/Home/substrat_glim.html
[W] Black dots appear.

LEED Measurements The LEED is mounted in an Omicron vacuum system at a base pressure $< 1 \times 10^{-10}$ mbar. A fast entry load lock is used to insert the samples which are mounted on a Omicron sample holder. The sample holder can be cooled done to 150 K, which is beneficial to cool the sample after sputtering and annealing. The chamber is shown in figure 66.

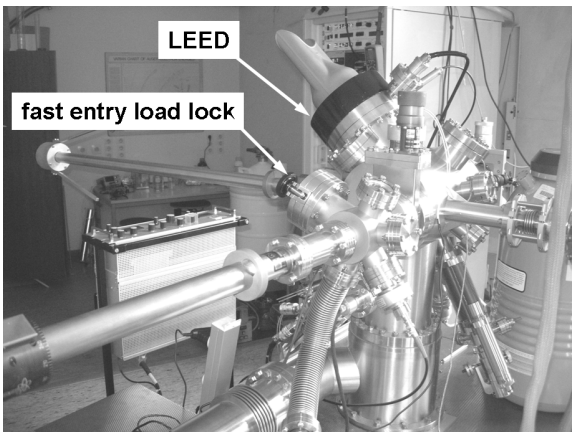

Figure 66: UHV-chamber at the AG Molekulare Festkörperphysik including a fast entry load lock and a LEED.

AFM and STM Measurements For the AFM and STM measurement a Agilent Technologies 5500 Scanning Probe Microscopy was used (figure 67). This microscope operates under ambient condition and is mounted in a special cabinet to minimize vibrations and other impact from outside .

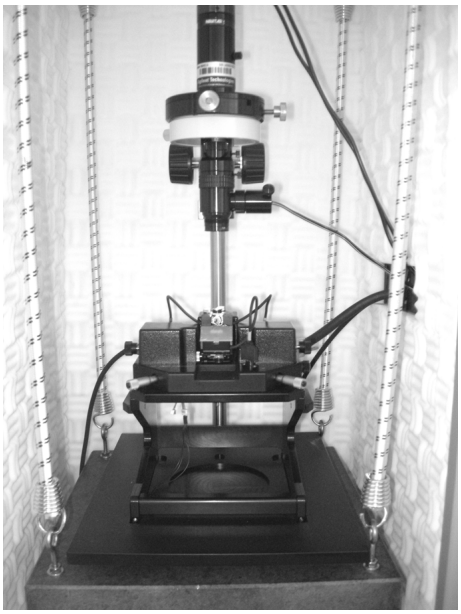

Figure 67: Agilent Technologies 5500 Scanning Probe Microscopy at the AG Molekulare Festkörperphysik.

For the AFM measurements the taping mode was used. The resonance frequency of the cantilever was measured to be 320.91 kHz. For STM a fresh cut Pt-Ir wire was used. The wire was just cut with an usual wire cutter.

FTIR Measurements To follow the photo-Fries rearrangement of Au-Naphthyl a Perkin Elmer 'Spectrum One' FT-IR microscope was used (see figure 68). The Au-Naphthyl molecule was investigated in a liquid layer by spin casting a solution of Au-Naphthyl in acetone on a CaF_2 substrate. For background subtraction, a cleaned CaF_2 substrate was used. The liquid layer was subsequently illuminated three times with UV-light (254 nm) under Nitrogen atmosphere for 20 minutes. Before illumination and after each illumination step a FT-IR spectrum has been taken (10 scans, 4000 to 850 cm^{-10})

Figure 68: Perkin Elmer 'Spectrum One' FTIR microscope at the Institute of Polymeric Materials, University Leoben, Austria. (Image from http://ssfp.unileoben.ac.at/FTIR.htm)

Results and Discussion The novel molecule 16-mercaptohexadecanoic-acid-naphth-1-yl--ester (Au-Naphthyl) is first tested on the ability to perform the photo-Fries rearrangement which is shown in figure 69.

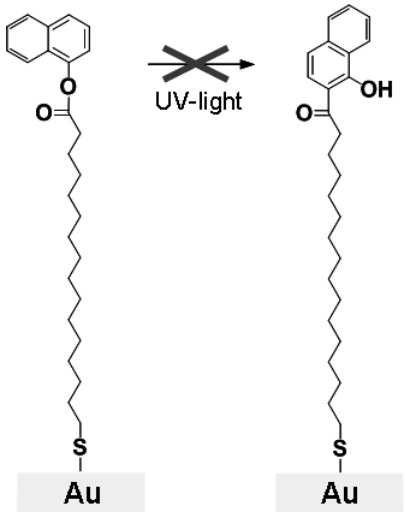

Figure 69: The Au-Naphthyl SAM on gold containing as functional head group the naphthyl ester **does not** perform the photo-Fries rearrangement due to UV illumination.

A liquid film on CaF_2 substrate is investigated with FT-IR spectroscopy before illumination and after 20, 40 and 80 minutes illumination with UV-light with a wavelength of 254 nm. The results are shown in figure 70. No new signals due to illumination are detected in FT-IR. In all spectra following signals arises: due to aromatic CH vibrations at 3063 cm^{-1} , due to aliphatic vibrations CH at 2915 cm^{-1} and 2845 cm^{-1}, due to thiolate at 2566 cm^{-1} and due to the C=O stretching in the ester group at 1748 cm^{-1}. No in-

creasing signal with illumination time at 1630 cm^{-1} due to formed hydroxy ketones is seen which indicates that unfortunately no photo-fries rearrangement occurs in the Au-Naphthyl molecule. This result is somehow understandable when comparing the yield of photo-Fries rearrangement of different aryl ester measured in reference 107. Here the benzoic acid esters have a significant higher yield (around 70%) than the naphthalene-1-carboxylic acid esters (just around 30%).

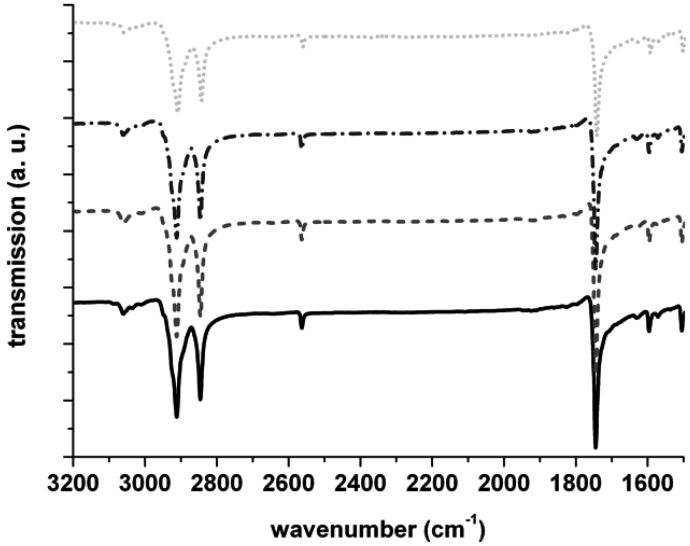

Figure 70: FTIR spectra of a liquid film of Au-Naphthyl before illumination (solid black), after 20 minutes (red dashed), 40 minutes (blue dashed dotted) and 80 minutes (green dotted) illumination with UV-light.

The loss of the ability to pattern the surface with UV-light does not exclude the formation of a well ordered SAMs using the Au-Naphthyl molecule. A critical point here is the use of the proper substrates. Therefore gold on mica was used to prepare a Au-Naphthyl-SAM.

The gold on mica was first flame annealed with a simple butane/oxygen flame to remove organic contaminations and to allow the gold forming (111) terraces. Additional sputtering and annealing in UHV as described in section 3.3.2 leads to large Au(111) terraces on mica determined with LEED. The LEED images at different voltage are shown in figure 71.

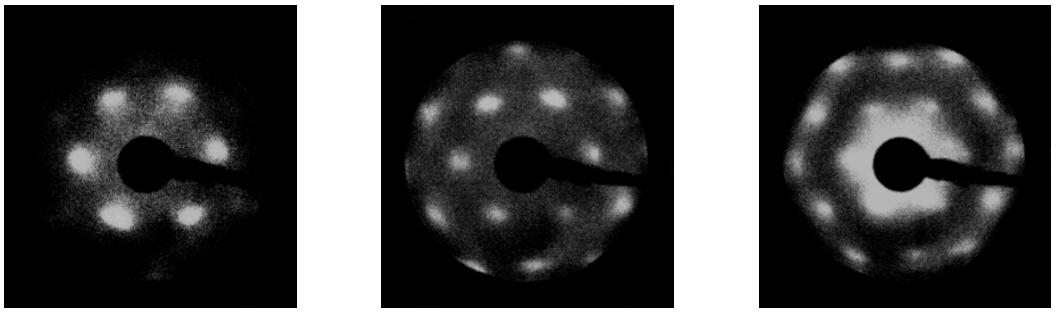

(a) (b) (c)

Figure 71: LEED images of the pretreated gold on mica substrate after three sputtering and annealing procedures (a) at 119 V, (b) at 150 V and (c) at 190 V.

The substrate is then ex-situ immersed in a ethanolic solution of Au-Naphthyl for one day, rinsed and dried. First the SAM on gold is investigated with AFM under ambient conditions. Figure 72a shows that the surface of the Au-Naphthyl SAM is very smooth with a roughness of 5 nm, clean and homogeneous. The triangle (angle=60°) structure in figure 72b arises from the gold substrate underneath the SAM and is an indication for well ordered Au(111) terraces. The depth of the hole in this terrace is 2.4 nm, which corresponds to 10 gold layers. The steps shown in figure 72c correspond to the height of two to three gold layers. In all images bright spots are visible on the whole surface. The spots could be explained as a molecular multilayer or as encapsulated solvent molecules, but additional heating of the SAM did not lower the concentration of these bright spots. It is assumed that the spots arise due to undefined organic impurities but with XPS no specific contamination could be detected.

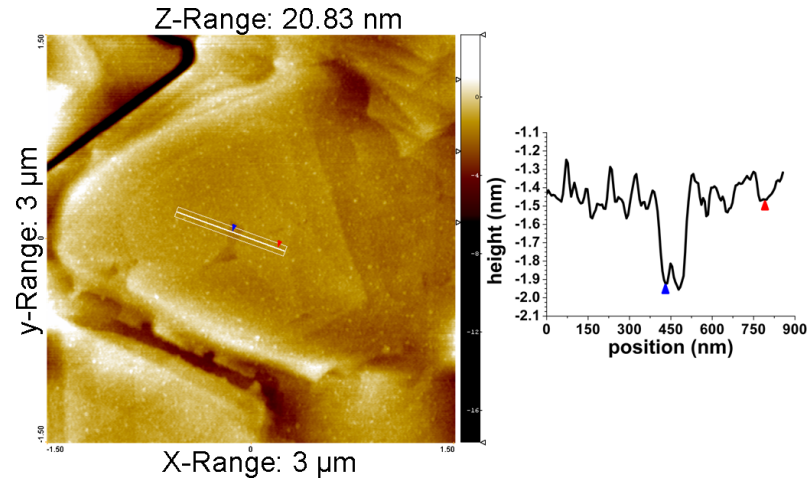

(a)

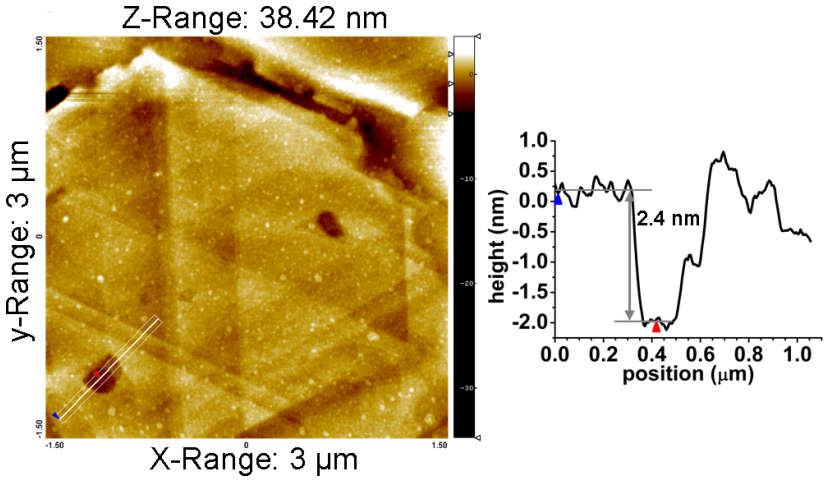

(b)

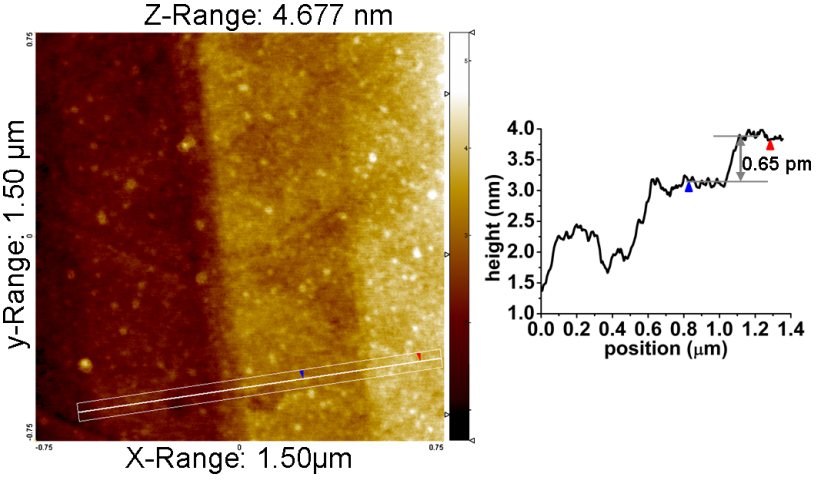

(c)

Figure 72: AFM images and depth profiles of the Au-Naphthyl SAM on gold/mica.

Afterwards the same sample was investigated with STM under ambient conditions. Large scan images show atomic steps and large ares of perfect Au(111) planes (figure 73). Furthermore etch pits are visible homogeneously distributed on the whole surface.

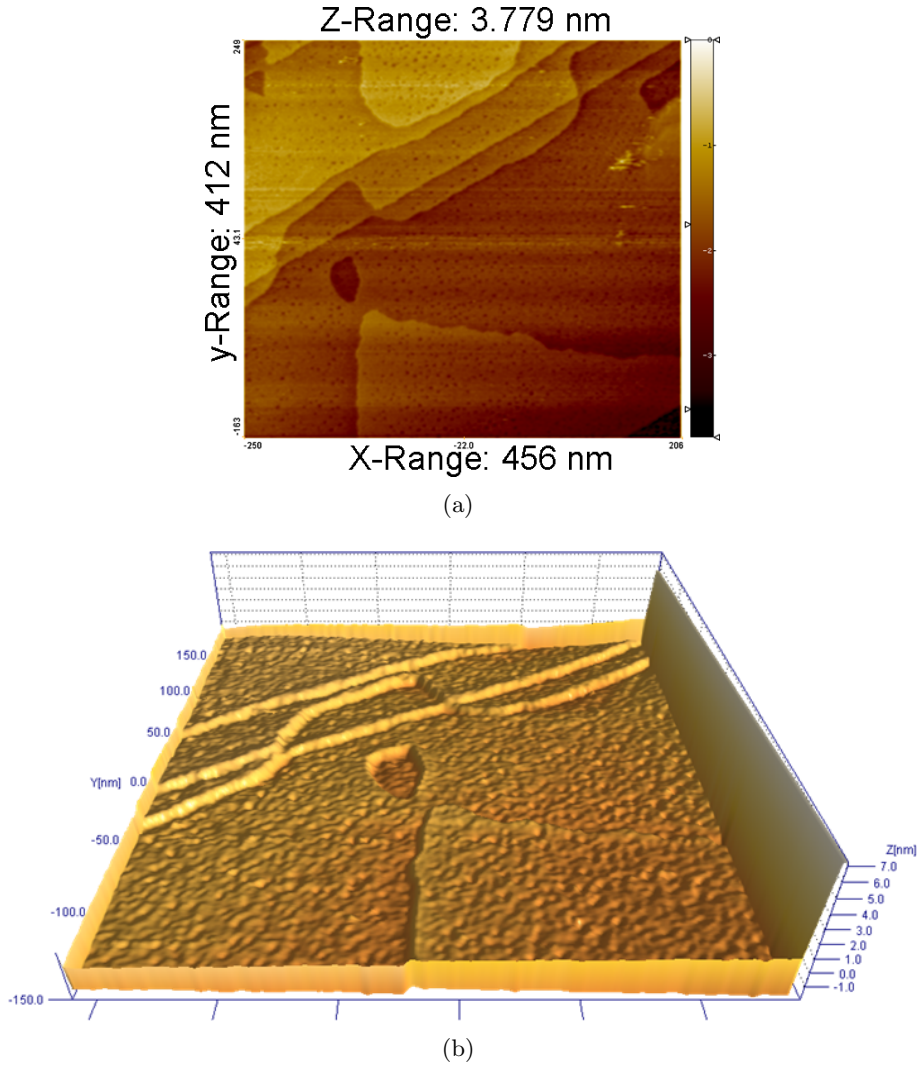

(a)

(b)

Figure 73: 412 nm×456 nm STM images of the Au-Naphthyl SAM on gold on mica (a) in 2D and (b) in 3D.

When looking at the etch pits in more detail (figure 74a) the depth is determined to be identical to one single-gold-atom step height. The etch pits are formed during the SAM adsorption as a corrosion process.[108] Unfortunately no molecular resolution was observed and no ordered SAM could be seen (compare figure 74b).

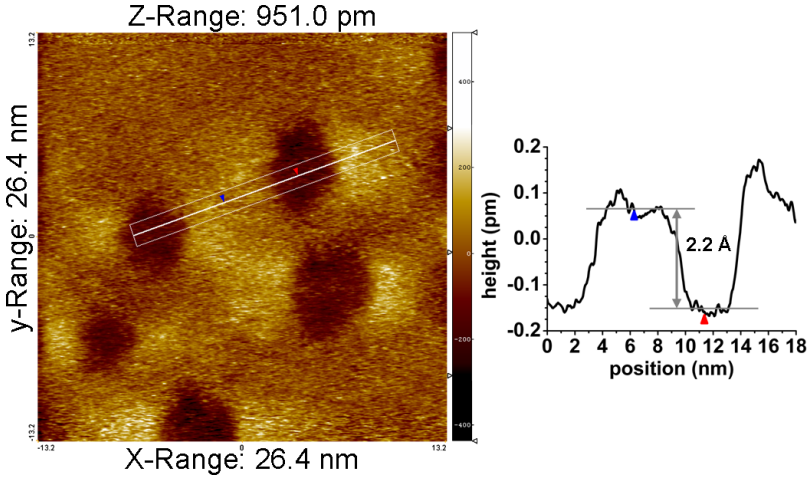

(a)

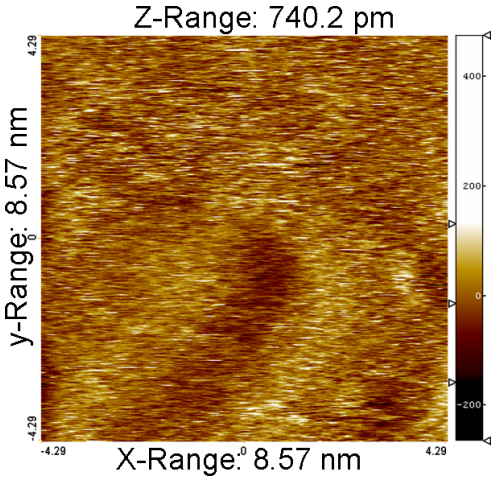

(b)

Figure 74: (a) 26.4 nm×26.4 nm with single atom step hight etch pits and (b) 8.57 nm×8.57 nm STM images of the Au-Naphthyl SAM on gold on mica. No ordering of the SAM is visible.

3.3.3 Conclusion

In this section is was shown, that the photo patterning can be extended from silicon oxide surfaces to gold surfaces. This enhances the application area of photo-reactive molecules, which can form thin films or SAMs.

For the patterning of gold surfaces, two new photoreactive thiol molecules with different spacer length, Au-PF and Au-PF-long, bearing both the photoreactive phenyl ester head group are well suited for the preparation of SAMs on gold substrates. The layers can be photochemically patterned by UV-illumination due to the photo-Fries rearrangement leading to the formation of reactive hydroxy ketones. By a subsequent and selective post-

modification reaction the polarity only of the illuminated regions of the patterned SAMs can be changed. Here, two different post-modification reactions are discussed. On the one hand, the post-reaction with perfluorobutyryl chloride leads to low-energy surfaces, which has been determined with contact angle measurements. On the other, hand a post modification using three separate preparations steps allows to immobilize fullerenes selectively on the surface. For all investigations XPS measurements have been used to determine the success of the SAM formation and the selective post-modification.

Afterwards, the formation of SAMs on a more defined substrate (gold on mica) has been characterized. For this investigation a novel thiol molecule has been synthesized. The 16-mercaptohexadecanoic-acid-naphth-1-yl-ester (Au-Naphthyl) is similar to the above used molecules (Si-PF and Au-PF), because it bears a naphthyl ester as functional head group. This group was supposed to follow the photo-Fries rearrangement. However, irradiation with UV-light with a wavelength of 254 nm did not change the IR-spectra and no formation of the corresponding hydroxy ketone via the photo-Fries arrangement was observed. Nevertheless, the formed SAMs have been characterized with AFM and STM. With AFM the underlying gold substrate is determined to have large Au(111) terraces. In STM the formation of etch pits is seen which arises from covalent bonded monolayers. No molecular resolution and with it long range order was observed in STM. LEED of the SAM is difficult due to beam damage so that non-observation of an ordered pattern does not necessarily mean the film was disordered.[109]

4 The Role of the Dielectric Interface in Organic Transistors: a Combined Device and Photoemission Study

After showing the possibility to change the surface of metals and metal oxides, the effect of surface modification in a thin film transistor is investigated.

4.1 Foreword

This work has been performed in cooperation with DI Philipp Stadler from the Linz Institute for Organic Solar Cells at the Johannes Kepler University Linz. Here we investigated each layer of two organic thin-film transistor (OTFT) with ultraviolet photoelectron spectroscopy (UPS) and X-ray photoelectron spectroscopy (XPS) to determine which interface is crucial for a better device performance. The two devices just differ by the organic divinyltetramethyldisiloxane-bis(benzocyclobutene) (BCB) interlayer. All devices and their characterization have been performed by Philipp Stadler (Linz), while the photoelectron spectroscopy (PES) measurements have been performed in Graz. The results have been published in reference 110(figure 75) and will be largely reproduced in this section.

Organic Electronics 11 (2010) 207–211

Contents lists available at ScienceDirect

Organic Electronics

journal homepage: www.elsevier.com/locate/orgel

The role of the dielectric interface in organic transistors: A combined device and photoemission study

Philipp Stadler [a,*], Anna M. Track [b], Mujeeb Ullah [c], Helmut Sitter [c], Gebhard J. Matt [c], Georg Koller [b], Thokchom B. Singh [a], Helmut Neugebauer [a], N. Serdar Sariciftci [a], Michael G. Ramsey [b]

[a] Linz Institute for Organic Solar Cells (LIOS) and Institute for Physical Chemistry, Johannes Kepler University Linz, Altenbergerstr. 69, 4040 Linz, Austria
[b] Institute for Physics, University of Graz, Universitätsplatz 3, 8010 Graz, Austria
[c] Institute of Semiconductor and Solid State Physics, Johannes Kepler University Linz, Altenbergerstr. 69, 4040 Linz, Austria

Figure 75: Copy of part of the first page of reference 110 including all coauthors and their affiliations.

4.2 Introduction

To design OTFTs with acceptable electrical transport properties interface engineering has become the key issue. The crucial part is the interface between the dielectric and the organic semiconductor.[111] Recent publications demonstrate well performing transistors with passivation layers of various organic materials like polymers and self-assembled monolayers (SAMs) grown on silicon dioxide and Al_2O_3.[112,113,114,115,116,117] Factors ranging from film

morphology,[118,119] control of the carrier density,[120] through to issues of electronic level alignment[121] could all be playing a role.

While device activity has concentrated on modifying the inorganic dielectric surface with SAMs or polymer dielectrics, little work has considered the possibility of charge rearrangements at the interfaces of such interlayer with the organic semiconductor. Theoretical modeling has suggested recently that improvements in transfer characteristics and rigid shifts of the threshold voltage can result from the introduction of permanent space charges or dipole layers at the interface between the dielectric interface and the organic semiconductor.[122]

An outstanding example is the introduction of a BCB interlayer between the inorganic dielectric (Al_2O_3, SiO_2) and the organic semiconductor. It has been reported to yield low operating voltages and high mobilities.[112,113,114] Apart from suggestions of BCB acting as a passivation layer due to the removal of hydroxyl groups from the semiconductor dielectric interface little is known of the function of the BCB interlayer. With UPS measurements the electronic structure of the interlayer can be measured for a better understanding of the electronic alignment with the organic semiconductor, but till now very few combined studies of device characteristic and photoemission investigations of the energy level alignment of device structures can be found in literature.[123] Moreover, to our knowledge there have been no reliable studies where a comparison of device structures with and without interlayer has been made.

In this section, we compare C_{60} as organic semiconductor on two dielectrics: Al_2O_3 and a BCB-Al_2O_3 bilayer. The later has been reported to have low operation voltage ($\sim$1 V) and high mobilities ($< 3\,cm^2V^{-1}s^{-1}$).[112,113] The difference in the transistors were used to explore the impact of teh BCB interlayer on the improved performance. Therefore, a systematic study of both (with and without BCB) insulator-C_{60} structures is made. The performance of the OTFTs are compared and one can show that the improvement of the device containing the BCB interlayer can be directly related to the differences in energy level alignment as measured by UPS. Because of a built-in potentials formed due to the BCB interlayer, the whole UPS spectrum is shifted to higher binding energies resulting in a 0.8 eV higher work function of C_{60}. A comparable shift in the same direction also was found in the C1s XPS signal of C_{60}.

4.3 Experimental Section

We use the same OTFT system as reported in reference 113 for a systematically comparison of the interface of C_{60} and BCB - Al_2O_3 to the interface of C_{60} and Al_2O_3 alone to understand its role in the improved performance. To allow meaningful comparison we fabricated two bottom-gate / top contact transistors, such that both the Al_2O_3 alone and

the bilayer Al_2O_3 - BCB exhibit the same geometric capacitance of $55\,\mathrm{nFcm^{-2}}$ (compare figure 76). This geometric capacitance of the dielectric layers provide transistors operating at gate voltages in the range of 1 V and a mobility of $1\,\mathrm{cm^2V^{-1}s^{-1}}$. The same metal-insulator-semiconductor (MIS) structures are studied by UPS with the samples prepared in a controlled way using the same batch at once and a blind sample as a reference for the surface characterization.

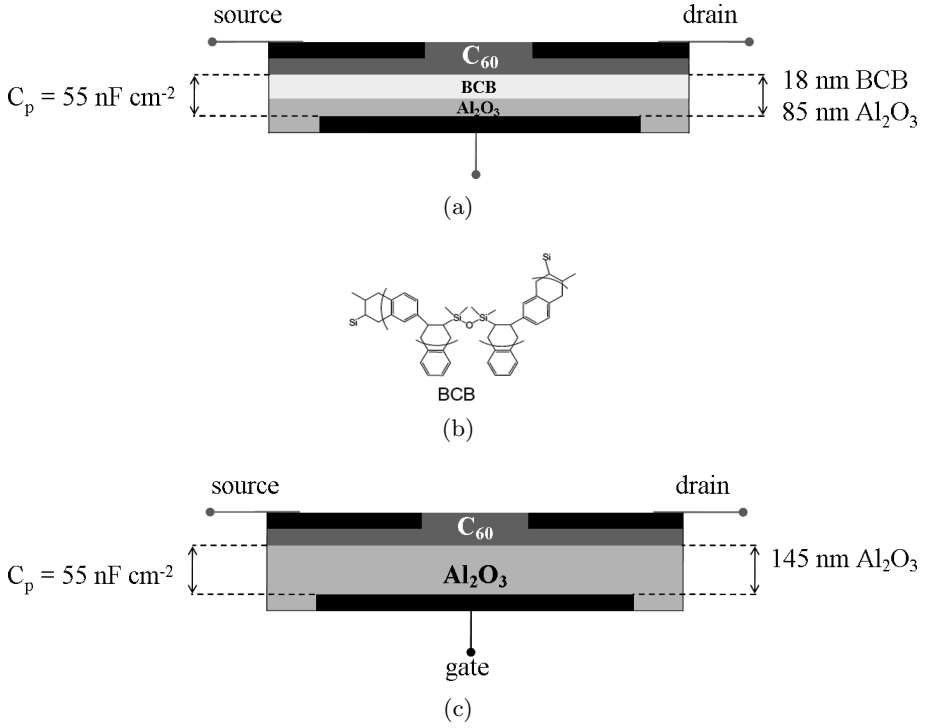

Figure 76: Schematic of the OTFT structures studied with (a) and without (c) a BCB layer on Al_2O_3. Both structures exhibit the same geometric capacitance of $55\,\mathrm{nFcm^{-2}}$. The chemical structure of BCB is shown in (b).(Largely identical to reference 110.)

Sample Fabrication for OTFT Characterization On a glass substrate 200 nm of aluminum are deposited at a rate of $10\,\mathrm{s^{-1}}$. For the gate insulator a 145 nm and an 85 nm film of Al_2O_3 respectively is electrochemically grown on the aluminum.[124,125] The generated oxide was then washed with distilled water at 80°C in the ultra sonic bath and dried at 200°C. For the BCB layer a 1 w% precursor solution[A] in mesitylene was spun onto the 85 nm thick Al_2O_3 and afterwards cross linked by annealing at 150°. Both structures (Al_2O_3 layer and Al_2O_3 - BCB bilayer) show similar surface roughness of 1.5 nm RMS and the same measured geometric capacitance (C_p) of $55\,\mathrm{nFcm^{-2}}$. The thicknesses of the aluminum oxide were measured by capacitance measurements (Al - Al_2O_3-Al) and checked by cross section

[A] Purchased from Aldrich

scanning electron microscopy. As semiconductor a 300 nm C_{60}[B] film was deposited in high vacuum using the hot wall epitaxy technique (substrate: 140°C, growth rate:0.5 s^{-1} [126]). With atomic force microscopy (AFM) the morphology of C_{60} was determied to by simial on both substrates. As source-drain contacts LiF/Aluminium (0.6 nm and 50 nm) [127] was used by evaporationg through a 70 μm shadow mask for the channel length and a channel width (W) of 2 mm. The OTFTs were characterized using Agilent E5273A 2-channel-source unit.

Sample Fabrication for UPS and XPS Characterization For the UPS measurements, the metal-insulator-semiconductor structures were prepared in the following way: A 5 nm thin layer of Al_2O_3 was electrochemically grown on aluminum and then treated as mentioned in section 4.3. For the BCB layer, a 1% precursor solution was directly spun onto aluminum oxide and cross linked at 200°C. In a further step a 2 nm (3-4 molecule layers)[C] C_{60} was deposited by thermal evaporation at a rate of 1 As^{-1} at a substrate temperature of 78 K in order to guarantee homogenous covering and avoiding islnd grouwth. The samples were then characterised by UPS using a HeI (21.2 eV) lampe and by XPS using $Mg - K_\alpha$ (1253.6 eV) irradiation in ultra high vacuum using a Specs PHIOBOS hemispherical energy analyser. The valance band spectra were recorded in both normal and 45° off normal emission angles and the work functions were determined from the secondary electron cut off in normal emission with a bias of 10 V. All XPS spectra are taken 45° off normal emission to be more surface sensitive and all spectra are calibtrated to the Al2p(Al_2O_3-peak having the binding energy of 75.6 eV.

4.4 Results and Discussion

4.4.1 OTFT Characterization

The output characteristics and the transfer characteristics taken in the linear regime ($U_{gate} > U_{drain}$) of the two device with and without BCB are compared in figure 77.[D]

[B] Purchased from Merck and purified in a re-sublimation process

[C] The layerthickness was determined by a quartz microbalance calibrated for C_{60}

[D] Data presented here are recorded when the gate voltage U_{gate} as well as the drain voltage U_{drain} are applied in ascending and descending mode with 1 s integration time per step.

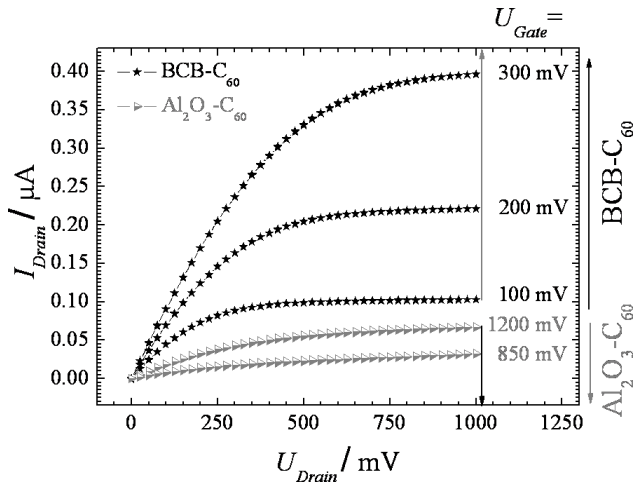

(a)

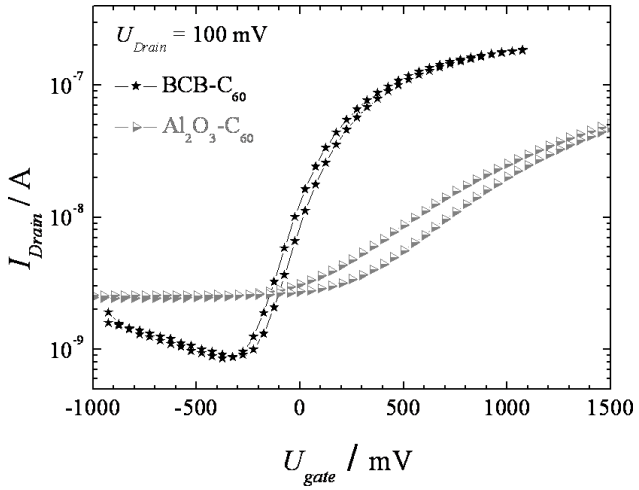

(b)

Figure 77: Output characteristics (a) and transfer characteristics (b) in the linear regime ($U_{drain} < U_{gate} - U_{th}$) of both OTFTs with (dark) and without (light) BCB layer on Al_2O_3.(Identical to reference 110.)

Both figures (77a and77b) reflect a same trend of both devices, however, the transistor with the BCB interlayer performs significantly better in all respects. It has

- a higher source-drain current I_{ds},
- a higher depletion and accumulation amplitude,
- a sharper onset
- a higher on/off ratio and
- a lower hysteresis.

The observed hysteresis in the transfer curve is reduced for the BCB - C_{60} and the charge charier mobility μ is in the range of $1\,cm^2V^{-1}s^{-1}$, which is in good agreement with earlier results.[112,128,129]

The most remarkable difference of the two systems (Al_2O_3 and Al_2O_3-BCB) is the reproducible change in the threshold voltage U_{th}. To extract the exact threshold voltage value in the linear regime, the transconductance change or second derivative (SD) method is selected.[1E] The resulting second derivative of the transfer characteristics d^2I/dU_{gate}^2 is presented in figure 78a and shows two maxima -one for each device. The device containing BCB has a distinct and sharp peak, whereas for the device without BCB the peak is broader and more ill-defined. The threshold voltage U_{th} shifts from +725 mV in the transistor with the Al_2O_3 - C_{60} interface system to -75 mV for the transistor containing the Al_2O_3 - BCB - C_{60} interface system. The device with the BCB interlayer has a 0.8 V lower U_{th}.

[E] This method estimates U_{th} as the gate voltage at which the derivative of the transconductance (dI/dU_{gate}) is maximal.[29] It works around the problem of series resistances and is shown to give reliable values for organic (n-channel) systems.[24]

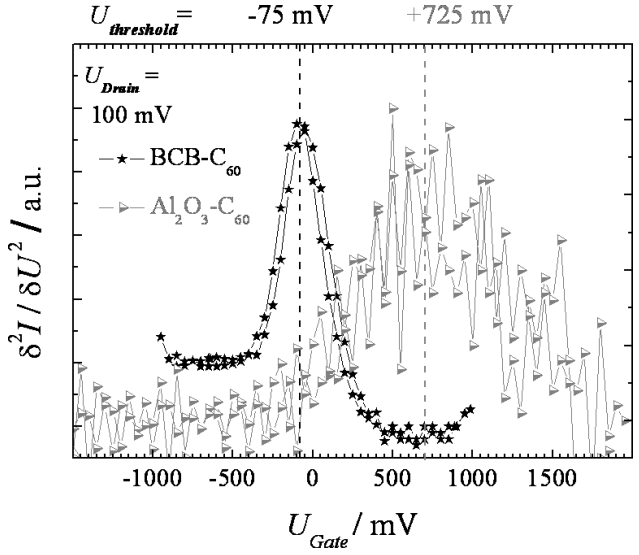

(a)

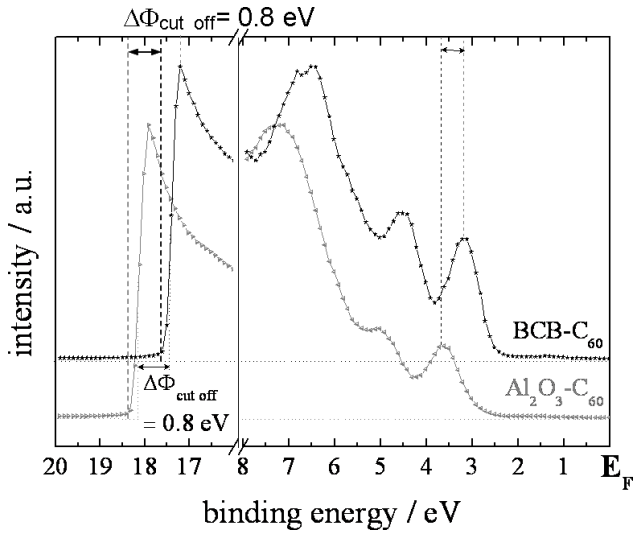

(b)

Figure 78: (a) Shift of threshold voltage ΔU_{th} as seen in the second derivative of the transfer characteristics in OTFTs with (dark) and without (light) BCB layer. (b) The UV photoemission spectrum of C_{60} on Al_2O_3 (light) and on BCB (dark) referenced to the Fermi energy. The shift in the HOMO and in the secondary electron cut-off $\Delta\Phi$ is indicated. (Identical to reference 110.)

4.4.2 Photoemission Studies

Photoemission measurements of ex-situ prepared films on dielectric substrates are particularly challenging as contamination and charging effects can be misleading and care has to be taken. In figure 78b the UPS spectra of Al/Al_2O_3/BCB/C_{60} and Al/Al_2O_3/C_{60} thin

film structures are shown referenced to the Fermi energy obtained from a metal substrate. In both cases, the valence band fingerprint of the uppermost C_{60} layer is well defined with a quality approaching that of in-situ ultrahigh vacuum (UHV) prepared C_{60} films.[21] This, combined with the fact that the ionisation potential of C_{60} in both cases are in agreement with literature values[21], shows that contamination and charging effects are minor.

The comparison of figure 78a and 78b illustrates the link between the device thresholds U_{th} and the electronic level alignment observed in the UPS spectra with BCB and without BCB. Clearly, introducing the BCB interlayer leads to a rigid shift of the entire photo emission spectrum to lower binding energy relative to the Fermi level. The shift of the HOMO-peak is measured to be 0.6 eV whereas the shift in the secondary cut-off,i. e., the change in the work function, is 0.8 eV. Thus the change in the measured C_{60} electronic level alignment induced by the BCB layer is the same as the lowered threshold voltage measured in the device with BCB.

The rigid shift is also found in the core level of C_{60} with and without BCB shown in figure 79. Binding Energy of C_{60} without BCB layer underneath in the C1s signal has a maximum 285.6 eV whereas for C_{60}on top of theBCB interlayer it is 285.3 eV. The resulting shift is in the same direction compared to the UPS spectra, but the magnitude is less (0.3 eV). The deviation can be explained via the surface sensitivity difference of the two methods UPS and XPS. The difference is determined by the variation of the mean free path length shown in figure 3. UPS is far more surface sensitive compared to the C1s XPS making the offset in the valence band a more precise measure of the differences in build-in-potential. The core level of the top layer should have the same shift, however, the C1s signal is not purely from the surface and includes emission from the BCB. This can be seen in the height difference of the two peaks.

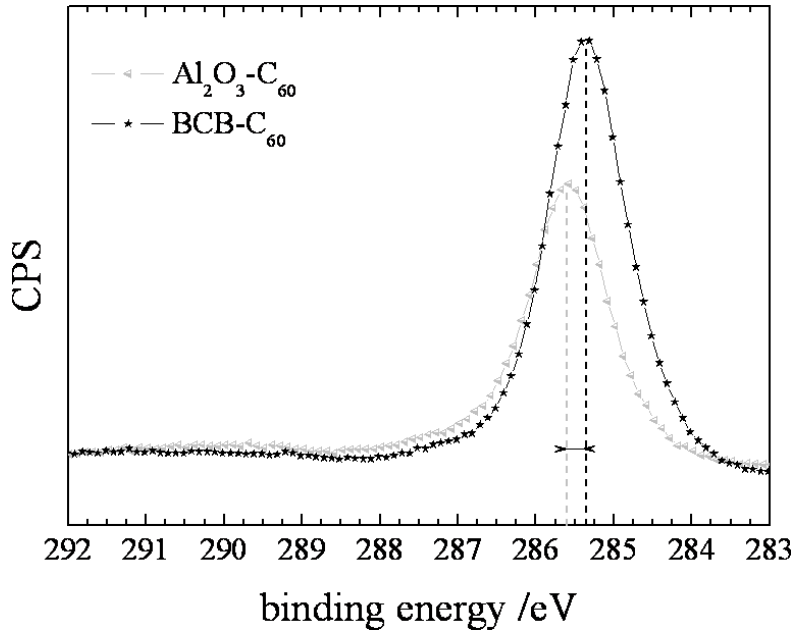

Figure 79: XPS spectra of the C1s region of C_{60} on BCB (dark) and on Al_2O_3 (light) interlayer. The shift is in then same direction as in the UPS spectra.

For sake of completeness, the survey spectra of $Al/Al_2O_3/BCB$, of $Al/Al_2O_3/C_{60}$ and of $Al/Al_2O_3/BCB/C_{60}$ are shown in figure 80. In all spectra, aluminum and aluminum oxide were found and, due to the BCB, silicon was detected. No impurities, which can implemented in the sample during careless preparation, e. g. Sodium, have been found.

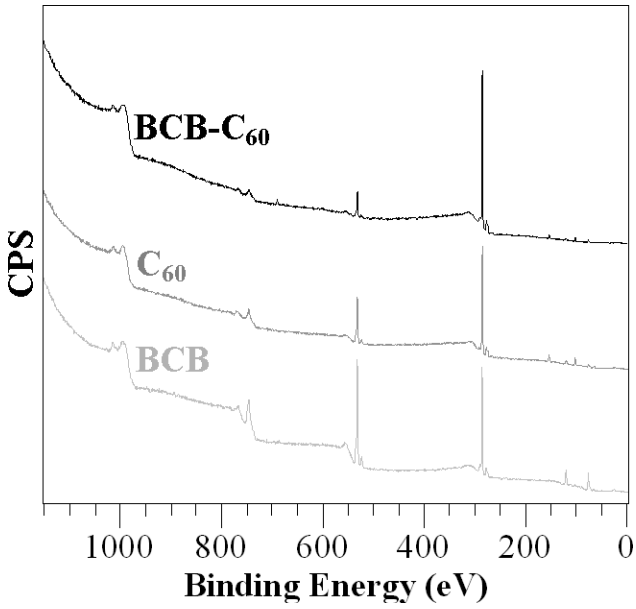

Figure 80: XPS survey spectra of $Al/Al_2O_3/BCB$ (light gray), of $Al/Al_2O_3/C_{60}$ (dark gray) and of $Al/Al_2O_3/BCB/C_{60}$ (black).

To determine where and why the BCB has lowered the threshold voltage, UPS spectra were measured at each layer in the device. This means that after each layer deposition the sample was investigated. The spectra are shown in figure 81.

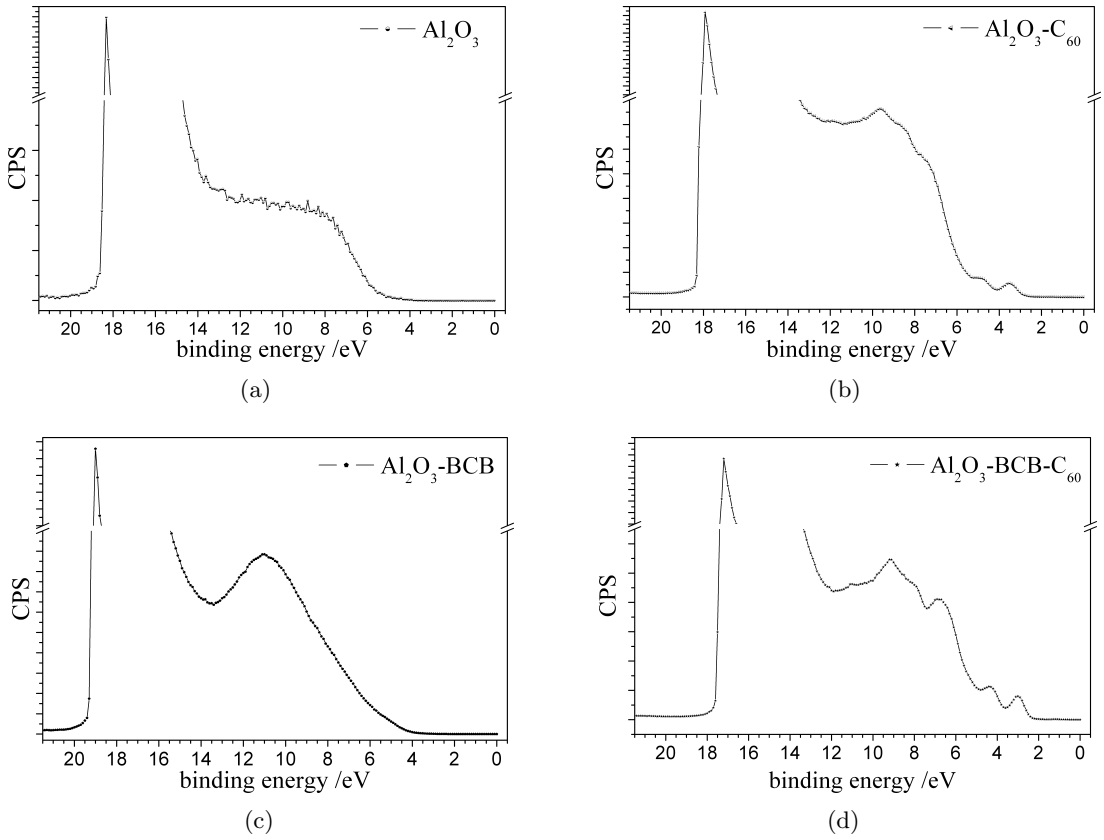

Figure 81: UPS spectra showing the valence region and the secondary electron cut off (a) bare aluminum oxide, (b) of C_{60} on aluminum oxide, (c) of BCB on aluminum oxide and (d) C_{60} on BCB on aluminum oxide.

The results extracted from UPS measurements are summarized in figure 82, where the energy relations of the studied MIS systems for all interfaces with the work function measured for each layer are indicated. For the device without BCB (figure 82b), we measured a large work function drop to 2.7 eV on oxidation of the aluminum surface followed by a very small increase of the work function to 2.9 eV when the C_{60} film is grown on the oxide. Similar changes have been observed in in-situ model studies.[130,131] In contrast, what is seen in figure 82a, is that on applying BCB to the Al_2O_3 surface the work function drops further to 2 eV. Then, when C_{60} is grown on the BCB, surface there is a large increase of the work function to 3.7 eV. At both BCB interfaces (Al_2O_3 and C_{60}) significant dipoles are formed and clearly BCB cannot be considered simply a passive spacer layer. The large work function increase at the BCB - C_{60} interface is the prime determinant of the improved

device performance.

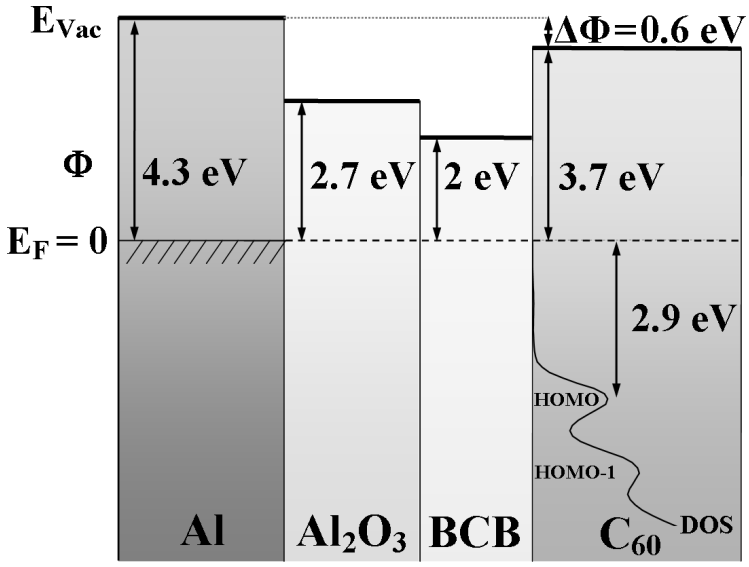

(a)

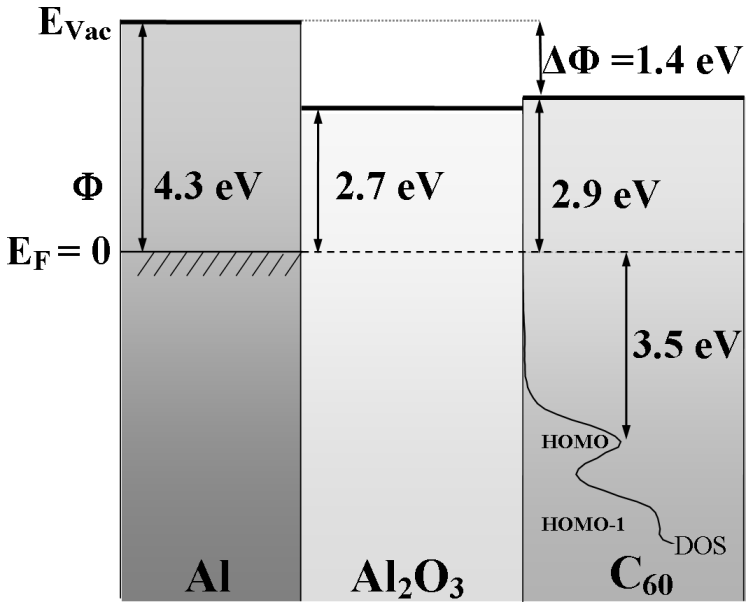

(b)

Figure 82: Measured energy level diagrams of the two metal-insulator-semiconductor (MIS) structures studied with (a) and without (b) BCB between C_{60} and Al_2O_3. The Fermi level is the reference level and the work function at each layer are indicated. Note the large work function change at the BCB - C_{60} interface (b) and that the difference in the final work function between the two structures is 0.8 eV. (Largely identical to reference 110.)

The result suggests that a significant interface dipole is formed at the BCB - C_{60} interface.

This is surprising as usually organic-organic interfaces display vacuum level alignment with no significant interface dipoles. However in recent model studies[132] significant interface dipoles at organic-organic interfaces have been observed and were attributed to integer charge transfer (ICT) that is the formation of polaronic charge transfer states. Indeed the observed work function increase for C_{60} on P3HT has been attributed to this effect.[132]

The C_{60} level alignments on the two gate dielectrics measured in the UPS are consistent with the two threshold voltages measured for the OTFTs. Gate voltages of -0.075 V (BCB - C_{60}) and +0.725 V (Al_2O_3 - C_{60}), would shift the HOMO level in both cases to around 2.8 eV below the Fermi level of the source. This is schematically illustrated in figure 83, where the lowest unoccupied molecular orbital (LUMO) (given by the electron affinity) relative to the highest occupied molecular orbital (HOMO) is taken from reference 132,133. As C_{60} is a n-type semiconductor it is the LUMO relative to the Fermi energy of the source that is critical. Given a C_{60} affinity level of $\sim$ 2.5 eV above the HOMO[132,133] one sees that the device threshold is obtained when the electron affinity is positioned slightly below the Fermi level of the source. This also expresses well that one can view the work-function changes as if they were acting as an inbuilt potential.

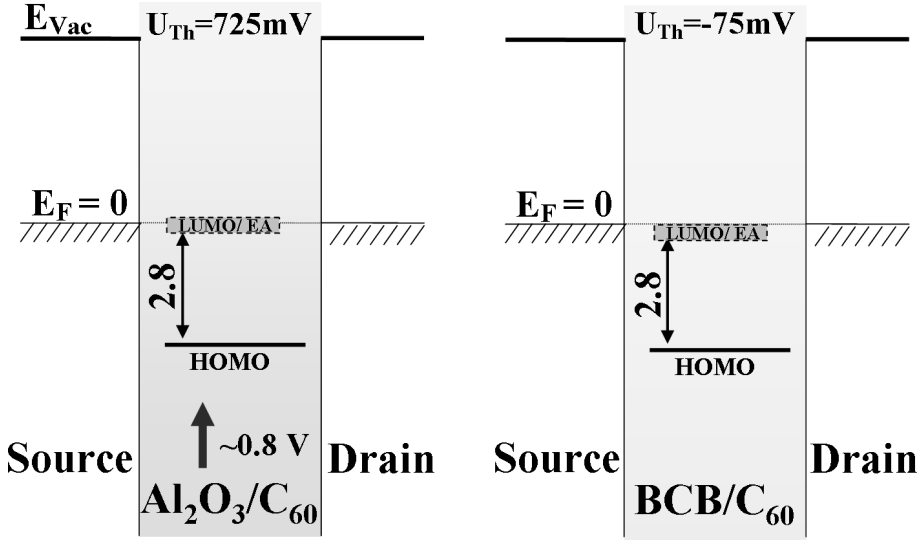

Figure 83: Energy level alignment at the threshold voltage for the device without BCB (left) and for the device with BCB (right). The threshold occurs when the electron affinity level is set to the Fermi energy of the source. In the case **without** BCB this is done by applying a gate voltage of $\tilde{0}.8$ V (left) and in the case **with** BCB this has been done by the interface dipole at the BCB/C_{60} interface (right).

4.5 Conclusions

To conclude we studied two different interfaces between an organic semiconductor (C_{60}) and oxide (Al_2O_3) and an organic polymer (BCB) respectively. At the BCB interlayer dipoles

are formed, which lower the threshold voltage and improve the transistor performance. The 0.8 V difference in the threshold voltage of the two device structures has been shown to be directly related to the 0.8 eV work function differences and is consistent with the band offset of C_{60}in each device. Photoemission investigations at all interfaces clearly indicate that the dipole formed at the BCB - C_{60}interface is the prime determinant for the improved device threshold. The magnitude and mechanism of this shift suggests detailed studies into tailoring organic-organic interfaces on the gate dielectric could be very promising for optimizing device performance.

5 Theoretical Calculations to Obtain a Detailed Insight into Self-Assembly on Metals

After evaluating the surface modification experimentally with X-ray photoelectron spectroscopy (XPS) and after showing the impact of surface modification in a device, here, the modification of surfaces was investigated theoretically. This allows more detailed insight in the change of the surface due to organic molecules.

5.1 Fundamental Investigations of Binding Preferences of Thiolates and Selenolates on Gold

5.1.1 Foreword

In this section the fundamentals for section 5.2, concerning the bonding of self-assembled monolayers (SAMs) to the metal surface, are shown. This work has been performed in the beginning of my thesis. Therefore, a lot of help of my collages Dr. Georg Heimel, Dr. Lorenz Romaner, Dr. Gerold Rangger and Oliver Hofmann needs to be acknowledged.

5.1.2 Introduction

The self-assembly of organic molecules on metal surfaces attracted a lot of interest, because SAMs allow the change of the surface over a wide range - from more reactive to more inert.[64,134] The formation and structure of SAMs on metal surfaces has been a subject of intensive research. As a prototypical system thiolate-SAMs on Au(111) are often studied (see e. g. reference 65) to understand their exact bonding behavior.[135,136,137,138]

In this section, general bonding preferences of thiolates and selenolates are investigated and compared. These calculations serve as basis for section 5.2. For the sake of simplicity, the smallest possible "backbone" - a methyl group - is used to investigated the specific docking position on the surface depending on the different docking atoms. Then, the difference in the lateral corrugation of the binding energy hypersurface of the two docking groups is studied. Since we are interested in aromatic molecules due to their enhanced electronic properties, we also added aromatic groups (phenyl, anthrcene-2-yl) as backbone for studying the binding energy. All these parameters give a more detailed picture of the bonding of the SAM to the surface and can be used to predict the behavior of more complex SAM structures.

5.1.3 Methodology

We performed slab-type density functional theory (DFT) band structure calculations using the VASP-code[139,140,141,142] as described elsewhere, e. .g. in references 57,143 or in section

5.2.3.

Two different unit cells are are discussed in this section.

The systems methylselenolate (CH_3Se), methylthiolate (CH_3S), phenylselenolate (PhSe) and phenylthiolate (PhS) on Au(111) have been calculated in a (2×2) unit cell. Here, one molecule per unit cell is adsorbed on a slab of four gold layers and a $4 \times 4 \times 1$ Monkhorst-Pack[50] k-point grid was used (see figure 84).

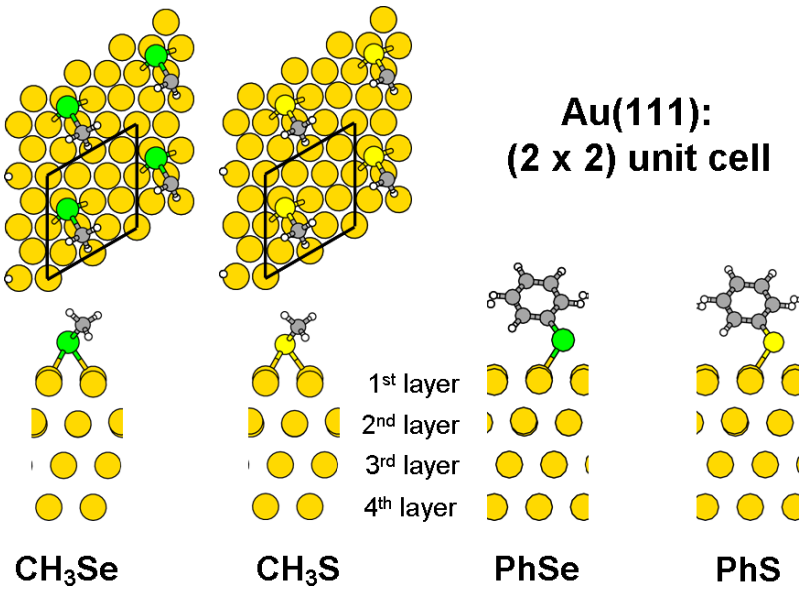

Figure 84: The *bridge* positions, which is slightly shifted towards *fcc-hollow* of the structures of methylselenolat (CH_3Se), methylthiolat (CH_3S), phenylselenolat (PhSe) and phenylthiolat (PhS) on a (2×2) unit cell on Au(111) are shown (top and side views). The numbering of the gold layers is indicated.

For the anthracene-2-selenolate (AntSe) and the anthracene-2-thiolate (AntS) on Au(111) a $(\sqrt{3}\times4)$rect unit cell with five gold layers(see figure 85) and two molecules per unit cell is used (compare section 5.2). This unit cell is the experimentally found unit cell for AntSe.[52] To calculate AntS, the same unit cell is used to allow a comparison between those systems, although for AntS another (more complex) unit cell was determined experimentally.[144]

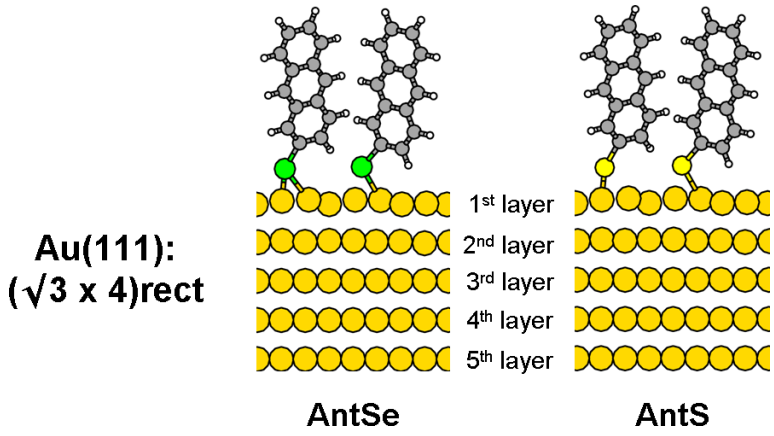

Figure 85: The structures of anthracene-2-selenolate (AntSe) and anthracene-2-thiolate (AntS) on Au(111) in a ($\sqrt{3}$×4)rect unit cell is shown (side views, molecular arrangement **A**). The numbering of the gold layers is indicated. Form more detail compare figure 91.

The investigated systems are denoted by following naming convention: metal|docking group|backbone. The 'docking group|backbone' can be collected as 'SAM'. When investigating the binding energy, the position of the breaking is denoted with a '–', e. g., Au|Se–CH3.

Docking Site To investigate the docking site of CH_3Se and CH_3S on Au(111) in all calculations the third and fourth gold layer were fixed in their bulk position[A], and the second gold layer was allowed to relax without any restriction. The first gold layer also was fixed in x- and y-position and was optimized just in z-direction. This complex situation was important to allow comparison of the energy of all calculated docking sites, because the system with the *on-top* docking site falls apart[B] during the optimization without the restrictions in the first gold layer.

A further limitation was introduced for the docking atoms (S or Se). To test the difference between the high symmetry docking sites (*hcp-hollow*, *fcc-hollow*, *bridge* and *on-top*) and the real docking sites (*hcp-hollow* shifted towards *bridge*, *bridge* shifted towards *fcc-hollow* and *fcc-hollow* shifted towards *bridge*) the position of the sulfur atoms and the selene atoms were either fixed in x- and y-direction or freely optimized, respectivly.

The influence of the backbone (methyl/phenyl) and the impact of the docking group (selenolate/thiolate) on the adsorption energy (E_{ads}) is studied, depending on the different docking sites. For that reason the total energy of the following units[C] has to be calculated:

- the combined system (SAM on metal) at the different docking positions: $E_{SAM|Au}$,

[A] This two layers represent the bulk gold.
[B] The bonds between the docking atom and the gold surface breaks.
[C] The same unit cell was used for all different calcualtions.

- the metal alone (slab) with all atoms in the optimal bulk position, which represents the metal surface before bonding of the SAM: E_{Au} ,
- the not bonded optimized SAM molecule, which is saturated at the docking atom $E_{H|SAM}$
  and
- one H_2 molecule (in the same unit cell): E_{H_2} .

The adsorption energy can then be calculated by

$$E_{ads} = E_{Au|SAM} - \left[E_{Au} + \left(E_{H|SAM} - \frac{E_{H_2}}{2} \right) \right] . \tag{48}$$

Note, that the obtained energy for H_2 has to divided by two, if only one molecule per unit cell is adsorbed on the metal, which is the case in the (2×2) unit cell.

Lateral Corrugation The lateral corrugation of the CH_3Se- and CH_3S-SAM on Au(111) was investigated by displacing the molecules from the exact *bridge* position along the ⟨110⟩ and the ⟨112⟩ direction (indicated in figure 86) in steps of 0.02 Å (10 steps).

For that study, the methyl group was positioned exactly above the docking atom and whole adsorbate was allowed to relax only in its z- coordinates.[D] All Gold atoms were fixed in their bulk positions.

Binding Energy The binding energy E_{bind} of the SAM to the gold, as well as, the binding energy backbone to the docking group is calculated for all systems (CH_3Se, CH_3S, PhSe, PhS, AntSe and AntS) on Au(111) in their lowest energy conformation in terms of docking site and molecular packing arrangement [13]. The position of the breaking of the bond is denoted with a '–', e. g., Au|Se–Ph or Au–Se|Ph .

For that reason, following subdivisions have to be calculated for each system:

- the slab alone: E_{Au} ,
- the slab with the docking group (Se or S): e. g. $E_{Au|Se}$,
- the whole molecule (backbone and docking group): e. g. $E_{Se|Ph}$,
- the molecular backbone alone e. g. E_{Ph}
  and
- the combined system (SAM on metal) at the different docking positions: e. g. $E_{Au|Se|Ph}$.

[D] The positions of the hydrogen atoms was optimized before.

Note, for these calculations no further optimization of any part has been done.

As an examples, the equation to calculate the binding energy of the bond between gold and PhSe (equation 49) and the of the bond between phenyl backbone and the selenolate docking group (equation 50) is shown here:

$$E_{bind}(Au - Se|Ph) = \big(E_{Au} + E_{Se|Ph}\big) - E_{Au|Se|Ph} \tag{49}$$

and

$$E_{bind}(Au|Se - Ph) = \big(E_{Au|Se} + E_{Ph}\big) - E_{Au|Se|Ph}. \tag{50}$$

For closed shell system the calculations have been performed in a non spin polarized (ISPIN=1) manner, whereas for all open shell systems spin polarized calculations were performed.

5.1.4 Results and Discussion

Docking Site The first point of interest is the different bonding of thiolates and selenolates in terms of docking site. Therefore, the most simple organic backbone, the methyl backbone, was chosen to get insight into the energies of those two docking groups. From a chemical point of view they should react the same way, since sulfur and selenium are positioned in the same group of the periodic table and have similar electro negativities (Pauling's), of 2.58 and 2.55, respectively.

A schematic for the docking positions for *hcp-hollow*, *bridge*, *fcc-holow* and *ontop* is shown in figure 86.

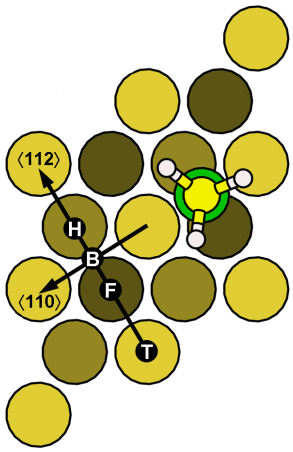

Figure 86: Schematic of a (2×2) unit cell of Au(111). The gold atoms from the first (uppermost) layer are yellow and become darker for the second and third layer. The main four docking positions are indicated: **T** (*ontop*), **F** (*fcc-hollow*), **B** (*bridge*) and **H** (*hcp-hollow*).

Besides the 'exact' docking positions indicated in figure 86, the 'real' docking positions have been calculated by allowing the adsorbate to shift to finding its minimum energy (see section 5.1.3: freely optimized). The obtained 'real' docking sites are shown in figure 87, where

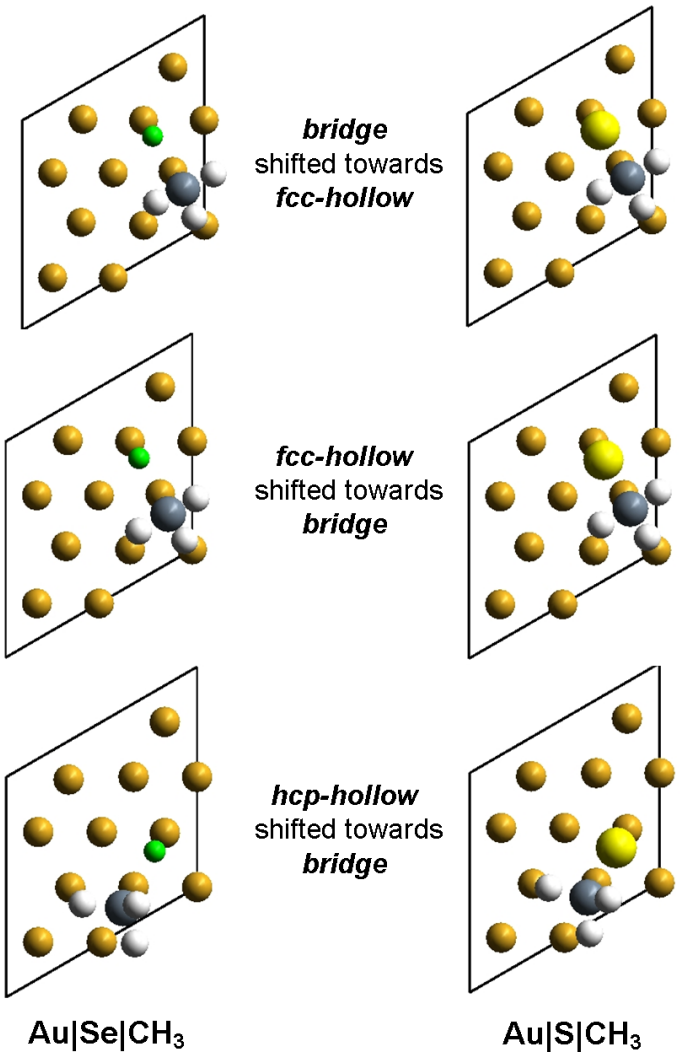

Figure 87: Resulting 'real' docking sites, if the adsorbate is allowed to move freely in all directions for methylselenolate (left panel) and methylthiolate (right panel) on Au(111). Note, that no bonds are shown. (Gold:Au, green: Se, yellow:S, gray:C,white: H)

All calculated total energies obtained for the different docking sites of CH_3Se and CH_3S on Au(111) are given in table 8 and the resulting adsorption energies (E_{ads}) are shown in figure 88.[E]

[E]The calculated values for E_{Au} is -48.745373 eV, for E_{H_2} is -6.7292638 eV , for $E_{H|Se|CH_3}$ is -26.590599 eV, for $E_{H|S|CH_3}$ is -27.576935 eV.

Table 8: Total Energies ($E_{Au|SAM}$ (in eV) of all calculated systems for different docking positions.

	Au|Se|CH_3	Au|S|CH_3
hcp-hollow	-72.188686	-72.725423
hcp-hollow → *bridge*	-72.351116	-72.924777
bridge	-72.311467	-72.894387
bridge → *fcc-hollow*	-72.354843	-72.938813
fcc-hollow	-72.221340	-72.763293
fcc-hollow → *bridge*	-72.354371	-72.938573
ontop	-72.043814	-72.648066

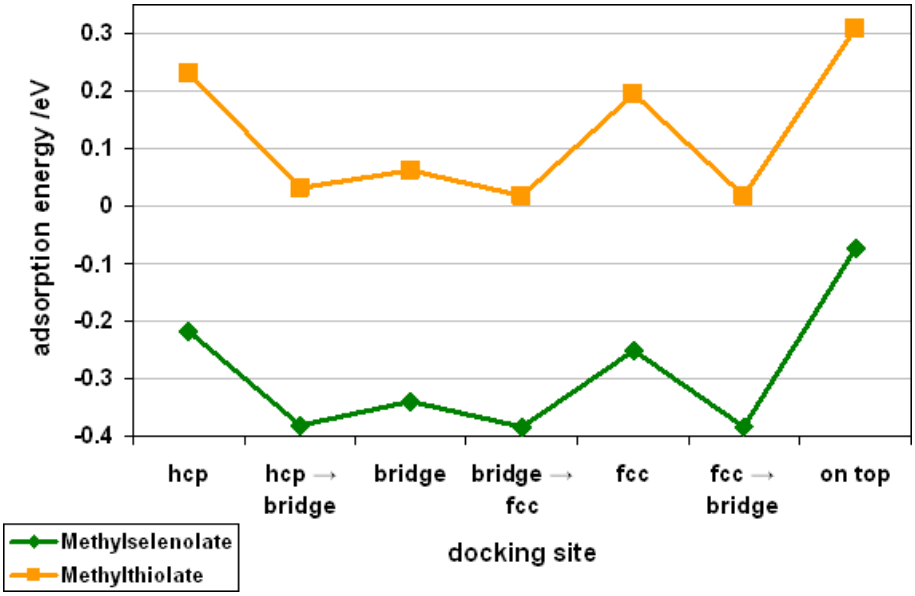

Figure 88: Adsorption energies for methylselenolate (green squares) and methylthiolate (yellow diamonds) on Au(111) for different docking sites. The abbreviation hcp and fcc are used for the docking positions *hcp-hollow* and *fcc-hollow*, respectively.

E_{ads} indicates the energy balance of replacing a covalent bond (here $Au - Se|CH_3$ for $H - Se|CH_3$ and $Au - S|CH_3$ for $H - S|CH_3$). A positive value indicates that the adsorption process is energetically unfavorable whereas a negative value of E_{ads} are dedicated to a favorable adsorption process. In our calculations we were not able to include van der Waals interactions, which would lead to an energetically (more) favorable process. Hence we can assume that our calculations underestimates the adsorption of the SAM to the surface leading to positive values for the SAMs having a sulfur as docking group.

One can see, that the docking position with the lowest energy is the *bridge* shifted

towards *fcc-hollow* site, independent the docking groups. Starting from the *bridge* or *fcc-hollow* site leads to the exact same structure (see figure 87) and the same total energy (compare table 8). This results for are in good agreement with literature[145,137,136,146,57], in which the docking position between *bridge* and *fcc-hollow* was calculated to be always lowest in energy for methylthiolate and phenylthiolate on Au(111).

The difference in the adsorption energy between Au|S|CH_3 and Au|Se|CH_3 for all calculated docking positions is 0.5±0.05 eV indicating that the selenolate are stronger bonded to the surface than the thiolate. In literature the relative stability of the Au-Se and the Au-S bond is not clear. Both, a higher[147,148,149,150] and a lower[151,152] stability for the Se-Au bond was found.

Lateral Corrugation The dependence of the lateral corrugation of the binding energy hypersurface is investigated in this section. In literature the difference of the lateral corrugation of the binding energy hypersurface of selenolates and thiolates is related to the difference in their ability to order. Selenolates exhibit better long range ordering.[152,153,150] For that reason, we performed calculations in which the adsorbate (CH_3Se or CH_3S) is moved away from the *bridge* position in small steps. The movement has been performed along the ⟨112⟩ and the ⟨110⟩ direction on the surface (indicated in figure 86).

To exclude any interferences due to differently relaxed metal layers, all gold atoms were fixed in their bulk position. Furthermore, to avoid steric influence of the methyl group, we decided to arrange the methyl group exactly above the docking group, allowing the whole adsorbate to relax just in z-direction.

In figure 89 the change of the total energy, which is proportional lateral corrugation of the binding energy hypersurface, and the change in the height of the docking group due to the different displacement are shown.

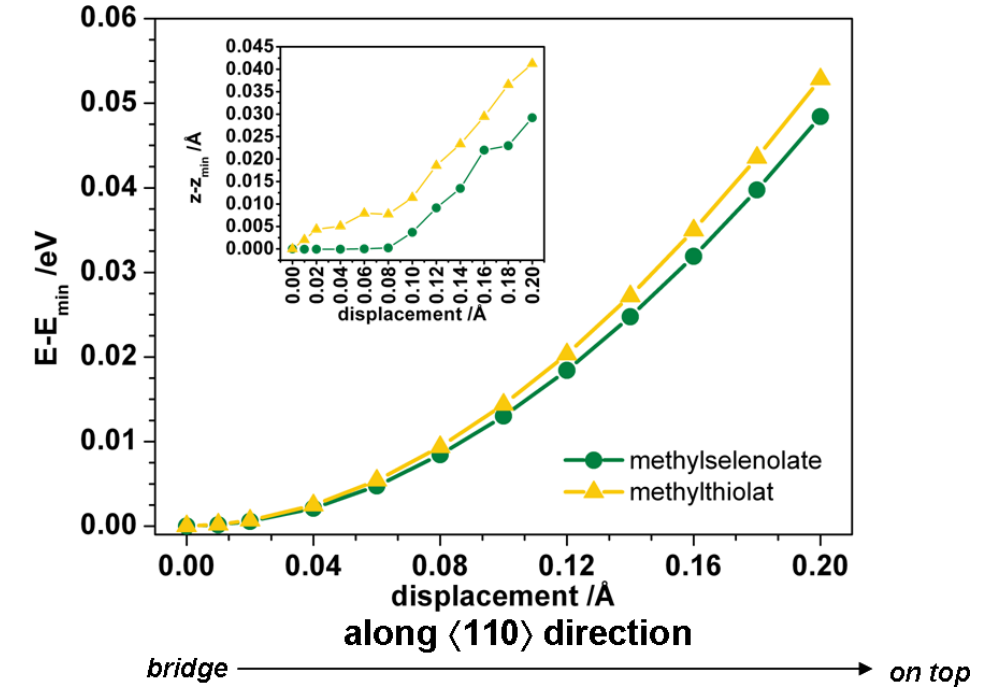

(a)

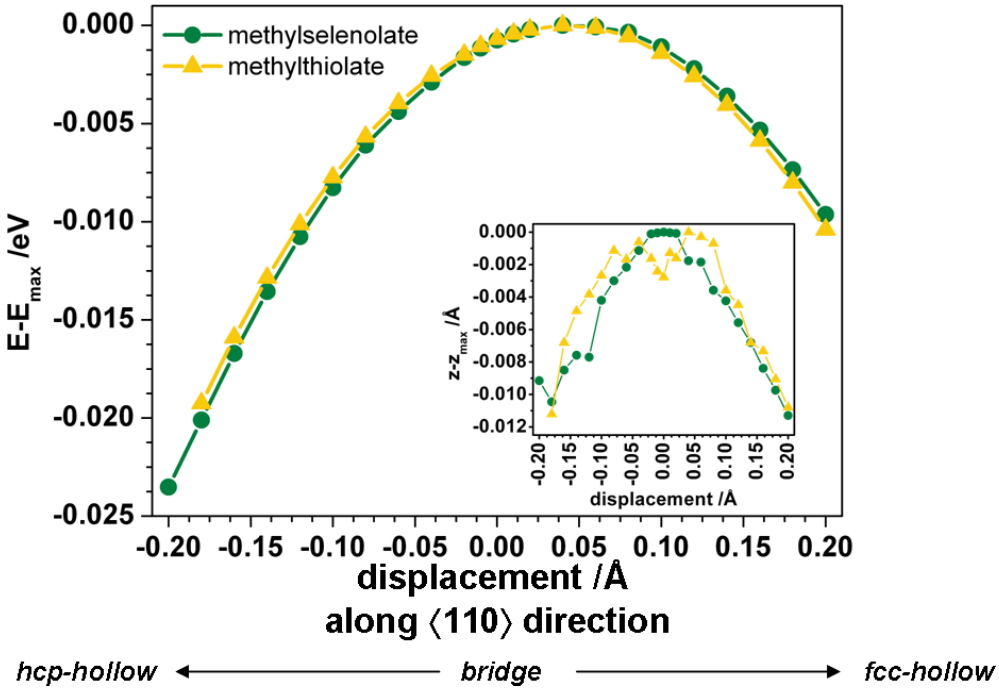

(b)

Figure 89: Differences in the total energies (E-E$_{min}$ or E-E$_{max}$) as a function of the displacement from the *bridge* position along (a) the ⟨110⟩ direction and (b) the ⟨112⟩ direction of methylselenolate (yellow triangles) and methylthiolate (green circles). The plots represent the lateral corrugation of the energy hypersurface. The insets show the height changes (z-z$_{min}$ or z-z$_{max}$) of the docking groups due to the displacement.

Only a negligible difference in the lateral corrugation of the energy hypersurface along both directions between CH_3Se and CH_3S has been calculated. From our results of the lateral corrugation of the energy hypersurface, the different ordering behavior of selenolates and thiolates can be not explained, as it has been done in literature.[152,153,150] The change in height of the docking groups due to the displacement shows a little more dependence on the different systems. It is, however, not clear to what extent that wouldexplain the different degrees of order in the SAMs.

Binding Energy Finally, the bonding differences of thiolates and selenolates can be investigated in terms of their binding energies. Furthermore, this analysis allows to calculate, which bond breaks first, when desorbing the molecule: the metal docking-group bond or the docking-group backbone bond.[F] All different fragments for on gold adsorbed CH_3Se, CH_3S, PhSe, PhS, AntSe and AntS have been calculated as described in section 5.1.3. The resulting values are shown in table 9 and they are in good agreement with published values.[57,135,136]

Table 9: The binding energies for methylselenolate (Se|CH_3), methylthiolate (S|CH_3), phenylselenolate (Se|Ph), phenylthiolat (S|Ph), anthraceneselenolate (Se|An) and anthracenethiolate (S|An) on Au(111) (Au), as well as the binding energies to break the bond between the methyl- (CH_3), phenyl- (Ph) and anthracene-backbone (An) and the docking group, which is remains adsorbed on the gold surface (Au|Se) and (Au|S). the broken bond is indicated as '–'.

	E_{bind} /eV		E_{bind} /eV		E_{bind} /eV
Au–Se|CH_3	1.65	Au–Se|Ph	1.45	Au–Se|Ant	1.73
Au–S|CH_3	1.67	Au–S|Ph	1.32	Au–S|Ant	1.82
Au|Se–CH_3	2.31	Au|Se–Ph	2.36	Au|Se–Ant	2.76
Au|S–CH_3	2.62	Au|S–Ph	2.80	Au|S–Ant	3.15

For all calculated systems, the breaking of the bond between the metal and the docking-group is energetically much more favorable compared to the breaking of the docking-group to backbone bond. For selenolates, the difference of the two breaking possibilities is in the range of 0.7 to 1.0 eV, whereas for thiolates the difference is between 1.0 to 1.5 eV.

All binding energies including the selenium as docking group are only slightly lower (except the Au-Se|Ph) compared to the according results with the sulfur docking group. Thus, the calculation indicate, that thiolates and selenolates show the same desorption behavior. This is not consistent with the experimental literature, which shows different thermal

[F] A homolytic fission is assumed.

desorption spectroscopy (TDS) spectra measured for thiolates and selenolates (compare reference 152 and 12.

5.1.5 Conclusion

In this section, we have investigated in detail the bonding of thiolates and selenolates on Au(111) with different backbones. The docking site for CH_3Se and CH_3S were found to be between the *bridge* and the *fcc-hollow* position, whereas the selenolates are stronger bonded to the surface. The lateral corrugation of the binding energy hypersurface was found to be the same for CH_3Se and CH_3S. Finally we have shown that the breaking of the metal/docking-group bond is easier that the breaking of the docking-atom/backbone bond for all systems, but the energy difference between the two breaking possibilities is always smaller for the selenolates.

5.2 Simultaneously Understanding the Geometric and Electronic Structure of Anthraceneselenolate on Au(111): A Combined Theoretical and Experimental Study

5.2.1 Foreword

This work has been performed in cooperation with Dr. Georg Heimel (Institut für Physik, Humboldt-Universität zu Berlin) and the Group of Prof. Gregor Witte (AG Molekulare Festkörperphysik, Philipps-Universität Marburg, Germany). Based on the experimental results[12] measured by Dr. Daniel Käfer and Dr. Asif Bashir (both members of the Witte-Group) theoretical simulation have been performed (with the help of Dr. Heimel) using band structure calculations. The results are published in reference 13 (see figure 90).

J. Phys. Chem. C **2010,** *114,* 2677–2684 **2677**

Simultaneously Understanding the Geometric and Electronic Structure of Anthraceneselenolate on Au(111): A Combined Theoretical and Experimental Study

Anna M. Track,[†,‡] Ferdinand Rissner,[†] Georg Heimel,[§] Lorenz Romaner,[†,∥] Daniel Käfer,[⊥] Asif Bashir,[#] Gerold M. Rangger,[†] Oliver T. Hofmann,[†] Tomáš Bučko,[▽] Gregor Witte,[○] and Egbert Zojer*[,†]

Institut für Festkörperphysik, Technische Universität Graz, Petersgasse 16, A-8010 Graz, Austria, Institut für Physik, Karl-Franzens Universität Graz, Universitätsplatz 5, 8010 Graz, Austria, Institut für Physik, Humboldt-Universität zu Berlin, Newtonstrasse 15, 12489 Berlin, Germany, Lehrstuhl für Atomistic Modeling and Design of Materials, Montanuniversität Leoben, Franz-Josef-Strasse 18, 8700 Leoben, Austria, Lehrstuhl für Physikalische Chemie I, Ruhr-Universität Bochum, 44780 Bochum, Germany, Max-Planck-Institut für Eisenforschung, Max-Planck-Strasse 1, 40237 Düsseldorf, Germany, Computational Materials Physics, Faculty of Physics, University of Vienna, 1090 Austria, and Molekulare Festkörperphysik, Philipps-Universität Marburg, 35032 Marburg, Germany

Figure 90: Copy of part of the first page of reference 13 including all coauthors and their affiliations.

In this section we provide a detailed description of layers consisting of AntSe on Au(111), which display extraordinarily well and long-range ordered structures. [12] SAMs of π-conjugated organic molecules have attracted significant interest in the field of molecular and organic electronics because of their ability to change electrode work functions combined with a considerable conductivity and studies simultaneously addressing both the geometrical and morphological structure as well as their electronic properties are, however, scarce. By combining experimental data with results of slab-type band-structure calculations we are able to unambiguously determine the alignment of the molecules on the surface. The electronic structure of the SAMs is then determined by ultraviolet photoelectron spectroscopy (UPS)) and by DFT) based simulations.

5.2.2 Introduction

Covalently bonded SAMs[65,63,64] on metals have attracted great interest due to the various applications they enable by changing the macroscopic and microscopic properties of the substrate surface. These include the modification of wetting, adhesion and corrosion properties[70,71,69] (macroscopic) or the change of the substrate work function, Φ, (microscopic), which allows the tuning of barriers for charge-carrier injection into materials in contact with SAM covered electrodes.[6,154,155,156] The latter is also significantly influenced by the alignment of the electronic levels of the SAM relative to the metal substrate, which determines the tunnel barrier the carriers need to overcome when "crossing" the SAM. The energy-level alignment is also a crucial quantity in molecular electronics, where either individual molecules[157,158,159] or monomolecular layers[160] are the active components of the device.

When aiming at improved electronic properties of metal electrodes, semiconducting SAMs consisting of conjugated molecules are used as contact primers. They are typically linked to the metal via thiolates. The properties of such aromatic SAMs are very sensitive to their structure[161] which is on the one hand determined by the local chemical, electronic and geometric structure at the metal-molecule interface. On the other hand, the properties are controlled through the intermolecular interaction of the SAM backbones. In particular the charge transport from one to the next molecule is important when looking forward to self-assembled-monolayers field-effect-transistors (SAMFET), where the SAM is the semiconductor (as well as the dielectric).[106] Therefore, precisely controlled experiments are required to minimize local fluctuations and defects and to maximize homogeneity and long-range order within the SAMs. Moreover, highly ordered and well-defined layers are important model systems for deriving a conclusive relationship between the morphology and electronic structure of a SAM and the properties of the individual building blocks.

The geometrical structure of aromatic SAMs has been thoroughly studied both experimentally and theoretically in the past.[162,91,144] Nevertheless, a combination of scattering and scanning probe techniques determining the structure of conjugated SAMs and simultaneous measurements of their electronic properties are scarce. Additionally, to interpret experiments and to elucidate the microscopic origin of the SAM properties, input from quantum-mechanical modeling is crucial. In previous modeling studies, the influence of individual molecular units of the SAM on the resulting electronic properties of the interface has been analyzed mainly conceptually[143,163] but without a direct comparison to experimental data.

As an important prerequisite for such a comparative study, improved order is important. One possibility to achieve that is the introduction of a flexible spacer between the rigid π-conjugated backbone and the anchoring unit.[91,164,165,166,167] The disadvantage of

this approach is that such an aliphatic spacer decouples the electrons in the organic π-system from those in the metal.[167] An alternative method not suffering from that disadvantage has recently been suggested. By replacing the frequently used thiolate anchoring groups of the SAM with selenolate groups, a significant increase of ordering has been observed.[168,169,170,152] Of particular interest for the present study are fully conjugated SAMs utilizing rigid anthracene backbones and selenolate anchoring groups.[12] These films not only exhibit a particularly high degree of long range ordering but also consist of rigid molecules, which eliminate intramolecular twisting and bending as an additional degree of freedom that needs to be considered when interpreting experimental and modeling data.[57,171,172] Moreover, the fully conjugated nature of acenes results in a reduced energy gap, compared to, for example, oligophenylene based systems, which is expected to be beneficial for charge injection.

In a previous study, the structure and bonding of the AntSe SAM have been characterized by means of low-energy electron diffraction (LEED), scanning tunneling microscopy (STM), TDS, reflection adsorption infrared spectroscopy (RAIRS), and near-edge X-ray absorption (NEXAFS), as described in reference 12. Sharp LEED spots reveal a $(\sqrt{3}\times4)$rect surface unit cell and imply a high degree of long-range order.[12] Moreover, high resolution STM images show the presence of two molecules per unit cell, which arrange in a herringbone pattern[12] consistent with the anthracene bulk structure.[173] From the appearance of a sharp single peak in the TDS spectra it can be concluded that the adsorption sites of the two molecules in the unit cell are isoenergetic (compare section 5.1).[12] In spite of this multitude of experimental data, a certain degree of ambiguity exists regarding the details of the molecular arrangement within the SAM because the molecules exhibit no axial symmetry, thus leading to different possible molecular packing arrangement within the film (*vide infra*).

Here, we show that quantum-mechanical modeling can help to distinguish between different molecular packing arrangement. Knowing the actual film structure, we can then use the calculations to predict the electronic properties of the SAM. The validity of those data and, thus, the applicability of the chosen methodology can eventually be benchmarked by comparing the calculated work-function modification, $\Delta\Phi$, and the density of states in the molecular region (MDOS) to the corresponding data obtained by UPS. This is of particular interest in the present case, as, to the best of our knowledge, this study is the first one in which it is ensured that the structure assumed in the calculations is equivalent to that of the sample for which the electronic properties are determined experimentally. Finally, we show how information on the electronic coupling between the molecules can be gained from the lateral (i. e., in-plane) band structure of the SAM.

5.2.3 Methodology

Computational Approach We performed DFT based slab-type band structure calculations using the Vienna ab-initio simulation package (VASP) code.[139,140,141,142] Exchange and correlation were treated with the generalized gradient approximation (GGA), chosing the PW91 functional.[43] The valence Kohn-Sham pseudo wave functions were expanded in a plane-wave basis set with a cutoff energy of about 20.13 Ry and the projector augmented-wave (PAW) method was employed to describe the valence-core interactions.[48] To model the AntSe monolayer on the Au(111) surface, we studied two molecules per unit cell arranged in a herringbone pattern in the experimentally determined ($\sqrt{3}\times4$)rect surface unit cell.[12] A $(8 \times 4 \times 1)$ Monkhorst-Pack[50] type k-point grid and a Methfessel-Paxton[174] occupation scheme (broadening of 0.2 eV) were used. All calculations were done in a spin-restricted manner.

Five layers of gold were chosen to represent the Au(111) surface. The atoms in the bottom three layers were fixed at their bulk positions, while the top two layers were optimized. This allows for a local relaxation of the Au surface but cannot account for the large-scale ($23\times\sqrt{3}$) reconstruction observed for clean Au(111) surfaces.[175] We note, however, that for densely packed SAMs this reconstruction is usually lifted and only survives for films with low areal density of anchoring units such as the dilute stripe phase[176] or SAMs of spacious molecules.[177]

For deriving the bond-dipole, i.e., the effect of the charge rearrangements upon bonding between SAM and substrates, on the potential energy of the electrons, adsorption was treated to proceed on the Au(111) surface upon hydrogen removal from selenol units and subsequent formation of gold-selenolate bond, although an acetate protection group was used in the experiments for practical purpose (*vide infra*). The geometry optimizations were started with the selenolates in the fcc-hollow sites. In the converged geometry, the adsorption site was found to be shifted from fcc-hollow towards the bridge site for both molecules. This final adsorption site is commonly found for thiol-SAMs in DFT calculations[57,145,136,146] and was calculated to be the energetically most stable in test calculations of methylselenolate on Au(111) (compare section 5.1).

A vacuum gap of about 20 Å in z-direction was introduced between the topmost atom of the SAM and the subsequent gold slab to avoid spurious interactions of the slabs in the 3D band-structure calculations. To compensate the asymmetry of the slabs (only one side of the slab is covered with a SAM), a dipole layer was introduced in the middle of the vacuum gap (see reference 51)

Geometry optimizations were performed using the internal coordinate optimizer GADGET[52] until all remaining forces were smaller than 0.0005 a. u. (0.026 eV/Å) and the energy difference between the last two geometries during the geometry optimization was lower than

1×10^{-5} Hartree. GADGET allows optimization using internal coordinates, on the basis of the direct inversion in the iterative subspace (DIIS) method.[55] We emphasize that optimization utilizing Cartesian coordinates according to a damped molecular-dynamics based strategy as implemented in VASP resulted in higher energy structures (even for the tighter convergence criteria of 0.01 eV/Å for the maximum forces) in which the tilt angle of the molecules is significantly underestimated compared to experiment (compare section 5.2.6).

Additionally, test calculations using the Ceperly-Alder[178] local density approximation (LDA) for the exchange-correlation functional, as parameterized by Perdew and Zunger[179] (CA-PZ), were performed starting from the final PW91 geometry.

Furthermore, the possibility of gold adatoms was considered by introducing an extra gold atom exactly beneath each Selene atom as suggested by Yu et al. for thiolates.[180,181] The x- and y-coordinates of the gold adatoms were held fixed during PW91 (GGA) geometry optimization.

STM images were simulated using the Tersoff-Hamann approach.[59,61] For calculating isosurfaces of constant current, the local density of states (LDOS) was integrated between the Fermi Energy (E_F) of the system and the energy E_F - 0.2 eV, which corresponds to the experimental sample bias of -200 mV.[12G] Furthermore, STM images were produced including the complete highest occupied molecular orbital (HOMO), setting the second integration boundaries to 1.64, 1.75, and 1.71 eV below E_F for the three investigated molecular packing arrangement (**A-C**), respectively. To obtain more realistic images and to account for the finite experimental resolution, the calculated LDOS was averaged over 59 points on the model of a spherical tip with a diameter of ∼2 Å.[57] All molecular structures and calculated STM images were visualized with the XcrysDen program.[182]

The quantity compared to the experimental UPS spectra is the molecular density of states (MDOS) which represents the density of states (DOS) projected onto the atoms of the SAM.

To obtain the band structure along high-symmetry directions, calculations were performed with a k-point mesh from $\overline{X}$ [$\frac{1}{2}$,0,0] along the k_x-axis to $\overline{\Gamma}$[0,0,0] and $\overline{\Gamma}$ along the k_y-axis to $\overline{Y}$ [0,$\frac{1}{2}$,0] with 50 points in each direction. The calculations were performed in a non-self-consistent manner, relying on the charge density from the above-described (8×4×1) Monkhorst-Pack grid. Band structures were computed for the isolated H-saturated SAM as well as for the full slab with the SAM bonded to the metal substrate.

Experimental Methodology AntSe SAMs were prepared by immersing Au(111) substrates into an ethanolic solution (0.1 μM) of selenolacetic-acid-Se-anthracene-2-yl-ester for at least

[G] In this context, due to the deviations in level alignment between theory and experiment resulting from the underestimation of the energy gap by GGA based DFT discussed in more detail when comparing the experimental UPS spectrum and the calculated density of states

24 h, followed by thorough rinsing with ethanol and drying in a nitrogen stream. The acetate protection group was used to avoid the formation of insoluble aromatic diselenides as well as a possible oxidation of selenium, hence enabling the preparation of monolayer films by immersion (for synthesis and details see reference 12). The gold substrates were prepared by evaporating 140 nm gold at 450 K under high-vacuum conditions onto freshly cleaved mica sheets, which had previously been heated to 590 K for 48 h to remove residual crystal water. After deposition, the gold/mica substrates were flame-annealed in a butane/oxygen flame, yielding high-quality Au-films with flat terraces of several 100 nm exhibiting a (111) surface orientation (compare to section 3.3.2]. In a previous study, the adsorption and formation of AntSe-SAMs was characterized by means of RAIRS, TDS, XPS, NEXAFS, low current micro-channel plate LEED and STM as described in reference 12.

Moreover, the electronic valence structure was characterized by employing photoelectron spectroscopy using a gas discharge He-I vacuum UV light source (21.22 eV) and a hemispherical electron energy analyzer (Leybold EA200). All UPS spectra were recorded at normal emission with an acceptance angle of $\sim 10^{\circ}$. The energy scale is referenced to the Fermi edge of the Au substrate.

The STM data were recorded under ambient conditions with a Jeol JSPM 4210 microscope using tips prepared mechanically by cutting a 0.25 mm Pt0.8Ir0.2 wire (Goodfellow). Typically low tunneling currents of 150 pA were used in constant-current mode at -200 mV sample bias, thus avoiding tip-induced changes to the SAM. No differences were found in the STM images acquired before and after the UPS measurements, indicating that possible radiation damage of the SAM can be safely excluded.

5.2.4 Results and Discussion

Structural Aspects In a previous study it has been shown that AntSe-SAMs on Au(111) form a ($\sqrt{3}$x4)rect structure with two molecules per unit cell. In addition to the herringbone arrangement of adjacent molecules, characteristic stripes along the $\langle 11\overline{2} \rangle$ direction can be observed in the STM data (see figure 91), suggesting an inhomogeneous molecular packing within the SAM. Since the AntSe molecules exhibit no axial symmetry - the Se anchoring unit is necessarily attached to the lowest ring of the anthracene backbone in a nonsymmetric fashion - one can distinguish between different inclinations and positions (i.e., left or right) of the anthracene backbone relative to the Se-C bond (cf. figure 91, molecular packing arrangement **A**-**C**). As a consequence, different relative molecular packing arrangements can be realized that comply with the same lateral periodicity. Thus, in spite of the multitude of experimental data (cf. section 5.2.2), still a certain degree of ambiguity exists regarding the details of the molecular arrangement within the monolayer. Further clarifi-

cation might be provided by X-ray scattering experiments which are, however, difficult to perform for SAMs on Au(111).[183] Therefore, in this study a different approach is adopted. The geometry of several possible packing arrangements is optimized computationally and a number of observables are calculated. By comparing them with the experiment, the best agreement is proposed as the most likely structure.

Three molecular packing arrangements (labeled as **A**, **B** and **C**) can be envisioned that are a priori consistent with the above mentioned lateral periodicity, i.e., they all have the same unit cell dimensions with molecules packed in a herringbone pattern, including characteristic stripes in the STM images. The resulting three molecular packing arrangements are sketched in the bottom part of figure 91. At this point it is worth mentioning that the apparent (dark) stripes seen in the tunneling micrographs reflect an unequal lateral separation of the topmost rings of the aromatic backbones which are essentially imaged by STM (as shown below). This does, however, not necessarily reflect the actual positions and the relative arrangement of the anchoring units, since the molecules are not perfectly upright-oriented but tilted. In all molecular packing arrangements the selenium atoms (green circles in figure 91) adopt an inhomogeneous lateral packing with alternating separations of 1.5 and 2.5 gold rows along the $\langle\bar{1}10\rangle$ direction. Interestingly, only in molecular packing arrangement **A**, all Se atoms are equivalently oriented with respect to the backbone[H] and their larger separation coincides with the dark stripes. In contrast, in molecular packing arrangements **B** and **C** neighboring backbones are tilted in opposite directions and the separation of the anchoring units is out-of-phase with the dark stripes.

[H] The mirror domain of molecular packing arrangement **A**, where the backbones are tilted in the opposite way relative to the Se-C bond is not exactly symmetry equivalent to molecular packing arrangement **A** due to the ABC stacking along the Au[111] direction. As the differences are found only in the second Au row, which is seen found to have an only minor impact on the SAM-adsorption energetics (compare, for example, the very small differences in fcc and hcp docking sites) this molecular packing arrangement will not be separately considered here.

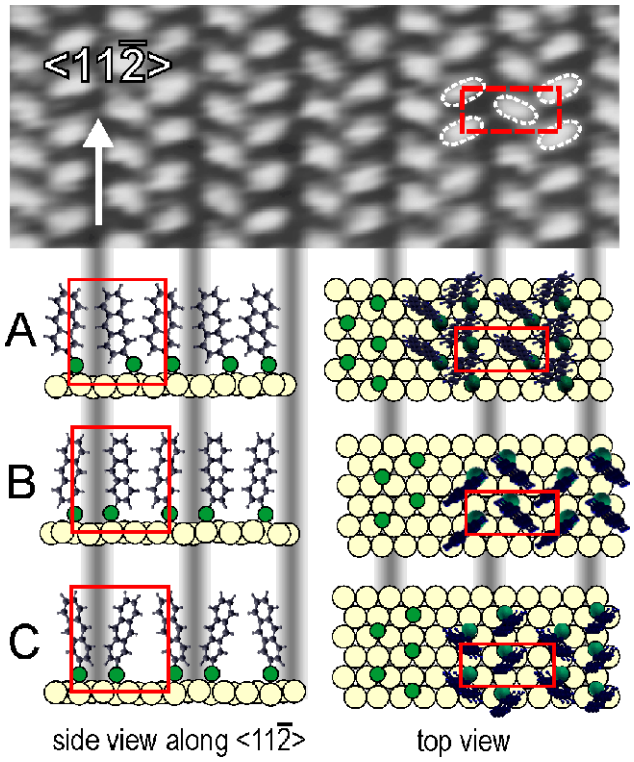

Figure 91: Top: Experimental STM images of AntSe on Au(111) (compare reference 12) The stripe-like growth of the molecules in the $\langle 11\bar{2} \rangle$ direction is indicated with an arrow and the dark spaces between the bright stripes are highlighted below with grey-scaled bars. Bottom: The side views of all molecular packing arrangements display the AntSe molecules and the uppermost gold layer. In the top view, the uppermost Au-layer, the anchoring selenium atoms, and the anthracene backbone are shown. Only in molecular packing arrangement **A** the bright stripes correspond to two molecules attached to the surface via two close-lying Se atoms. In molecular packing arrangements **B** and **C** the distance between the anchoring Se atoms is lager *within* the bright stripes. For all molecular packing arrangements the relative position of the unit cell to the stripes is marked. (Identical to reference 13.)

A first estimate of which of the molecular packing arrangements is most likely adopted can be made from the total energy per unit cell calculated for all three structures. Molecular packing arrangement **A** is found to have the lowest energy, whereas in molecular packing arrangements **B** and **C** the energies are higher by 0.013 eV and 0.183 eV, respectively (see table 10). Since the total energies of **A** and **B** are rather similar, no unambiguous conclusions regarding the lowest energy structures can be made. Regarding the accuracy of such calculation, it must be kept in mind that in DFT studies based on local or gradient-corrected functionals, van der Waals interactions are not properly accounted for. Previously, it has been shown by a combined theoretical and experimental study that this plays no

role for the orientation of the molecules in the bulk anthracene crystals as a function of pressure.[184,185,186] Still, it cannot be excluded that variations in the van der Waals energy of the different molecular packing arrangements are larger than the obtained energy differences for the various geometries. Therefore, to determine the actual microstructure one has to go beyond purely energetic reasoning.

Table 10: Difference in the total energies per unit cell (ΔE), the tilt angle φ and the herringbone angle Θ as calculated for the three packing molecular packing arrangements and measured by NEXAFS and STM (experimental data from reference 12). For a definition of those angles see figure 92.

	A	**B**	**C**	Experiment[12]
ΔE /eV	0	0.013	0.138	-
φ	19°/10°	8°/5°	11°/12°	33° (NEXAFS)
Θ	48°	86°	79°	$48° \pm 3°$ (STM)

Additional insight can be gained from comparing a number of experimental observables like the tilt angle, φ the herringbone angle, Θ, and STM images to the corresponding calculated quantities. The tilt angle of the molecules, φ, is defined as the angle between the molecular backbone of the anthracene backbone and the surface normal (see figure 92). Relatively small tilt angles of 11° and 12° (for the two nonequivalent molecules in the unit cell) are found for molecular packing arrangement **C**, which decrease slightly for **B** to values of 8° and 5°. The averaged tilt is maximized in for molecular packing arrangement **A**, where tilt angles of 19° and 10.° are found (see table 10). The latter orientation correlates best with an average tilt angle of 33° determined from NEXAFS measurements.[12] A possible origin of the small discrepancy between calculation and experiment could be residual disorder of the molecules on the surface (e.g., existence of less ordered domains and adsorption at defects); also a dynamic contribution cannot be excluded originating from the fact that the experiments have been performed at room temperature, while the calculations correspond to the situation at 0 K. Moreover, even though DFT performs very well when calculating the tilt angles in anthracene crystals,[185,186] the neglect of van der Waals interactions can have some impact.

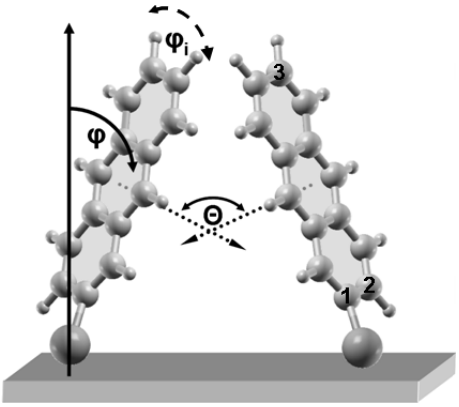

Figure 92: Relative positions of two AntSe molecules in the herringbone structure. The definitions of the tilt angle, φ, the in-plane tilt, φ_i, and the herringbone angle, Θ, are indicated. Numbers 1 to 3 mark the atoms which are chosen to define the molecular plane (note that the molecular backbone is slightly distorted). (Identical to reference 13.)

To test the impact of inter-molecular interactions, we also performed geometry optimizations using LDA instead of GGA, as the former is known to overestimate (rather than underestimate) the binding between aromatic systems,[31] which to some extent compensates the neglect of van der Waals interactions in DFT. This results in significantly increased tilt angles of 44° and 42° in molecular packing arrangement **A**, now clearly larger than the experimental value, which implies that stronger inter-molecular interactions indeed favors larger tilt angles.

We also tested the impact of introducing an additional gold atom exactly underneath the Se-atom for molecular packing arrangement **A** to generate a layer of adatoms as suggested in reference 180 and 181 for thiolate SAMs. Here, a smaller impact on the tilt angles (24° and 13°) is observed, and the results would, in principle, fit the experimental data better. However, the resulting work-function modification for this geometry is found to significantly deviate from the experimental value (*vide infra*).

Next, the herringbone angle, Θ, which is defined as the angle between the vectors normal to the planes of the two neighboring AntSe molecules (see figure 92) has been considered. For molecular packing arrangements **B** and **C** the anthracene backbones are arranged nearly perpendicular (Θ equals 85° for molecular packing arrangement **B** and 79° for molecular packing arrangement **C**), while for structure **A** an angle of 48° is obtained in excellent agreement with the experimental herringbone angle of $48° \pm 3°$, determined from STM data.[12I]

[I] In this context, we note that because of the molecular tilt relative to the surface sample normal the STM data provide only a 2D projection of the aromatic backbone planes which can differ slightly from the true herringbone angle.

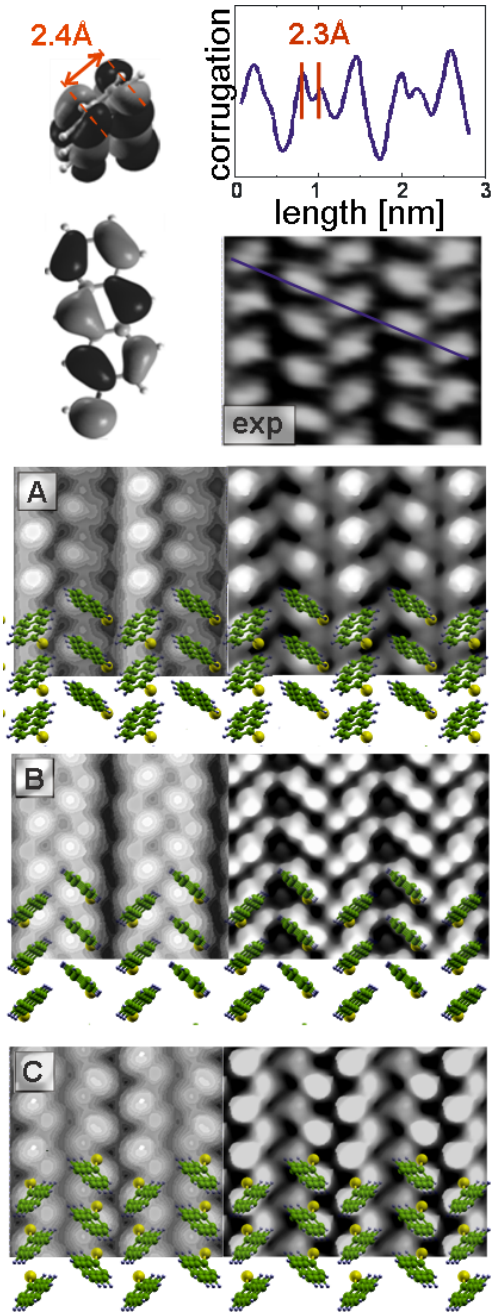

Figure 93: Comparison of calculated and experimental STM images. Top left: HOMO of a single H-saturated AntSe molecule calculated in gas phase. Top right: experimental STM images (-200 mV sample bias) and associated line scan. Panel A-C: simulated STM images with corresponding molecular geometry for molecular packing arrangement **A**-**C** respectively. In the left part the experimental voltage was used (see section 5.2.3); in the right part the voltage was increased to include the entire HOMO peak. Only molecular packing arrangement **A** can reproduce the experimental STM images. (Identical to reference 13.)

The data presented above point towards molecular packing arrangement **A** to be prevalent in the AntSe-SAMs. As a next step, STM images obtained by tunneling through states between E_F and 0.2 eV below E_F (corresponding to the experimental sample bias) as well as between E_F and a voltage chosen to include the HOMO of the SAM (cf., section 5.2.3) have been calculated. The small bias voltage in the experiments had to be used, as at larger voltages indications for a degradation of the SAM were observed. Since no SAM-related features are discernable within the narrow energy range between E_F and -0.2 V sample bias has to occur through the tails of the HOMO-derived and potentially deeper lying states. The corresponding calculated images are shown in the left halves of figure 93 A-C. For comparative reasons and to depict a better defined tunneling situation, the images obtained when including the complete HOMO are shown in the right halves of the panels. Due to the much larger tunneling currents at higher sample bias the iso-current values to generate these simulated STM images are increased by a factor of 10.

A first estimate of what is to be expected in the STM images can be made on the basis of the shape of the HOMO of an isolated AntSeH molecule, which is shown in the top left panel of figure 93. When tunneling from the STM tip into the HOMO of the molecule, ideally four lobes of the HOMO orbital (two on each side of the molecular plane) should be visible in the STM experiments for perfectly upright-aligned molecules and appropriate resolution. For a nonperpendicular (i. e., a not perfectly upright) alignment of the molecules, the shape of the STM spots depends in a subtle way on the molecular orientation: A tilt of the molecular plane (φ in figure 92) will result in STM images where only the "upper" π-lobes of the molecular plane are clearly visible. The experimental line scan shown in the top part of figure 93 indeed exhibit a pronounced double-peak structure for one of the features, and the observed separation between the two π-lobes on one side of the molecular plane closely matches the separation between the molecular orbital lobes (as indicated in the figure). A tilt of the long molecular axis within the molecular plane will result in the dominance of one of the two π-lobes of the HOMO from one side of the molecular plane. This reasoning can be used to directly link the shape of the simulated STM images to the molecular orientation.

For molecular packing arrangement **B**, indeed, all four HOMO π-lobes are resolved at least for one of the molecules in the unit cell in the STM images calculated at an assumed sample bias of -1.75 V. The HOMO-related π-lobes partly overlap with those from the neighboring molecules, although the ones "below" the molecular plane are clearly weaker. The latter trend is even more pronounced in molecular packing arrangement **C**, which is consistent with the larger tilt angles (see table 10). At -0.2 V sample bias the separation between the two lobes on each side of the molecular plane diminishes in the calculated STM images. This is the result of the changed tunneling situation with the tip Fermi level being so close to E_F tunneling occurs only through intra-gap hybrid states. These hybrid

states can be associated with the tails of the features originating from various molecular orbitals. However, independent of the tip bias, the occurrence of STM spots above and below the molecular plane and the large apparent herringbone angle for molecular packing arrangements **B** and **C** are inconsistent with the experimental data. Due to the large tilt φ of the "upper" two π-lobes are visible; i. e., also as far as the STM pictures are concerned, the calculated results for molecular packing arrangement **A** are in best agreement with experiments.

Nevertheless, also here certain deviations to the experimental STM images are observed. In particular, the calculated STM features are less elongated than the experimental ones: i.e., they are close to spherical. This hints towards a deviation in the "inplane tilt" angle φ_i between experiments and calculations. In this context it should, however, also be kept in mind that the actual shape of the tip in the experiments is not known and thus cannot be taken into account in simulations.

Electronic Structure of Anthraceneselenolate SAM In the following, the focus will lie on the electronic structure of AntSe-SAMs on Au(111) using molecular packing arrangement **A**.

Conceptually, the work-function modification due to SAM formation can be separated into two contributions.[163,172,187] First, the chemical bond between SAM and surface affects the electron potential energy. This effect is denoted as the bond dipole (ΔE_{BD}). ΔE_{BD} results from charge rearrangements in the region of the metal-SAM interface due to the bond formation (which is here defined as replacing the Se-H by a Se-Au bond).[J] It can be calculated by solving the one-dimensional Poisson equation with the x, y-plane averaged charge rearrangements, $\Delta\rho(z)$ from the DFT calcualtion as the source term. The latter is given by[187]

$$\Delta\rho(z) = [\rho_{System}(z) - (\rho_{Au}(z) + \rho_{SAM}(z) - \rho_{H}(z))] \tag{51}$$

Here, $\rho_{System}(z)$, $\rho_{Au}(z)$, $\rho_{SAM}(z)$, and $\rho_{H}(z)$ represent the plane-averaged charge densities of the combined system, the gold slab only, the free-standing SAM only with the Selene atoms saturated by hydrogen, and these H-atoms only (all in their final geometries), respectively.[172]

As a second contribution, the change of the electron potential energy across the SAM in the hypothetical situation of an ordered layer not bonded to the surface is given by ΔE_{vac}.[171] ΔE_{vac} arises from the permanent dipoles of the SAM forming molecules and, thus, is a measure for the molecular contribution to the work-function modification. In total, one obtains the change in the work function to be $\Delta\Phi = \Delta E_{BD} + \Delta E_{vac}$. ΔE_{vac} can

[J] An alternative partitioning scheme would be to consider $-\mathrm{Se}^{\bullet}$ radicals as intermediate states; the ΔE_{BD} would represent the formation of the Se-Au bond; the actual partitioning, while determine ΔE_{BD} has no impact on the net work-function change as explicitly shown in reference 188.

be calculated from the z-component of the molecular dipole moments via the Helmholtz equation as long as depolarization effects within the SAM are considered.[163,189,190,191]

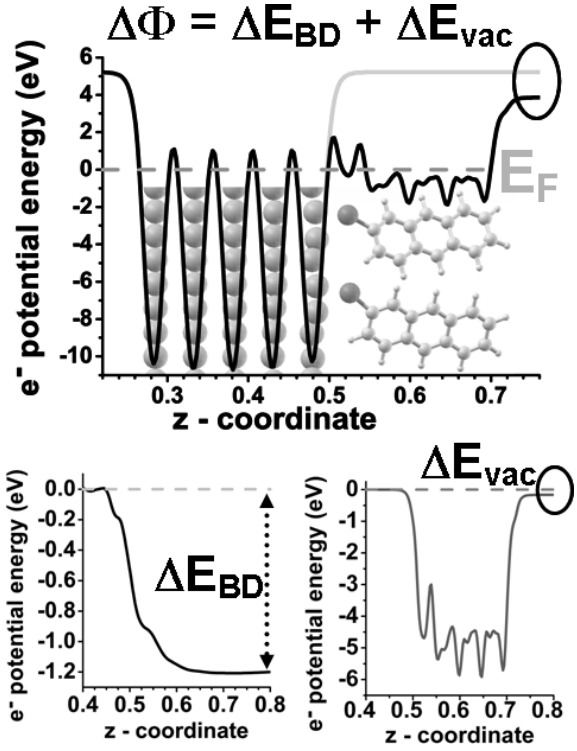

Figure 94: Top: Plane-averaged electron potential energy of the Au slab (gray) and the Au slab covered by the AntSe SAM (black). The work-function change due to SAM adsorption ($\Delta\Phi$) is highlighted. The bond dipole ΔE_{BD} induced step in the electron energy of -1.20 eV and the step in the electron energy caused by the permanent dipoles of the AntSe molecules (ΔE_{vac}) of -0.17 eV are visible in the lower diagrams; these two contributions add up to a total $\Delta\Phi$ of -1.37 eV. (Identical to reference 13.)

The resulting electron potential energy across the metal slab (light gray line) and for the SAM-covered slab (black line) are shown in the top part of figure 94. A reduction of the vacuum level above the SAM with respect to the clean metal slab is clearly visible for the combined system, corresponding to a net work-function decrease due to SAM adsorption. The contributions of ΔE_{BD} and ΔE_{vac}, shown in the bottom part of figure 94, clearly reveal the dominant role of the bond dipole. It decreases the work function by -1.20 eV, while ΔE_{vac} results in a work-function shift of only -0.17 eV, consistent with the fact that the SAM-forming molecules do not contain polar substituents. In this context it should be mentioned that a very similar value for ΔE_{BD} has been calculated for thiolate anchoring groups as long as a similar SAM packing density is assumed.[172] As a net effect, the calculated work function of the Au(111) surface is decreased by -1.37 eV from 5.22 eV to

3.85 eV due to AntSe SAM. These values are in excellent agreement with those determined by the measured valence band UPS(see figure 95). The secondary cutoffs (not shown) point to an experimental work-function shift $\Delta\Phi$ of -1.3 eV from 5.2 eV for the pristine Au(111) surface to 3.9 eV for Au covered with the AntSe SAM. This indicates that the applied methodology has the potential to quantitatively predict SAM-induced work-function modifications, at least as long as experiments are performed on a well-ordered monolayers of known structure.

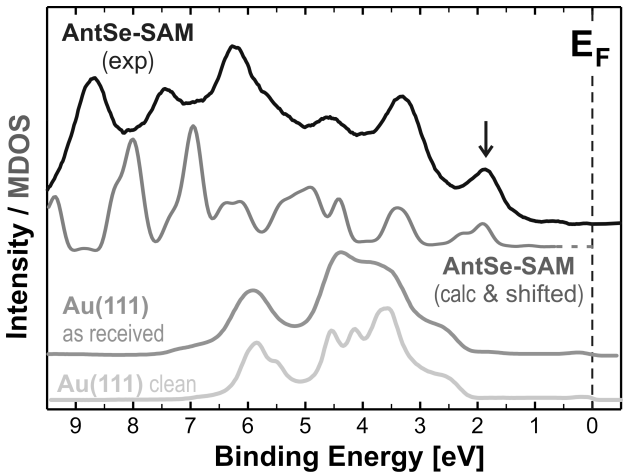

Figure 95: Measured UPS spectra of cleaned (sputtered) Au(111) (lowest), ex-situ cleaned Au(111) (second) and AntSe-SAM on Au(111) (third). The calculated density of states for the combined Au-SAM system projected onto all atoms of the SAM (MDOS) is shown in black (uppermost). This quantity corresponds to the contribution of the SAM to the total density of states. The position of the MODS features relative to E_F *is shifted* by -1.17 eV (details see text). (Identical to reference 13.)

Finally, the density of states projected onto all the atoms of the SAM (MDOS) is calculated. It is depicted in figure 95 for comparison with the measured UPS data where, to accentuate the position of the photoemission peaks arising from the molecular species and to compensate for the emission of secondary electrons (from the gold substrate), a smooth, cubic background has been subtracted. Note that the photoionization cross-sections are not considered in the calculations. Thus, a direct comparison of peak intensities is not possible, in particular, when considering the very pronounced dependence of the relative peak intensities on the experimental takeoff angle, as measured, for example, for pentacene.[192] It should also be mentioned that DFT is a ground-state method while UPS is a final-stat spectroscopic technique. The calculated MDOS in figure 95 is shifted by -1.17 eV. This is inevitable,[193] because band gaps are severely underestimated as a result of the lack of derivative discontinuities of the (semi) local exchange-correlation functionals.[194,195] With this shift applied (compare reference 136), the obtained correspondence between the exper-

imental spectrum and the MDOS is quite satisfactory. Similar observation has been made for alkyl chains on semiconductors, where DFT calculations reproduced the experimental work-function changes,[196] but the reasons mentioned above, a satisfactory agreement between UPS and inverse photoelectron spectra and the calculated DOS was obtained only after properly increasing the HOMO-lowest unoccupied molecular orbital (LUMO) gap.[197] We note that, without in-situ cleaning of the substrate, the fine structure of the gold d-band cannot be resolved, reflecting the influence of adsorbates on the surface density of states.

On the basis of the work-function modification as the most relevant and most directly comparable experimental observable, a comparison of the results for molecular packing arrangement **A** with those obtained for the other investigated structures yields the following three results: (i) similar work-function changes are obtained for the used LDA and GGA functionals (cf., section 5.2.3). With LDA an only slightly increased $\Delta\Phi$ of -1.43 eV is obtained in spite of the considerably larger tilt angle; (ii) a work-function change of only -0.92 eV is calculated for the geometry including an adatom at the fcc-hollow site, which is inconsistent with the experiment; (iii) very similar values of $\Delta\Phi$ = -1.43 eV for molecular packing arrangement **B** and $\Delta\Phi$ = -1.36 eV for molecular packing arrangement **C**. Here, also very similar molecular densities of states were obtained (see figure 96.

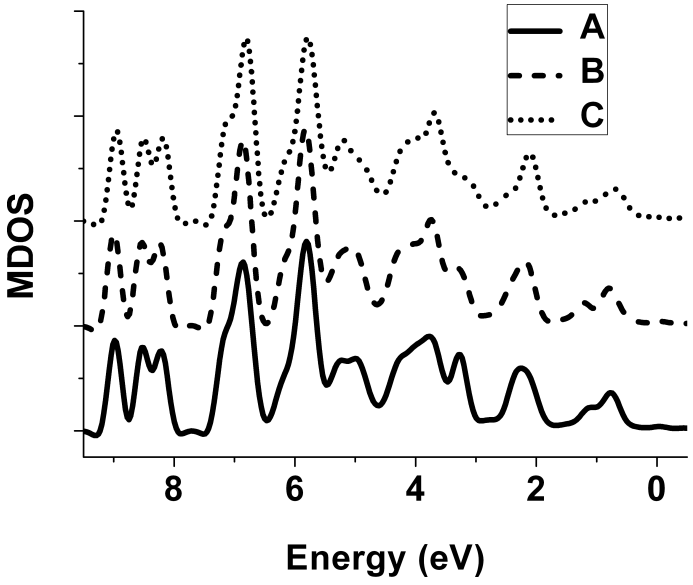

Figure 96: The molecular density of states (MDOS) is plotted for the molecular packing arrangement **A** (solid line), the molecular packing arrangement **B** (dashed line) and the molecular packing arrangement **C** (dotted line). For this plot, *no shifts* have been applied. (Identical to the supporting information in reference 13.)

The only minor dependence of the work-function modification on the tilt angle is at least in part a consequence of the vanishing intrinsic molecular dipole moment of the anthracene

backbones, which do not contain electron donating or withdrawing substituents.

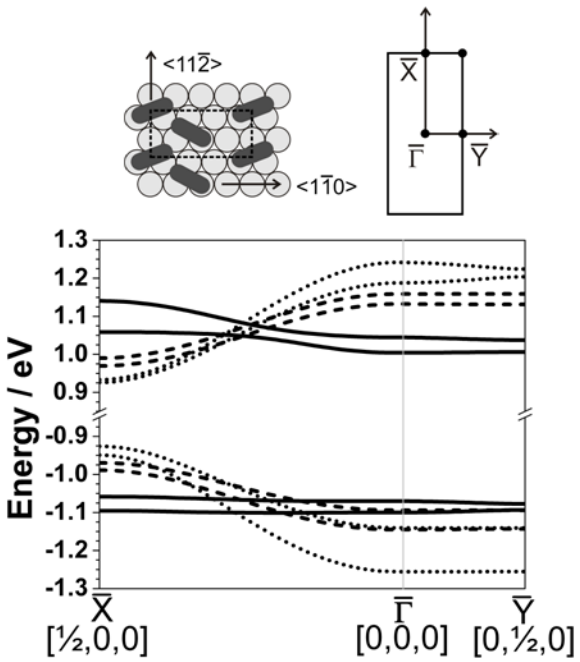

Figure 97: Band structure for molecular packing arrangement **A** (solid lines), **B** (dashed lines) and molecular packing arrangement **C** (dotted lines) along $\overline{\Gamma}\,\overline{X}$ and $\overline{\Gamma}\,\overline{Y}$ (i.e., parallel to the short and long unit-cell axes in real space, respectively) for the free standing H-saturated SAM. The origin of the energy scale is set to the middle of the band gap. (Identical to reference 13.)

However, this apparent similarity in the electronic structure of the three molecular packing arrangements vanishes when, instead of the MDOS, the full lateral 2D band structure of the SAM is considered. The latter is shown in figure 97 for the free-standing hydrogen-saturated monolayer in all three molecular packing arrangements **A**, **B**, and **C**. The dispersion of the bands is a direct measure for in-plane electronic coupling between the molecules. Hereby, the resulting band widths would bear direct relevance for charge transport within the layer. This role is somewhat diminished by the presence of the Au substrate, albeit it has recently been shown that lateral charge transport within the monolayer can be a quantity of immediate importance for tunneling from an STM tip through a monolayer.[177] The two HOMO and the two LUMO-derived bands are a consequence of the presence of two inequivalent molecules in the unit cell. All bands are flat between the $\overline{\Gamma}$ and $\overline{Y}$ points, which can be easily understood from the striped structure of the SAM that results in very weak coupling between molecular pairs in the direction perpendicular to the stripes. Between $\overline{\Gamma}$ and $\overline{X}$ a significant dispersion is observed for molecular packing arrangement **B** and even stronger for **C** with band widths of several tenths of an electronvolt for all involved bands, similar to what has been found for phenyl thiolates on noble metals.[198] Only for

A the dispersion remains small, indicating that for this actually formed packing molecular packing arrangement intermolecular electronic coupling is small in all directions.

The band structure for the SAM bonded to the Au(111) surface is shown in figure 98. The colored dots represent the projected contribution of the C- and H-atoms of the molecules onto the entire band structure. Similar to the band structure of the saturated monolayer (figure 97), the bands arising from the molecular backbone are flat between the $\overline{\Gamma}$ and $\overline{Y}$ points. Between $\overline{\Gamma}$ and $\overline{X}$ a dispersion is observed for molecular packing arrangement **B** (blue) and **C** (green). Only for the molecular packing arrangement **A** (red) the dispersion remains small.

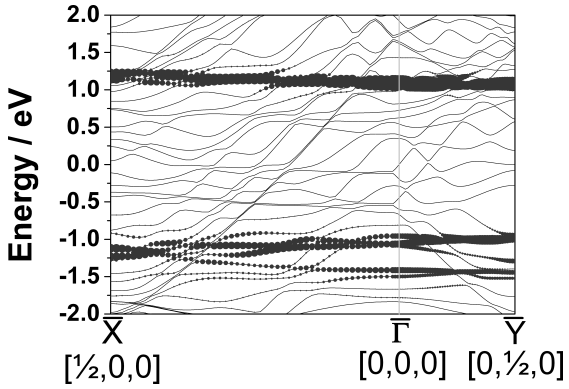

(a)

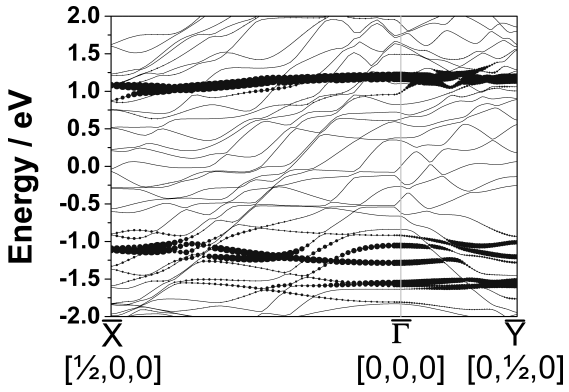

(b)

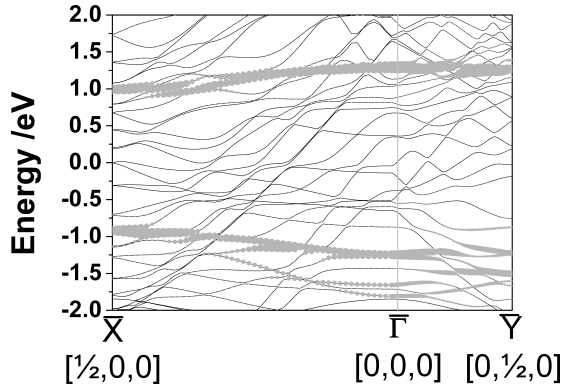

(c)

Figure 98: Band structure of the AntSe-SAM bonded to Au(111). The contribution of the molecular backbone (all C- and H-atoms) is shown with colored dots for (a) molecular packing arrangement **A**, (b) for molecular packing arrangement **B** and (c) for molecular packing arrangement **C**. (Identical to the supporting information in reference 13.)

5.2.5 Summary and Conclusions

We present a joint theoretical and experimental characterization of a self assembled monolayer of anthracene-2-selenolates on Au(111). This system can be considered as a prototypical system for π-conjugated SAMs, as it exhibits a particularly high degree of order, which has been well characterized by LEED, STM, NEXAFS, RAIRS and TDS experiments (cf., reference 12). Interestingly, even this large number of characterization techniques turns out to be not sufficient to unambiguously determine the details of the molecular packing arrangement. Therefore, in this study, the measured physical observables are compared to the results of calculations carried out for various possible packing arrangements of the SAM. This allows identifying the most probable SAM structure.

Knowing the atomistic structure of the SAM, its electronic properties are calculated in a second step. The calculated work-function reduction is in excellent agreement with the experimental value derived from UPS spectroscopy, lending credibility to the applied theoretical methodology. This is further supported by the fact that also the calculated molecular density of states and the UPS spectrum agree reasonably well. A much less favorable agreement between theory and experiment is observed when studying, e.g., a structure with a Au ad-atom between the selenolate group and the fcc-hollow site of the Au(111) surface.

While differences in the studied molecular packing arrangement have little impact on the work.function modifications, the resulting changes in the intermolecular interactions significantly affects the dispersion of the two-dimensional (2D) band structure in the SAMs.

5.2.6 Appendix A: Improving the Geometry Optimization of Self-Assambled Monolayers on Metals Using Internal Coordinates

Foreword and Introduction This work has been performed in collaboration with Dr. Tomáš Bučko from the Center for Computational Materials Science (Vienna). He developed the new optimization software GADGET[52] which was used for the geometry optimization using internal coordinates. Ferdinand Rissner tested this optimizer for the usage to calculate organic molecules on surfaces and was in strong contact to Dr. Tomáš Bučko to obtain reliable results. Ferdinand Rissner showed me in details how to use GADGET and helped me with every upcoming problem.

When calculating the structure of SAMs multiple energetic minima for different molecular geometries were found in DFT and molecular dynamics based simulations.[199] Even in a well ordered monolayer, the structure of the SAM (e.g., the coverage) can influence its functionality quantitatively as well as qualitatively.[163] Although the importance of geometric aspects is well recognized, no emphasizes is usually placed on the optimization technique used in computational investigations of SAMs.

In this section, we apply a more sophisticated internal-coordinates (IC) based strategy besides a simple damped molecular dynamics (dMD) relaxation performed in Cartesian coordinates. The idea of using an IC based optimizer for relaxing SAMs is that it might proof useful for the description of the molecular part of the unit cells. For the geometry optimization of molecular systems, a general superiority of internal coordinates over Cartesians is well known, regarding speed as well as the quality of the results.[200,201,202,203,204,205,206] For periodic systems, in contrast, the utilization of internal coordinates is a quite recent development.[207,208,52,209] Therefore we choose the free software GADGET[52] to calculate the geometry in IC and compare the results with those obtained in earlier work for AntSe on Au(111), where a dMD strategy (in Cartesian coordinates) was used with VASP[139,140,141,142] (compare section 2.4.3).

R&D: Geometrical and Electronic Structure Generally different quantities are used to describe the structure of SAMs on metal substrates. Here especially the experimental available quantities are of interest, because a comparison allows evaluation of the calculated values. For the AntSe the tilt angle, φ, which is defined as the angle between the molecular plane and the z-axis, and the herringbone angle, Θ, which is the angle between the vectors normal to the planes of the two neighboring AntSe molecules (compare figure 92), are calculated. The obtained final geometries for the two different optimization methods are shown in figure 99 (tilt angle) and figure 100 (lowermost fraction: herringbone angle) and the calculated values for the tilt angle and the herringbone angle are given in table 11. When using the IC-direct inversion in the iterative subspace (DIIS) much more tilted

molecules are obtained in the final geometry whereas with the dMD method the anthracene-backbone has quasi no tilt. Similar discrepancy is seen in the herringbone angle. After optimization using the IC φ is 48° whereas for the Cartesian coordinates optimization Θ is much higher (80°). For both angles the IC-DIIS results are much better in agreement with the experimental values of 33° for φ and 48° for Θ.[12,13].

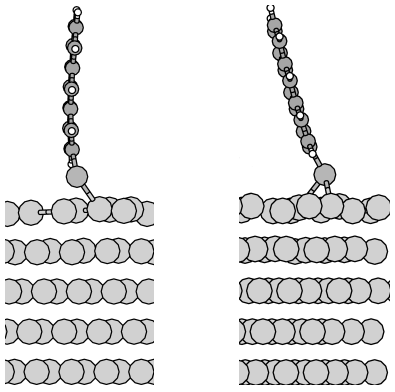

Figure 99: Side view of the final geometry after optimization (a) using dMD and (b) IC-DIIS for one molecule of the unit cell.

An very important issue of theoretical calculations is the differences in the total energy per unit cell (ΔE). For AntSe on Au(111) the energy is lowered by 0.21176 eV when using the IC-DIIS optimization method (see table 11). This difference in total energy is a obvious indication, that geometry optimization using IC leads to more reliable structures for SAMs.

Table 11: Comparison of dMD and IC-DIIS results of the total energy per unit cell for (δE), the work-function modification ($\Delta\Phi$), the tilt angle (φ), the herringbone angel (Θ) and the offset between the Fermi energy and the highest occupied and lowest unoccupied molecular orbital (ΔE_{HOMO} and ΔE_{LUMO}) of AntSe on Au(111).

	ΔE /eV	$\Delta\Phi$ /eV	φ	Θ	ΔE_{HOMO} /eV	ΔE_{LUMO} /eV
dMD	:=0	-1.46	6°/2°	48°	-0.80	1.41
IC-DIIS	-0.21176	-1.37	19°/10°	80°	-0.77	1.44

Another issue to address is the change due to difference in the final geometric structures on the electronic structure of the calculated system. Here, the work-function modification ($\Delta\Phi$) of the metal due to the adsorption of the SAM can be strongly influenced by a variation of the tilt angle, if the molecule consist of a decent dipole moment.[187] In the case of AntSe the molecular backbone does not have a strong dipole moment which results

in similar $\Delta\Phi$ for both optimization methods. Additionally the energetic position of the HOMO and thLUMO is not much affected by the change of the geometric structure due to the different used optimization methods. (Results see table 11)

R&D: Scanning Tunneling Microscopy If one wants to reproduce the experimental STM image of AntSe on Au(111), choosing a proper optimizer becomes important. It is clearly visible (compare figure 99), that the dMD optimization leads to more upright standing molecules (6° and 2° for the two molecules per unit cell) in comparison to IC-DIIS with larger tilt angles of 19° and 10°.[13] The experimental and the calculated STM images of both optimized structures are shown in figure 100.

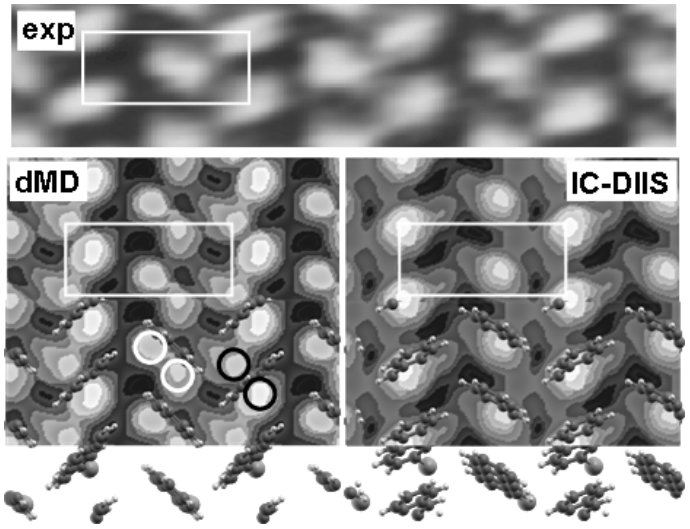

Figure 100: Top: Experimental STM image of AntSe on Au(111) showing two spots per unit cell referred to two molecules per unit cell.[12] Bottom: (left: dMD, right: IC-DIIS optimized results) plain calculated STM images (topmost part), calculated STM images cutting through the uppermost benzyl-ring of the anthracene backbone (middle region) and the AntSe molecules alone (lowermost fraction). The surface unit cell is indicated as a whit rectangle in each picture, white and black circles emphasize the relative position of the STM spot relative to the backbone.

Due to the discrepancy in the calculated tilt angles extremely different STM images are obtained. The difference in the images is visible on the one hand due to the number of STM spots per molecules and on the other hand due to the position of the STM spots with respect to the molecular backbone. For the dMD optimized structure to two bright spots per molecule (for both molecules in the unit cell) are seen and the spots are either on the same side of the backbone (white circles in figure 100) or on each side of the backbone (black circles in figure 100). In contrast, the IC-DIIS structure shows just one spot per

molecule on on one side of the backbone (see figure 100-right). For both structures the calculated STM is not in perfect agreement with the experimental STM image, however, the STM image obtained for the IC-DIIS optimized structure is much more comparable with the experiment. Here, the strong dependence of STM images on the tilt angle is shown and a perfect agreement between calculated and experimental STM image can be assumed, if the tilt angle are the same (calculated and experimental).

Conclusion The use of the decent optimization method is crucial to obtain the correct geometric structure of SAMs. Here, the differences obtained using a Cartesian optimization method (dMD) and an IC optimizing strategy (IC-DIIS) are shown for AntSe on Au(111). This test system has been characterized experimentally in great detail. [12,13]

Using the IC-DIIS method leads to a lower energy structure with stronger tilted molecules. Due to the difference in tilt, calculated STM images are quantitatively in complete contrast to the images obtained for the molecular structure optimized with dMD. All results obtained with the internal coordinate optimization are better compareable with the experimental result.

Acronyms

E_F Fermi Energy.

E_b binding energy.

E_{kin} kinetic energy.

ΔE_{BD} bond dipole.

Φ work function.

CH_3Se methylselenolate.

CH_3S methylthiolate.

2D two-dimensional.

AFM atomic force microscopy.

AntS anthracene-2-thiolate.

AntSe anthracene-2-selenolate.

ARUPS angle-resolved ultraviolet photoelectron spectroscopy.

ASF atomic sensitivity factor.

Au-Naphthyl 16-mercaptohexadecanoic-acid-naphth-1-yl-ester.

Au-PF 11-mercaptoundecanoic-acid-phenyl-ester.

Au-PF-long 16-mercaptohexadecanoic-acid-phenyl-ester.

BCB divinyltetramethyldisiloxane-bis(benzocyclobutene).

BZ Brillouin zone.

DFT density functional theory.

DIIS direct inversion in the iterative subspace.

dMD damped molecular dynamics.

DOS density of states.

FFM friction force microscopy.

FT-IR Fourier-transformation infrared.

FWHM full width at half maximum.

GGA generalized gradient approximation.

HOMO highest occupied molecular orbital.

IC internal-coordinates.

KS Kohn-Sham.

LDA local density approximation.

LDOS local density of states.

LEED low-energy electron diffraction.

LUMO lowest unoccupied molecular orbital.

MDOS molecular density of states.

MIS metal-insulator-semiconductor.

NEXAFS near-edge X-ray absorption.

OTFT organic thin-film transistor.

PAW projector augmented-wave.

PES photoelectron spectroscopy.

PhS phenylthiolate.

PhSe phenylselenolate.

RAIRS reflection adsorption infrared spectroscopy.

SAM self-assembled monolayer.

SAMFET self-assembled-monolayers field-effect-transistors.

SD second derivative.

Si-PF 4-(2-(trichlorosilyl)ethyl)phenylester.

Si-PF-long 11-(trichlorosilyl)undecanoic-acid-phenyl-ester.

Si-SCN trimethoxy[4-(thiocyanatomethyl)phenyl]silane.

STM scanning tunneling microscopy.

TDS thermal desorption spectroscopy.

UHV ultrahigh vacuum.

UPS ultraviolet photoelectron spectroscopy.

UV ultraviolet.

VASP Vienna ab-initio simulation package.

W channel width.

XPS X-ray photoelectron spectroscopy.

XRR X-ray refectometry.

References

[1] G. Horowitz. Organic Field-Effect Transistors. *Advanced Materials*, 10:365–377, 1998.

[2] J. H. Burroughes, D. D. C. Bradley, A. R. Brown, R. N. Marks, K. Mackay, R. H. Friend, P. L. Burns, and A. B. Holmes. Light-Emitting-Diodes Based on Conjugated Polymers. *Nature*, 347:539–541, 1990.

[3] H. Hoppe and N. S. Sariciftci. Organic Solar Cells: An Overview. *Journal of Materials Research*, 19:1924–1945, 2004.

[4] B. Adhikari and S. Majumdar. Polymers in Sensor Applications. *Progress in Polymer Science*, 29:699–766, 2004.

[5] N. Koch. Organic electronic devices and their functional interfaces. *ChemPhysChem*, 8(10):1438–1455, 2007.

[6] H. Ishii, K. Sugiyama, E. Ito, and K. Seki. Energy Level Alignment and Interfacial Electronic Structures at Organic/Metal and Organic/Organic Interfaces . *Advanced Materials*, 11:605–625, 1999.

[7] S. Braun, W. R. Salaneck, and M. Fahlman. Energy-Level Alignment at Organic/Metal and Organic/Organic Interfaces. *Advanced Materials*, 21:1450–1472, 2009.

[8] A. Lex, G. Trimmel, W. Kern, and F. Stelzer. Photosensitive Polynorbornene Containing the Benzyl Thiocyanate Group - Synthesis and Patterning. *Journal of Molecular Catalysis A: Chemical*, 254:174–179, 2006.

[9] T. Höfler, A. M. Track, P. Pacher, Q. Shen, H.-G. Flesch, G. Hlawacek, G. Koller, M. G. Ramsey, R. Schennach, R. Resel, C. Teichert, W. Kern, G. Trimmel, and T. Griesser. Photoreactive Molecular Layers Containing Aryl Ester Units: Preparation, UV Patterning and Post-Exposure Modification. *Materials Chemistry and Physics*, 119:287–293, 2010.

[10] T. Griesser, A. M. Track, G. Koller, M. G. Ramsey, W. Kern, and G. Trimmel. Photoreactive Self Assembled Monolayers for Tuning the Surface Polarity. *Springer Proceeding in Physics*, 129:113–117, 2009.

[11] Christoph Stadler, Soren Hansen, Ingo Kroger, Christian Kumpf, and Eberhard Umbach. Tuning intermolecular interaction in long-range-ordered submonolayer organic films. *Nat Phys*, 5(2):153–158, 2009. 10.1038/nphys1176.

[12] A. Bashir, D. Käfer, J. Müller, Ch. Wöll, A. Terfort, and G. Witte. Selenium as a Key Element for Highly Ordered Aromatic Self-Assembled Monolayers. *Angewandte Chemie-International Edition*, 47:5250–5252, 2008.

[13] A. M. Track, F. Rissner, G. Heimel, L. Romaner, D. Käfer, A. Bashir, G. M. Rangger, O. T. Hofmann, T. Bučko, G. Witte, and E. Zojer. Simultaneously Understanding

the Geometric and Electronic Structure of Anthraceneselenolate on Au(111): A Combined Theoretical and Experimental Study. *The Journal of Physical Chemistry C*, 114:2677–2684, 2010.

[14] K. Oura, V. G. Lifshits, A. A. Saranin, A. V. Zotov, and M. Katayama. *Surface Science: An Introduction*. Springer-Verlag, 2003.

[15] M. Henzler and W. Göpel. *Oberflächenphysik des Festkörpers*. Teubner Studienbücher, 1994.

[16] A. Winkler. *Oberflächenanalytik*. Lecture notes, 2009.

[17] M. P. Seah and W. A. Dench. Quantitative Electron Spectroscopy of Surfaces: A Standard Data Base for Electron Inelastic Mean Free Paths in Solids. *Surface and Interface Analysis*, 1:2–11, 1979.

[18] G. Beamson and D. Briggs. *High Resolution XPS of Organic Polymers - The Scienta ESCA300 Database*. John Wiley & Sons, 1992.

[19] C. D. Wagner, W. M. Riggs, L .E. Davis, and J. F. Moulder. *Handbook of X-Ray Photoelectron Spectroscopy - A Reference Book of Standard Data For Use In X-Ray Photoelectron Spectroscopy*. Perkin-Elmer Corporation, 1979.

[20] N. Failrley. *CasaXPS*. Casa Software Ldt., version 2.3.14dev38 edition, 1999-2000.

[21] S. J. Kang, Y. Yi, C. Y. Kim, S. W. Cho, M. Noh, K. Jeong, and C. N. Whang. Energy Level Diagrams of C-60/Pentacene/Au and Pentacene/C-60/Au. *Synthetic Metals*, 156:32–37, 2006.

[22] G. Horowitz. *Organic Field-Effect Transistors*, chapter Charge Transport in Oligomers, pages 73–101. CRC Press, 2007.

[23] E. Zojer. *Organic Thin Fim Transistors*. Lecture notes, 2009.

[24] D. Boudinet, G. Le Blevennec, C. Serbutoviez, J.-M. Verilhac, H. Yan, and G. Horowitz. Contact Resistance and Threshold Voltage Extraction in n-Channel Organic Thin Film Transistors on Plastic Substrates. *Journal of Applied Physics*, 105(8):084510, APR 15 2009. ISSN 0021-8979. doi: {10.1063/1.3110021}.

[25] G. Horowitz, R. Hajlaoui, H. Bouchriha, R. Bourguiga, and M. Hajlaoui. The Concept of "Threshold Voltage" in Organic Field-Effect Transistors. *Advanced Materials*, 10: 923–927, 1998.

[26] R. Schroeder, L. A. Majewski, and M. Grell. A Study of the Threshold Voltage in Pentacene Organic Field-Effect Transistors. *Applied Physics Letters*, 83:3201–3203, 2003.

[27] E. J. Meijer, C. Tanase, P. W. M. Blom, E. van Veenendaal, B. H. Huisman, D. M. de Leeuw, and T. M. Klapwijk. Switch-on Voltage in Disordered Organic Field-Effect Transistors. *Applied Physics Letters*, 80:3838–3840, 2002.

[28] private comunication with Thomas Obermüller.

[29] H. S. Wong, M. H. White, T. J. Krutsick, and R. V. Booth. Modeling of Transconductance Degradation and Extraction of Threshold Volatge in Thin Oxide MOSFET. *Solid-State Electronics*, 30:953–968, 1987.

[30] A. Gross. *Theoretical Surface Science.* Springer, Berlin, 2003.

[31] F. Jensen. *Introduction to Computational Chemistry.* Wiley, 2007.

[32] W. Koch and M.C. Holthausen. *A Chemist's Guide to Density Functional Theory.* Wiley-VCH, 2001.

[33] M. Born and J.R. Oppenheimer. Über die Theorie der Molekeln. *Annalen der Physik*, 84:457, 1927.

[34] P. Hohenberg and W. Kohn. Inhomogeneous electron gas. *Physical Review B*, 136: B864–B871, 1964.

[35] W. Kohn and L. J. Sham. Self-Consistent Equations Including Exchange and Correlation Effects. *Physical Review*, 140:1133, 1965.

[36] L. H. Thomas. The Calculation of Atomic Fields. *Proceedings of the Cambridge Philosophical Society*, 23:542–548, 1927.

[37] E. Fermi. Un Metodo Statistice per la Determinazione di Alcune Priorieta dell'Atomo. *Rend. Accad. Lincei*, 6:602, 1927.

[38] F. Bloch. The Electron Theory of Ferromagnetism and Electron Conductivity. *Zeitschrift für Physik*, 57:545, 1929.

[39] P. A. M. Dirac. Note on Exchange Phenomena in the Thomas Atom. *Proceedings of the Cambridge Philosophical Society*, 26:376, 1930.

[40] M. Dion, H. Rydberg, E. Schröder, D. C. Langreth, and B. I. Lundqvist. Van der Waals Density Functional for General Geometries. *Physical Reviews Letters*, 92: 246401, 2004.

[41] H Rydberg, M Dion, N Jacobson, E Schroder, P Hyldgaard, SI Simak, DC Langreth, and BI Lundqvist. Van der Waals Density Functional for Layered Structures. *Physical Review Letters*, 91:126402, 2003.

[42] L. Romaner, D. Nabok, P. Puschnig, E. Zojer, and C. Ambrosch-Draxl. Theoretical Study of PTCDA Adsorbed on the Coinage Metal Surfaces, Ag(111), Au(111) and Cu(111). *New Journal of Physics*, 11:053010, 2009.

[43] J. P. Perdew, J. A. Chevary, S. H. Vosko, K. A. Jackson, M. R. Pederson, D. J. Singh, and C. Fiolhais. Atoms, Molecules, Solids, and Surfaces - Applications of the Generalized Gradient Approximation for Exchange and Correlation. *Physical Review B*, 46:6671–6687, 1992.

[44] J. P. Perdew, K. Burke, and M. Ernzerhof. Generalized Gradient Approximation Made Simple. *Physical Review Letters*, 77:3865–3868, 1996.

[45] D. S. Sholl and J . A. Steckel. *Denisty Functional Theory: A Practrical Introduction.* John Wiley & Sons, 2009.

[46] F. Bloch. Über die Quantenmechanik der Elektronen in Kristallgittern. *Zeitschrift für Physik*, 52:555–600, 1928.

[47] C. Kittel. *Einführung in die Festkörperphysik.* Oldenbourg Wissentschaftsverlag, 2006.

[48] P. E. Blöchl. Projector Augmented-Wave Method. *Physical Review B*, 50:17953–17979, 1994.

[49] G. Kresse and D. Joubert. From Ultrasoft Pseudopotentials to the Projector Augmented-Wave Method. *Physical Review B*, 59:1758–1775, 1999.

[50] H. J. Monkhorst and J. D. Pack. Special Points for Brillouin-Zone Integrations. *Physical Review B*, 13:5188–5192, 1976.

[51] J. Neugebauer and M. Scheffler. Adsorbate-Substrate and Adsorbate-Adsorbate Interactions of Na and K Adlayers on Al(111). *Physical Review B*, 46:16067–16080, 1992.

[52] T. Bučko, J. Hafner, and J. G. Ángyán. Geometry Optimization of Periodic Systems Using Internal Coordinates. *The Journal of Chemical Physics*, 122:124508–10, 2005.

[53] G. Kresse and J. Furthmüller. Efficiency of Ab-Initio Total Energy Calculations for Metals and Semiconductors Using a Plane-Wave Basis Set. *Computational Materials Science*, 6:15–50, 1996.

[54] E. B. J. Wilson, J. C. Decius, and P. C. Cross. *Molecular Vibirations. The Theory of Infrared and Raman Vibrational Spectra.* Dover, 1955.

[55] P. Császár and P. Pulay. Geometry Optimization by Direct Inversion in the Iterative Subspace. *Journal of Molecular Structure*, 114:31–34, 1984.

[56] Ö. Farkas and H. B. Schlegel. Methods for Optimizing Large Molecules - Part III. An Improved Algorithm for Geometry Optimization Using Direct Inversion in the Iterative Subspace (GDIIS). *Physical Chemistry Cchemical Physics*, 4:11–15, 2002.

[57] G. Heimel, L. Romaner, J. L. Bredas, and E. Zojer. Organic/Metal Interfaces in Self-Assembled Monolayers of Conjugated Thiols: A First-Principles Benchmark Study. *Surface Science*, 600:4548–4562, 2006.

[58] J. Bardeen. Tunneling from a many-Particle Point of View. *Physical Review Letters*, 6:57, 1961.

[59] J. Tersoff and D. R. Hamann. Theory and application for the scanning tunneling microscope. *Physical Review Letters*, 50:1998–2001, 1983.

[60] J. F. Wolf. *Rastertunnelmikroskopie an 2D-Molekülkristallen an der Fest/Flüssig-Grenze*. Lecture Notes, 2000.

[61] J. Tersoff and D. R. Hamann. Theory of the scanning tunneling microscope. *Physical Review B*, 31:805–813, 1985.

[62] R. Hoffmann. *Solids and Surfaces: A Chemist's View of Bonding in Extended Structures* . Wiley, 1989.

[63] A. Ulman. Formation and Structure of Self-Assembled Monolayers. *Chemical Reviews*, 96:1533–1554, 1996.

[64] J. C. Love, L. A. Estroff, J. K. Kriebel, R. G. Nuzzo, and G. M. Whitesides. Self-Assembled Monolayers of Thiolates on Metals as a Form of Nanotechnology. *Chemical Reviews*, 105:1103–1169, 2005.

[65] F. Schreiber. Structure and Growth of Self-Assembling Monolayers. *Progress in Surface Science*, 65:151–256, 2000.

[66] W. Senaratne, L. Andruzzi, and C. K. Ober. Self-Assembled Monolayers and Polymer Brushes in Biotechnology: Current Applications and Future Perspectives. *Biomacromolecules*, 6:2427–2448, 2005.

[67] S. Onclin, B. J. Ravoo, and D. N. Reinhoudt. Engineering Silicon Oxide Surfaces Using Self-Assembled Monolayers. *Angewewnadte Chemie International Edition*, 44: 6282–6304, 2005.

[68] D. K. Aswal, S. Lenfant, D. Guerin, J. V. Yakhmi, and D. Vuillaume. Self Assembled Monolayers on Silicon for Molecular Electronics. *Analytica Chimica Acta*, 568:84 – 108, 2005.

[69] T. Shimura and K. Aramaki. Self-Assembled Monolayers of p-Toluene and p-Hydroxymethylbenzene Moieties Adsorbed on Iron by the Formation of Covalent Bonds between Carbon and Iron Atoms for Protection of Iron from Corrosion. *Corrosion Science*, 49:1378–1393, 2007.

[70] P. E. Laibinis and G. M. Whitesides. ω-Terminated Alkanethiolate Monolayers on Surfacees of Copper, Silver, and Gold Have Similar Wettabilites. *Journal of the American Chemical Society*, 114:1990–1995, 1992.

[71] B. D. Beake and G. J. Leggett. Friction and Adhesion of Mixed Self-Assembled Monolayers Studied by Chemical Force Microscopy. *Physical Chemistry Chemical Physics*, 1:3345–3350, 1999.

[72] K. Ichimura, S. K. Oh, and M. Nakagawa. Light-Driven Motion of Liquids on a Photoresponsive Surface. *Science*, 288:1624–1626, 2000.

[73] J. Lahann, S. Mitragotri, T. N. Tran, H. Kaido, J. Sundaram, I. S. Choi, S. Hoffer, G. A. Somorjai, and R. Langer. A Reversibly Switching Surface. *Science*, 299:371–374, 2003.

[74] M.-S. Chen, C. S. Dulcey, L. A. Chrisey, and W. J. Dressick. Deep-UV Photochemistry and Patterning of (Aminoethylaminomethyl)phenethylsiloxane Self-Assembled Monolayers. *Advanced Functional Materials*, 16:774–783, 2006.

[75] C. S. Dulcey, J. H. Georger Jr., V. Krauthamer, D. A. Stenger, T. L. Fare, and J. M. Calvert. Deep UV Photochemistry of Chemisorbed Monolayers: Patterned Coplanar Molecular Assemblies. *Science*, 252:551–554, 1991.

[76] K. Critchley, J. P. Jeyadevan, H. Fukushima, M. Ishida, T. Shimoda, R. J. Bushby, and S. D. Evans. A Mild Photoactivated Hydrophilic/Hydrophobic Switch. *Langmuir*, 21:4554–4561, 2005.

[77] K. Tamada, H. Akiyama, and T. X. Wei. Photoisomerization Reaction of Unsymmetrical Azobenzene Disulfide Self-Assembled Monolayers Studied by Surface Plasmon Spectroscopy: Influences of Side Chain Length and Contacting Medium. *Langmuir*, 18:5239–5246, 2002.

[78] T. Griesser, J. Adams, J. Wappel, W. Kern, G. J. Leggett, and G. Trimmel. Micrometer and Nanometer Scale Patterning Using the Photo-Fries Rearrangement: Toward Selective Execution of Molecular Transformations with Nanoscale Spatial Resolution. *Langmuir*, 24:12420–12425, 2008.

[79] T. Höfler. *Photoreactive Polymers and Surfaces Layers Based upon the Photo-Fries Rearrangement*. PhD thesis, Technische Universität Graz, 2005.

[80] A. Lex, P. Pacher, O. Werzer, A. M. Track, Q. Shen, R. Schennach, G. Koller, G. Hlawacek, E. Zojer, R. Resel, M. G. Ramsey, C. Teichert, W. Kern, and G. Trimmel. Synthesis of a Photosensitive Thiocyanate-Functionalized Trialkoxysilane and its Application in Patterned Surface Modifications. *Chemistry of Materials*, 20:2009–2015, 2008.

[81] U. Mazzucato, G. Beggiato, and G. Favaro. Reversible Photoisomerisationof Benzyl Thiocyanateand Isothiocyanate. *Tetrahydron Letters*, 45:5455, 1966.

[82] T. E. Parks and L. A. Spurlock. Photolytically Induced Interconversions of Benzyl Thiocyanates and Isothiocyanates. *Journal of Organic Chemistry*, 38:3922–3924, 1973.

[83] G. Langer, T. Kavc, W. Kern, G. Kranzelbinder, and E. Toussaere. Refractive Index Changes in Polymers Induced by Deep UV Irradiation and Subsequent Gas Phase Modification. *Macromol. Chem. Phys.*, 202:3459–3467, 2001.

[84] L. G. Parratt. Surface Studies of Solids by Total Reflection of X-Rays. *Physical Review*, 95:359–369, 1954.

[85] L. Nevot and P. Croce. Caractérisation des Surfaces par Réflexion Rasante de Rayons X. Application à l'étude du Polissage de Quelques Verres Silicates. *Revue Physique Appliqueé*, 15:761–779, 1980.

[86] Y. L. Wang and M. Lieberman. Growth of Ultrasmooth Octadecyltrichlorosilane Self-Assembled Monolayers on SiO_2. *Langmuir*, 19:1159–1167, 2003.

[87] G. Hlawacek, Q. Shen, C. Teichert, A. Lex, G. Trimmel, and W. Kern. Hierarchy of Adhesion Forces in Patterns of Photoreactive Surface Layers. *Journal of Chemicla Physics*, 130:5, 2009.

[88] W. Kern and K. Hummel. Photoreactive Polymers of 4-Vinylbenzyl Thiocyanate. *European Polymer Journal*, 31:437–443, 1995.

[89] J. F. Moulder, W. F. Stickle, P. E. Sobol, and K . D. Bomben. *Handbook of X-Ray Photoelectron Spectroscopy*. Physical Electronics , Inc., 1995.

[90] M. D. Ellison and R. J. Hamers. Adsorption of Phenyl Isothiocyanate on Si(001): A 1,2-Dipolar Surface Addition Reaction. *Journal of Physical Chemistry B*, 103: 6243–6251, 1999.

[91] P. Cyganik, M. Buck, W. Azzam, and C. Wöll. Self-Assembled Monolayers of ω-Biphenylalkanethiols on Au(111): Influence of Spacer Chain on Molecular Packing. *Journal of Physical Chemistry B*, 108:4989–4996, 2004.

[92] C. D. Wagner, L. E. Davis, M. V. Zeller, J. A. Taylor, R. H. Raymond, and L. H. Gale. Emperical Atomic Sensitiviy Factors for Quantitative-Analyse by Electron-Spectroscopy for Chemical-Analysis. *Surface and Interface Analysis*, 3:211–225, 1981.

[93] T. Kavc, G. Langer, W. Kern, G. Kranzelbinder, G. A. Toussaere, E.and Turnbull, I. D. W. Samuel, K. F. Iskra, T. Neger, and A. Pogantsch. Index and Relief Gratings in Polymer Films for Organic Distributed Feedback Lasers. *Chemistry of Materials*, 14:4178–4185, 2002.

[94] A. Lex. Synthese und Charakterisierung photosensitiver Benzylthiocyanatverbindungen. Master's thesis, Technische Universität Graz, 2004.

[95] C. Auner. Herstellung von photreactiven dünnen Schichten auf Basis von Benzylthiocyanate und Benzylsulfonen. Master's thesis, Technische Unitversität Graz, 2006.

[96] I. Novak. *The Chemistry of Organic Derivatives of Gold and Silver*, chapter The Photoelectron Spectroscopy of Organic Derivatives of Gold and Silver, pages 103–129. Wiley, 1999.

[97] T. Griesser, S. Hoefler, T.and Temmel, W. Kern, and G. Trimmel. Photolithographic Patterning of Polymer Surfaces Using the Photo-Fries Rearrangement: Selective Postexposure Reactions. *Chemistry of Materials*, 19:3011–3017, 2007.

[98] S. Flink, F. C. J. M. van Veggel, and D. N. Reinhoudt. Functionalization of Self-Assembled Monolayers on Glass and Oxidized Silicon Wafers by Surface Reactions. *Journal of Physical Organic Chememistry*, 14:407–415, 2001.

[99] J. C. Anderson and C. B. Reese. Photo-Induced Fries Rearrangements. *Proceedings of the Chemical Society Londondon*, 6:217, 1960.

[100] D. Belluš. *Advances in Photochemistry*, chapter Photo-Fries Rearrangement and Related Photochemical [1,j] -Shifts (j = 3, 5, 7) of Carbonyl and Sulfonyl Groups, pages 109–159. Wiley, 1971.

[101] C. E. Kalmus and D. M. Hercules. Mechanistic Study of Photo-Fries Rearrangement of Phenylacetate. *Journal of the American Chemical Scociety*, 96:449–456, 1974.

[102] C. K. Wang and Y. Luo. Current-votage characteristics of single molecular junction: Dimensionality of metal contacts. *Journal of Chemical Physics*, 119:4923–4928, 2003.

[103] M. Morita, T. Ohmi, E. Hasegawa, M. Kawakami, and M. Ohwada. Growth of Native Oxide on a Silicon Surface. *Journal of Applied Physics*, 68:1272–1281, 1990.

[104] S. Iwata and A. Ishizaka. Electron Spectroscopic Analysis of the SiO_2/Si System and Correlation with Metal-Oxide-Semiconductor Device Characteristics. *Journal of Applied Physics*, 79:6653–6713, 1996.

[105] D. K. Owens and R. C. Wendt. Estimation of Surface Free Energy of Polymers. *Journal of Applied Polymer Science*, 13(8):1741, 1969. ISSN 0021-8995.

[106] E. C. P. Smits, S. G. J. Mathijssen, P. A. van Hal, S. Setayesh, T. C. T. Geuns, K. A. H. A. Mutsaers, E. Cantatore, H. J. Wondergem, O. Werzer, R. Resel, M. Kemerink, S. Kirchmeyer, A. M. Muzafarov, S. A. Ponomarenko, B. de Boer, P. W. M. Blom, and D. M. de Leeuw. Bottom-Up Organic Integrated Circuits. *Nature*, 455:956–959, 2008.

[107] T. Höfler, T. adn Griesser, M. Gruber, G. Jakopic, G. Trimmel, and W. Kern. Photo-Fries Rearrangement in Polymeric Media: An Investigation on Fully Aromatic Esters Containg the Naphthyl Chromophore. *Macromolecular Chemistry and Physics*, 209: 488–498, 2008.

[108] G. E. Poirier and M. J. Tarlov. The c(4×2) Superlatticeof n-Alkanethiol Monolayers Self-Assembled on Au(111). *Langmuir*, 10:2853–2856, 1994.

[109] private comunication in the group of Prof. Witte.

[110] P. Stadler, A. M. Track, M. Ullah, H. Sitter, G. J. Matt, G. Koller, T. B. Singh, H. Neugebauer, N. S. Sariciftci, and M. G. Ramsey. The Role of the Dielectric Interface in Organic Transistors: A Combined Device and Photoemission Study. *Organic Electronics*, 11:207–211, 2010.

[111] G. Mottaghi, M.and Horowitz. Field-Induced Mobility Degradation in Pentacene Thin-Film Transistors. *Organic Electronics*, 7:528–536, 2006.

[112] X. H. Zhang and B. Kippelen. Low-Voltage C_{60} Organic Field-Effect Transistors with High Mobility and Low Contact Resistance. *Applied Physics Letters*, 93:133305, 2008.

[113] X.-H. Zhang, B. Domercq, and B. Kippelen. High-Performance and Electrically Stable C_{60} Organic Field-Effect Transistors. *Applied Physics Letters*, 91:092114, 2007.

[114] L. L. Chua, J. Zaumseil, J. F. Chang, E. C. W. Ou, P. K. H. Ho, H. Sirringhaus, and R. H. Friend. General Observation of n-Type Field-Effect Behaviour in Organic Semiconductors. *Nature*, 434:194–199, 2005.

[115] C. Celle, C. Suspene, J.-P. Simonato, S. Lenfant, M. Ternisien, and D. Vuillaume. Self-Assembled Monolayers for Electrode Fabrication and Efficient Threshold Voltage Control of organic Transistors with Amorphous Semiconductor Layer. *Organic Electronics*, 10:119–126, 2009.

[116] H. Klauk, U. Zschieschang, and M. Halik. Low-Voltage Organic Thin-Film Transistors with Large Transconductance. *Journal of Applied Physics*, 102:074514, 2007.

[117] M.-H. Yoon, C. Kim, A. Facchetti, and T. J. Marks. Gate Dielectric Chemical Structure-Organic Field-Effect Transistor Performance Correlations for Electron, Hole, and Ambipolar Organic Semiconductors. *Journal of the American Chemical Society*, 128:12851–12869, 2006.

[118] Y. Y. Lin, D. J. Gundlach, S. F. Nelson, and T. N. Jackson. Stacked Pentacene Layer Organic Thin-Film Transistors with Improved Characteristics. *IEEE Electron Device Letters*, 18:606–608, 1997.

[119] D. J. Gundlach, J. A. Nichols, L. Zhou, and T. N. Jackson. Thin-Film Transistors Based on Well-Ordered Thermally Evaporated Naphthacene Films. *Applied Physics Letters*, 80:2925–2927, 2002.

[120] S. Kobayashi, T. Nishikawa, T. Takenobu, S. Mori, T. Shimoda, T. Mitani, H. Shimotani, N. Yoshimoto, S. Ogawa, and Y. Iwasa. Control of Carrier Density by Self-Assembled Monolayers in Oorganic Field-Effect Transistors. *Nature Materials*, 3: 317–322, 2004.

[121] H. Ishii, H. Oji, E. Ito, N. Hayashi, D. Yoshimura, and K. Seki. Energy level alignment and band bending at model interfaces of organic electroluminescent devices. *Journal of Luminescence*, 87-89:61–65, 2000.

[122] S. K. Possanner, K. Zojer, P. Pacher, E. Zojer, and F. Schuerrer. Threshold Voltage Shifts in Organic Thin-Film Transistors Due to Self-Assembled Monolayers at the Dielectric Surface. *Advanced Functional Materials*, 19:958–967, 2009.

[123] Y. Jang, J. H. Cho, D. H. Kim, Y. D. Park, M. Hwang, and K. Cho. Effects of the Permanent Dipoles of Self-Aassembled Monolayer-Treated Insulator Surfaces on the Field-Effect Mobility of a Pentacene Thin-Film Transistor. *Applied Physics Letters*, 90:132104, 2007.

[124] L. A. Majewski, R. Schroeder, M. Grell, P. A. Glarvey, and M. L. Turner. High Capacitance Organic Field-Effect Transistors with Modified Gate Insulator Surface. *Journal of Applied Physics*, 96:5781–5787, 2004.

[125] R. Schroeder, L. A. Majewski, and M. Grell. All-Organic Permanent Memory Transistor Using an Amorphous, Spin-Cast Ferroelectric-Like Gate Insulator. *Advanced Materials*, 16:633+, 2004.

[126] A. Y. Andreev, C. Teichert, G. Hlawacek, H. Hoppe, R. Resel, D. M. Smilgies, H Sitter, and NS Sariciftci. Morphology and Growth Kinetics of Organic Thin Films Deposited by Hot Wall Epitaxy. *Organic Electronics*, 5:23–27, 2004.

[127] C. J. Brabec, S. E. Shaheen, C. Winder, N. S. Sariciftci, and P. Denk. Effect of LiF/Metal Electrodes on the Performance of Plastic Solar Cells. *Applied Physics Letters*, 80:1288–1290, 2002.

[128] T. D. Anthopoulos, B. Singh, N. Marjanovic, N. S. Sariciftci, A. M. Ramil, H. Sitter, M. Colle, and D. M. de Leeuw. High Performance n-Channel Organic Field-Effect Transistors and Ring Oscillators Based on C-60 Fullerene Films. *Applied Physics Letters*, 89:213504, 2006.

[129] T. B. Singh and N. S. Sariciftci. Progress in Plastic Electronics Devices. *Annual Rieview of Materials Research*, 36:199–230, 2006.

[130] J. Ivanco, B. Winter, F. P. Netzer, M. G. Ramsey, L. Gregoratti, and M. Kiskinova. Oxygen as a Surfactant for Al Contact Metallization of Organic Layers. *Applied Physics Letters*, 85:585–587, 2004.

[131] R. I. R. Blyth, S. A. Sardar, F. P. Netzer, and M. G. Ramsey. Influence of Oxygen on Band Alignment at the Organic/Aluminum Interface. *Applied Physics Letters*, 77: 1212–1214, 2000.

[132] W. Osikowicz, M. P. de Jong, and W. R. Salaneck. Formation of the Interfacial Dipole at Organic-Organic Interfaces: C-60/Polymer Interfaces. *Advanced Materials*, 19:4213–4217, 2007.

[133] I. F. Torrente, K. J. Franke, and J. I. Pascual. Spectroscopy of C_{60} Single Molecules: the Role of Screening on Energy Level Alignment. *Journal of Physics-Condensed Matter*, 20:184001, 2008.

[134] D. Chen and L. Jinghong. Interfacial Design and Functionization on Metal Electrodes Through Self-Assembled Monolayers. *Surface Science Report*, 61:445–463, 2006.

[135] J. Nara, S. Higai, Y. Morikawa, and T. Ohno. Density Functional Theory Investigation of Benzenethiol Adsorption on Au(111). *Journal of Chemical Physics*, 120: 6705–6711, 2004.

[136] A. Bilic, J. R. Reimers, and N. S. Hush. The Structure, Energetics, and Nature of the Chemical Bonding of Phenylthiol Adsorbed on the Au(111) Surface: Implications for Density-Functional Calculations of Molecular-Electronic Conduction . *Journal of Chemical Physics*, 122(9):094708, 2005.

[137] Y. Yourdshahyan, H. K. Zhang, and A. M. Rappe. n-Alkyl Thiol Head-Group Interactions with the Au(111) Surface. *Physical Review B*, 63:081405, 2001.

[138] A. Franke and E. Pehlke. Adsorption and Diffusion of SCH_3 radicals and $Au(SCH_3)_2$ Complexes on the Unreconstructed Au(111) Surface in the Submonolayer Coverage Regime. *Physical Review B*, 79:235441, 2009.

[139] G. Kresse and J. Furthmüller. Efficient Iterative Schemes for Ab Initio Total-Energy Calculations Using a Plane-Wave Basis Set. *Physical Review B*, 54:11169–11186, 1996.

[140] G. Kresse and J. Hafner. Ab Initio Molecular Dynamics for Liquid Metals. *Physical Review B*, 47:558–561, 1993.

[141] G. Kresse and J. Hafner. Ab Initio Molecular Dynamics for Open-Shell Transition Metals. *Physical Review B*, 48:13115, 1993.

[142] G. Kresse and J. Hafner. Ab-Initio Molecular-Dynamics Simulation of the Liquid-Metal Amorphous-Semiconductor Transition in Germanium. *Physical Review B*, 49: 14251–14269, 1994.

[143] G. M. Rangger, L. Romaner, G. Heimel, and E. Zojer. Understanding the Properties of Interfaces between Organic Self-Assembled Monolayers and Noble Metals - a Theoretical Perspective. *Surface and Interface Analysis*, 40:371–378, 2008.

[144] D. Käfer, G. Witte, P. Cyganik, and C. Terfort, A.and Wöll. A Comprehensive Study of Self-Assembled Monolayers of Anthracenethiol on Gold: Solvent eEfects, Structure, and Stability. *Journal of the American Chemical Society*, 28:1723–1732, 2006.

[145] Y. Morikawa, T. Hayashi, C. C. Liew, and H. Nozoye. First-Principles Theoretical Study of Alkylthiolate Adsorption on Au(111). *Surface Science*, 507:46–50, 2002.

[146] J. Nara, S. Higai, Y. Morikawa, and T. Ohno. Adsorption Structure of Benzenethiol on Au(111): First-Principles Study. *Applied Surface Science*, 237:433–438, 2004.

[147] F. K. Huang, R. C. Horton, D. C. Myles, and R. L. Garrell. Selenolates as Alternatives to Thiolates for Self-Assembled Monolayers: A SERS Study. *Langmuir*, 14:4802–4808, 1998.

[148] C. K. Yee, A. Ulman, J. D. Ruiz, A. Parikh, H. White, and M. Rafailovich. Alkyl Selenide- and Alkyl Thiolate-Functionalized Gold Nanoparticles: Chain Packing monkand Bond Nature. *Langmuir*, 19:9450–9458, 2003.

[149] S. Mankefors, A. Grigoriev, and G. Wendin. Molecular Alligator Clips: a Theoretical Study of Adsorption of S, Se and S-H on Au(111). *Nanotechnology*, 14:849–858, 2003.

[150] K. Szelagowska-Kunstman, B. Cyganik, P. adn Schüpbach, and A. Terfort. Relative Stability of Thiol and Selenol Based SAMs on Au(111) - Exchange Experiments. *Physical Chemistry Chemical Physics*, 12:4400–4406, 2010.

[151] K. Yokota, M. Taniguchi, and T. Kawai. Control of the Electrode-Molecule Interface for Molecular Devices. *Journal of the American Chemical Society*, 129:5818, 2007.

[152] D. Käfer, A. Bashir, and G. Witte. Interplay of Anchoring and Ordering in Aromatic Self-Assembled Monolayers. *Journal of Physical Chemistry C*, 111:10546–10551, 2007.

[153] P. Cyganik, K. Szelagowska-Kunstman, A. Terfort, and M. Zharnikov. Odd-Even Effect in Molecular Packing of Biphenyl-Substituted Alkaneselenolate Self-Assembled Monolayers on Au(111): Scanning Tunneling Microscopy Study. *Journal of Physical Chemistry C*, 112:15466–15473, 2008.

[154] D. M. Alloway, M. Hofmann, D. L. Smith, N. E. Gruhn, A. L. Graham, R. Colorado, V. H. Wysocki, T. R. Lee, P. A. Lee, and N. R. Armstrong. Interface Dipoles Arising from Self-Assembled Monolayers on Gold: UV-Photoemission Studies of Alkanethiols and Partially Fluorinated Alkanethiols. *Journal of Physical Chemistry B*, 107(42): 11690–11699, 2003.

[155] R. W. Zehner, B. F. Parsons, R. P. Hsung, and L. R. Sita. Tuning the Work Function of Gold with Self-Assembled Mmonolayers Derived from $X-[C_6H_4-C\equiv C-]_nC_6H_4-SH(n=0,1,2;X=H,F,CH_3,CF_3,\text{and}OCH_3)$. *Langmuir*, 15:1121–1127, 1999.

[156] I. H. Campbell, J. D. Kress, R. L. Martin, D. L. Smith, N. N. Barashkov, and J. P. Ferraris. Controlling Charge Injection in Organic Electronic Devices Using Self-Assembled Monolayers. *Applied Physics Letters*, 71(24):3528–3530, 1997.

[157] L. A. Bumm, J. J. Arnold, M. T. Cygan, T. D. Dunbar, T. P. Burgin, L. Jones, D. L. Allara, J. M. Tour, and P. S. Weiss. Are Single Molecular Wires Conducting? *Science*, 271:1705–1707, 1996.

[158] M. Elbing, R. Ochs, M. Koentopp, M. Fischer, C. von Hanisch, F. Weigend, F. Evers, H.B. Weber, and M. Mayor. A Single-Molecule Diode. *Proceedings of the National Academy of Science of the United States of America*, 102:8815–8820, 2005.

[159] P. Jiang, G.M. Morales, W. You, and L.P. Yu. Synthesis of Diode Molecules and their Sequential Assembly to Control Electron Transport. *Angewandte Chemie- International Edition*, 43:4471–4475, 2004.

[160] H. B. Akkerman, P. W. M. Blom, D. M. de Leeuw, and B. de Boer. Towards Molecular Electronics with Large-Area Molecular Junctions. *Nature*, 441(7089):69–72, 2006.

[161] P Cyganik, M. Buck, T. Strunskus, A. Shaporenko, J. D. E. T. Wilton-Ely, M. Zharnikov, and C. Wöll. Competition as a Design Concept: Polymorphism in Self-Assembled Monolayers of Biphenyl-Based Thiols. *Journal of the American Chemical Society*, 128:13868–13878, 2006.

[162] S. Frey, V. Stadler, K. Heister, W. Eck, M. Zharnikov, M. Grunze, B. Zeysing, and A. Terfort. Structure of thioaromatic Self-Assembled Monolayers on Gold and Silver. *Langmuir*, 17:2408–2415, 2001.

[163] L. Romaner, G. Heimel, and E. Zojer. Electronic Structure of Thiol-Bonded Self-Assembled Monolayers: Impact of Coverage. *Physical Review B*, 77:045113, 2008.

[164] M. Zharnikov, .S Frey, H. Rong, Y. J. Yang, K. Heister, M. Buck, and M. Grunze. The Effect of Sulfur-Metal Bonding on the Structure of Self-Assembled Monolayers. *Physical Chemistry Chemical Physics*, 2:3359–3362, 2000.

[165] K. Heister, H. T. Rong, M. Buck, M. Zharnikov, M. Grunze, and L. S. O. Johansson. Odd-Even Effects at the S-Metal Interface and in the Aromatic Matrix of Biphenyl-Substituted Alkanethiol Self-Assembled Monolayers. *Journal of Physical Chemistry B*, 105:6888–6894, 2001.

[166] N. K. Chaki, M. Aslam, T. G. Gopakumar, J. Sharma, R. Pasricha, I. S. Mulla, and K. Vijayamohanan. Effect of Chain Length and the Nature of the Monolayer on the Electrical Behavior of Hydrophobically Organized Gold Clusters. *Journal of Physical Chemistry B*, 107:13567–13574, 2003.

[167] G. Heimel, L. Romaner, J. L. Bredas, and E. Zojer. Odd-Even Effects in Self-Assembled Monolayers of ω-(Biphenyl-4-yl)alkanethiols: A First-Principles Study. *Langmuir*, 24:474–482, 2008.

[168] M. H. Dishner, J. C. Hemminger, and F. J. Feher. Scanning Tunneling Microscopy Characterization of Organoselenium Monolayers on Au(111). *Langmuir*, 13:4788–4790, 1997.

[169] A. Shaporenko, P. Cyganik, M. Buck, A. Ulman, and M. Zharnikov. Self-Assembled Monolayers of Semifluorinated Alkaneselenolates on Noble Metal Substrates. *Langmuir*, 21:8204–8213, 2005.

[170] A. Shaporenko, A. Ulman, A. Terfort, and M. Zharnikov. Self-Assembled Monolayers of Alkaneselenolates on (111) Gold and Silver. *The Journal of Physical Chemistry B*, 109:3898–3906, 2005.

[171] G. Heimel, L. Romaner, J. L. Bredas, and E. Zojer. Interface Energetics and level Alignment at Covalent Metal-Molecule Junctions: π-Conjugated Thiols on Gold. *Physical Review Letters*, 96:196806, 2006.

[172] G. Heimel, L. Romaner, E. Zojer, and J. L. Bredas. Toward Control of the Metal-Organic Interfacial Electronic Structure in Molecular Electronics: A First-Principles Study on Self-Assembled Monolayers of π-Conjugated Molecules on Noble Metals. *Nano Letters*, 7:932, 2007.

[173] R. Mason. Crystallography of Anthracene at 95°K + 290°K. *Acta Crystallographica*, 17:547, 1964.

[174] M. Methfessel and A. T. Paxton. High-Precision Sampling for Brillouin-Zone Integration in Metals. *Physical Review B*, 40:3616–3621, 1989.

[175] J. V. Barth, H. Brune, G. Ertl, and R. J. Behm. Scanning Tunneling Microscopy Observations on the Reconstructed Au(111) Surface - Atomic-Structure, Long-Range superstructure, Rotational Domains, and surface-Defectsda. *Physical Review B*, 42: 9307–9318, 1990.

[176] S. B. Darling, A. W. Rosenbaum, Y. Wang, and S. J. Sibener. Coexistence of the (23 x root 3) Au(111) Reconstruction and a Striped Phase Self-Assembled Monolayer. *Langmuir*, 18:7462–7468, 2002.

[177] D. Käfer, A. Bashir, X. Dou, G. Witte, K. Müllen, and C. Wöll. Evidence for Band-Like Transport in Graphene-Based Organic Monolayers. *Advanced Materials*, 21:1–5, 2009.

[178] D. M. Ceperley and B. J. Alder. Ground State of the Electron Gas by a Stochastic Method. *Phys.ical Review Letter*, 45:566–569, 1980.

[179] J. P. Perdew and A. Zunger. Self-interaction Correction to Density-Functional Approximations for Many-Electron Systems. *Physicla Review B*, 23:5048–5079, 1981.

[180] M. Yu, N. Bovet, C. J. Satterley, S. Bengio, K. R. J. Lovelock, P. K. Milligan, R. G. Jones, D. P. Woodruff, and V. Dhanak. True Nature of an Archetypal Self-Assembly System: Mobile Au-Thiolate Species on Au(111). *Pysical Review Letters*, 97:4, 2006.

[181] A. Chaudhuri, T. J. Lerotholi, D. C. Jackson, D. P. Woodruff, and V. Dhanak. Local Methylthiolate Adsorption Geometry on Au(111) from Photoemission Core-Level Shifts. *Physical Review Letters*, 102:126102, 2009.

[182] A. Kokalj. Computer graphics and Graphical user interfaces as Tools in Simulations of Matter at the Atomic Scale. *Computational Materials Science*, 28:155–168, 2003.

[183] A. Cossaro, R. Mazzarello, R. Rousseau, L. Casalis, A. Verdini, A. Kohlmeyer, L. Floreano, S. Scandolo, A. Morgante, M. L. Klein, and G. Scoles. X-Ray Diffraction and Computation Yield the Structure of Alkanethiols on Gold(111). *Science*, 321:943–946, 2008.

[184] M. Oehzelt, R. Resel, and A. Nakayama. High-Pressure Structural Properties of Anthracene up to 10 GPa. *Physical Review B*, 66:5, 2002.

[185] M. Oehzelt, G. Heimel, R. Resel, P. Puschnig, K. Hummer, C. Ambrosch-Draxl, K. Takemura, and A. Nakayama. High Pressure X-Ray Study on Anthracene. *Journal of Chemical Physics*, 119:1078–1084, 2003.

[186] K. Hummer, P. Puschnig, and C. Ambrosch-Draxl. Ab Initio Study of Anthracene Under High Pressure. *Physical Review B*, 67:7, 2003.

[187] G. Heimel, L. Romaner, and J.-L. Zojer, E.and Bredas. The Interface Energetics of Self-Assembled Monolayers on Metals. *Accounts of Chemical Research*, 41:721–729, 2008.

[188] G. Heimel, L. Romaner, E. Zojer, and J.-L. Bredas. A theoretical view on self-assembled monolayers in organic electronic devices. In *Organic Optoelectronics and Photonics III*, volume 6999, pages 699919–12, Strasbourg, France, 2008. SPIE.

[189] A. Natan, L. Kronik, H. Haick, and R. T. Tung. Electrostatic Properties of Ideal and Non-Ideal Polar Organic Monolayers: Implications for Electronic Devices. *Advanced Materials*, 19:4103–4117, 2007.

[190] D. Cornil, Y. Olivier, V. Geskin, and J. Cornil. Depolarization Effects in Self-Assembled Monolayers: A Quantum-Chemical Insight. *Advanced Functional Materials*, 17(7):1143–1148, 2007.

[191] L. Romaner, G. Heimel, C. Ambrosch-Draxl, and E. Zojer. The Dielectric Constant of Self-Assembled Monolayers. *Advanced Functional Materials*, 18(2):3999–4006, 2008.

[192] S. Berkebile, P. Puschnig, G. Koller, M. Oehzelt, F. P. Netzer, C. Ambrosch-Draxl, and M. G. Ramsey. Electronic band structure of pentacene: An experimental and theoretical study. *Physical Review B*, 77:115312, 2008.

[193] N. Marom and L. Kronik. Density Functional theory of Transition Metal Phthalocyanines, I: Electronic Structure of NiPc and CoPc-Self-Interaction Effects. *Applied Physics A-Materials Science & Processing*, 95:159–163, 2009.

[194] L. Kümmel, S.and Kronik. Orbital-Dependent Density Functionals: Theory and Applications. *Reviews of Modern Physics*, 80:3–58, 2008.

[195] M. J. Allen and D. J. Tozer. Eigenvalues, Integer Discontinuities and NMR Shielding Constants in Kohn-Sham Theory. *Molecular Physics*, 100:433–439, 2002.

[196] I. Magid, L. Burstein, O. Seitz, L. Segev, L. Kronik, and Y. Rosenwaks. Electronic Characterization of Si(100)-Bound Alkyl Monolayers Using Kelvin Probe Force Microscopy. *Journal of Physical Chemistry C*, 112:7145–7150, 2008.

[197] L. Segev, A. Salomon, A. Natan, D. Cahen, L. Kronik, F. Amy, C. K. Chan, and A. Kahn. Electronic Structure of Si(111)-Bound Alkyl Monolayers: Theory and Experiment. *Physical Review B*, 74:165323–6, 2006.

[198] V. Perebeinos and M. Newton. Electronic Structure of S-C6H5 Self-Assembled Monolayers on Cu(111) and Au(111) Substrates. *Cchmical Physics*, 319:159–166, 2005.

[199] Y.-H. Kim, S. S. Jang, and W. A. Goddard. Conformations and Charge Transport Characteristics of Bbiphenyldithiol Self-Assembled-Monolayer Molecular Electronic Devices: A Multiscale Computational Study. *Journal of Chemical Physics*, 122: 244703, 2005.

[200] P. Pulay, G. Fogarasi, F. Pang, and J. E. Boggs. Sytematic Abinitio Gradient Calculation of Molecular Geometries, Force Constants, and Dipol-Moment Derivatives. *Journal of the American Chemical Society*, 101:2550–2560, 1979.

[201] G. Fogarasi, X. F. Zhou, P. W. Taylor, and P. Pulay. The Calculation of Abinitio Molecular Geometries - Efficient Optimization by Natural Internal Coordinates and Empirical Correction by Offset Forces. *Journal of the American Chemical Society*, 114:8191–8201, 1992.

[202] P. Pulay and G. Fogarasi. Geometry Optimization in Redundant Internal Coordinates. *Journal of Chemical Physics*, 96:2856–2860, 1992.

[203] J. Baker, A. Kessi, and B. Delley. The Generation and Use of Delocalized Internal Coordinates in Geometry Optimization. *Journal of Chemical Physics*, 105:192–212, 1996.

[204] J. Baker and P. Pulay. Geometry Optimization of Atomic Microclusters Using Inverse-Power Distance Coordinates. *Journal of Chemical Physics*, 105:11100–11107, 1996.

[205] H. B. Schlegel. *Ab initio methods in Quantum Chemistry Part 1*, chapter Optimization of Equilibrium Geometries and Transition Structures, pages 249–286. Wiley, 1987.

[206] E. F. Koslover and D. J. Wales. Geometry Optimization for Peptides and proteins: Comparison of Cartesian and Internal Coordinates. *Journal of Chemical Physic*, 127: 234105, 2007.

[207] K. N. Kudin, G. E. Scuseria, and H. B. Schlegel. A Redundant Internal Coordinate Algorithm for Optimization of Periodic Systems. *Journal of Chemical Physics*, 114: 2919–2923, 2001.

[208] J. Andzelm, R. D. King-Smith, and G. Fitzgerald. Geometry Optimization of Solids Using Delocalized Internal Coordinates. *Chemical Physics Letters*, 335:321–326, 2001.

[209] K. Németh and M. Challacombe. Geometry Optimization of Crystals by the Quasi-Independent Curvilinear Coordinate Approximation. *Journal of Chemical Physics*, 123:194112, 2005.